

The University of Sheffield



**Investigation of Parasitic Effects in Stator
Wound Field and Hybrid Excited
Synchronous Machines**

Xiaoyong Sun

A thesis submitted for the degree of Doctor of Philosophy

Department of Electronic and Electrical Engineering

The University of Sheffield

Mappin Street, Sheffield, S1 3JD, UK

May 2021

Abstract

Wound field and hybrid excited synchronous machines (WFSMs/HEMs) are good candidates for applications with variable-speed requirements due to controllable field excitation. The performances of WFSMs and HEMs are significantly influenced by not only machine topologies but also parasitic effects. This thesis comprehensively investigates the DC winding induced voltage pulsation, a significant parasitic effect, in stator WFSMs and HEMs, with particular emphasis on hybrid excited switched flux machines (HESFMs).

In this thesis, the investigations of the DC winding voltage pulsation initiate from the stator WFSMs and then extend to the HESFMs. Firstly, the phenomena and production mechanisms of the voltage pulsations under different conditions are investigated. It reveals that the on-load voltage pulsation contains two components, i.e., the open-circuit induced voltage and the armature current induced voltage, respectively. In the stator WFSMs, the open-circuit induced voltage is caused by the self-inductance harmonics of DC winding. While in HESFMs, due to the presence of PMs, the open-circuit induced voltage is caused by the self-inductance harmonics of DC winding and the equivalent mutual-inductance harmonics between DC winding and PMs. The armature current induced voltage is caused by the mutual-inductance harmonics between AC and DC windings in both stator WFSMs and HESFMs. The self- and mutual-inductance harmonics are introduced by the modulation effect of salient-pole rotors.

Further, the influences of stator slot and rotor pole number combinations and machine topologies on the DC winding voltage pulsations are investigated. It reveals that the voltage pulsations can be actively suppressed by selecting appropriate slot/pole number combinations and machine topologies to eliminate low-order induced voltage harmonics.

Finally, various rotor-based passive reduction methods are proposed and employed, including unequal rotor teeth, unevenly distributed rotor teeth, rotor step skewing, rotor pole arc pairing, rotor pole notching, and rotor pole shaping. Overall, all these methods can effectively reduce the DC winding voltage pulsation, cogging torque, back-EMF harmonics, and torque ripple, albeit with slight reduction of average on-load torque.

All theoretical and finite element analyses (FEA) have been validated by experiments.

Acknowledgements

Foremost, I would like to express my deepest gratitude to my supervisor, Professor Zi-Qiang Zhu, for his valuable technical discussions, guidance, and support during my PhD study. Without his help, it would be impossible for me to complete this PhD thesis. During my PhD study, Professor Zhu helped me develop good research habits and logical thinking skills, which laid a solid foundation for my future career development.

I would also like to thank all members of the Electrical Machines and Drives Group, The University of Sheffield, for their help and valuable discussions.

I would like to thank my parents for their financial support and other family members for their care. Although they are in China, I can feel their love all the time.

I would also like to express my special thanks to my wife, Shujuan Jia, for her continuous love and encouragement over the past 12 years, especially for her companionship and care in the UK over the past 5 years.

Finally, I would like to thank myself for my effort and persistence during my study at The University of Sheffield, U.K., over the past 8 and a half years, starting from my undergraduate study.

Contents

Abstract	I
Acknowledgements	II
Nomenclatures	VII
Abbreviations	X
CHAPTER 1.....	1
General Introduction.....	1
1.1 Permanent Magnet Machines	2
1.1.1 Rotor PM Machines.....	2
1.1.2 Stator PM Machines	8
1.2 Wound Field Synchronous Machines	14
1.2.1 Rotor Wound Field Synchronous Machines	14
1.2.2 Stator Wound Field Synchronous Machines.....	15
1.3 Hybrid Excited Synchronous Machines	17
1.3.1 Rotor Excitation HEMs	17
1.3.2 Stator Excitation HEMs.....	18
1.3.3 Partitioned Stator HEMs.....	25
1.3.4 Mixed Excitation HEMs.....	27
1.4 Typical Parasitic Effects in Synchronous Machines.....	29
1.4.1 Cogging Torque and Torque Ripple.....	29
1.4.2 Losses	30
1.4.3 PM Demagnetization	32
1.4.4 Uncontrolled Overvoltage Fault	33
1.4.5 Unbalanced Magnetic Force	33
1.4.6 Noise and Vibration	33
1.4.7 On-Load AC Winding Voltage Distortion	34
1.4.8 DC Winding Induced Voltage.....	35
1.4.9 Influence of DC Winding Induced Voltage	36
1.5 Research Scope and Contributions of Thesis	39
1.5.1 Research Scope.....	39
1.5.2 Major Contributions of Thesis.....	41
CHAPTER 2.....	44
Analysis of Excitation Winding Induced EMF in Non-Overlapped Stator Wound Field Synchronous Machines.....	44
2.1 Introduction	44

2.2 Machine Topology	48
2.3 Induced EMF in Excitation Winding.....	54
2.3.1 Phenomenon	54
2.3.2 Impact of Slot/Pole Combinations.....	57
2.4 Experimental Validation	73
2.5 Conclusion	79
CHAPTER 3.....	80
Investigation of DC Winding Induced Voltage in Hybrid Excited Switched Flux Permanent Magnet Machine	80
3.1 Introduction	81
3.2 Machine Topology	83
3.3 DC Winding Induced Voltage.....	86
3.3.1 Phenomenon	86
3.3.2 Open-Circuit Induced DC Winding Voltage.....	94
3.3.3 Armature Current Induced DC Winding Voltage.....	100
3.4 Reduction of On-Load DC Winding Induced Voltage.....	104
3.4.1 Rotor Step Skewing.....	104
3.4.2 Unequal Rotor Teeth.....	111
3.5 Experimental Validation	118
3.5.1 Prototype and Test Rig.....	118
3.5.2 Back-EMF	121
3.5.3 Open-Circuit DC Winding Induced Voltage.....	122
3.5.4 On-Load DC Winding Induced Voltage	125
3.6 Conclusion.....	128
CHAPTER 4.....	129
Influence of Stator Slot and Rotor Pole Number Combination on Field Winding Induced Voltage Ripple in Hybrid Excitation Switched Flux Machine	129
4.1 Introduction	130
4.2 Hybrid Excitation Switched Flux Machine	133
4.2.1 Machine Topology and Operation Principle.....	133
4.2.2 Feasible Stator Slot and Rotor Pole Number Combination.....	135
4.2.3 Armature Winding Connection.....	136
4.2.4 Torque Performance.....	140
4.3 Field Winding Induced Voltage Ripple.....	142
4.3.1 No-Load Induced Voltage.....	142

4.3.2 Armature Current Induced Voltage	152
4.3.3 On-Load Induced Voltage	160
4.3.4 Influence of PM Position	165
4.3.5 Influence of Field Winding Induced Voltage Ripple	169
4.4 Experimental Validation	172
4.4.1 Prototype and Test Rig	172
4.4.2 Back-EMF	174
4.4.3 No-Load Induced Voltage	176
4.4.4 On-Load Induced Voltage	179
4.5 Conclusion	182
CHAPTER 5.....	183
Analysis and Suppression of DC Winding Induced Voltage in Partitioned Stator Hybrid	
Excited Switched Flux Machines	183
5.1 Introduction	184
5.2 Machine Topology	186
5.3 DC Winding Induced Voltage	189
5.3.1 Phenomenon	189
5.3.2 Mechanism	197
5.3.3 Influence of Current Advance Angle	202
5.3.4 Influence of Slot/Pole Number Combination	204
5.4 Reduction of Open-Circuit DC Winding Induced Voltage	209
5.4.1 Rotor Pole Arc Pairing	209
5.4.2 Unevenly Distributed Rotor Teeth	214
5.5 Reduction of On-Load DC Winding Induced Voltage	221
5.5.1 Rotor Pole Arc Pairing	221
5.5.2 Unevenly Distributed Rotor Teeth	228
5.6 Experimental Validation	233
5.7 Conclusion	236
CHAPTER 6.....	237
Voltage Pulsation Induced in DC Field Winding of Different Hybrid Excitation Switched	
Flux Machines	237
6.1 Introduction	237
6.2 Hybrid Excitation Switched Flux Machine Topologies	241
6.2.1 Machine Topologies	241
6.2.2 Operation Principles	243

6.3 Voltage Pulsation Induced in DC Field Winding.....	245
6.3.1 No-load Induced Voltage	245
6.3.2 AC Current Induced Voltage.....	253
6.3.3 On-load Induced Voltage	258
6.3.4 Influence of Phase Current Advance Angle.....	262
6.4 Suppression of On-load Induced Voltage Pulsation in Field Winding	265
6.4.1 Rotor Step Skewing.....	266
6.4.2 Rotor Pole Notching	268
6.4.3 Rotor Pole Shaping.....	270
6.4.4 Comparison of Suppression Methods.....	272
6.5 Experimental Validation	277
6.6 Conclusion.....	283
CHAPTER 7.....	284
General Conclusions and Future Work.....	284
7.1 General Conclusions.....	284
7.1.1 Phenomena and Production Mechanisms	284
7.1.2 Major Influential Factors	286
7.1.3 Suppression Methods.....	289
7.2 Future Work.....	291
References.....	292
Appendix A: Potential to Eliminate Excitation Winding Induced EMF Using Open-Winding	309
Appendix B: Analytical Derivations of DC Winding Induced Voltage Harmonic Orders for HESFMs and PS-HESFMs	319
Appendix C: Mesh of the Investigated HE3 Machine.....	322
Publications	323

Nomenclatures

A	Cross-sectional area	mm^2
B_m	Amplitude of flux density	T
B_r	Radial air-gap flux density	T
B_t	Tangential air-gap flux density	T
C_T	Goodness factor	-
E_e	Open-circuit phase fundamental back-EMF under positive field current	V
E_f	DC winding induced voltage pulsation	V
E_{PM}	Open-circuit phase fundamental back-EMF under sole PM excitations	V
E_w	Open-circuit phase fundamental back-EMF under negative field current	V
f	Fundamental electrical frequency	Hz
f_p	Air-gap radial magnetic force density	N/mm^2
I_{ac}	Armature current	A
i_d	D -axis current	A
i_{dc}	Field current	A
i_q	Q -axis current	A
I_{rms}	RMS value of current	A
J_{dc}	DC winding slot current density	A/mm^2
k_c	Classic eddy current loss coefficient	W/m^3
k_e	Excess eddy current loss coefficient	W/m^3
k_h	Hysteresis loss coefficient	W/m^3

k_{pf}	Slot packing factor	-
L	Length of conductor	mm
l_a	Active axial length	mm
L_d	D -axis inductance	mH
L_q	Q -axis inductance	mH
m	Armature winding phase number	-
M_{df}	Mutual inductance between d -axis and field windings	mH
N_{dc}	Number of turns for each DC coil	-
N_r	Rotor pole number	-
N_s	Stator slot number	-
p	Rotor pole-pair number	-
P_{cu}	Copper loss	W
P_{cuf}	Field winding copper loss	W
P_{cut}	Total copper loss	W
P_{fe}	Iron loss	W
P_m	Mechanical loss	W
R	Resistance	Ω
R_{dc}	DC winding resistance	Ω
S_b	DC winding slot area for coil side	mm ²
T_{ave}	Average on-load electromagnetic torque	Nm
T_{max}	Maximum on-load electromagnetic torque	Nm

T_{min}	Minimum on-load electromagnetic torque	Nm
α	Current advance angle	rad
θ_e	Rotor electrical position	rad
θ_m	Rotor mechanical position	rad
μ_o	Permeability of free space	H/m
ρ_{cu}	Electrical resistivity of copper	$\Omega \cdot m$
Ψ_d	D-axis flux-linkage	mWb
Ψ_f	DC winding flux-linkage	mWb
Ψ_q	Q-axis flux-linkage	mWb
ω_e	Electrical angular velocity	rad/s
Ω_e	Rotor electrical speed	rpm
ω_m	Mechanical angular velocity	rad/s
Ω_m	Rotor mechanical speed	rpm

Abbreviations

2D	Two dimensional
3D	Three dimensional
AC	Alternating current
CPSR	Constant power speed range
DC	Direct current
DSPM	Doubly salient permanent magnet
EMF	Electromotive force
EV	Electrical vehicle
FEA	Finite element analysis
FRPM	Flux reversal permanent magnet
HEM	Hybrid excited machine
HEV	Hybrid electrical vehicle
IM	Induction machine
IPM	Interior permanent magnet
LCM	Least common multiple
MMF	Magnetomotive force
NdFeB	Neodymium iron boron
PM	Permanent magnet
PMSM	Permanent magnet synchronous machine
PS	Partitioned stator

RMS	Root mean square
RWFSM	Rotor wound field synchronous machine
SFPM	Switched flux permanent magnet
SMC	Soft magnetic composite
SPM	Surface mounted permanent magnet
SRM	Switched reluctance machine
SSPM	Stator slot permanent magnet
SWFSM	Stator wound field synchronous machine
UMF	Unbalanced magnetic force
WFSFM	Wound field switched flux machine
WFSM	Wound field synchronous machine

CHAPTER 1

General Introduction

Permanent magnet (PM) machines, especially those equipped with rare-earth PMs, exhibit high torque/power density, high efficiency, and high power-factor [CHA07] [ZHU07a] [CHA08]. Therefore, PM machines have been developed and applied to various applications, ranging from hybrid electrical vehicles/electrical vehicles (HEVs/EVs) through domestic appliances to aerospace etc. [ZHU07a] [ZWY09] [CAO12]. However, PM machines are still confronted with some challenges. PM machines suffer from relatively poor flux-weakening performance since the PMs excitation is fixed. For applications with variable-speed requirements, e.g., HEVs/EVs, excellent flux-weakening capability is essential for wide constant power speed range (CPSR) and hence high-speed operation [CHA07] [BIA16]. To operate beyond the base speed, the control strategy with negative d -axis current ($-i_d$) is generally required in PM machines for flux-weakening since the power inverters have current and voltage limits [SOO94] [ELR05]. With $-i_d$ control strategy, the efficiency and power factor under high-speed region may be reduced and $-i_d$ component has the potential to irreversibly demagnetize the PMs [SOO02]. Besides, the drive system may be damaged by uncontrolled generator fault if the control signals of power switches disappear at high speed [JAH99] [LIA05] [RAM11].

Wound field synchronous machines (WFSMs) are potential candidates for variable-speed applications since the excitation field can be flexibly controlled by DC current [LIU12a] [CHU14a]. Moreover, due to the PM-free structure, WFSMs are also suitable for cost-sensitive applications [SUL11] [GAU12] [JIA16a]. However, compared with PM machines, WFSMs feature reduced torque/power density, reduced efficiency, and lower power factor due to pure DC excitation [CHU14a].

As an alternative solution to the issues associated with PM machines and WFSMs, hybrid excited machines (HEMs) having both PMs and DC coils have been emerged. Due to the synergy of PMs excitation and DC excitation, HEMs inherit high torque density from PM

machines as well as excellent flux-controllability from WFSMs [HEN94] [AMA11] [ZHA12] [AFI15]. Due to the introduction of DC excitation, the peak torque at low-speed can be enhanced by positive DC current, whilst for high-speed operation the PM induced back-EMF can be counteracted using negative DC current, or simply reducing the DC current excitation since the PM induced back-EMF is usually designed to be low in HEMs. Besides, the flux-weakening control strategy is more flexible in HEMs since an additional control parameter, i.e., DC current (i_{dc}) component, is introduced [CHU15]. With appropriate control strategies, the operating speed range and high efficiency operation region can be considerably extended in HEMs compared with pure PM machines [ZHA15b] [KEF10] [POT19]. Moreover, by controlling DC excitation, the uncontrolled generator fault at high speed can be mitigated in HEMs [ZHU19b].

This thesis investigates the parasitic effects in wound field and hybrid excited synchronous machines, with a particular focus on DC winding induced voltage.

This chapter firstly reviews various synchronous machine topologies, including PM machines, WFSMs, and HEMs. Then, typical parasitic effects associated with synchronous machines are introduced, with a particular emphasis on DC winding induced voltage, which is the focus of this thesis. Finally, the research outline and major contributions of this thesis are highlighted.

1.1 Permanent Magnet Machines

In this section, various pure PM machine topologies having PMs in rotor or stator side will be introduced.

1.1.1 Rotor PM Machines

According to the location of PMs, PM machines can be broadly divided into two categories, i.e., rotor PM machines and stator PM machines. Rotor PM machines are very conventional and popular PM machine topologies, in which the PMs are positioned in rotor side while the

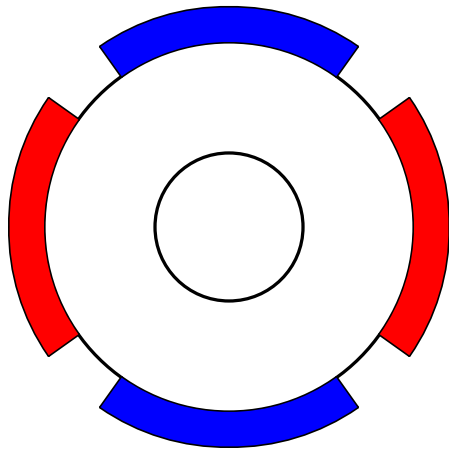
armature windings are wound on stator [ZHU07a] [CHA08]. As shown in Fig. 1.1, based on the configuration of PMs in rotor core, rotor PM topologies can be further categorized into surface-mounted PM (SPM), surface-inset PM (Inset-PM), I-shape interior PM (I-IPM), V-shape interior PM (V-IPM), and spoke-shape interior PM (Spoke-IPM).

In SPM machines, Fig. 1.1(a), the PMs are affixed to the surface of rotor core. As such, SPM machines feature relatively large equivalent air-gap length and hence small armature reaction and inductance as the relative permeability of PMs is low and close to that of air. In SPM machines, the PMs can either radially or parallelly magnetized. The PM demagnetization withstand capability is relatively weak in SPM machines as the PMs directly face the air-gap. SPM machines exhibit negligible reluctance torque since the difference between d -axis and q -axis inductances is negligible. For high-speed applications, non-magnetic sleeves are usually required for SPM machines to retain PMs and increase the mechanical strength.

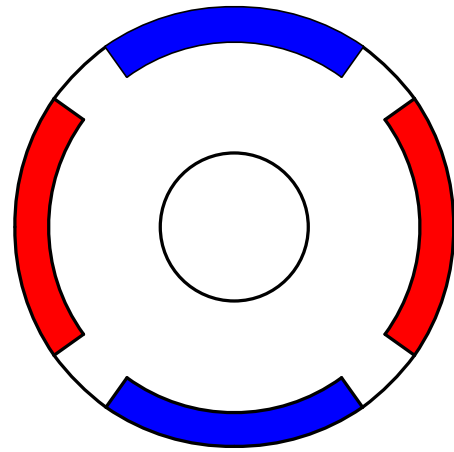
As shown in Fig. 1.1(b), for inset-PM machines, the PMs are inset into the surface of rotor core. Therefore, inset-PM machines possess relatively poor demagnetization withstand capability, which is similar to that of SPM machines. Reluctance torque component can be utilized in inset-PM machines since the relative permeability of iron poles is significantly higher than that of PM poles. Compared with SPM machines, the PM flux-leakage in inset-PM machines may be increased due to the introduction of iron poles but the assembly of PMs is much easier.

For I-IPM machines, the PMs are embedded in the rotor core as shown in Fig. 1.1(c). I-IPM machines feature relatively good demagnetization withstand capability since the rotor core can protect the PMs. Reluctance torque can be utilized in I-IPM machines due to rotor saliency. To balance the mechanical strength and the PM flux-leakage, the design of iron bridges in rotor side should be well considered.

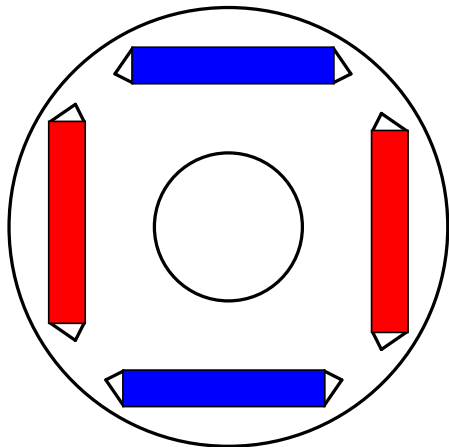
In spoke-IPM machines, Fig. 1.1(e), the PMs are circumferentially magnetized and buried in the rotor core. Spoke-IPM machines exhibit reluctance torque component and good demagnetization withstand capability, which is similar to that of I-IPM machines. Besides, spoke-IPM machines feature flux-focusing effect and hence high torque density, i.e., the flux of one-pole in the air-gap is excited by two adjacent PMs. However, due to the utilization of iron bridges, spoke-IPM machines exhibit relatively large PM flux-leakage. V-IPM machines, Fig. 1.1(d), as one variation of I-IPM machines, can still utilize reluctance torque and flux-focusing effect to enhance the output torque/power.



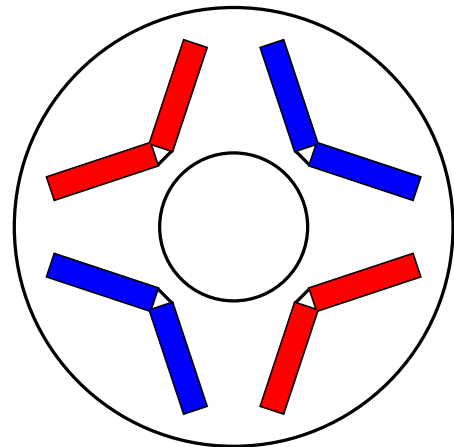
(a) SPM



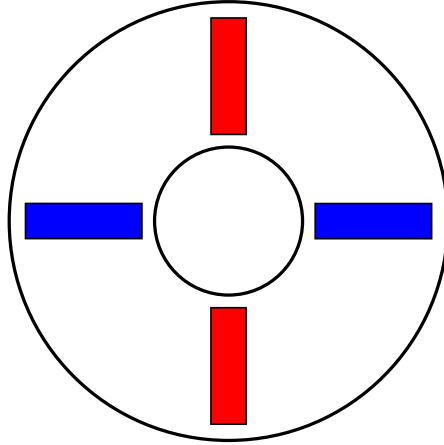
(b) Inset-PM



(c) I-IPM



(d) V-IPM



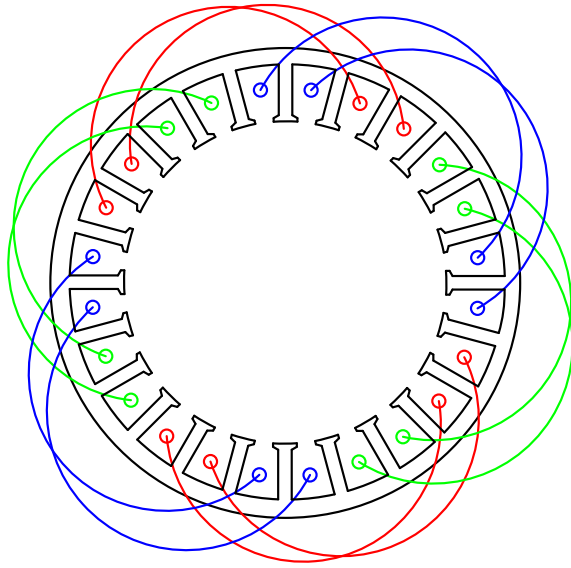
(e) Spoke-IPM

Fig. 1.1. PM rotor topologies [ZHU07a] [CHA08].

For the PM rotor topologies shown in Fig. 1.1, there are two commonly used stator winding topologies, i.e., overlapping windings, Fig. 1.2, and non-overlapping windings, Fig. 1.3 [ZHU07a] [ELR10]. According to the number of slots per pole per phase, i.e., q , PM machines fall into two categories, i.e., integer-slot machines and fractional-slot machines. Taking a three-phase PM machine having 24-slot/4-pole, Fig. 1.2(a), as an example, q is an integer in this machine, i.e., $q=2$. Therefore, the three-phase 24-slot/4-pole PM machine is an integer-slot machine. Similarly, a three-phase PM machine having 12-slot/4-pole, Fig. 1.2(b), is an integer-slot machine as well since q is an integer, i.e., $q=1$.

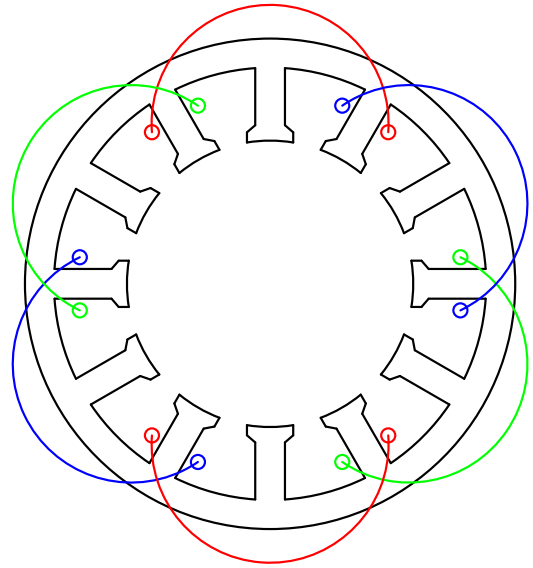
For integer-slot PM machines, overlapping windings are usually employed to obtain higher winding factor and hence better torque performance [CHE00] [POL06]. For integer-slot PM machines having overlapping windings, the reluctance torque component can be utilized to increase the output torque/power density. Moreover, the air-gap field excited by armature windings contains less high-order harmonics, which is beneficial for the reduction of torque ripple, loss, and noise. However, the PM machines with overlapping windings often suffer from longer end-winding and axial lengths, higher copper loss, and lower fault-tolerant capability.

For fractional-slot PM machines, q is a fraction. For example, the three-phase 6-slot/4-pole PM machine shown in Fig. 1.3 is a fractional-slot PM machine since q is a fraction, i.e., $q=0.5$. Non-overlapping windings are usually used for fractional-slot PM machines to achieve high winding factor as well as short end-winding and axial lengths [BIA06b]. The stator teeth can be all wound, Fig. 1.3(a), or alternately wound, Fig. 1.3(b), which are often referred to as double layer or single layer windings, respectively. Fractional-slot PM machines with non-overlapping windings always exhibit shorter end-winding and axial lengths, lower copper loss, and higher fault-tolerant capability. Besides, fractional-slot PM machines also feature high slot filling factor and low cogging torque. However, the abundant air-gap field harmonics in fractional-slot PM machines tend to cause additional parasitic effects [ISH06] [ELR10].



(a) Overlapping distributed winding

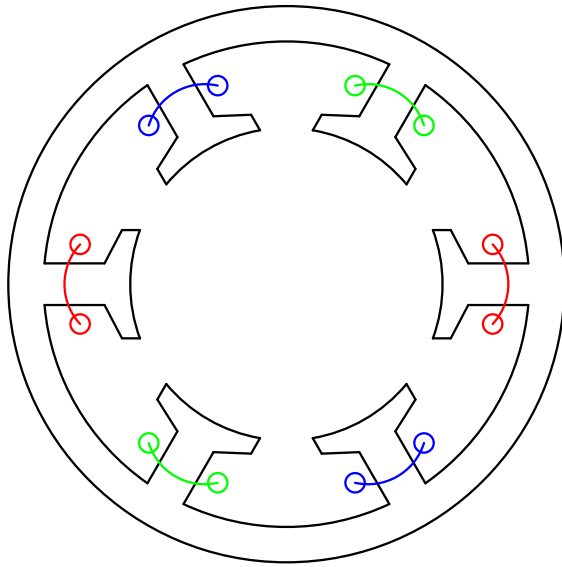
(24-slot/4-pole, $q=2$)



(b) Overlapping concentrated winding

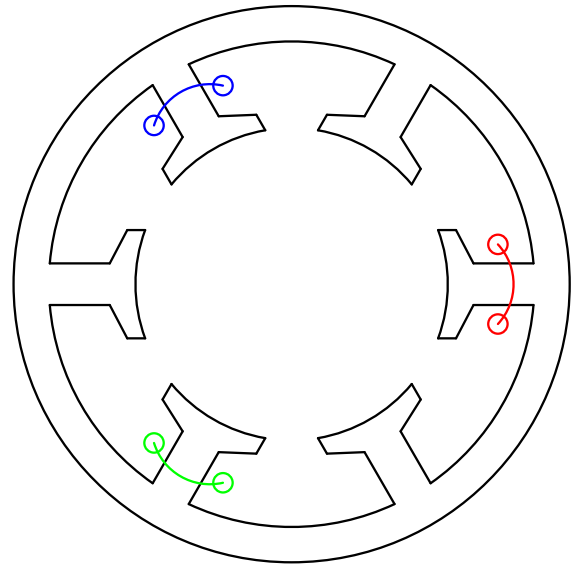
(12-slot/4-pole, $q=1$)

Fig. 1.2. Overlapping winding topologies [ZHU07a] [ELR10].



(a) Non-overlapping double layer winding

(6-slot/4-pole, $q=0.5$)



(b) Non-overlapping single layer winding

(6-slot/4-pole, $q=0.5$)

Fig. 1.3. Non-overlapping winding topologies [ZHU07a] [ELR10].

1.1.2 Stator PM Machines

In stator PM machines, the PMs and armature coils are both arranged in stator side [CHE11b]. As such, salient-pole rotors without any PMs or windings are always employed. Salient-pole rotors are very simple, robust, and easy to manufacture. Therefore, stator-PM machines share some common features, which can be summarized as follows:

- Salient-pole rotors are purely iron-cored and do not contain any PMs or windings, which makes them promising for both low-speed/high-torque and relatively high-speed applications;
- Non-overlapping windings are usually employed in stator PM machines for shorter end-winding/axial lengths, lower copper loss, and higher packing factor;
- Since all active parts, i.e., armature coils and PMs, are positioned in stator side, the thermal management is easier. Effective and advanced cooling techniques can be employed to deal with the temperature rise of PMs since it is much easier to remove heat from stationary PMs than that from rotating PMs;
- PM excited torque is the dominating torque component while the reluctance torque component is normally negligible.

According to the location of PMs in stator side, stator PM machines mainly fall into four typical groups, i.e., doubly salient PM machines, switched flux PM machines, flux reversal PM machines, and magnet in stator slot PM machines. Each group has its own characteristics, which will be introduced in detail as follows.

1.1.2.1 Doubly Salient PM Machines

As derived from the conventional switched reluctance machines (SRMs), the doubly salient PM (DSPM) machines are obtained by inserting PMs into the stator yokes. For example, the three-phase 6-slot/4-pole DSPM machine shown in Fig. 1.4(a) can be obtained by inserting two PM pieces with circumferential magnetization direction into the stator yokes of the 6-slot/4-pole SRM [LIA95]. As such, DSPM machines feature improved torque performance compared with the conventional SRMs. However, due to asymmetric flux paths in armature windings, the DSPM machine shown in Fig. 1.4(a) suffers from asymmetric phase back-EMFs and hence high torque ripple. To achieve symmetrical flux paths and back-EMFs in phase windings, the DSPM machine with “T-shape” stator core segment can be employed as shown in Fig. 1.4(b) [WU14]. As such, the torque ripple can be significantly reduced but the PM usage efficiency is reduced as well. Besides, the conventional full bridge converter can be used to drive such DSPM machines since the armature windings feature bipolar AC excitation. Although the torque density is enhanced compared with the conventional SRMs, DSPM machines exhibit limited torque/power density due to unipolar coil flux-linkage. The manufacturing and assembly of DSPM machines are also very challenging since the stator core is modular due to inserted PMs in stator yokes.

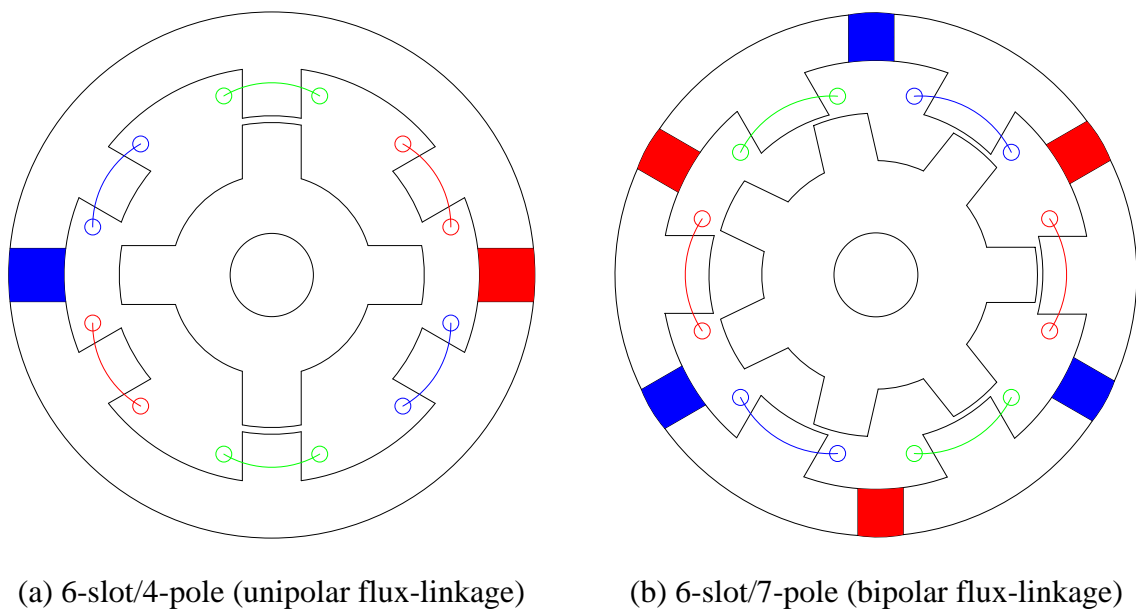


Fig. 1.4. Doubly salient PM machines [LIA95] [WU14].

1.1.2.2 Flux Reversal PM Machines

In flux reversal PM (FRPM) machines, the PMs are mounted on the surface of stator tooth tips as shown in Fig. 1.5. The single-phase FRPM machine is firstly developed in [DEO97], as shown in Fig. 1.5(a). Subsequently, the three-phase counterpart is proposed in [WAN99]. Fig. 1.5(b) shows a conventional three-phase 12-slot/14-pole FRPM machine having two PM pieces on the inner surface of stator tooth tips. FRPM machines feature bipolar coil flux-linkage and hence higher torque density compared with DSPM machines. Besides, the manufacturing and assembly of stators in FRPM machines are much simpler and easier than the modular stators of DSPM machines. However, FRPM machines may suffer from high PM eddy current loss and high risk of PM demagnetization as the PMs directly face the air-gap having abundant field harmonics. Moreover, FRPM machines feature relatively large equivalent air-gap length, which may restrict the modulation effect of rotor teeth and hence the torque density.

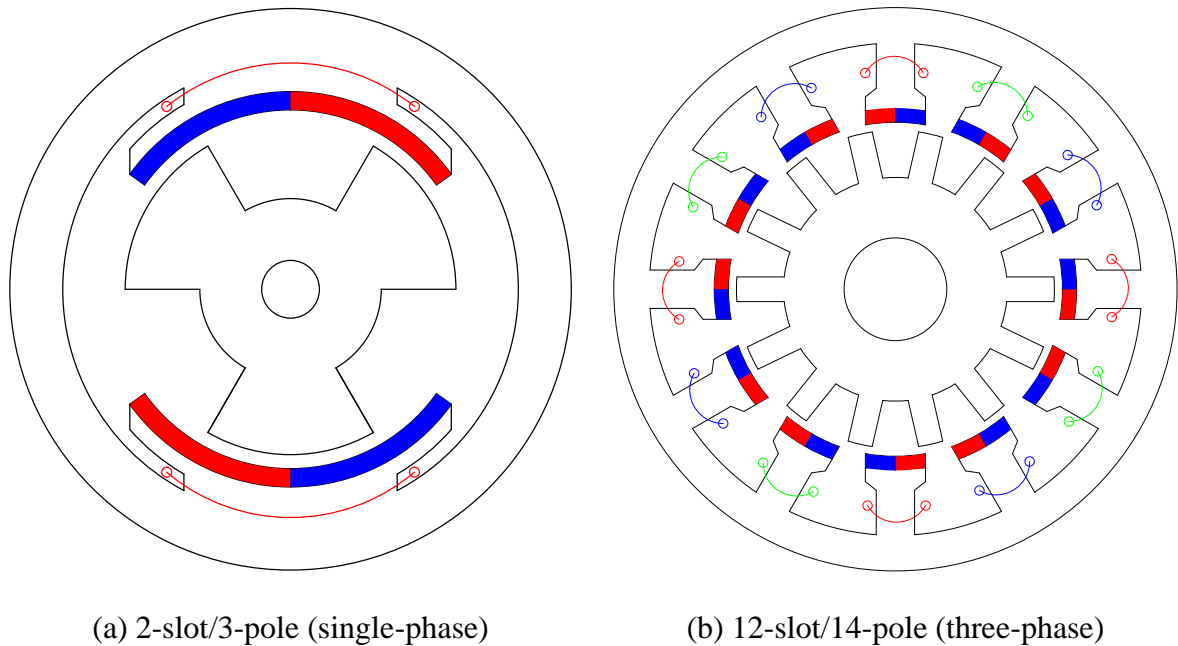


Fig. 1.5. Flux reversal PM machines [DEO97] [WAN99].

1.1.2.3 Switched Flux PM Machines

The switched flux PM (SFPM) machines are developed based on the “switched-flux” principle proposed in a single-phase alternator in 1955 [RAU55]. Fig. 1.6(a) shows a conventional three-phase 12-slot/10-pole SFPM machine having U-core stator segment and the PMs are inserted into the stator teeth [HOA97]. The SFPM machines exhibit bipolar phase flux-linkage, more sinusoidal phase back-EMF, and hence low torque ripple. The SFPM machines also feature high torque density since the flux-focusing effect is utilized, similar to the spoke-IPM shown in Fig. 1.1(e), and thus, the SFPM machines have drawn increasing interest in the past two decades [CHE10a] [CHE10b] [CHE10c]. One variant of the U-core SFPM machine is the C-core SFPM machine, Fig. 1.6(b), in which the number of stator slots is reduced by half and therefore the stator segment is of C-core shape [CHE11c]. It has been proved that the torque density and the PM usage efficiency have been significantly improved in the C-core SFPM machine compared with the U-core counterpart. Based on the C-core stator segment, a novel E-core SFPM machine is achieved by introducing additional stator teeth as shown in Fig. 1.6(c) [CHE11d]. It has shown that the E-core machine can offer higher torque density than the conventional U-core machine. However, its torque density is lower than the C-core machine. Besides, a novel multi-tooth SFPM machine is proposed in [ZHU08], Fig. 1.6(d), for direct-drive high-torque applications. However, the SFPM machines may suffer from highly-saturated stator core, which restricts their overload capabilities. Similar to the DSPM machines, the SFPM machines feature modular stator core as well, which increases the difficulty and cost of manufacturing and assembly.

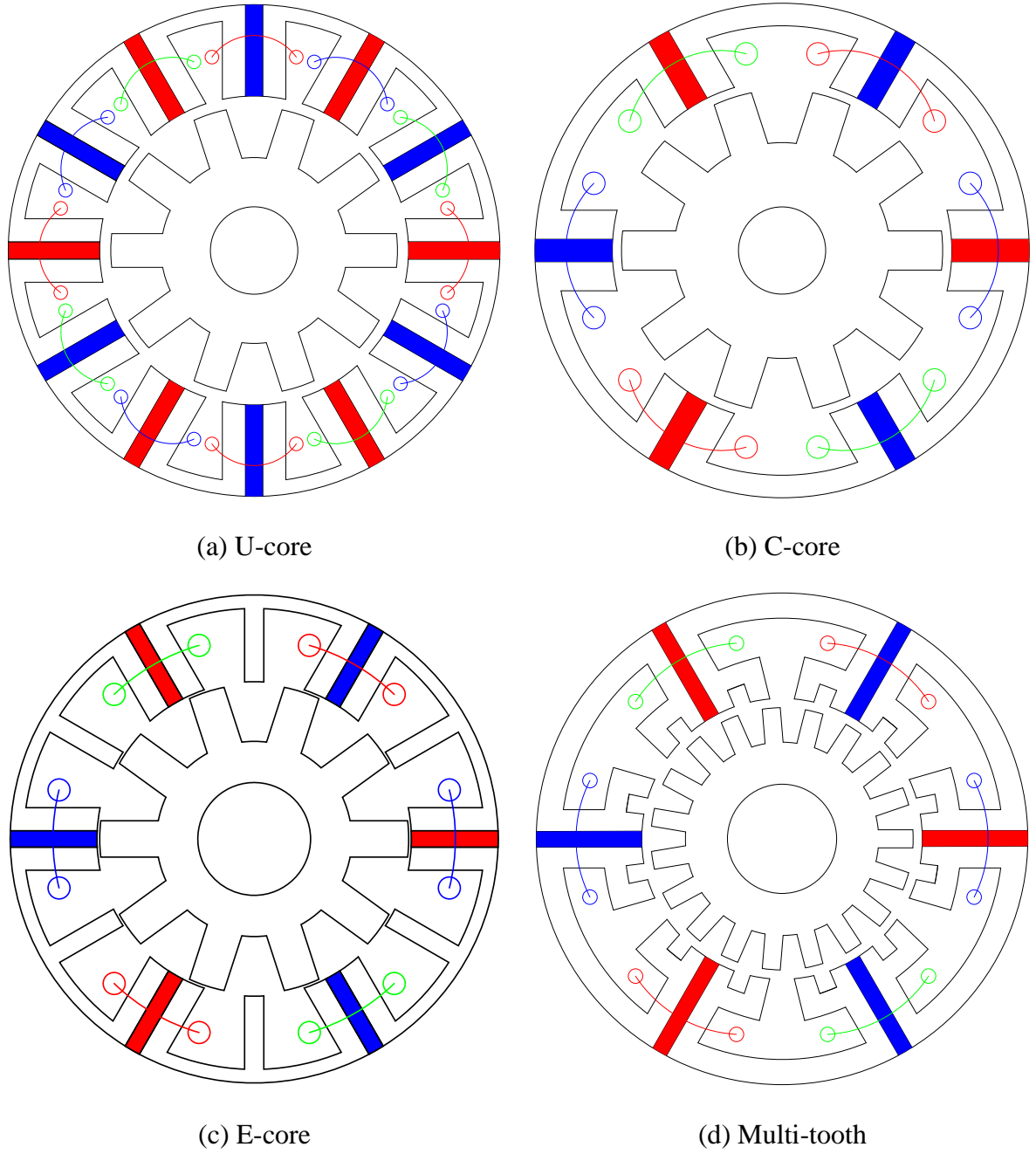


Fig. 1.6. Switched flux PM machines [HOA97] [CHE11c] [CHE11d] [ZHU08].

1.1.2.4 Magnet in Stator Slot PM Machines

To further improve the torque density of the conventional SRMs, the magnet in stator slot PM (SSPM) machines are emerged. Fig. 1.7(a) shows a three-phase 12-slot/8-pole SSPM machine, which is developed from the conventional SRM with 12-slot/8-pole by positioning the circumferentially magnetized PMs in the slot openings of stator [NAK07]. The aim of using such PMs is to mitigate the magnetic saturation in stator core and hence to further increase the output torque. It has shown that the torque density of the SSPM with 12-slot/8-pole is 25% higher than the SRM counterpart under the same unipolar armature excitations. If the armature windings are excited by bipolar AC currents, more stator slot and rotor pole number combinations will be available, e.g., the 12-slot/10-pole counterpart, Fig. 1.7(b) [AFI16]. The SSPM machines feature negligible phase back-EMFs at open-circuit since the main fluxes of the PMs are self-short-circuited in stator side and hardly pass the rotor. Such feature makes the SSPM machines very suitable for applications with high fault-tolerant requirements. However, the SSPM machines may suffer from high risk of PM demagnetization since the PMs are adjacent to the air-gap. Besides, the magnets are adjacent to the stator armature windings, which often have the highest temperature. As such, the magnets will also experience elevated temperature, leading to possible irreversible demagnetizations.

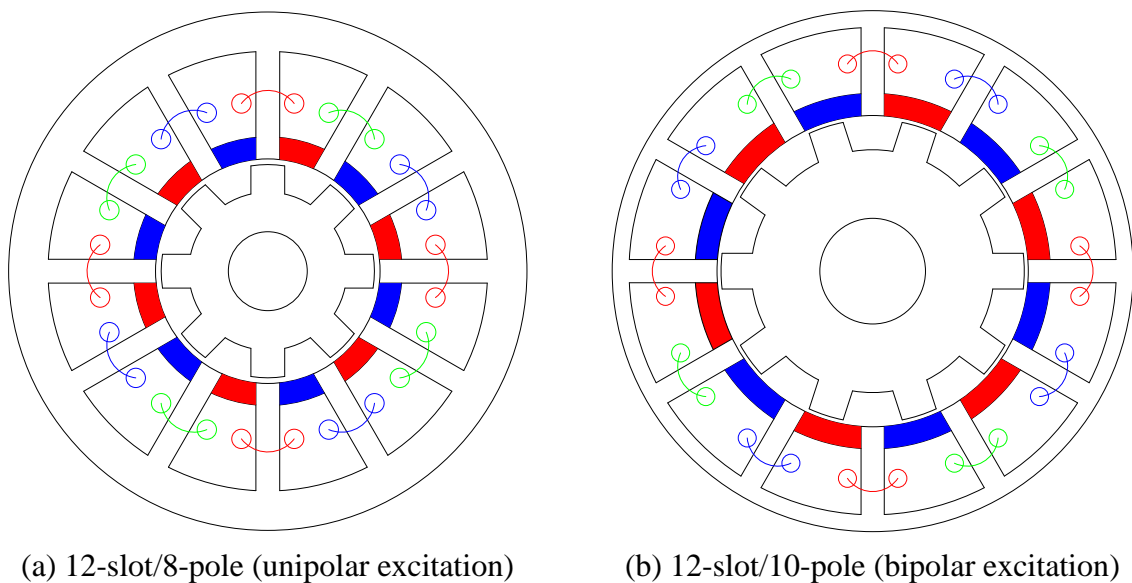


Fig. 1.7. Magnet in stator slot PM machines [NAK07] [AFI16].

1.2 Wound Field Synchronous Machines

In this section, various wound field synchronous machines having DC windings in rotor or stator side will be introduced.

1.2.1 Rotor Wound Field Synchronous Machines

Rotor wound field synchronous machines (RWFSMs) are very conventional synchronous machine topologies, in which the field coils are allocated in rotor side while the armature coils are positioned in stator side [BAS11] [LIU12] [ELR13]. Fig. 1.8 shows a conventional 48-slot/8-pole RWFSM. Due to the PM-free structure, the RWFSM possesses good flux-controllability and is relatively low-cost. It has been shown that the RWFSM can exhibit a wider constant power speed range (CPSR) than that of an IPM machine [CHU14b]. Compared with PM machines, the most obvious drawbacks of RWFSMs are relatively low torque/power density and low efficiency. Moreover, the slip rings and brushes are required for field excitation, which potentially reduces the reliability and efficiency of the system. Special attention should be paid to the thermal management of rotor side, since the rotor side suffers from copper loss.

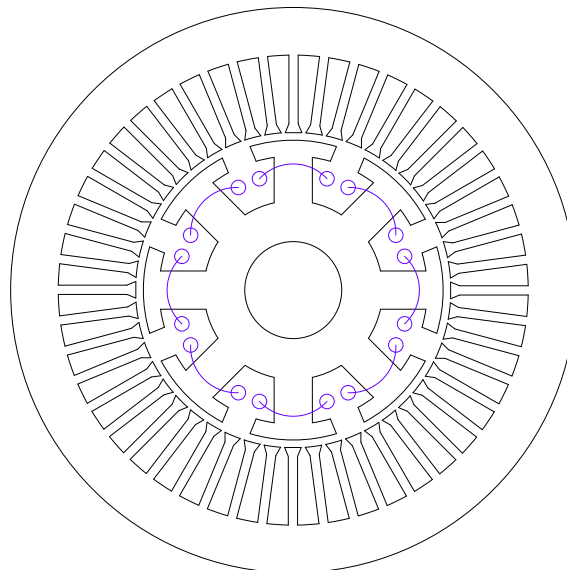
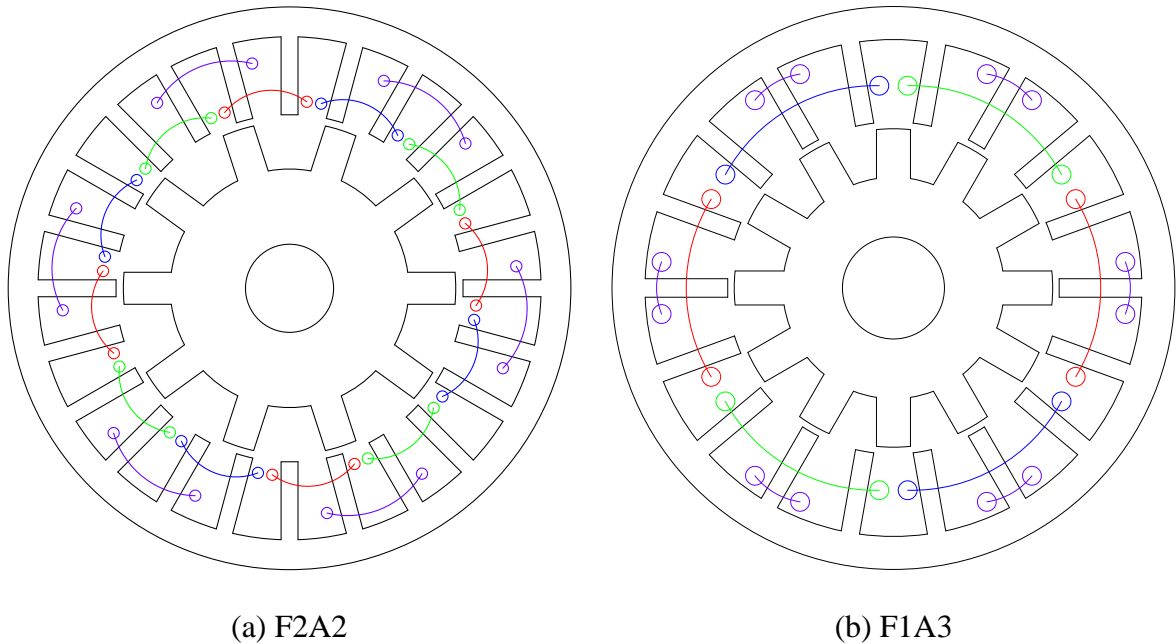
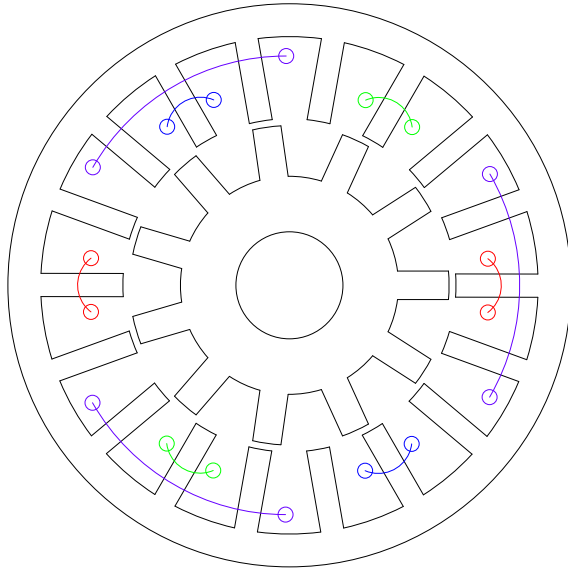


Fig. 1.8. Rotor wound field synchronous machine [ELR13].

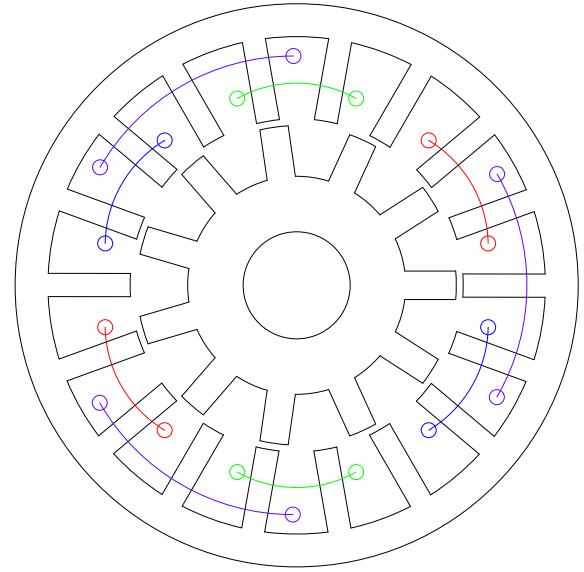
1.2.2 Stator Wound Field Synchronous Machines

In stator wound field synchronous machines (SWFSMs), the field and armature windings are arranged in stator side, which is different from the RWFSMs [POL99]. Fig. 1.9 shows some typical SWFSMs having different armature and field coil pitches [SUL11] [ZHO14a] [ZHO14b] [ZUL10] [KAH14] [ZHU15a]. The sliding contacts are eliminated in SWFSMs since the field coils are positioned in stator side. SWFSMs exhibit good flux regulation/flux weakening capability due to controllable field current. Moreover, the salient-pole rotors are very simple and robust, which is beneficial to high-speed operation and thermal management. However, SWFSMs may suffer from high core loss caused by the modulation of the salient-pole rotors. The torque density of SWFSMs may be reduced due to the spatial conflict between armature and field coils in stator side. Besides, SWFSMs may also suffer from limited overload capability due to serious stator magnetic saturation. As shown in Figs. 1.9(a)-(d), these SWFSMs feature long end-winding length of armature or field coils, which increases the copper loss and may reduce the efficiency. The SWFSM shown in Fig. 1.9(e) employs non-overlapping armature and field coils, resulting in short end-winding length, low copper loss and hence high efficiency.

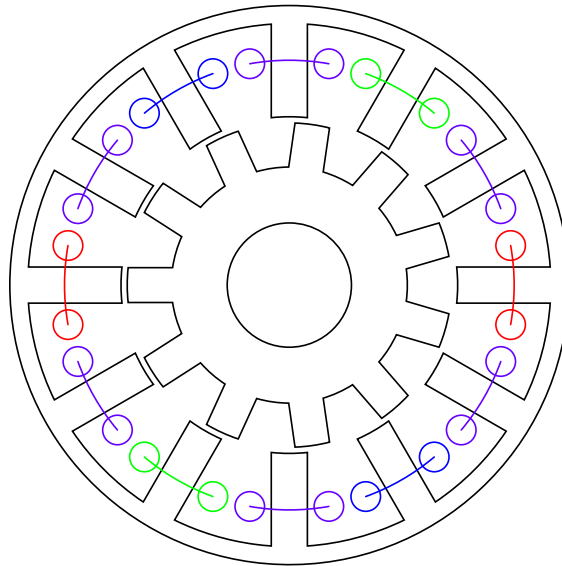




(c) F3A1



(d) F3A2



(e) F1A1

Fig. 1.9. Stator wound field synchronous machines having different armature and field coil pitches [POL99] [SUL11] [ZHO14a] [ZHO14b] [ZHU15a].

1.3 Hybrid Excited Synchronous Machines

In this section, various hybrid excited machines (HEMs) will be introduced. Based on the location of PMs and DC coils, HEMs can be divided into different groups as illustrated in Fig. 1.10, which will be introduced in detail as follows.

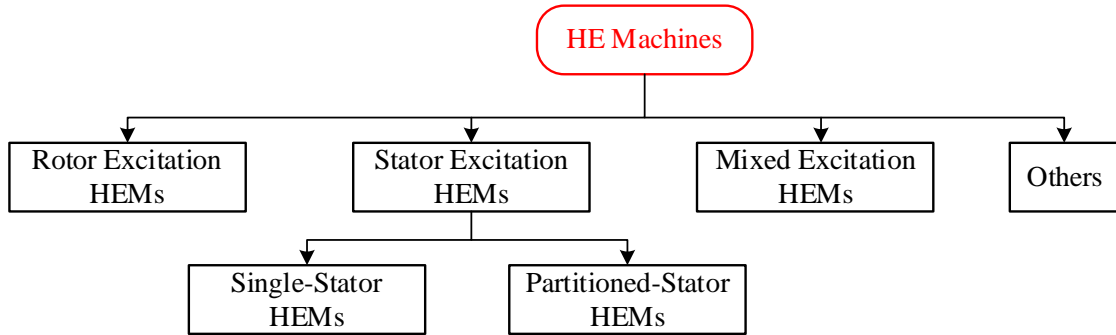
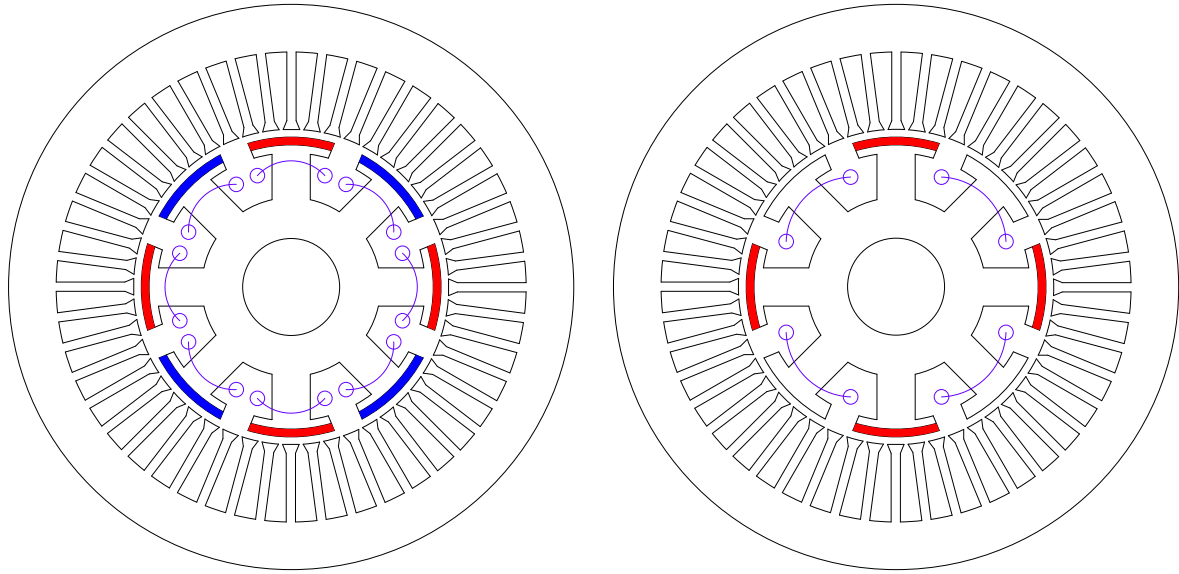


Fig. 1.10. Classification of HEMs based on the location of PMs and DC coils.

1.3.1 Rotor Excitation HEMs

Most of the rotor excitation HEMs are derived from the conventional rotor PM machines or RWFSMs by introducing DC coils or PMs in rotor side. Therefore, the rotor excitation HEMs can be perceived as the integration of rotor PM machines and RWFSMs. Fig. 1.11 shows two typical rotor excitation HEMs derived from the conventional rotor SPM machines [HEN94] [FOD07] [AKE00]. In rotor excitation HEMs, the armature coils are arranged in stator side while the PMs and DC coils are allocated in rotor side. Compared with the rotor PM machines, the rotor excitation HEMs exhibit better flux-controllability but reduced torque density due to the introduction of DC coils. Compared with the RWFSMs, the rotor excitation HEMs feature improved torque density but slightly reduced flux-regulation capability due to the spatial conflict between PMs and DC coils in rotor side. Overall, the rotor excitation HEMs exhibit high torque density and good flux-controllability. However, similar to the RWFSMs, the most obvious drawback of the rotor excitation HEMs shown in Fig. 1.11 is the requirement for slip rings and brushes, which degrades the reliability and efficiency of the system. Although the sliding contacts can be eliminated in some rotor excitation HEMs by introducing the harmonic winding and the rectifier in rotor side to feed DC current, the machine structure and drive circuit have been further complicated [ALI16] [HUS18].



(a) All-pole PM rotor

(b) Consequent-pole PM rotor

Fig. 1.11. Rotor excitation HEMs [HEN94] [FOD07] [AKE00].

1.3.2 Stator Excitation HEMs

Different from the rotor excitation HEMs, the PMs and DC coils are positioned in stator side in the stator excitation HEMs. As such, salient-pole rotors are employed in stator excitation HEMs to modulate the magnetic field generated by PMs and DC coils and hence generate the phase back-EMFs. Obviously, the slip rings and brushes are eliminated in stator excitation HEMs since the DC coils are arranged in stator side. Besides, the thermal management is easier in stator excitation HEMs since all active components are allocated in stator. According to the arrangement of PMs and DC coils in stator side, the stator excitation HEMs can be broadly divided into five typical groups, i.e., doubly salient HEMs, flux reversal HEMs, switched flux HEMs, stator slot HEMs, and partitioned stator HEMs. This classification method is very similar to that used for stator PM machines shown in section 1.1.2.

1.3.2.1 Doubly Salient HEMs

Doubly salient HEMs are derived from the conventional doubly salient PM machines by introducing DC coils in stator side. Fig. 1.12(a) shows a conventional doubly salient HEM, in which the DC excited flux passes through the PMs, i.e., series hybridization [LI95]. Fig. 1.12(b) shows an improved doubly salient HEM, in which the PMs are arranged in stator yoke and the PM usage is significantly reduced [CHA02]. However, due to series hybridization, this machine suffers from limited flux regulation capability and potential PM irreversible demagnetization. To achieve parallel hybridization in doubly salient HEMs, various methods have been proposed, including the introduction of additional air-gap and flux-bridge etc. [CHA03] [ZHU05] [ZHU06]. For the doubly salient HEMs with parallel hybridization, i.e., the paths of DC flux and PM flux are different, the flux regulation capability is improved whilst the PM demagnetization withstand capability is enhanced.

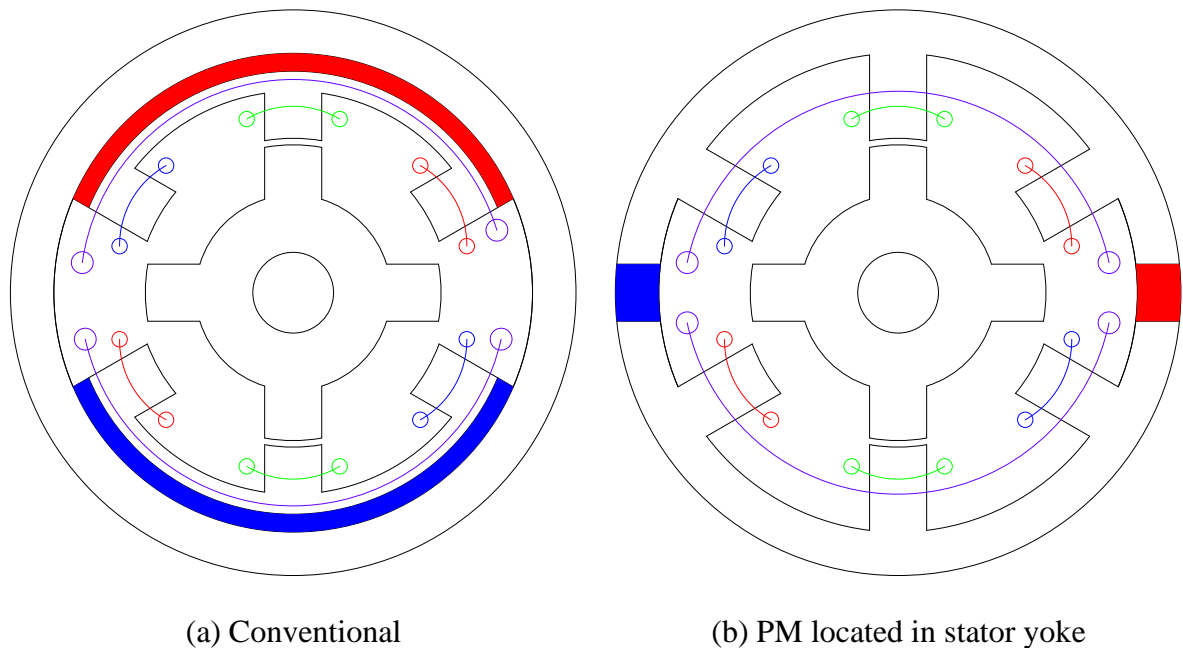


Fig. 1.12. Doubly salient HEMs [LI95] [CHA02].

1.3.2.2 Flux Reversal HEMs

Based on the flux reversal PM machines, the flux reversal HEMs can be developed by introducing DC coils in stator side. Fig. 1.13(a) shows a flux reversal HEM, in which the PMs are located at the edge of stator teeth and the armature and DC coils share the same slot [GAO18]. Alternatively, the PMs can be positioned at the middle of stator teeth to achieve a new flux reversal HEM, as shown in Fig. 1.13(b) [JIA16b]. These two machines feature parallel hybridization, which improves the flux-controllability. However, the torque density is reduced compared with the flux reversal PM machines due to spatial conflict between armature and field coils.

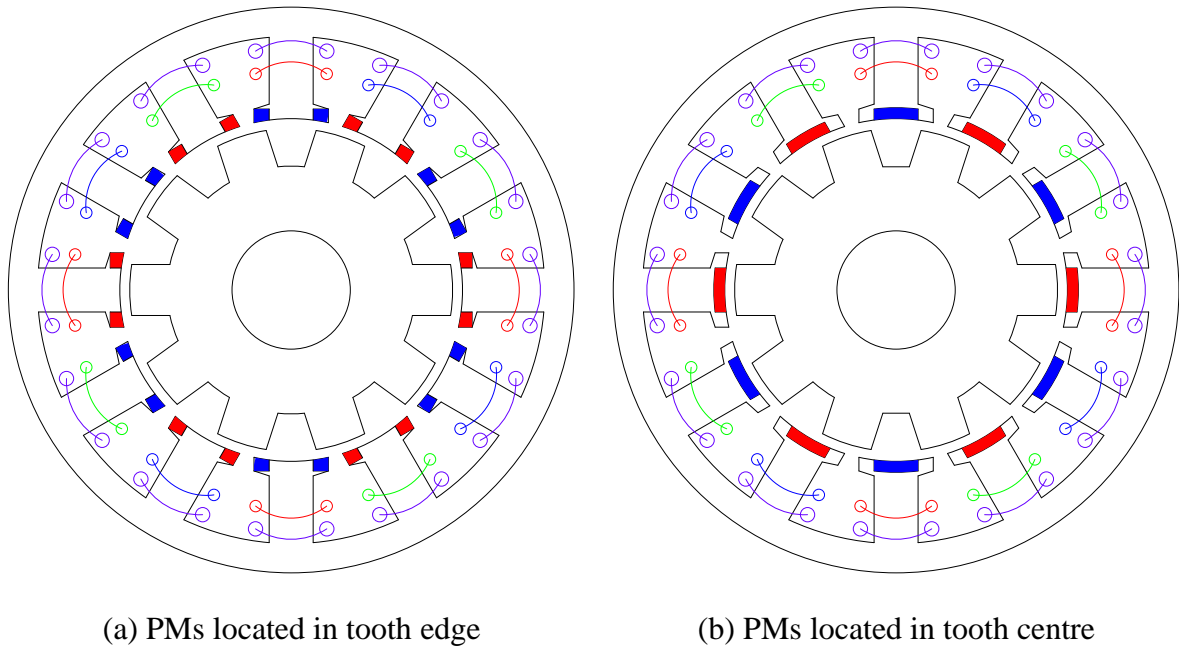
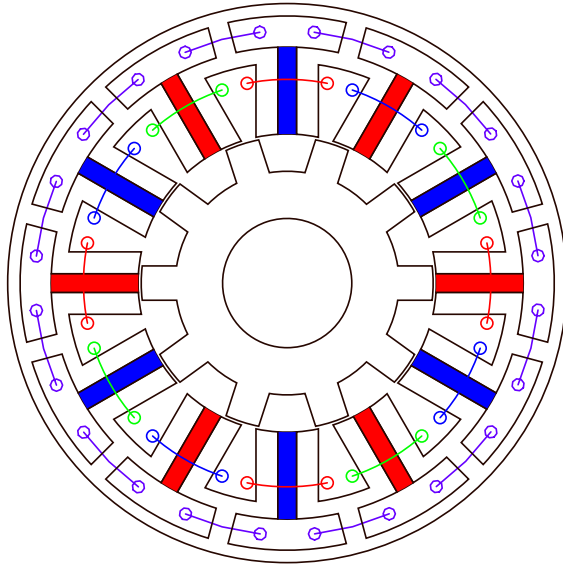


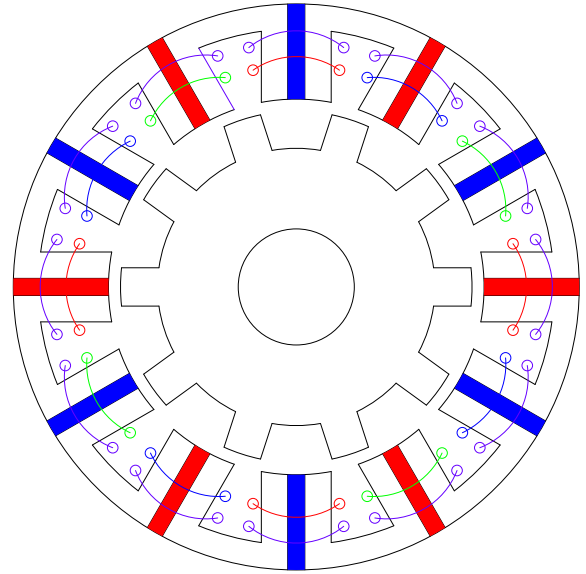
Fig. 1.13. Flux reversal HEMs [GAO18] [JIA16b].

1.3.2.3 Switched Flux HEMs

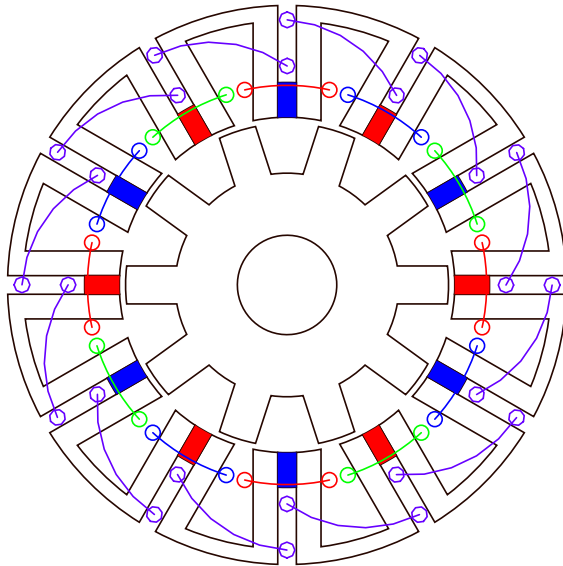
Based on the SFPM machines, the switched flux HEMs are developed by introducing field windings in stator side. The switched flux HEMs possess high torque density and good flux regulation capability since the flux-focusing effect and DC coils are utilized. As such, they are the most investigated HEM topologies. Based on the conventional U-core SFPM machine shown in Fig. 1.6(a), a switched flux HEM is achieved by introducing an outermost stator yoke to accommodate DC coils, as shown in Fig. 1.14(a) [HOA07]. This machine features improved flux regulation capability but enlarged stator outer diameter due to the additional stator yoke. The DC coils can be directly arranged in the armature slots of the U-core SFPM machine to achieve hybrid excitation, Fig. 1.14(b) [GAU14]. However, this machine cannot effectively achieve flux-enhancing but only flux-weakening due to magnetic saturation. Based on the conventional U-core SFPM machine, hybridization can also be achieved by reducing the volume of PMs and allocating DC coils in the saved space. Figs. 1.14(c)-(f) show four hybrid excitation variants of the conventional U-core SFPM machine, in which the PMs are located at the bottom, middle, and top of the corresponding slots, respectively [HUA09] [OWE09] [ZHA15a] [HUA15]. To further improve the flux-regulation capability of the switched flux HEM shown in Fig 1.14(c), iron bridges are employed to provide additional flux path for DC coils, as shown in Fig. 1.14(g) [OWE10]. Another way to achieve hybrid excitation is illustrated in Fig. 1.14(h), in which PMs excited pole-pair and DC coils excited pole-pair are alternately arranged along the stator [OWE09]. Alternately, hybridization can also be obtained by alternately allocating PM pole and DC pole along the stator as shown in Fig. 1.14(i) [OWE09]. Based on the conventional E-core SFPM machine, Fig. 1.6(c), a switched flux HEM is obtained by arranging DC coils in the E-core stator as shown in Fig. 1.14(j) [CHE11a].



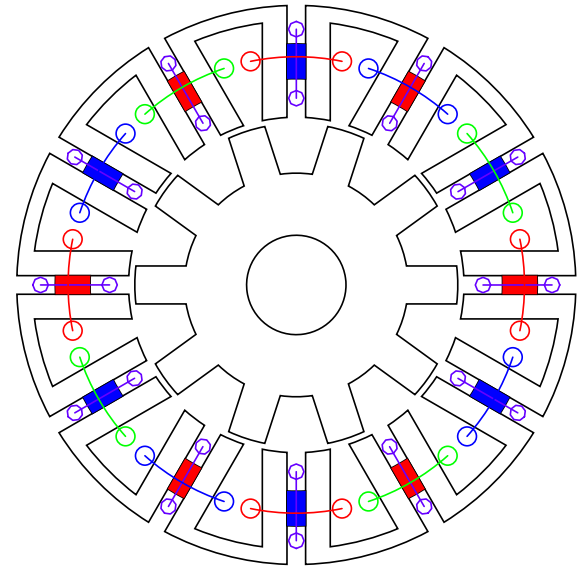
(a) DC coils in extra stator yoke [HOA07]



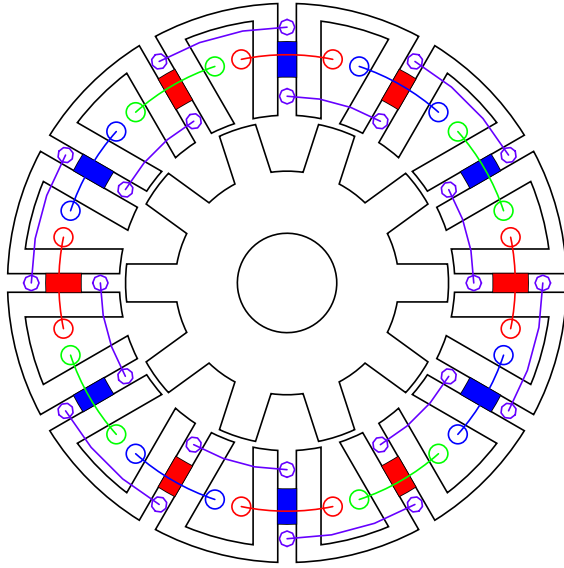
(b) DC coils in armature slots [GAU14]



(c) PM-bottom [HUA09]

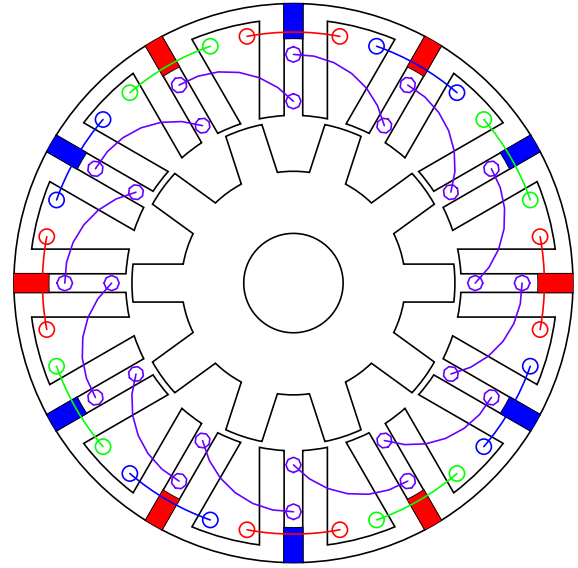


(d) PM-middle (toroidal DC coils) [OWE09]

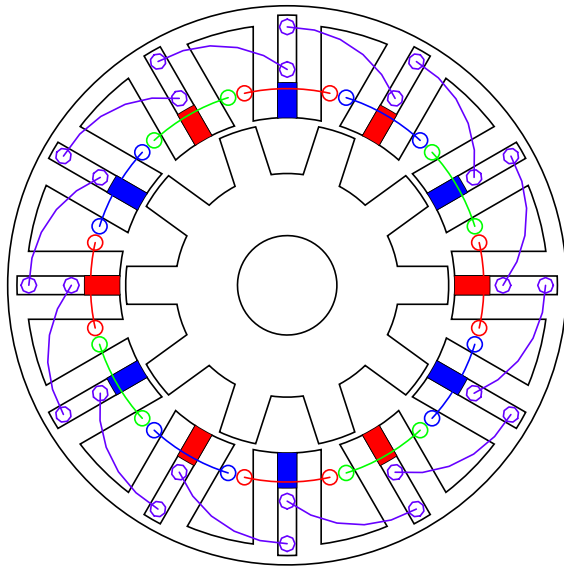


(e) PM-middle (concentrated DC coils)

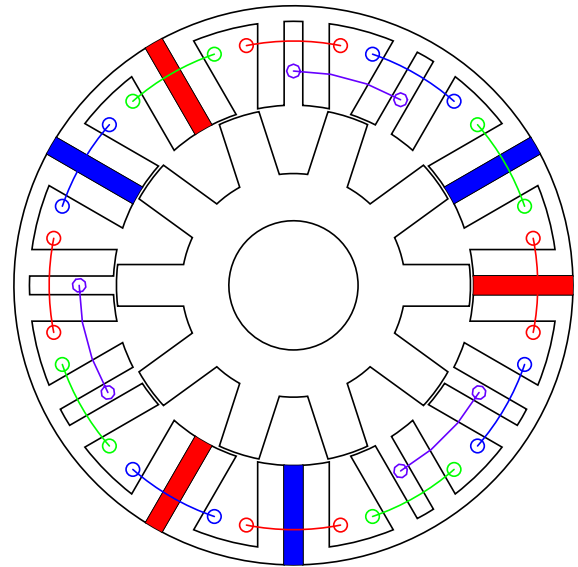
[ZHA15a]



(f) PM-top [HUA15]

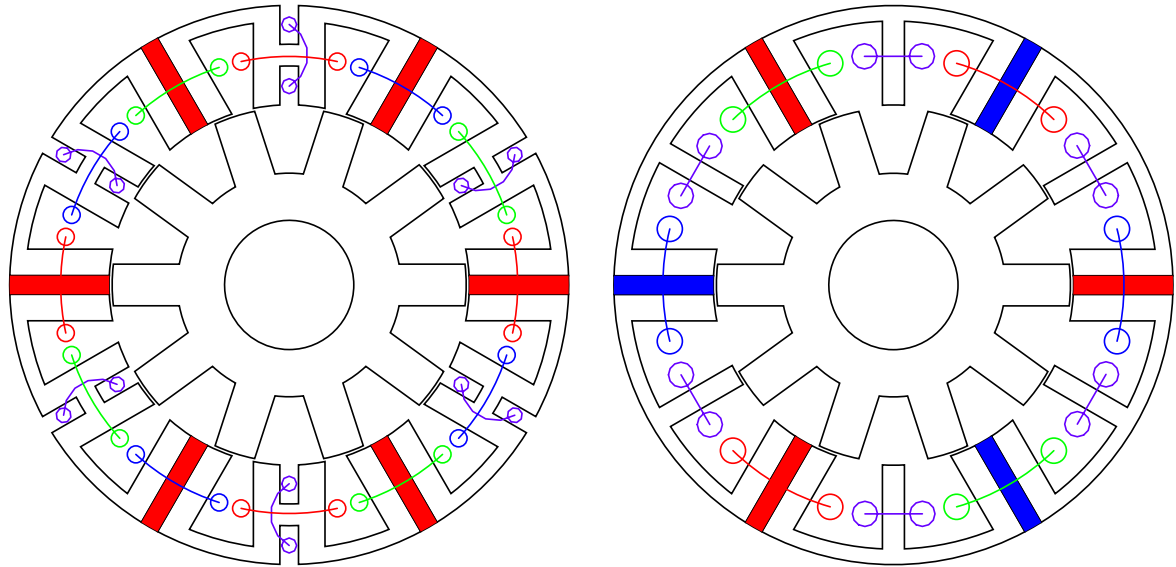


(g) PM-bottom with iron bridge [OWE10]



(h) Alternate PM pole-pair and DC pole-pair

[OWE09]



(i) Alternate PM pole and DC pole

(j) DC coils in E-core stator [CHE11a]

[OWE09]

Fig. 1.14. Switched flux HEMs.

1.3.2.4 Stator Slot HEMs

Based on the doubly salient PM machine shown in Fig. 1.7(b), a doubly salient HEM is achieved by introducing DC coils in the armature slots as shown in Fig. 1.15 [AFI15]. The most obvious advantage of this machine is the high fault-tolerant capability. At open-circuit, the flux excited by PMs is self-short-circuited in stator side and hence the induced phase back-EMF is negligible. If the DC current is injected, the PM excited flux will be pushed to the rotor side. As such, the air-gap field, the phase back-EMF, and the output torque can be effectively controlled by the field current.

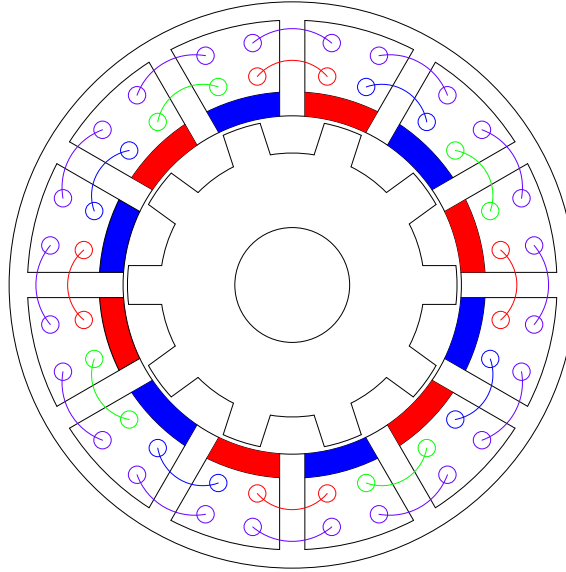
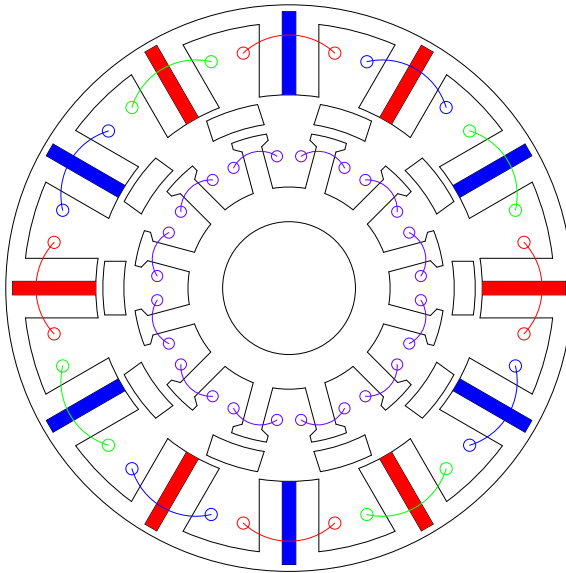


Fig. 1.15. Stator slot HEM [AFI15].

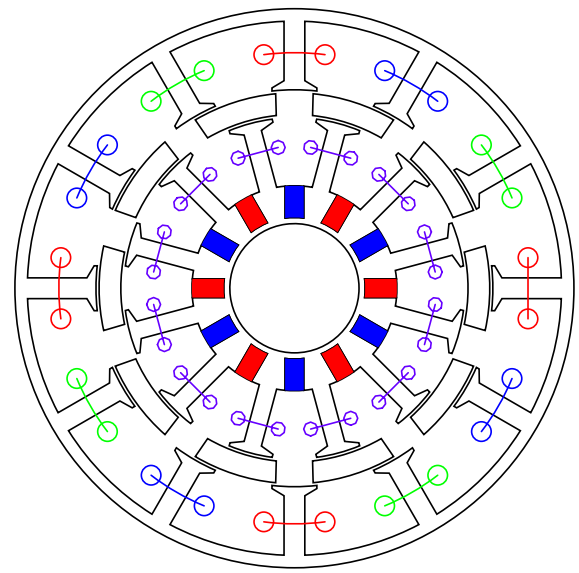
1.3.3 Partitioned Stator HEMs

Although the stator excitation HEMs feature brushless structure, good flux regulation capability and easy thermal management, the spatial conflict between active components in stator side inevitably reduces the torque density as well as the flux-controllability. Therefore, by introducing additional inner stators, partitioned stator HEMs have been developed to solve the spatial conflict in the HEMs having single stators. In partitioned stator HEMs, cup rotors are always employed. Fig. 1.16(a) shows a partitioned stator switched flux HEM, in which the PMs and armature coils are allocated in the outer stator while the DC coils are arranged in the inner stator [HUA16a]. Alternately, both DC coils and PMs can be placed in the inner stator while the outer stator only accommodates armature coils as shown in Fig. 1.16(b) [HUA17]. Besides, the inner stator with alternate PM pole and DC pole can also be employed to achieve a partitioned stator HEM as shown in Fig. 1.16(c) [HUA16b]. For the partitioned stator HEM shown in Fig. 1.16(d), the PM excited pole-pair and DC excited pole-pair are alternately positioned along the inner stator while the armature coils are wound on the outer stator [HUA16c]. There are also a lot of other partitioned stator HEMs developed from the single stator counterparts [JIA17] [WU17] [HUA19]. Overall, partitioned stator HEMs offer higher torque density and enhanced flux regulation capability compared with the single stator

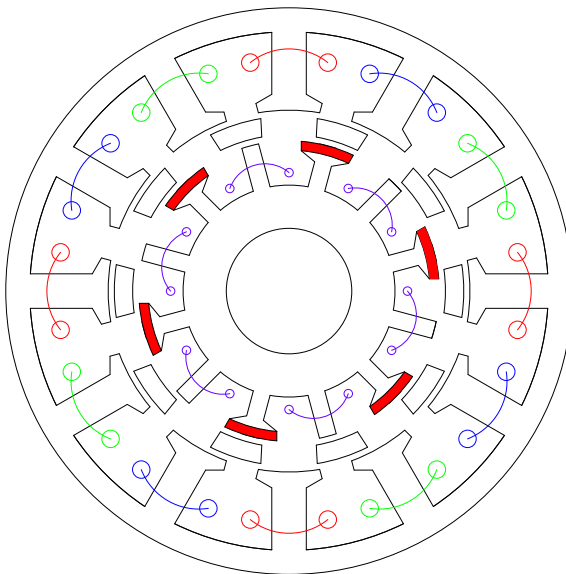
counterparts due to better inner space utilization. However, the manufacturing difficulty and mechanical weakness of the cup rotor should be concerned. Besides, the thermal management of partitioned stator HEMs is another big challenge.



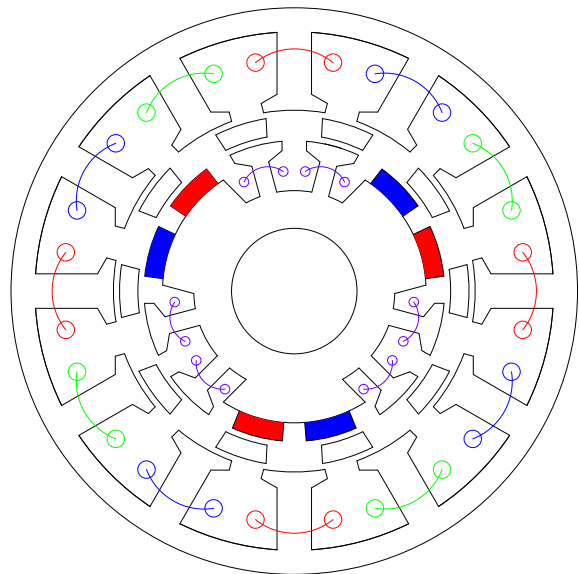
(a) Inner stator with DC coils



(b) Inner stator with PMs and DC coils



(c) Inner stator with alternate PM pole and DC pole

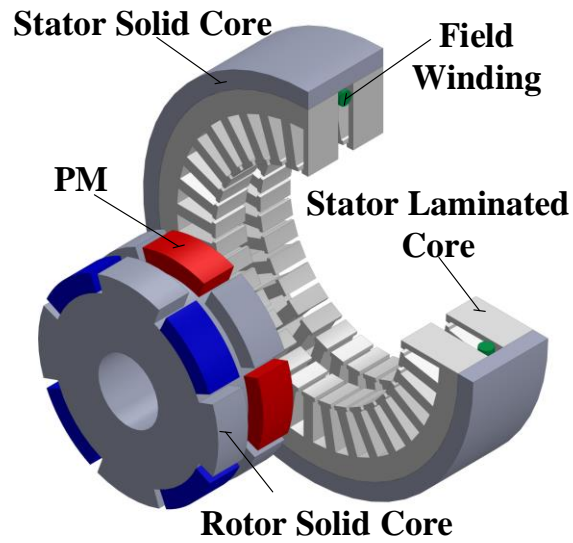


(d) Inner stator with alternate PM pole-pair and DC pole-pair

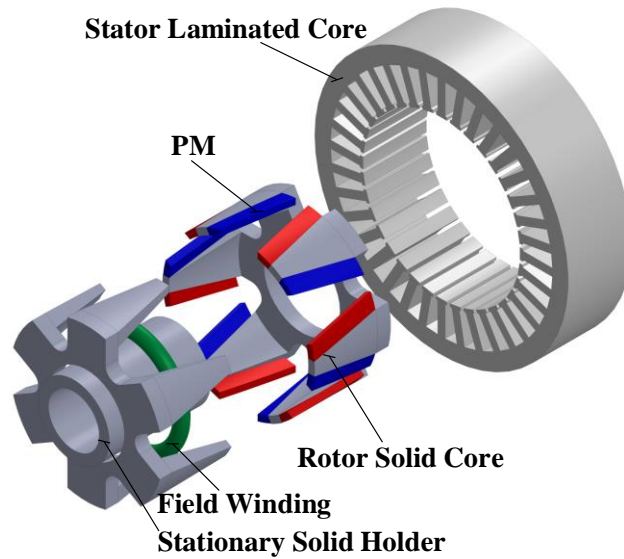
Fig. 1.16. Partitioned stator HEMs [HUA16a] [HUA17] [HUA16b] [HUA16c].

1.3.4 Mixed Excitation HEMs

As aforementioned, the most obvious drawback of rotor excitation HEMs is the requirement for slip rings and brushes. One solution for eliminating the slip rings and brushes is to position both DC coils and PMs in stator side, resulting in the stator excitation HEMs and the partitioned stator HEMs. Another way is to keep the PMs in rotor side while allocating the DC coils in stationary part, resulting in the mixed excitation HEMs. Fig. 1.17(a) shows a mixed excitation HEM, in which the PMs are affixed to the surface of the consequent-pole rotor while the toroidal field winding is positioned in stator side [MCC87] [TAP03]. In this machine, the rotor core is solid and an outermost solid stator core is employed, which is different from the conventional rotor PM machines. Such design enables the flux paths in both axial and radial directions. Based on the wound field claw pole machine, a mixed excitation HEM is obtained by introducing the PMs between rotor claws as shown in Fig. 1.17(b) [CHA96a]. The introduction of the PMs can help to improve the performance by reducing the flux-leakage. The sliding contacts are eliminated in this machine since the DC winding is allocated in the stationary inner stator. Overall, the mixed excitation HEMs feature brushless structure and controllable air-gap field. However, they usually exhibit three dimensional (3D) magnetic field and hence large flux-leakage. To allow the flux path in both radial and axial directions, solid material or soft magnetic composite (SMC) is normally required, which further complicates the manufacturing and assembling.



(a) Consequent-pole rotor and toroidal DC winding



(b) Claw-pole rotor and stationary inner stator with DC winding

Fig. 1.17. Mixed excitation HEMs [MCC87] [TAP03] [CHA96a].

1.4 Typical Parasitic Effects in Synchronous Machines

In the previous sections, various synchronous machine topologies have been reviewed, including PMSMs, WFSMs, and HEMs. Apart from the machine topologies, the performance of electrical machines is also significantly influenced by the parasitic effects. In this section, typical parasitic effects associated with synchronous machines will be introduced.

1.4.1 Cogging Torque and Torque Ripple

In PM machines, cogging torque is caused by the slotting effect [ZHU00]. More specifically, it is generated due to the interaction between air-gap permeance harmonics and PM magnetomotive force (MMF) harmonics under open-circuit. Normally, cogging torque is an undesired torque component since it does not contribute to the average torque but it causes additional torque/speed ripple, noise, and vibration, especially at low speed and light load. Cogging torque is position dependent and its waveform is periodic. In a mechanical period, the number of periods of cogging torque equals to the least common multiple (LCM) of the number of slot and PM pole [JUS07]. The higher the number of periods, the smaller the amplitude of cogging torque. Another way to indicate the amplitude of cogging torque is to use the “goodness” factor [ZHU00], i.e., C_T , which can be expressed as

$$C_T = \frac{2pN_s}{N_c} \quad (1.1)$$

where p is the number of PM pole pairs. N_s is the number of stator slots. N_c is the LCM of $2p$ and N_s .

For a given slot number, it has been proved that the larger the “goodness” factor, the higher the amplitude of cogging torque [ZHU09a].

Apart from the cogging torque, another factor for contributing to torque ripple is the interaction between armature currents and phase back-EMF harmonics [ISL05]. If the armature currents and phase back-EMFs are assumed to be sinusoidal waveforms and free from harmonics, a non-zero constant power and hence a steady torque will be generated if the phase

shift between armature current and phase back-EMF does not equal to 90 electrical degrees. However, in most cases, the phase back-EMFs are not pure sinusoidal waveforms and contain many harmonics. The interaction between armature currents and phase back-EMF harmonics will produce torque ripples with various orders. For example, the interaction between the 5th phase back-EMF harmonic and the fundamental phase current harmonic will produce the 6th torque harmonic [ATA03].

1.4.2 Losses

1.4.2.1 Copper Loss

The performance of electrical machines is significantly influenced by losses. In electrical machines, copper loss is a basic type of loss and it is generated when the current flows through conductors. At low-speed, the major loss component in electrical machine is usually the copper loss. The copper loss can be calculated by

$$P_{cu} = I_{rms}^2 R \quad (1.2)$$

$$R = \rho \frac{L}{A} \quad (1.3)$$

where P_{cu} is the copper loss. I_{rms} is the root mean square (RMS) value of the injected current. R , A and L are the resistance, the cross-sectional area, and the length of the conductor. ρ is the electrical resistivity.

When DC current or low-frequency AC current is injected, the current is assumed to be evenly distributed across the conductor. If the frequency of the current increases, the generated copper loss will be different from that under DC current or low-frequency AC current condition due to the influence of the skin effect and proximity effect [POP13]. Under high-frequency alternating magnetic field, the current is unevenly distributed and concentrated on the surface of the conductor. The closer to the surface of the conductor, the greater the current density [MEL11]. This phenomenon is referred to as the skin effect. As such, the conducting area of the conductor is reduced, resulting in increased copper loss. Proximity effect is another factor for

influencing the copper loss. When there are two or more conductors close to each other, the distribution of the current in one conductor is not uniform due to the magnetic field generated by the current in the other conductor. This phenomenon is termed as the proximity effect, due to which the conducting area is reduced and hence the copper loss is increased.

1.4.2.2 Iron Loss

As another major loss component in electrical machines, iron loss cannot be neglected, particularly at high speed. The calculation of iron loss is important since it directly affects the efficiency, the temperature rise, and potential PM demagnetization of electrical machines. A lot of models have been proposed to improve the accuracy of iron loss calculation since the iron loss is quite difficult to be accurately predicted in electrical machines [STE92] [BER85] [ATA92]. Overall, more effects, including the frequency, the flux density, and the temperature etc., have been considered in iron loss models to improve the accuracy [ION07] [BOG03] [CHE15] [XUE16]. One of the most used iron loss models is shown in (1.4) [BER85], in which the iron loss is divided into three components, i.e., the hysteresis loss, the classic eddy current loss, and the excess eddy current loss, respectively.

$$P_{fe} = k_h f B_m^2 + k_c f^2 B_m^2 + k_e f^{1.5} B_m^{1.5} \quad (1.4)$$

where P_{fe} is the iron loss. k_h is the hysteresis loss coefficient. k_c is the classic eddy current loss coefficient. k_e is the excess eddy current loss coefficient. f is the fundamental electrical frequency. B_m is the amplitude of the flux density in the core.

1.4.2.3 Magnet Loss

The PM eddy current loss is another loss component in PM machines. It can increase the temperature of PMs and hence lead to potential irreversible PM demagnetization and reduced efficiency [ATA00]. Therefore, the PM eddy current loss cannot be ignored, particularly under high-speed conditions. In PM machines, the PM eddy current loss is caused by the harmonics due to the armature reaction and the slotting effect. It has shown that the PM segmentation in

axial and circumferential directions is effective to reduce the PM loss [TOD04] [KAW09].

1.4.2.4 Mechanical Loss

Another important loss component in electrical machines is the mechanical loss, which includes the windage loss component and the bearing friction loss component [YAH14]. The mechanical loss P_m can be expressed as

$$P_m = B_m \omega_m^2 + T_k \omega_m \quad (1.5)$$

where B_m is the viscous friction coefficient. ω_m is the mechanical speed. T_k is the constant friction load. B_m and T_k can be identified by open-circuit test.

1.4.3 PM Demagnetization

PM machines exhibit high torque density and high efficiency. However, the potential irreversible PM demagnetization may lead to reduced torque density and increased noise and vibration [KAN17] [ZHU18b]. The demagnetization issue in PM machines is caused by the nonlinear magnetization curve of PMs [ZHO12]. For NdFeB magnets, the higher the temperature, the easier it is for PMs to demagnetize since the B-H curve is dependent on temperature. Apart from temperature, other factors can also cause the demagnetization issue, such as vibration, external magnetic field, and structure stress. If the permanent magnet is subjected to severe vibration, its internal magnetic domain may change. After the direction of the magnetic moment of the magnetic domain changes, the magnetic performance of the permanent magnet will deteriorate, which will cause the permanent magnet to demagnetize or even lose its magnetism irreversibly. To enhance the demagnetization withstanding capability of PMs, a lot of methods have been proposed and investigated. The most obvious method is to increase the thickness of PMs, which usually increases the PM material usage and hence the cost. Halbach array PM can be employed to improve PM demagnetization withstand capability [GAL15]. PM shaping is also an effective method to improve the demagnetization withstand capability by increasing the magnetic reluctance [HUA18].

1.4.4 Uncontrolled Overvoltage Fault

Uncontrolled overvoltage fault is one of the most serious failures that occurs at high speed. In PM machines, this fault is more serious since the PM excitation is fixed [JAH99] [LIA05] [RAM11]. Due to the voltage and current limits of power inverter, flux-weakening control is generally required for PM machines to operate beyond the base speed [SOO94] [SOO02] [ELR05]. During flux-weakening operation, if the gating signals of power switches unexpectedly disappear, the armature winding would become a large voltage source since it possesses high back-EMF at high speed. As such, the regenerated current will be delivered back to the DC-link and the power inverter could be damaged due to overvoltage. Recently, the stator slot HEM shown in Fig. 1.15 has been proved to possess high fault tolerant capability [ZHU19b]. The stator slot HEM can be protected from overvoltage damage through field excitation control since the open-circuit phase back-EMF without field current is negligible.

1.4.5 Unbalanced Magnetic Force

A lot of papers have investigated the unbalanced magnetic force (UMF) in electrical machine as it can lead to noise and vibration and affect bearing life [ZHU07b]. UMF occurs due to a lot of reasons, including winding faults, rotor eccentricity, asymmetric stator topology, and unbalanced winding distribution. It has shown that UMF could be resulted from two field harmonics differed by one [CHA96b]. Both analytical and FEA methods have been used to predict the UMF in electrical machines [LI17]. A lot of methods have also been investigated to reduce the UMF from the perspective of both machine control and machine design. Reduction methods from control side include field weakening commutation strategy and current injection [JIA04] [YAN14]. Suppression methods from machine design side include shaping and notching for stator/rotor [JAN91] [JAN93] [KAN09] [PAN14] [MA18]. Moreover, the UMF can also be effectively reduced by adopting appropriate PM magnetization patterns [MA17].

1.4.6 Noise and Vibration

Compared with IMs and SRMs, the noise and vibration of PM machines are relatively low

[SON20]. There are three types of sources that are responsible for the noise and vibration in electrical machines, i.e., electromagnetic source, mechanical source, and aerodynamic source, respectively. In low to medium range power rated electrical machines, the electromagnetic source could be the dominating source. Among various electromagnetic sources, the magnetic radial force, cogging torque, and torque ripple are the main sources that responsible for noise and vibration. When the following conditions are met, electrical machines will vibrate and deform [GIE06].

- The harmonic order of radial force equals to the mode of vibration
- The harmonic frequency of radial force is approximately equal to the modal frequency

Mechanical structures determine the modal frequency and the mode of vibration. In one mechanical period, the air-gap magnetic force density in radial direction f_p can be obtained by

$$f_p = \frac{B_r^2 - B_t^2}{2\mu_0} \quad (1.6)$$

where B_r and B_t are the radial and tangential components of the air-gap flux density, respectively. μ_0 is the permeability of free space.

There are a lot of methods that have been employed to reduce the noise and vibrations due to magnetic forces, including skewing, pole magnetization, pole shaping, and notching etc. [DEN19].

1.4.7 On-Load AC Winding Voltage Distortion

The on-load AC winding voltage distortion refers to the terminal voltage of phase winding distorted by the armature reaction at on-load condition. Based on a three-phase SPM machine having 12-slot/8-pole, it is revealed that the on-load AC winding voltage distortion is mainly caused by the local magnetic saturation in tooth-tips, particularly for the machines with small or closed slot-openings [WU15a]. Different from the open-circuit phase back-EMF, the on-load phase terminal voltage is distorted and contains a lot of high amplitude harmonics. The on-load

AC winding voltage distortion could lead to additional torque/speed ripples under constant torque region and reduced flux-weakening performance [WU15a] [ZHU15c] [LI16]. Furthermore, the on-load voltage distortion in a three-phase IPM machine with 12-slot/8-pole is illustrated [ZHU15b]. Moreover, the influence of slot/pole number combinations on on-load voltage distortion in both IPM and SPM machines have been illustrated in [ZHU16c] and [WU15b], respectively. For reducing the voltage distortion, rotor skewing and stator/rotor shaping have been proposed and validated, as reported in [WU16a] and [WU16b].

1.4.8 DC Winding Induced Voltage

Different from the open-circuit AC winding induced voltage, i.e., open-circuit phase back-EMF, the induced voltage in DC winding is detrimental to the performance of electrical machines under both no-load and on-load conditions. The DC winding induced voltage could lead to DC winding current ripple, unstable field excitation, additional torque ripple and losses, and even reduced torque density. Besides, it could impose challenges to the DC power source and control performance. The DC winding induced voltage pulsation is firstly investigated in [WU19a], in which the induced voltage under open-circuit is analyzed and then reduced by rotor skewing method based on the analytical deduced voltage harmonic orders. It reveals that the induced voltage under open-circuit is caused by the self-inductance harmonics of DC winding. Then, the analyses are extended to on-load condition by taking armature reaction into consideration in [WU20], in which the harmonic orders of the induced voltage caused by three-phase armature currents are derived. It shows that the induced voltage caused by armature current is due to the mutual-inductance harmonics between AC and DC windings. By using the finite element analysis (FEA) method, modified rotor skewing and rotor inner pole arc pairing are employed to suppress the on-load voltage pulsation [WU20]. Further, in [WU18], the influence of DC winding configuration, i.e., the number of DC coils and parallel branches, on the voltage pulsation is investigated and the corresponding voltage harmonic orders are deduced. It shows that the voltage pulsation can be actively reduced by selecting appropriate numbers of DC coils and parallel branches. However, it should be mentioned that all these investigations

are based on the wound field switched flux machines having complicated partitioned-stators (PS-WFSFMs). Based on the conventional single-stator F2A2 WFSFMs, the influence of armature winding phase number and slot/pole number combinations on DC winding voltage pulsation is reported in [WU19b]. It shows that the peak-to-peak values and harmonic orders of the voltage pulsations are significantly influenced by armature winding phase number and slot/pole number combinations. Besides, rotor pole chamfering and rotor pole arc optimization/axial pairing are proposed for reducing the voltage pulsation in [WU19b]. Moreover, based on the 24-slot/10-pole F2A2 WFSFM, the voltage pulsation reduction method of stator tooth-tip axial pairing is proposed in [ZHA20]. However, the pairing methods employed in [WU19b], [WU20], and [ZHA20] feature 3D structures, which further complicates the machine structures and manufacturing process. Furthermore, based on the single-stator five-phase WFSFMs having both concentrated and distributed windings, the air-gap field modulation principle has been used to qualitatively analyze the DC winding voltage pulsation in [ZHA21]. However, it can be observed that all above investigations have been focused on the DC winding induced voltage in WFSMs. Hybrid excited machines having both PMs and DC coils also suffer from the induced voltage pulsation in DC winding, which will be the focus of this thesis.

1.4.9 Influence of DC Winding Induced Voltage

Normally, the field current is considered as constant, e.g., the red line with markers shown in Fig. 1.18. Due to the influence of the induced voltage ripple, the field current suffers from the current ripple, as the black line with markers shown in Fig. 1.18. By applying the field currents shown in Fig. 1.18, the on-load torque waveforms are calculated and presented in Fig. 1.19. Due to the unstable field current, the torque ripple increases by 86.6% from 21.5% to 40.1%, whilst the average torque decreases by 2.4% from 0.88Nm to 0.86Nm. This is due to the fact that the unstable field current can introduce additional back-EMF harmonics and hence significantly change the back-EMF waveform. Apart from the torque and speed oscillations, the field winding induced voltage also brings challenges to the power supply and control system

as discussed as follows.

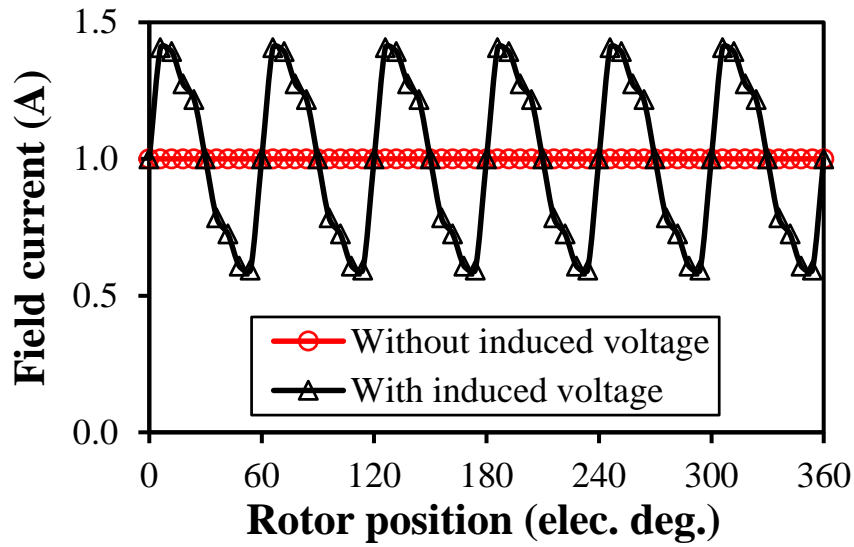


Fig. 1.18. Influence of on-load field winding induced voltage on field current of the 6-slot/5-pole PM-bottom HESFM with iron bridge.

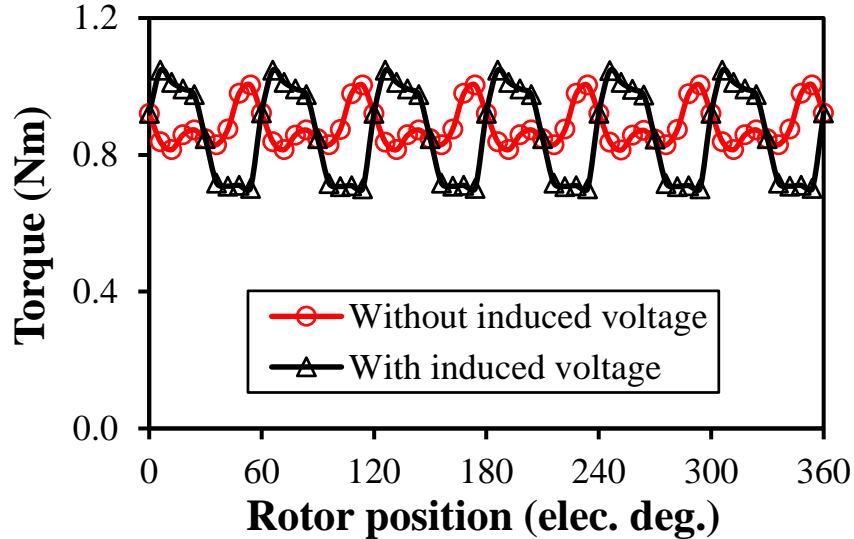


Fig. 1.19. Influence of on-load field winding induced voltage on torque of the 6-slot/5-pole PM-bottom HESFM with iron bridge.

In WFSMs and HEMs, the DC field winding can be either excited by a constant current power supply or H-bridge converters. When the field winding is excited by a constant current power supply, the influence of induced voltage ripple mainly lies in three aspects. Firstly, the

compliance voltage of the constant current power supply may be smaller than the required voltage at some rotor positions due to the existence of the field winding induced voltage ripple. Therefore, the actual current in the field winding will be reduced at some rotor positions, which leads to reduced torque and power density, especially at a higher speed. Secondly, a reverse input current may challenge the current power supply if the induced voltage ripple is higher than the compliance voltage over the whole range of rotor positions at a higher speed. Thirdly, the current power supply may also suffer from the challenge of a reverse voltage at higher speed owing to the negative value of the induced voltage ripple, which may lead to the activation of reverse voltage protection mechanism of the current power supply.

When the field winding is excited by a half or full H-bridge converter, the influence of the induced voltage ripple is as follows. In order to obtain a steady DC current in the field winding, the induced voltage ripple needs to be added into the control diagram as a disturbing voltage when applying closed-loop current control, which further complicates the control system. In order to balance the induced voltage, the DC bus voltage of the converter should be much higher, especially at a higher speed. This means that the operation speed of the machine is constrained if the DC bus voltage is of a certain value, owing to the existence of the induced voltage. In order to balance the negative value of the induced voltage at a higher speed, only a full H-bridge converter can be implemented, since the half H-bridge converter cannot provide a reverse output voltage. Consequently, the induced voltage ripple in field windings significantly influences the control system and operating characteristics of the HEMs and it also increases the KVA ratings and thus the cost of the converter feeding it, especially at a higher speed.

1.5 Research Scope and Contributions of Thesis

1.5.1 Research Scope

This thesis aims to investigate a significant parasitic effect, i.e., the DC winding induced voltage, in synchronous machines having DC windings, with a particular emphasis on its investigations in hybrid excited machines. Fig. 1.20 shows the research scope and arrangement of all chapters. Fig. 1.21 shows various machine topologies employed for investigations in this thesis. The detailed contents of all chapters are further summarized as follows.

Chapter 1: General Introduction

In this chapter, various synchronous machine topologies are introduced, including PMSMs, WFSMs, and HEMs. The advantages and limitations of each category are highlighted. Finally, typical parasitic effects associated with synchronous machines are reviewed.

Chapter 2: Analysis of Excitation Winding Induced EMF in Non-Overlapped Stator Wound Field Synchronous Machines

This chapter analyses the DC winding induced voltage in non-overlapped stator wound field synchronous machines (F1A1). Firstly, the induced voltage in DC winding is analyzed considering both no-load and on-load operations. Then, the influence of slot/pole number combinations on the induced voltage is illustrated. Next, two prototype machines are fabricated and tested to verify the finite element analyses (FEA). Finally, the potential to eliminate the DC winding and its induced voltage using open-winding inverter is demonstrated.

Chapter 3: Investigation of DC Winding Induced Voltage in Hybrid Excited Switched Flux Permanent Magnet Machine

This chapter investigates the DC winding induced voltage in a 12-slot/10-pole HESFPM machine. Firstly, the phenomenon and mechanism of the DC winding induced voltage are illustrated and explained considering both open-circuit and on-load conditions. Then, rotor step

skewing and unequal rotor teeth are proposed and employed to reduce the on-load DC winding induced voltage. Finally, a prototype machine is manufactured and tested to verify the finite element analyses (FEA).

Chapter 4: Influence of Stator Slot and Rotor Pole Number Combination on Field Winding Induced Voltage Ripple in Hybrid Excitation Switched Flux Machine

This chapter investigates the influence of stator slot and rotor pole number combination on DC winding induced voltage in a HESFPM machine. Firstly, the DC winding induced voltages caused by the open-circuit, the armature current, and the on-load are illustrated for different slot and pole number combinations. Then, the influences of PM position and iron bridge on DC winding induced voltage are investigated. Finally, to verify the FEA predictions, a prototype machine is fabricated and tested.

Chapter 5: Analysis and Suppression of DC Winding Induced Voltage in Partitioned Stator Hybrid Excited Switched Flux Machines

This chapter aims to analyze and suppress the DC winding induced voltage in partitioned-stator HESF machines. Firstly, based on a 12-slot/10-pole PS-HESF machine, the DC winding induced voltage of different operating conditions is illustrated. The influence of current advance angle and slot/pole combinations on DC winding induced voltage are subsequently investigated. Two methods, i.e., rotor pole arc pairing and unevenly distributed rotor teeth, are then proposed to reduce the induced voltage at open-circuit and on-load conditions, respectively. Finally, a prototype machine is built and tested to validate the FEA calculations.

Chapter 6: Voltage Pulsation Induced in DC Field Winding of Different Hybrid Excitation Switched Flux Machines

This chapter compares the DC winding induced voltage in different HESF machines. Firstly, based on five existing HESF machines, the DC winding induced voltage under different

conditions are comparatively illustrated. Further, the influence of current advance angle on on-load DC winding induced voltage is investigated. Three reduction methods, i.e., rotor step skewing, rotor pole notching, and rotor pole shaping are subsequently proposed and employed to reduce the on-load DC winding induced voltage. A prototype machine with both non-skewed and 2-step skewed rotors is fabricated and tested to verify the finite element analyses (FEA).

Chapter 7: General Conclusions and Future Work

Based on the investigations in this thesis, some general conclusions and potential future work are highlighted in this chapter.

1.5.2 Major Contributions of Thesis

The major contributions of this thesis are summarized as follows.

- The phenomenon and mechanism of the DC winding induced voltage under different conditions are illustrated and explained for HEMs, which provides a new perspective for analyzing the parasitic effects in HEMs.
- The influence of slot/pole number combinations and machine topologies on the DC winding induced voltage are investigated, which provides guidance for actively reducing the DC winding induced voltage at the initial design process.
- To further reduce the DC winding induced voltage, various passive suppression methods have been proposed, including rotor step skewing, rotor pole shaping, rotor pole notching, unequal rotor teeth, rotor pole arc pairing, and unevenly distributed rotor teeth.
- Based on the F1A1 WFSM, the potential to integrate AC and DC windings through open-winding inverter is demonstrated, which provides one possible solution to eliminate the DC winding induced voltage whilst improving the torque density for the machines having AC and DC conductors in the same slot.

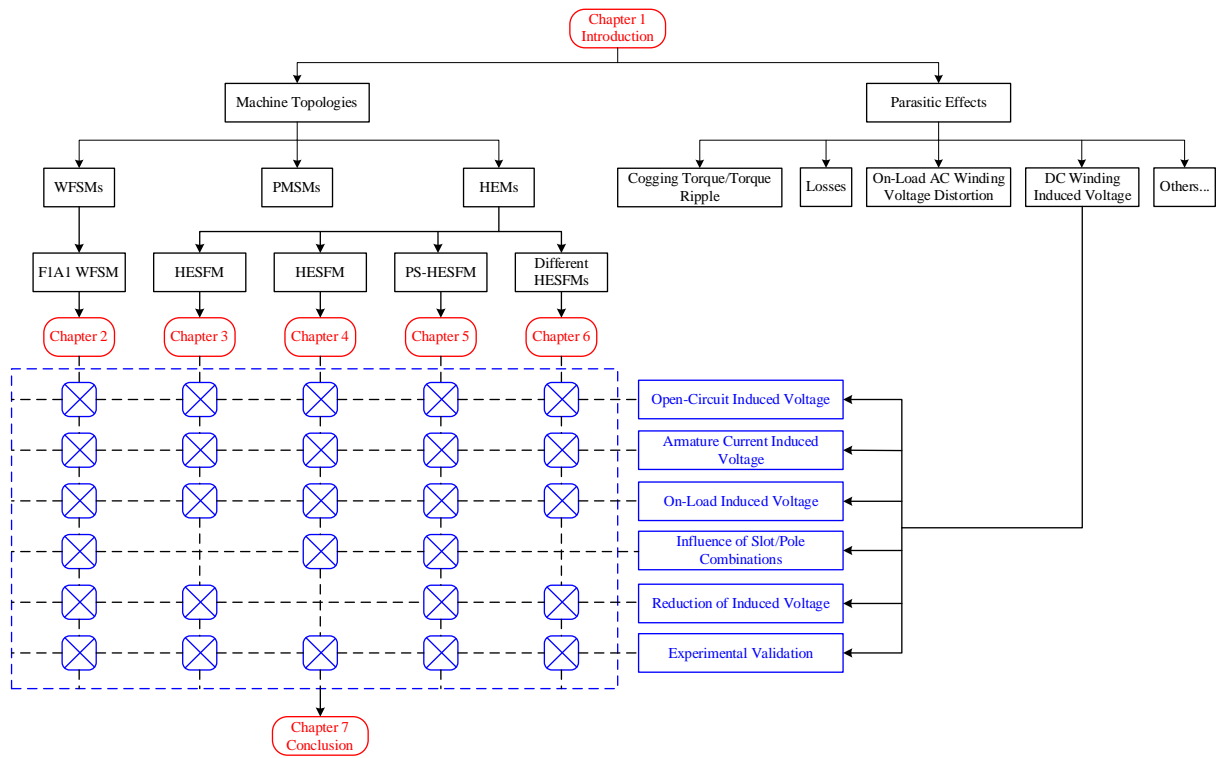


Fig. 1.20. Research scope and arrangement of chapters.

Chapter 2		
[ZHU15a]		
Chapters 3 and 4		
[OWE10]		
Chapter 5		
[HUA17]		
Chapter 6		
	[HOA07]	[OWE09]
[OWE10]	[CHE11a]	[HUA17]

Fig. 1.21. Various machine topologies investigated in this thesis.

CHAPTER 2

Analysis of Excitation Winding Induced EMF in Non-Overlapped Stator Wound Field Synchronous Machines

Different from the induced electromotive force (EMF) in armature winding, the induced EMF in excitation winding is detrimental to the performance of wound field synchronous machines by causing unstable excitation field and thus extra torque pulsation and losses. Moreover, it also imposes challenges to machine control, particularly for high-speed operation. This chapter investigates the induced EMF in the excitation winding of 3-phase non-overlapped stator wound field synchronous machines (SWFSMs). It has revealed that the amplitude of the excitation winding induced EMF is largely dependent on the slot-pole combination. Therefore, with suitable slot-pole combinations, the induced EMF issue will be significantly alleviated by eliminating low-order induced EMF harmonics. The finite element predictions are validated by measurements on two prototyped non-overlapped SWFSMs. Finally, the potential to eliminate the excitation winding and hence the corresponding induced EMF by open-winding inverter is investigated.

This chapter is based on the paper [SUN21c] published in IEEE Transactions on Energy Conversion.

2.1 Introduction

Rare-earth permanent magnet (PM) machines have been widely developed and applied, owing to high torque density/efficiency [ZHU07a] [CAO12] [LI10]. However, the rare-earth PM materials are expensive and the supply is unstable. Therefore, PM machines are confronted with big challenges for the development of low-cost applications [ZHO14a]. Moreover, PM machines also suffer from relatively poor flux-weakening performance, limited operating temperature, and potential irreversible demagnetization of PMs [SOO02]. Therefore, research on magnetless machines has drawn much interest in recent years. Magnetless machines mainly

include switched reluctance machines/synchronous reluctance machines (SRMs)/(SynRMs), wound field synchronous machines (WFSMs) and induction machines (IMs) [LEE18].

WFSMs can be further categorized as rotor WFSMs (RWFSMs) and stator WFSMs (SWFSMs). In conventional RWFSMs, the field coils are positioned on rotor side and therefore the sliding contacts are essential for field excitation [LIU12a]. While for SWFSMs, the field coils are arranged on stator side. Consequently, compared with RWFSMs, SWFSMs exhibit improved system stability and reliability due to the elimination of sliding contacts [JIA16a]. Compared with SynRMs and IMs, the rotor structure of SWFSMs and SRMs is very simple and robust, which is beneficial to manufacturing and thermal management [CHE10b]. SRMs are characterized by high torque pulsation and high noise/vibration, which can be significantly alleviated in SWFSMs due to more sinusoidal back electromotive forces (back-EMFs) in armature windings [LIU12b]. Consequently, SWFSMs have received much attention among magnetless machines recently.

There are two major types of SWFSMs that have been mostly investigated, i.e., variable flux RMs (VFRMs) and WF switched flux machines (WFSMs). Based on the principle of switched flux proposed in [RAU55], a single-phase WFSM is proposed in [POL99] and the armature coil pitch and field coil pitch are both 2 slot pitches (F2A2). It reveals that the efficiency of the F2A2 machine is improved compared with an IM. Subsequently, the three-phase counterpart is proposed and shown that it offers a higher efficiency of material usage than the SFPM machine [SUL11] [SUL12] [GAU12]. Nevertheless, it suffers from severe magnetic saturation and hence limited torque density. Consequently, an F1A3 WFSM is proposed in [ZHO14a] for improved torque density, in which the armature coil pitch and field coil pitch are 3 slot pitches and 1 slot pitch, respectively. However, this machine employs overlapped armature winding, which features long end-winding length, high copper loss, reduced efficiency, and poor fault-tolerant capability.

Based on a dual-winding reluctance machine proposed in [OJO97], a VFRM with non-overlapped field and armature coils is proposed in [FUK10] and [FUK12], which has shorter end-winding length due to concentrated coils. However, in VFRMs, the field and armature coils are positioned in the same slot, which reduces the available slot area for armature coils. Therefore, VFRMs suffer from relatively higher copper loss and lower efficiency. In [ZUL10], a non-overlapped SWFSM with segmented rotor is proposed, which shows enlarged slot area for both armature and field coils compared with VFRMs since the field and armature coils are alternately positioned along stator teeth. Nevertheless, it features relatively lower torque/power density caused by highly saturated rotor segments under on-load condition. Further, the segmented rotor structure also increases the difficulty and cost of fabrication. A novel non-overlapped SWFSM is proposed in [KHA14] by changing the segmented rotor to the conventional salient rotor. However, the average torque of this machine is almost the same as the original machine, which is attributed to high flux-leakage due to inappropriate field coil polarities. In [ZHU15a], novel non-overlapped SWFSMs with salient stators and rotors are developed by using field coils with identical polarities. It shows that the torque density has been significantly increased compared with the SWFSMs with segmented rotor and alternate field coil polarities, respectively. Moreover, the feasible slot-pole (s/r) number combinations are increased due to identical field coil polarities.

As a significant parasitic effect in WFSMs, the excitation winding induced EMF cannot be neglected, especially at high speed. Firstly, it results in current ripples in excitation winding and thus leading to unstable field excitation and reduced torque performance [ZUL10] [MEC06] [YU15]. In addition, it also imposes challenges to machine drives and DC power supplies. The induced EMF issue is firstly studied in [WU19a] [WU20] [WU18] based on WFSMs having partitioned stators. Furthermore, the investigations of the induced EMF issue are extended to hybrid excited machines (HEMs) [SUN20a] [SUN21a]. In [SUN20a], the induced EMF in a 12s/10r HESF machine is investigated and suppressed. Furthermore, in [SUN21a], the impact of slot-pole combinations is studied since the investigation in [SUN20a] is restricted to a specific slot/pole combination, i.e., 12s/10r. In HEMs, the induced EMF issue tends to be less

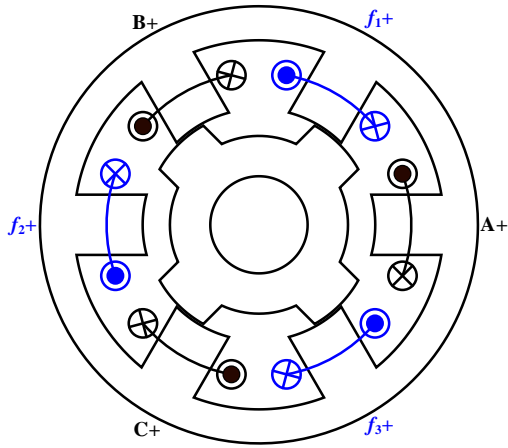
severe than that in WFSMs due to the influence of PMs. Although some investigations of the induced EMF issue have been carried out in WFSMs [WU19a] [WU20] [WU18], the investigations in these papers [WU19a] [WU20] [WU18] are restricted to a special machine topology with complicated partitioned stators. In [ZHU15a], a class of novel non-overlapped SWFSMs with simple stator/rotor structures and winding configurations (armature coil pitch=field coil pitch=1 slot-pitch) have been developed, Fig. 2.1, and the electromagnetic performances have been analyzed. However, the induced EMF issue is not addressed in these machines. This chapter aims to investigate the excitation winding induced EMF pulsation and the influence of slot-pole combinations in these non-overlapped SWFSMs.

The chapter is organized as follows. The structure and winding configuration of the 3-phase non-overlapped SWFSMs are introduced in section 2.2. Next, section 2.3 presents the excitation winding induced EMF and the impact of slot-pole combinations. In section 2.4, the finite element analyses (FEA) are validated by experiments on two prototyped non-overlapped SWFSMs. In section 2.5, general conclusions are summarized. Finally, the potential to eliminate the excitation winding induced EMF using open-winding inverter is investigated in section 2.6.

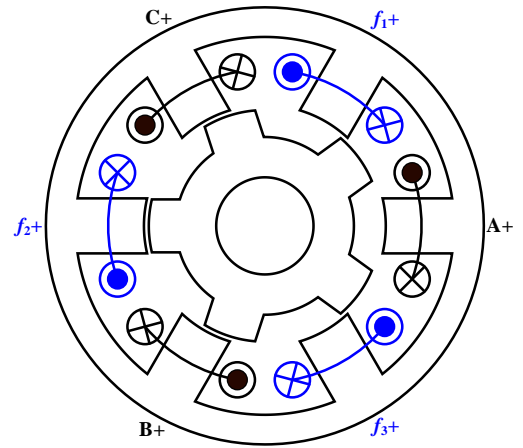
2.2 Machine Topology

The machine structure and winding configuration of the 3-phase non-overlapped SWFSMs with various slot-pole combinations are illustrated in Fig. 2.1. As can be found from Fig. 2.1, the non-overlapped SWFSMs are characterized by doubly salient structure, i.e., the stators and rotors with salient poles are adopted. As the name suggests, both armature and field coils are non-overlapped, i.e., coil pitch=1 slot-pitch, and alternately wound on the stator teeth. It is worth mentioning that the excitation coils possess the same polarities.

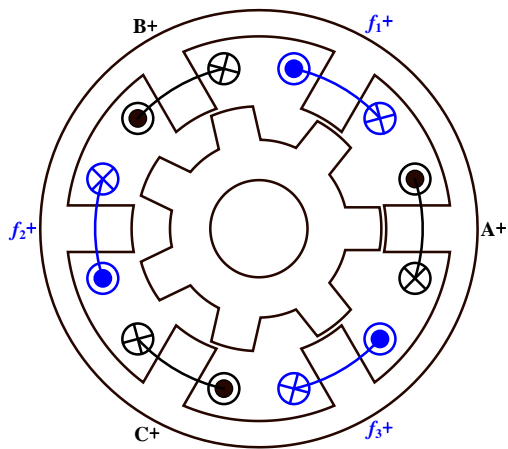
Fig. 2.2 shows the average torque versus current angle (α) curve of the 6s/7r SWFSM. It is shown that the average torque reaches the maximum value with $\alpha=10^\circ$. It reveals that the saliency ratio is approximately equal to 1 and therefore the reluctance torque component is negligible. Consequently, the control strategy with $i_d=0$ is more suitable for this machine to attain maximum torque per ampere (MTPA) operation. To achieve more stable torque output, brushless AC (BLAC) drive is employed for the armature windings in these machines, since the phase flux-linkage and back-EMF variation against rotor electric position (E.D.) at open-circuit are more sinusoidal, as shown in Figs. 2.3 and 2.4.



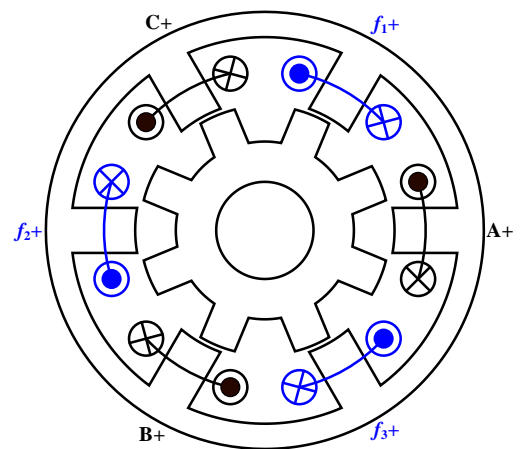
(a) 6s/4r



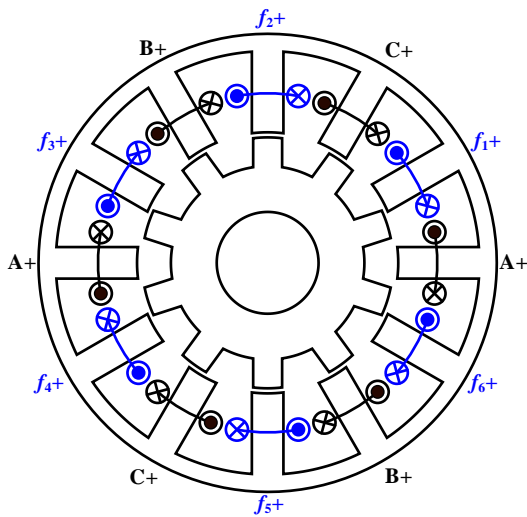
(b) 6s/5r



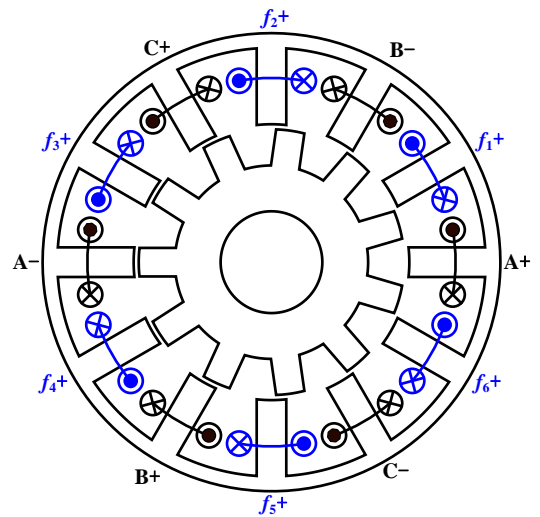
(c) 6s/7r



(d) 6s/8r



(e) 12s/10r



(f) 12s/11r

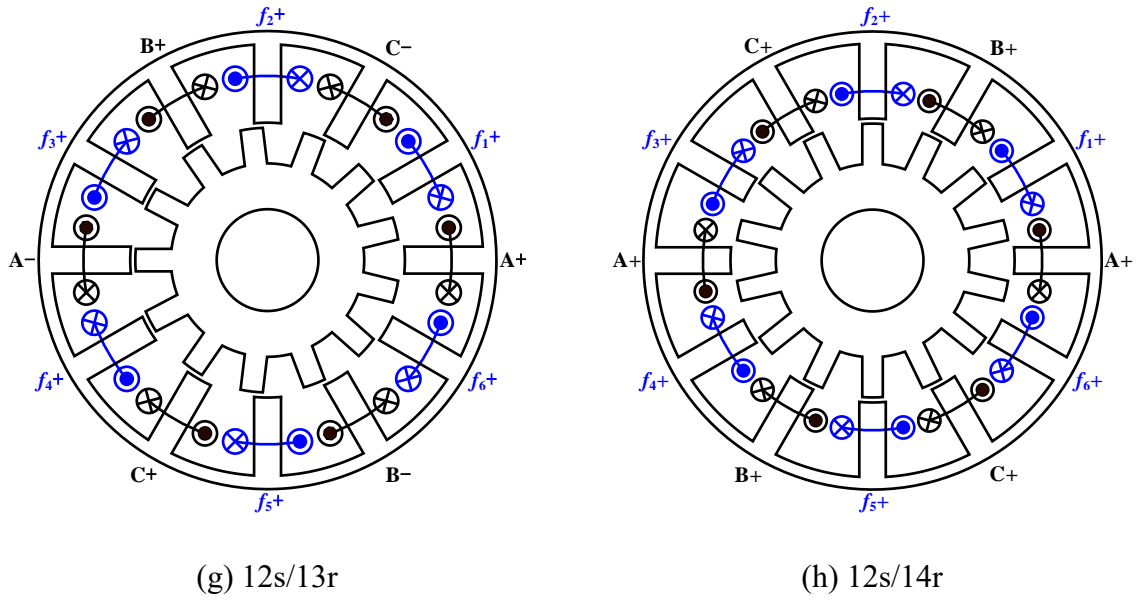


Fig. 2.1. Structure and winding configuration of the three-phase non-overlapped SWFSMs [ZHU15a].

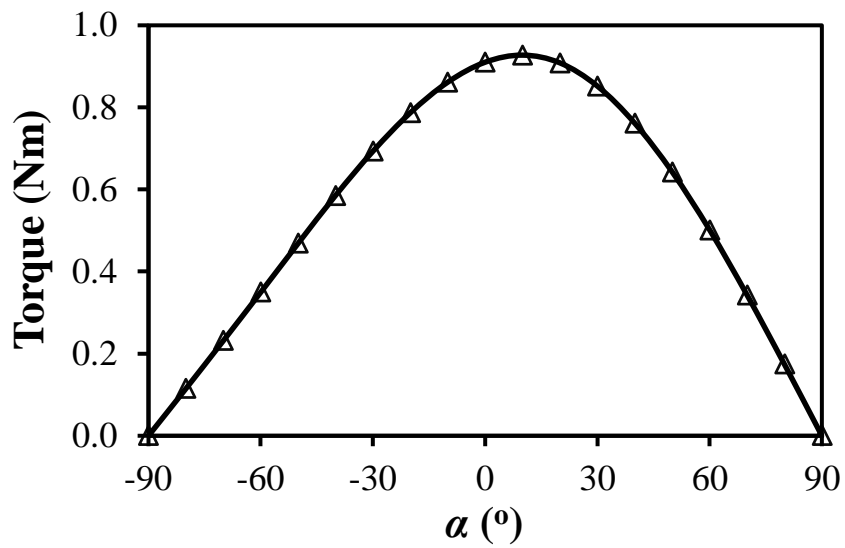
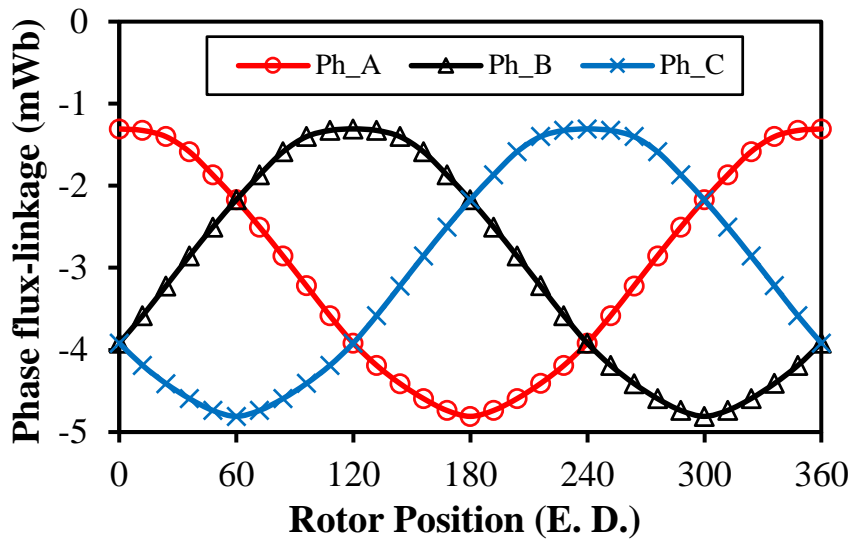


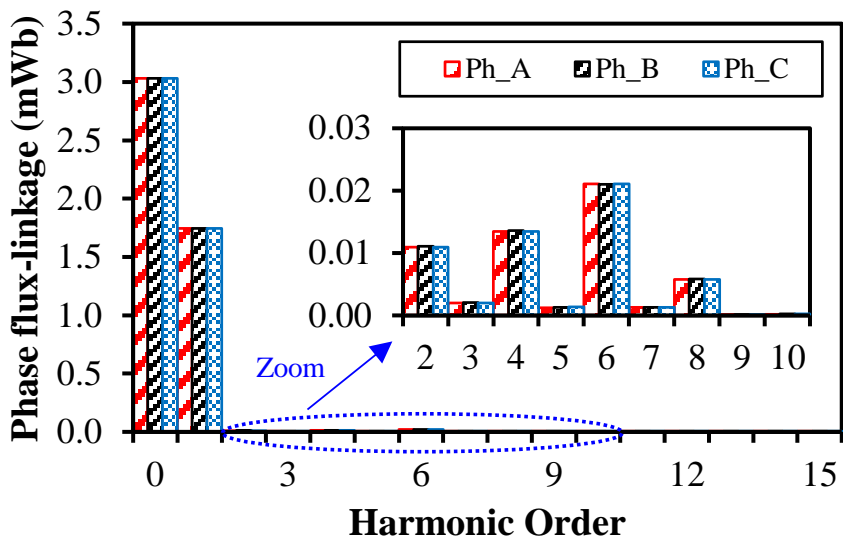
Fig. 2.2. Average electromagnetic torque versus α for the 6s/7r SWFSM.

Table 2.1 Design Parameters of Non-Overlapped SWFSMs

Items	Unit	Values							
Outer diameter of stator	mm	90							
Stator pole number	-	6	6	6	6	12	12	12	12
Rotor pole number	-	4	5	7	8	10	11	13	14
Axial length	mm	25							
Diameter of rotor shaft	mm	20							
Air-gap length	mm	0.5							
Stator yoke thickness	mm	7	6.1	5.4	5.2	3.4	2.9	2.6	2.4
Stator inner radius	mm	23.9	24.35	25.7	26.2	26.2	26.6	27.5	28.4
Stator tooth arc	°	30.1	26.4	21.1	20.1	13.6	12.1	11.1	10.5
Rotor yoke thickness	mm	8.3			9				
Rotor tooth arc	°	31.5	26.4	20.1	17.1	12.9	12.1	9.6	8.4
Number of turns per armature coil	-	18							
Number of turns per excitation coil	-	90							
Total copper loss	W	60							
Excitation winding copper loss ratio	-	0.55	0.57	0.59	0.59	0.54	0.55	0.56	0.58
Slot packing factor	-	0.4							

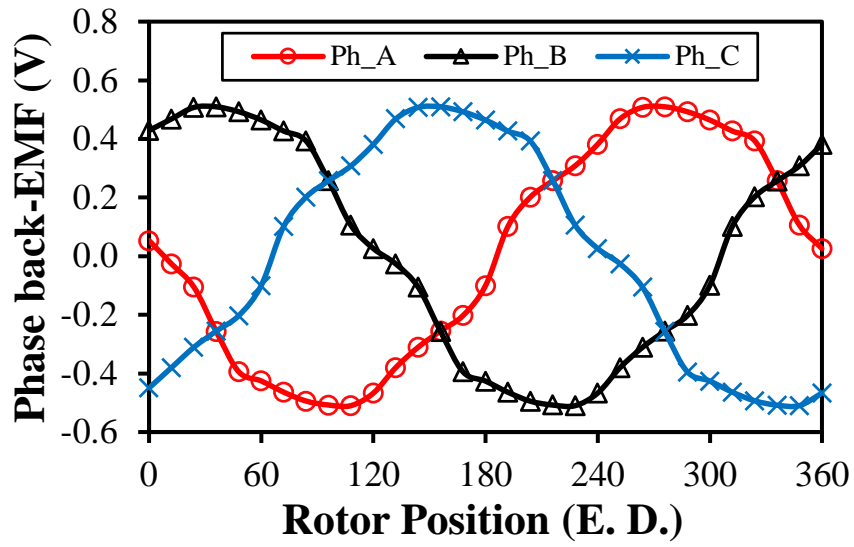


(a) Waveforms

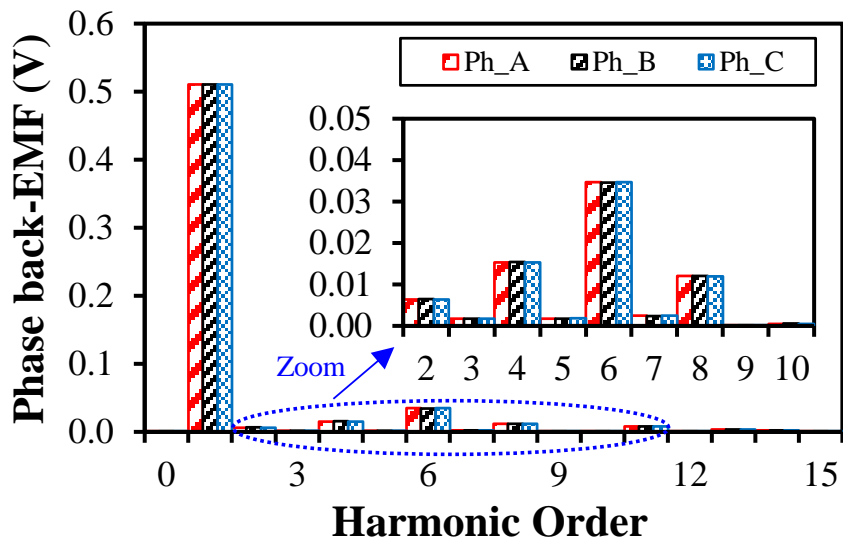


(b) Spectra

Fig. 2.3. Phase flux-linkage in the 6s/7r SWFSM at open-circuit.



(a) Waveforms



(b) Spectra

Fig. 2.4. Phase back-EMF in the 6s/7r SWFSM at open-circuit @400rpm.

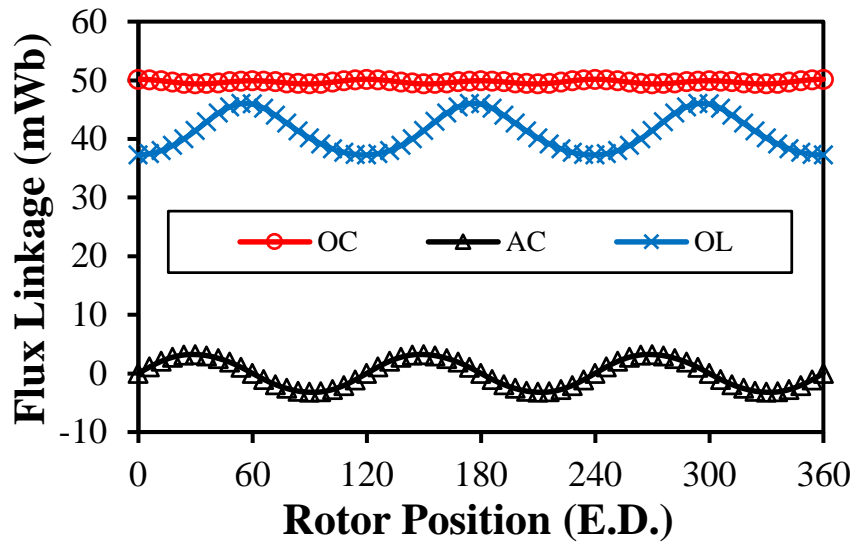
2.3 Induced EMF in Excitation Winding

2.3.1 Phenomenon

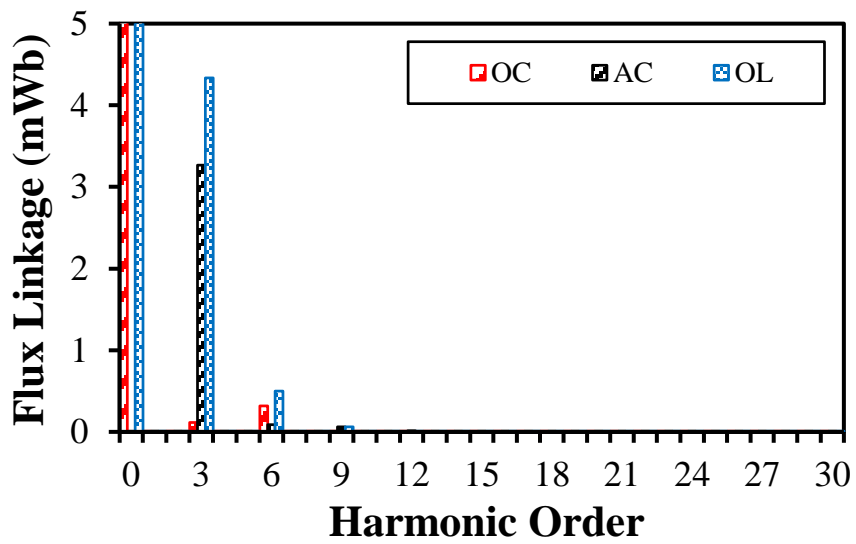
The excitation winding flux-linkages and the induced EMFs of the 6s/7r SWFSM under different cases (OC, AC, and OL) are shown in Figs. 2.5 and 2.6. Under open-circuit, the armature coils are open-circuited while the field coils are excited by constant DC current. Due to the salient-pole stators and rotors, the air-gap field harmonics are abundant in these SWFSMs. Therefore, the open-circuit armature winding flux-linkages and induced back-EMFs suffer from a lot of harmonics, as shown in Figs. 2.3 and 2.4. Similarly, because of doubly salient structure and air-gap field modulation, the excitation winding suffers from pulsating flux-linkage and induced EMF at open-circuit as well, which is the excitation winding induced EMF at open-circuit (OC), as shown by the red line with markers in Figs. 2.5(a) and 2.6(a).

If the excitation field is removed, i.e., $I_e=0$, while the phase windings are excited by three-phase sinusoidal currents, the excitation winding still suffers from induced EMF as depicted in Fig. 2.6(a). This induced EMF is because of the mutual inductance harmonics between two winding sets. For convenience, this EMF is defined as the armature induced excitation winding EMF (AC).

In the case of on-load operation, the induced EMF at open-circuit and the armature induced EMF exist in the excitation winding simultaneously, as shown by the blue line with markers in Fig. 2.6(a), which is defined as the on-load induced excitation winding EMF (OL). However, it should be mentioned that the induced EMF at on-load cannot be obtained by adding up the armature induced EMF and the open-circuit one since these two EMF components can be easily affected by magnetic saturation. It can also be observed that the excitation winding of the 6s/7r SWFSM exhibits the EMF harmonics of $3k$ under different excitations and k is a positive integer, as shown in Fig. 2.6(b).

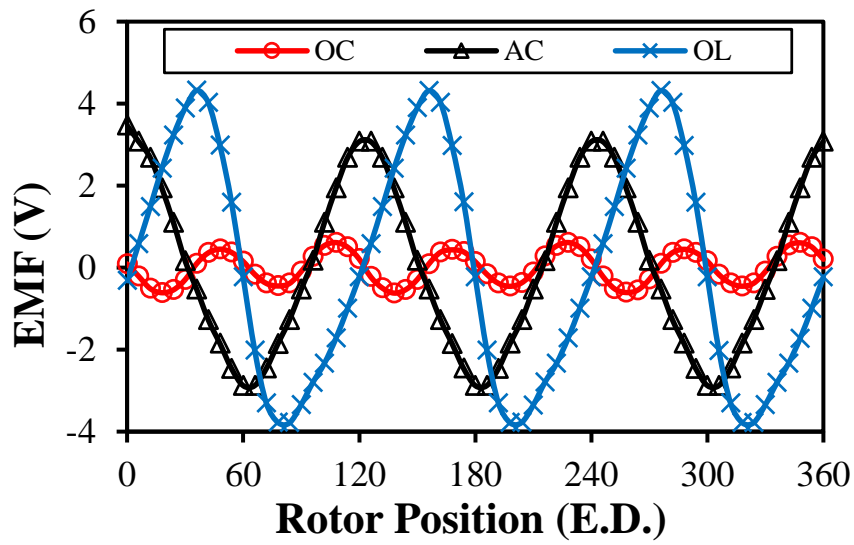


(a) Waveforms

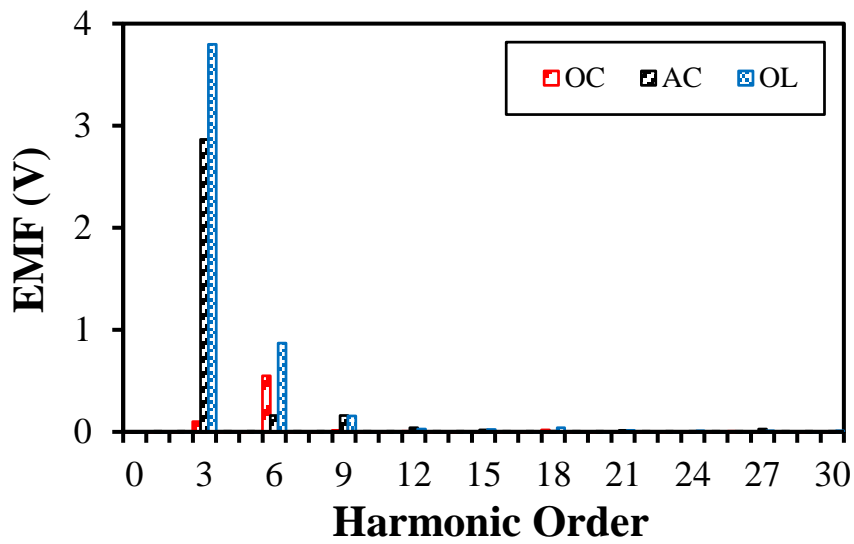


(b) Spectra

Fig. 2.5. Excitation winding flux-linkages in the 6s/7r SWFSM under different cases.



(a) Waveforms



(b) Spectra for all DC coils

Fig. 2.6. Excitation winding EMFs in the 6s/7r SWFSM under different cases.

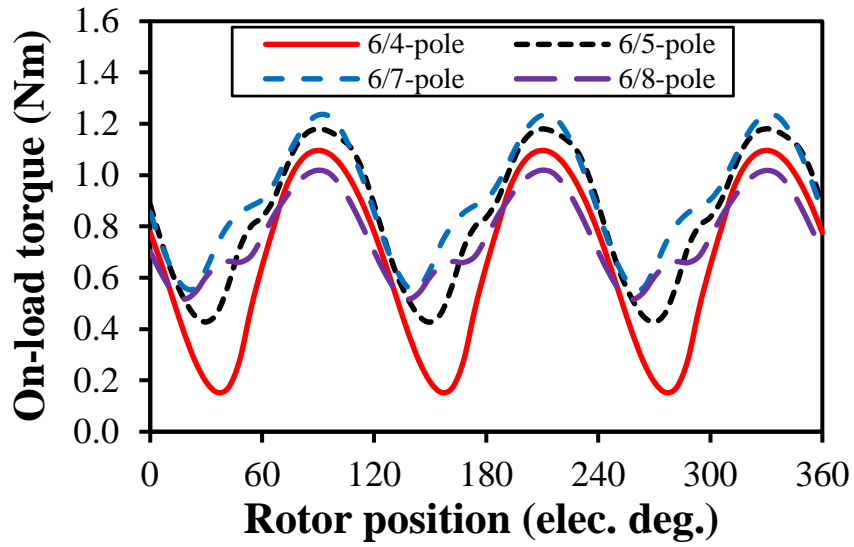
2.3.2 Impact of Slot/Pole Combinations

For the non-overlapped SWFSMs in Fig. 2.1, a lot of slot-pole combinations can be employed. In theory, except for the multiples of the armature winding phase number, any other integer rotor pole numbers can be employed. This kind of machines operate based on the modulation effect of the salient-pole rotors. If the rotor pole numbers are the multiples of armature winding phase number, the magnetic fields cannot be effectively modulated in the airgap to produce steady output torque. Among the three-phase 6-slot counterparts, the rotor pole number 4, 5, 7, and 8 are preferable. While for the three-phase 12-slot counterparts, 10, 11, 13, and 14 are more suitable due to higher winding factors and hence better torque performance. Therefore, these eight machines will be used to study the impact of the slot-pole combinations on EMF pulsations under different cases.

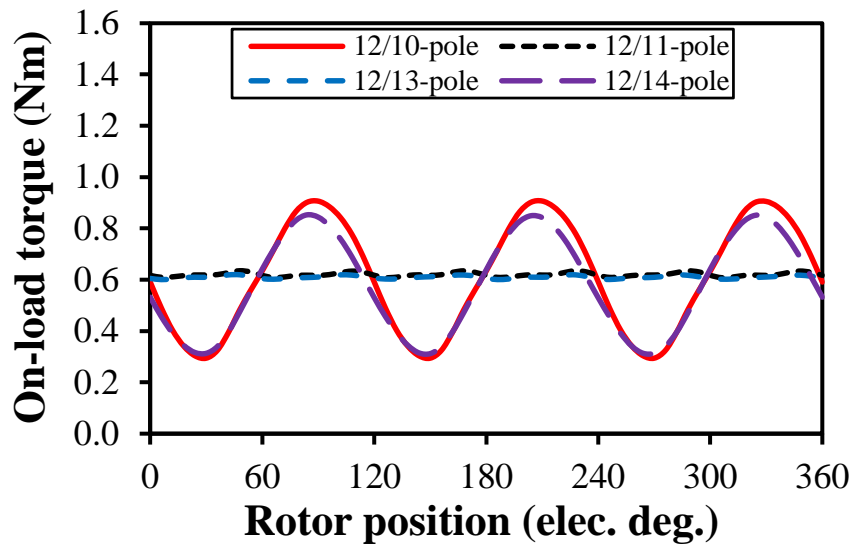
To perform a fair comparison, the SWFSMs having various slot-pole combinations are globally optimized by the commonly used genetic algorithm in Ansys Maxwell. During the global optimization, the total copper loss is fixed at 60W and other losses are not considered since the copper loss is the major loss component, owing to the relatively lower rated speed, i.e., 400rpm. For achieving the available maximum average torque for the non-overlapped SWFSMs, the optimal excitation winding copper loss to total copper loss ratio (P_{cuf}/P_{cut}) is 0.5 under a fixed total copper loss, which can be derived by using similar derivations illustrated in [CHE10b]. However, the optimal copper loss ratio will become higher than 0.5 under high saturation levels. Therefore, the copper loss ratio has also been considered in the optimizations.

During the global optimizations, the air-gap length, the outer diameter of stator, the axial length, and the radius of rotor shaft are fixed as well, as listed in Table 2.1 together with other optimized parameters. Fig. 2.7 shows the on-load torque waveforms of the optimized SWFSMs having different slot/pole number combinations. It shows that the 6-slot counterparts exhibit relatively higher torque ripples since their back-EMF waveforms suffer from both odd and even order harmonics. The average torques of the 6/5-pole and 6/7-pole machines are higher than those of the 6/4-pole and 6/8-pole machines due to higher winding factors. Similarly, due to

higher winding factors, the average torques of the 12/11-pole and 12/13-pole machines are higher than those of the 12/10-pole and 12/14-pole machines. The torque ripples of the 12/11-pole and 12/13-pole machines are much smaller than those of other machines since their back-EMF waveforms do not contain even order harmonics.



(a) 6-slot machines



(b) 12-slot machines

Fig. 2.7. On-load torque waveforms of the optimized non-overlapped SWFSMs having different slot/pole combinations.

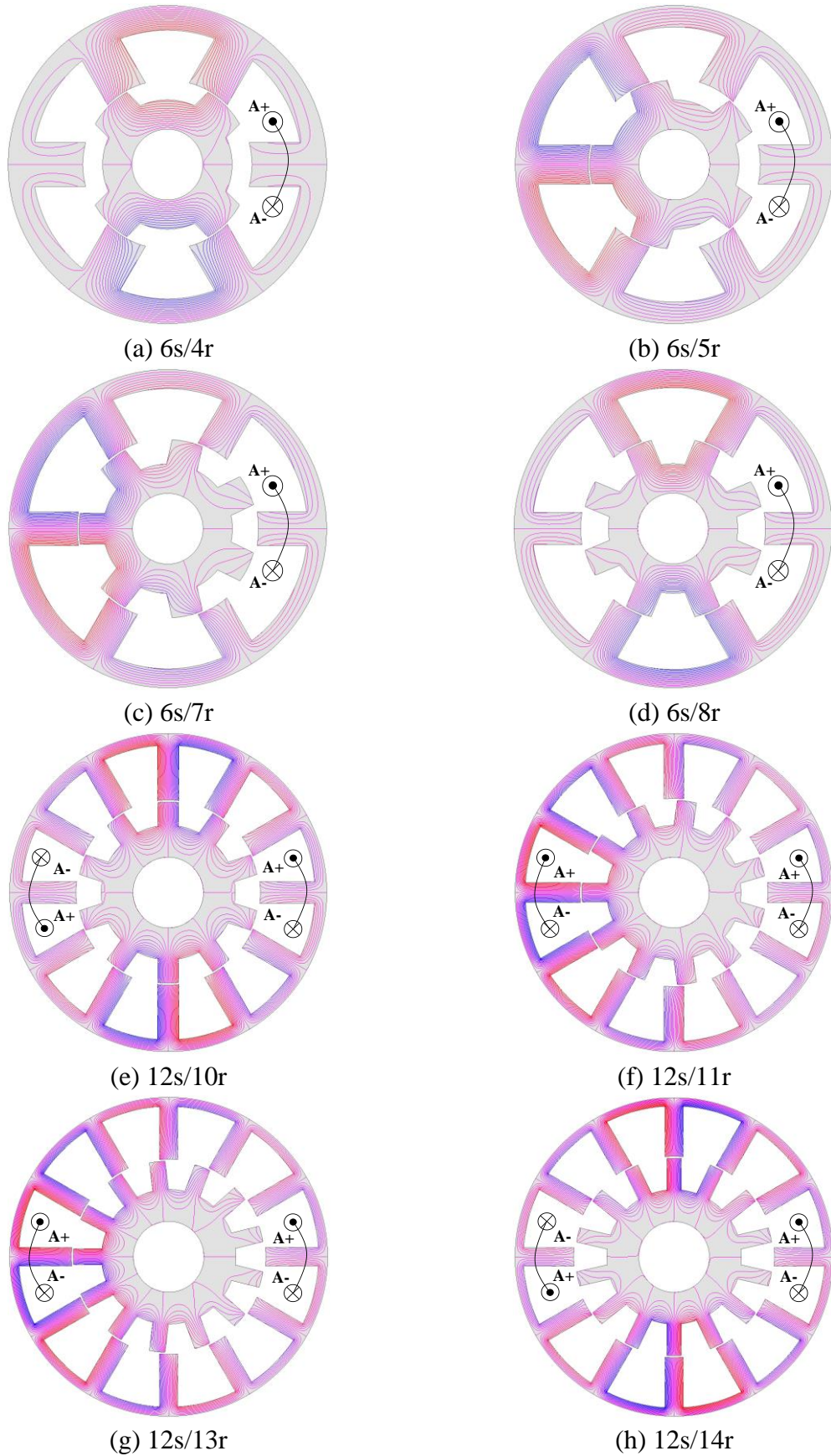


Fig. 2.8. Open-circuit flux distributions of the non-overlapped SWFSMs having different slot/pole combinations.

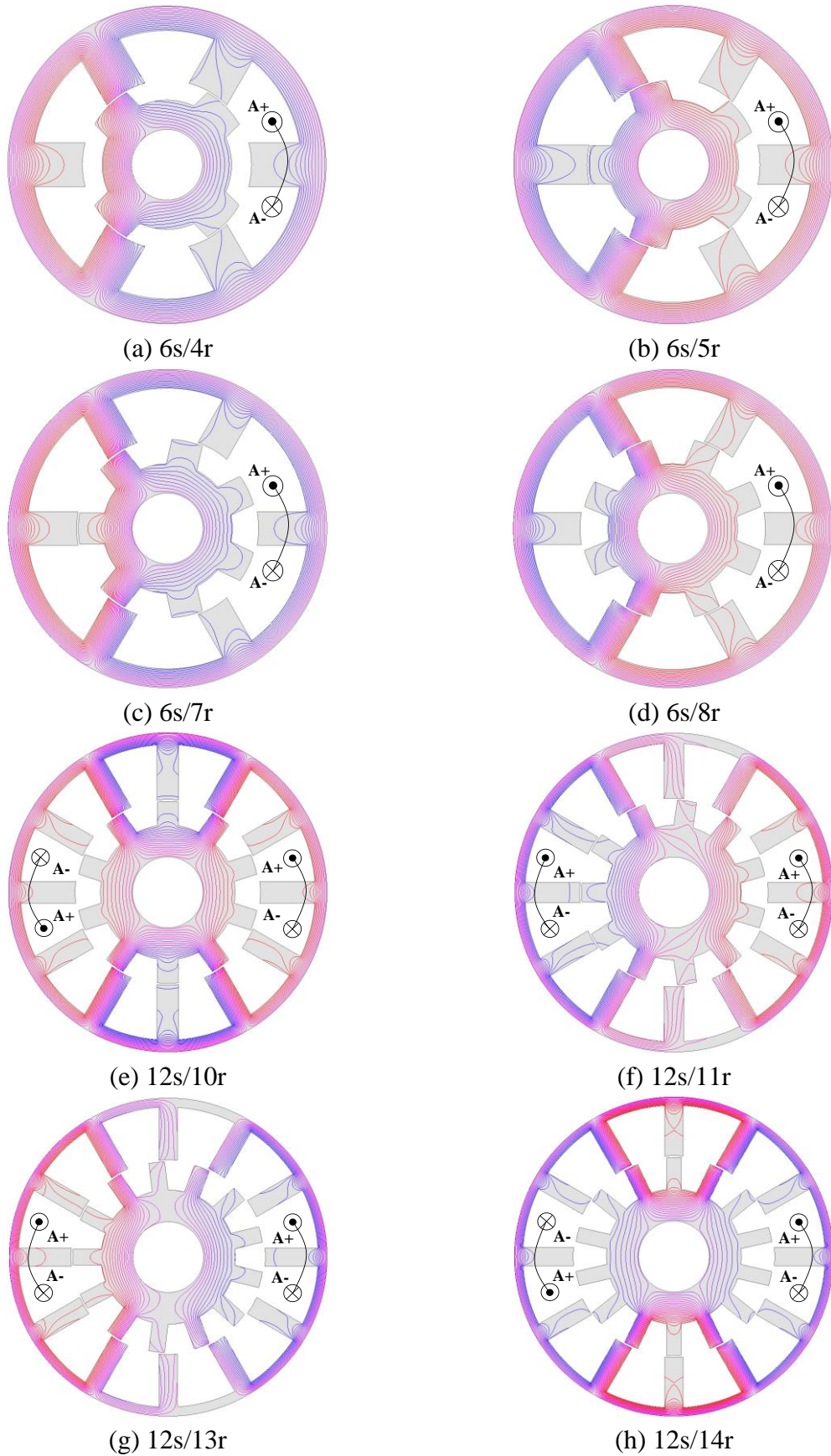


Fig. 2.9. Flux distributions of the non-overlapped SWFSMs having different slot/pole combinations under armature excitation only.

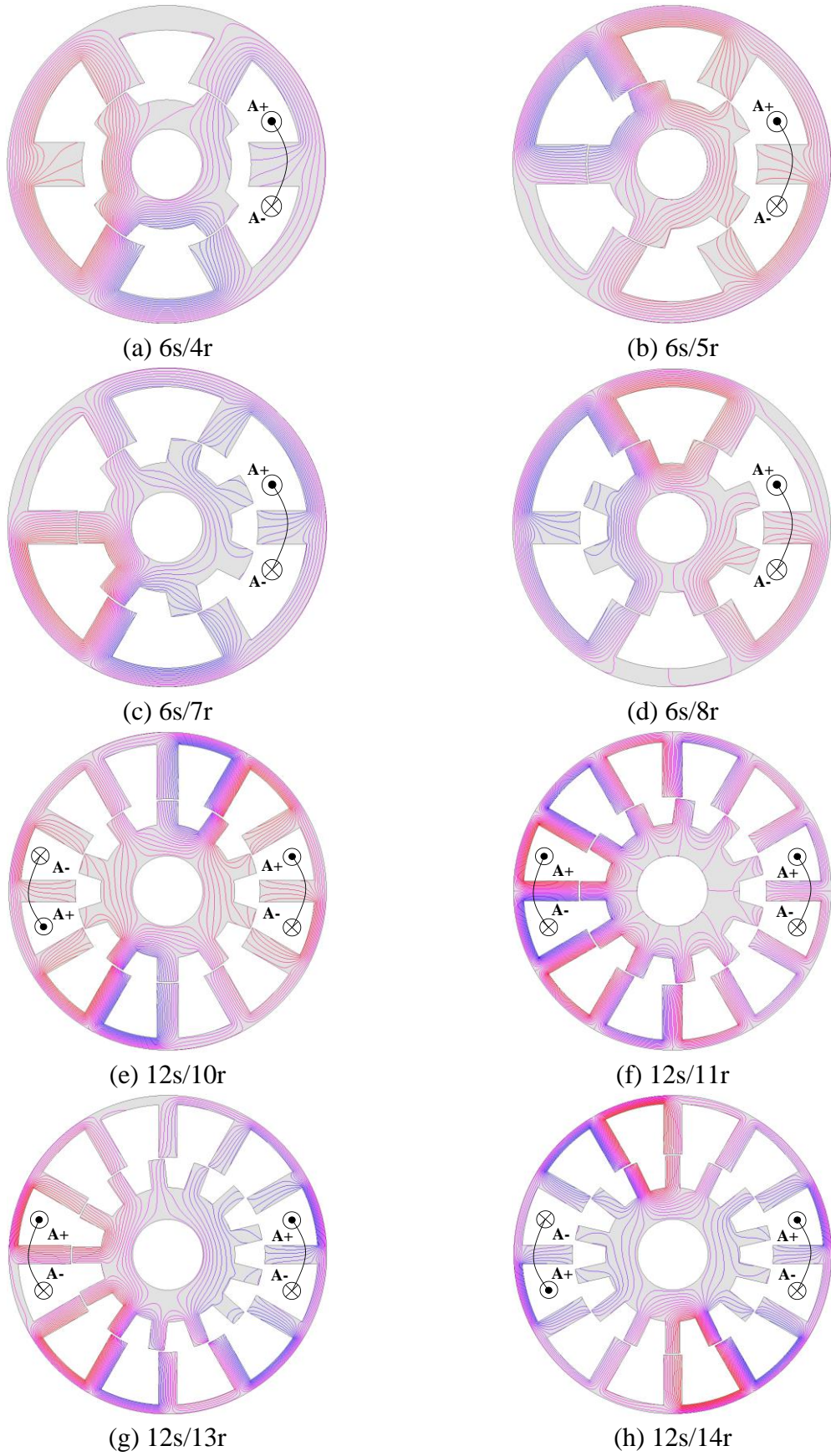


Fig. 2.10. On-load flux distributions of the non-overlapped SWFSMs having different slot/pole combinations.

Figs. 2.8-2.10 show the flux distributions of the SWFSMs having different slot and pole number combinations under open-circuit, armature excitation only and on-load, respectively.

To illustrate the operating principles of these non-overlapped SWFSMs, the 6s/7r machine is taken as an example. It is worth mentioning that, for the 6-slot machines, each phase only contains one armature coil. While for the 12-slot machines, each phase contains two armature coils. Fig. 2.11 shows the open-circuit flux distributions of the 6s/7r machine at different rotor electric positions (θ_e). At $\theta_e=0^\circ$, the flux-linkage of phase A is minimum since the stator tooth with phase A coil aligns with the rotor slot. While at $\theta_e=180^\circ$, the rotor tooth aligns with the stator tooth with phase A coil and therefore the flux-linkage of phase A is maximum. As such, back-EMFs are induced in armature coils as the salient-pole rotor rotates. It should be noted that, for the 6-slot machines, the flux-linkages of armature coils are unipolar. For the 12-slot machines having even number of rotor poles, e.g., 12s/10r and 12s/14r, the flux-linkages of armature coils and phase windings are both unipolar as well. While for the 12-slot machines having odd number of rotor poles, the flux-linkages of armature coils are unipolar but the flux-linkages of phase windings are bipolar. For these machines having unipolar phase flux-linkages, the induced phase back-EMFs are bipolar since the fundamental flux-linkage harmonic with high amplitude is the dominant harmonic and the zero flux-linkage harmonics do not induce any back-EMFs.

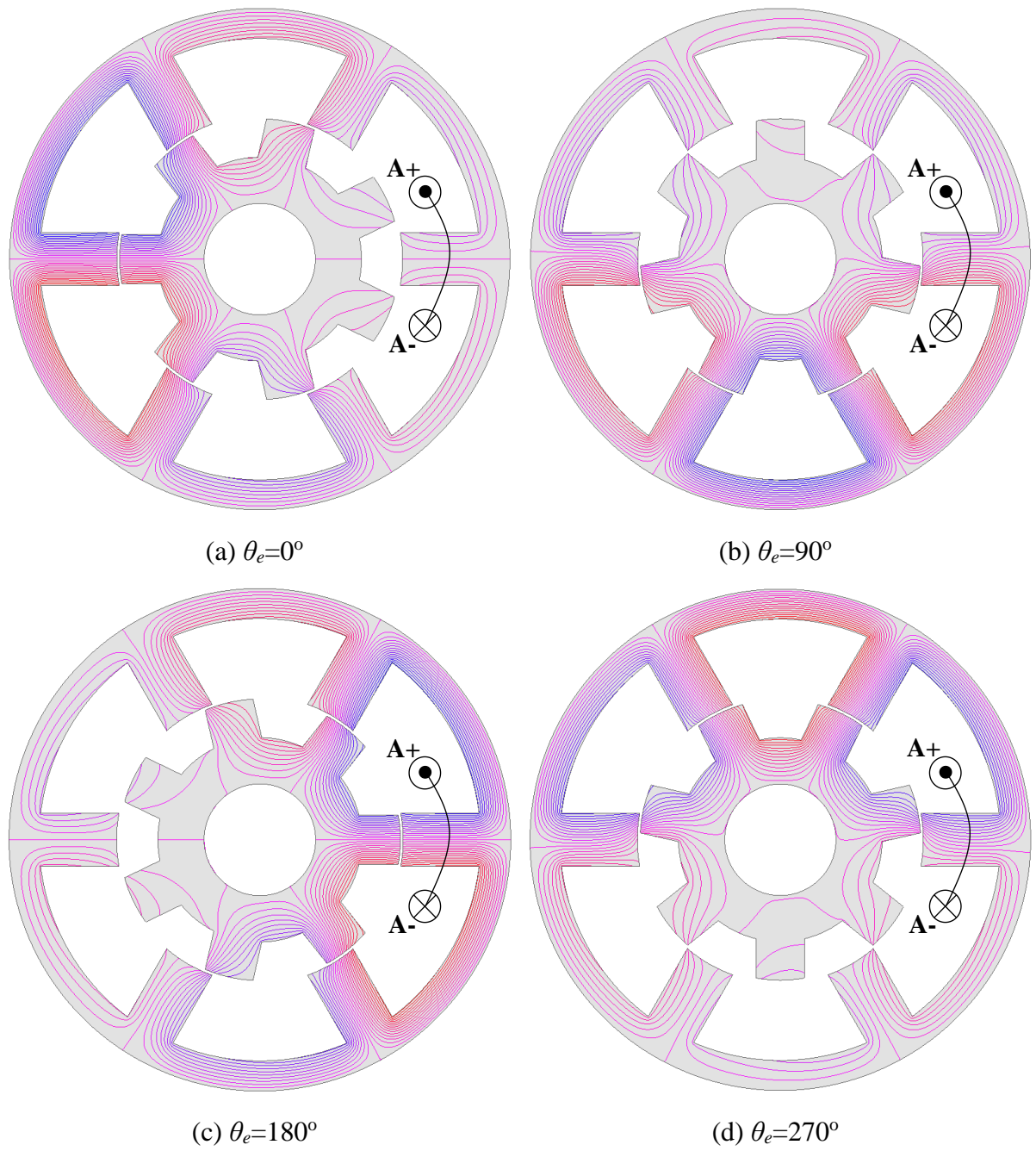
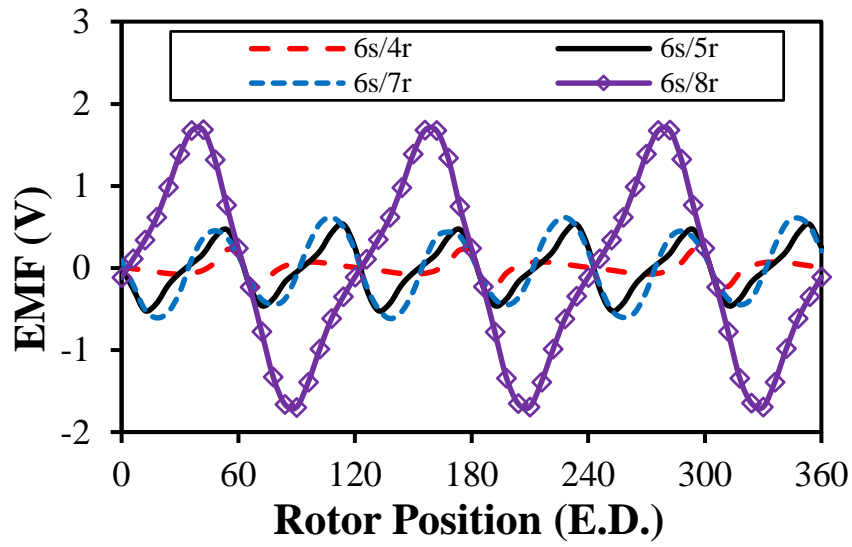


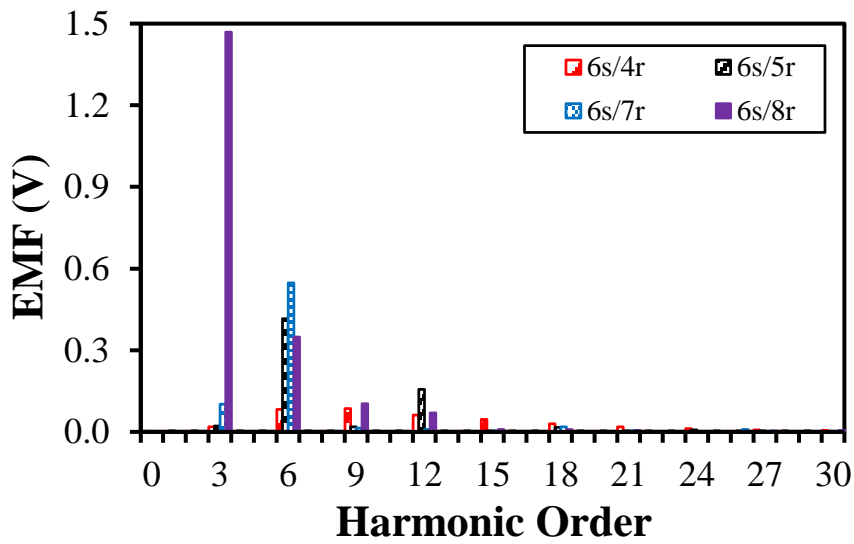
Fig. 2.11. Open-circuit flux distributions of the 6s/7r SWFSM at different rotor positions.

Fig. 2.12 shows the open-circuit induced excitation winding EMFs in 6-slot machines. It can be found that there is a periodical variation of the induced EMF against the rotor position for each machine. The highest induced EMF exists in the 6s/8r machine while the lowest one is observed in the 6s/4r machine. Moreover, the induced EMF waveforms of 6s/5r and 6s/7r machines are very similar. The difference between the induced EMFs is mainly attributed to low order harmonics amplitudes, i.e., 3rd and 6th etc. However, the EMF harmonic orders at open-circuit are the same for these four machines, i.e., $3k$, as depicted in Fig. 2.12(b).

As shown in Fig. 2.13, when the machines are loaded, the EMF of the 6s/4r machine is still the smallest while the 6s/5r machine has the second-smallest. Moreover, the 6s/7r and 6s/8r machines possess similar waveforms at on-load. For the 6-slot machines, they have the same armature induced EMF harmonic orders, i.e., $3k$, as illustrated in Fig. 2.14. Therefore, the EMF harmonic orders at on-load are $3k$ as well for these four machines, as displayed in Fig. 2.13(b).



(a) Waveforms

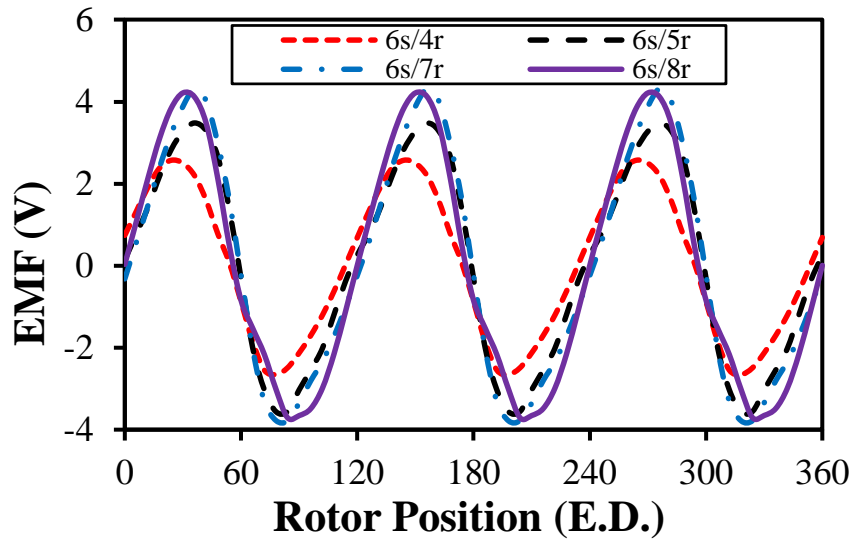


(b) Spectra

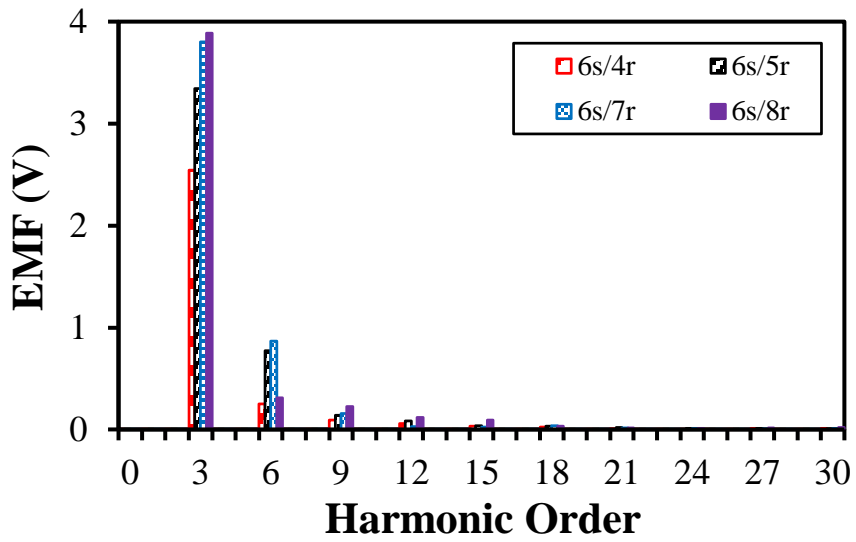
Fig. 2.12. Excitation winding EMFs in SWFSMs having 6-slot at open-circuit.

The EMF waveforms at open-circuit of the 12-slot counterparts are shown in Fig. 2.15(a). It reveals that the EMF of the 12s/10r machine is the highest at open-circuit while the 12s/14r machine is second to the 12s/10r machine. Furthermore, the EMF waveforms of the 12s/11r and 12s/13r machines are very similar and lower than those of other two machines. The EMF harmonic orders at open-circuit are $3k$ for the 12s/10r and 12s/14r machines but $6k$ for the 12s/11r and 12s/13r machines, which are different from the SWFSMs having 6-slots.

As shown in Fig. 2.16, under on-load condition, the 12s/14r machine shows the highest induced EMF while the EMF of the 12s/10r machine is the second-highest. Besides, the EMF waveforms of the 12s/11r and 12s/13r machines are almost coincident. For the 12-slot counterparts, the armature induced EMF harmonic orders are identical with that at open-circuit, as depicted in Fig. 2.17. Consequently, the EMF harmonic orders at on-load are $3k$ for the 12s/10r and 12s/14r machines and $6k$ for the 12s/11r and 12s/13r machines. Table 2.2 summarizes the EMF harmonic orders for various slot/pole number combinations under different cases.

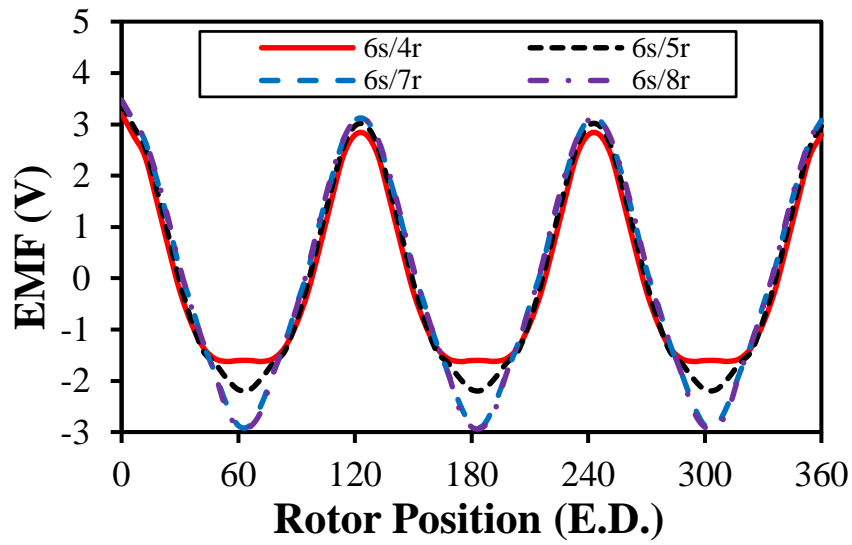


(a) Waveforms

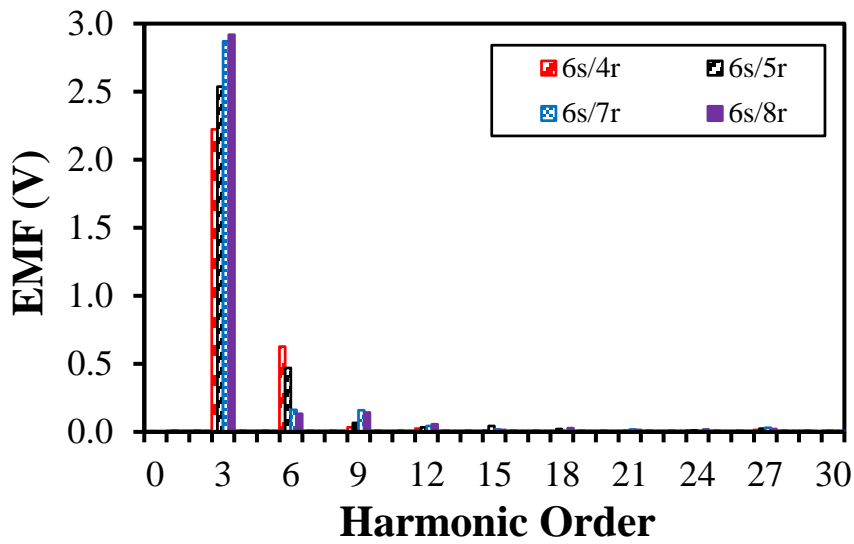


(b) Spectra

Fig. 2.13. Excitation winding EMFs in SWFSMs having 6-slot at on-load.

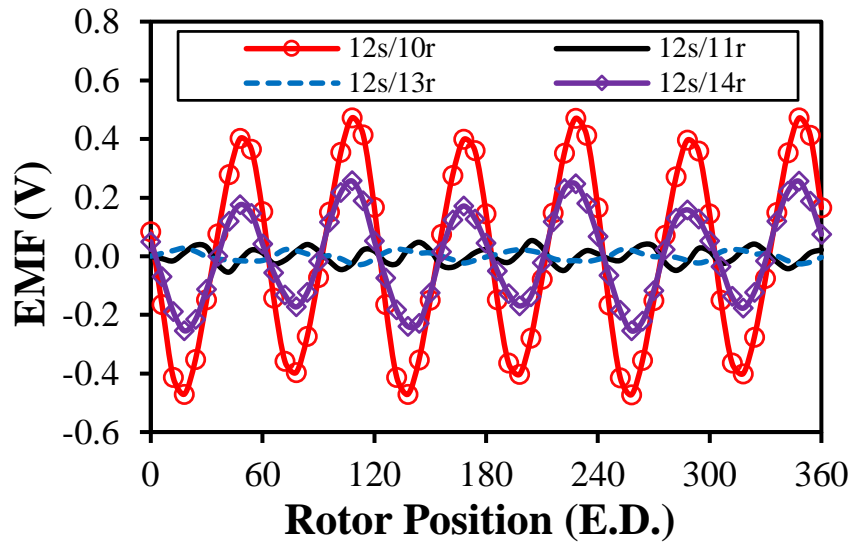


(a) Waveforms

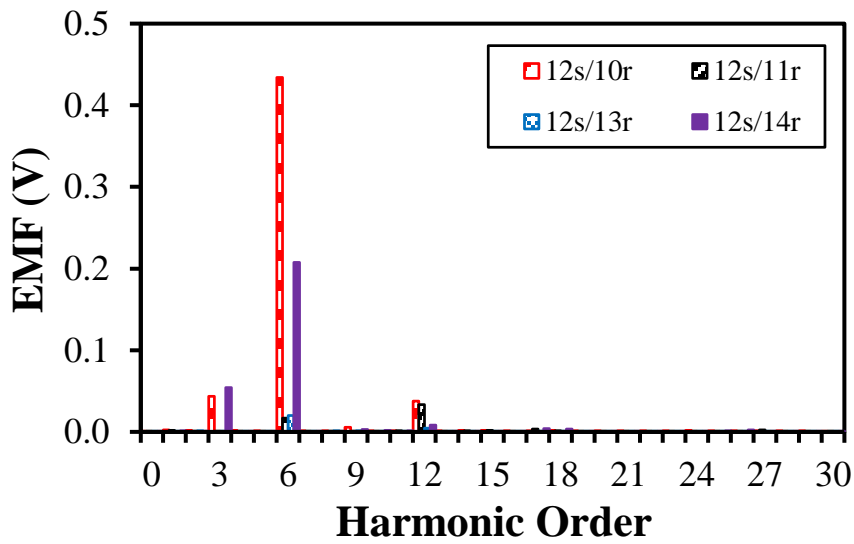


(b) Spectra

Fig. 2.14. Excitation winding EMFs in SWFSMs having 6-slot caused by armature currents.

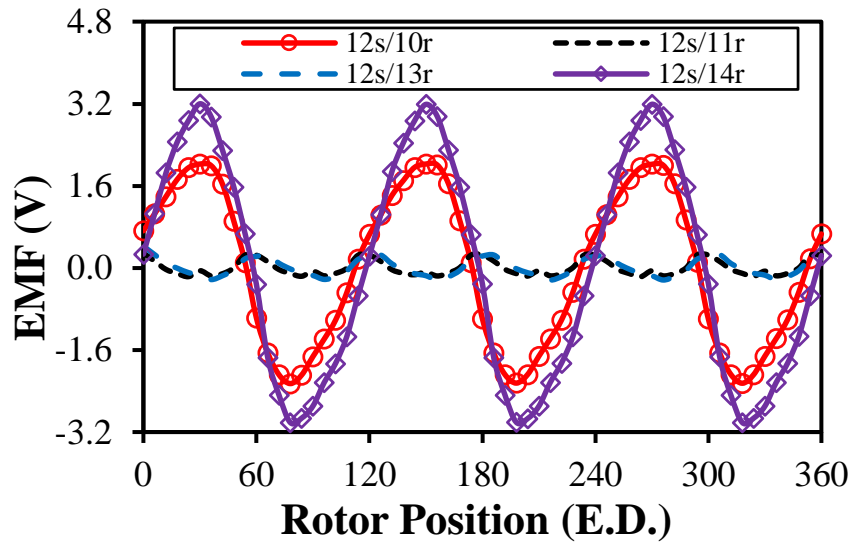


(a) Waveforms

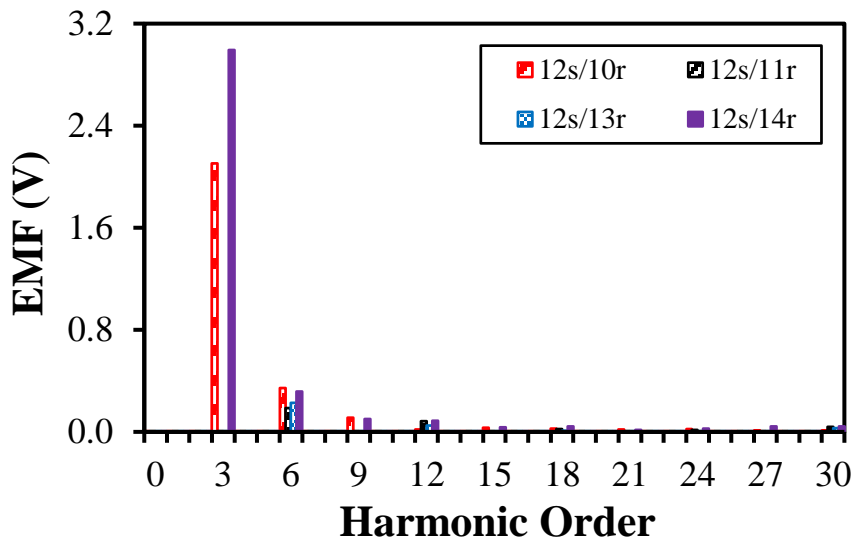


(b) Spectra

Fig. 2.15. Excitation winding EMFs in SWFSMs having 12-slot at open-circuit.



(a) Waveforms

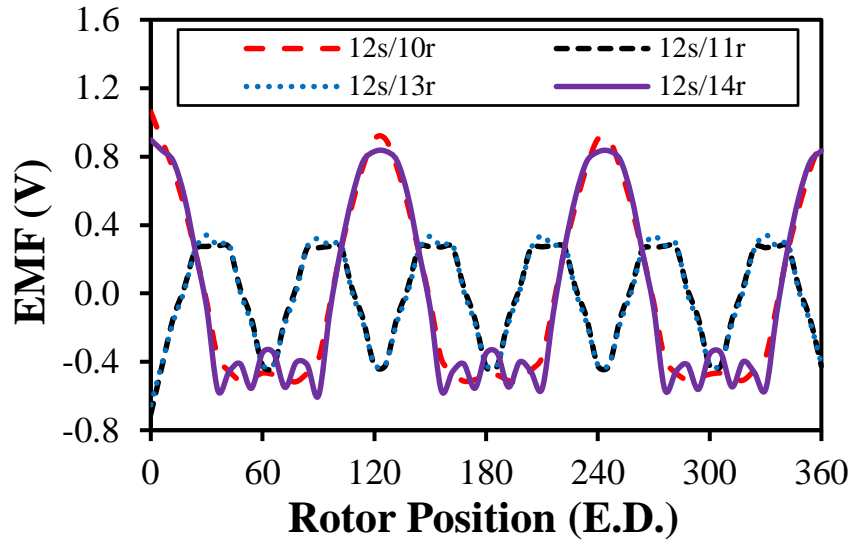


(b) Spectra

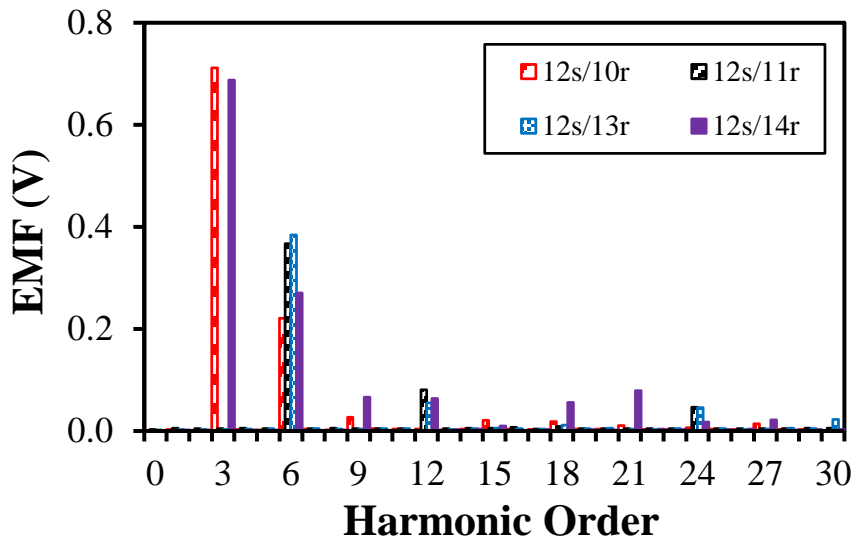
Fig. 2.16. Excitation winding EMFs in SWFSMs having 12-slot at on-load.

Fig. 2.18 shows the peak-to-peak excitation winding induced EMFs for various slot-pole combinations at open-circuit and on-load cases. As can be found that the 6-slot counterparts exhibit relatively larger peak-to-peak EMFs than the 12-slot counterparts at both open-circuit and on-load, due to abundant EMF harmonics and larger amplitudes of low order EMF harmonics. Furthermore, the peak-to-peak induced EMF of open-circuit is much smaller than that of on-load for each machine since the EMF at on-load is constituted of two EMF

components as aforementioned. Although the peak-to-peak induced EMF of each machine is subject to magnetic saturation, the EMF harmonic orders are not influenced by magnetic saturation.



(a) Waveforms



(b) Spectra

Fig. 2.17. Excitation winding EMFs in SWFSMs having 12-slot caused by armature currents.

Table 2.2 Excitation Winding Induced EMF Harmonic Orders

Slot/pole	Open-circuit	Armature induced	On-load
6/4	$3k$	$3k$	$3k$
6/5	$3k$	$3k$	$3k$
6/7	$3k$	$3k$	$3k$
6/8	$3k$	$3k$	$3k$
12/10	$3k$	$3k$	$3k$
12/11	$6k$	$6k$	$6k$
12/13	$6k$	$6k$	$6k$
12/14	$3k$	$3k$	$3k$

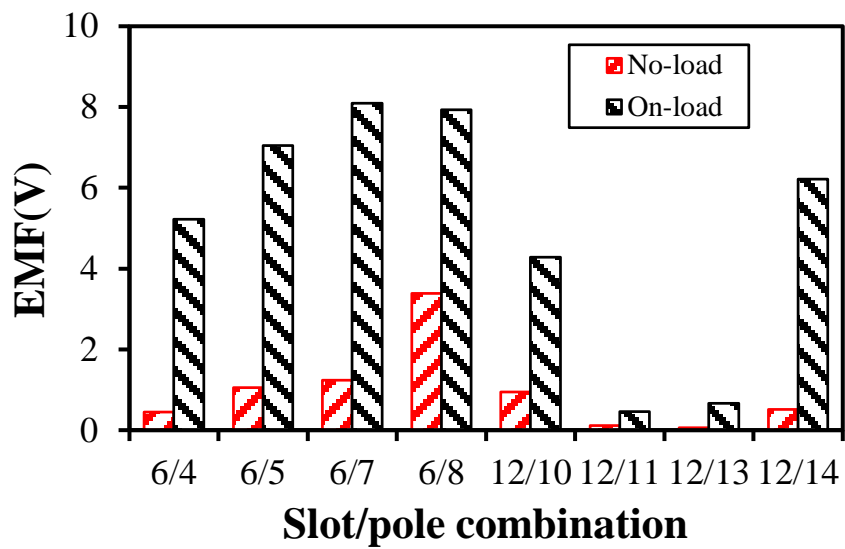
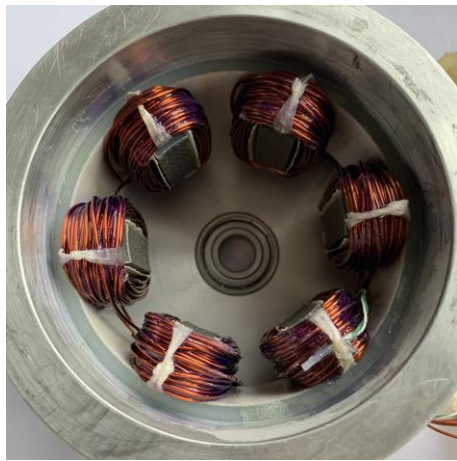


Fig. 2.18. Peak-to-peak excitation winding induced EMFs for various slot-pole combinations.

2.4 Experimental Validation

In order to verify the foregoing FEA simulations, two existing prototype SWFSMs (6s/8r and 12s/14r) from the previous research are employed as illustrated in Fig. 2.19. With 15A field current, the measured and 2D FEA predicted armature winding back-EMFs are comparatively shown in Fig. 2.20. It is worth mentioning that the following experiments have been carried out at the rated rotor speed, i.e., 400rpm. It is shown that there are good agreements between the test results and the 2D FEA calculated one and the difference between them is mainly caused by the end flux-leakage.



(a) 6-slot



(b) 8-pole



(c) 12-slot

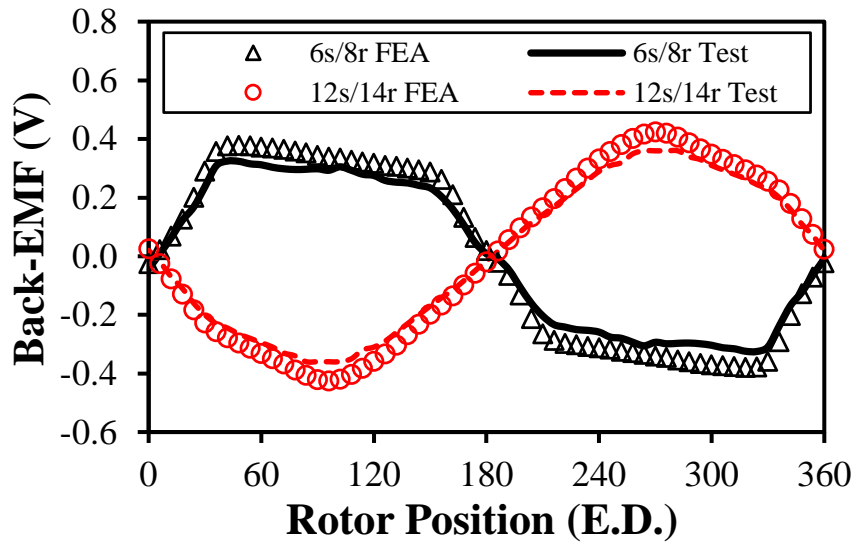


(d) 14-pole

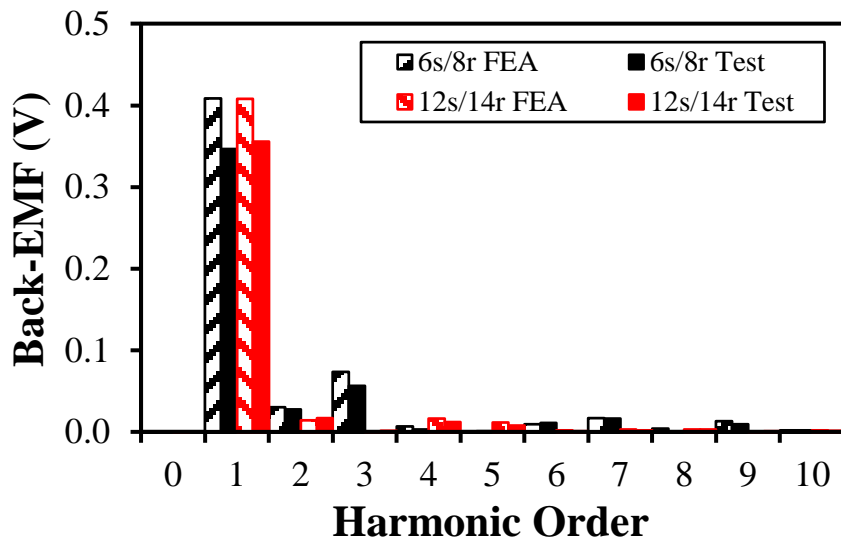
Fig. 2.19. Photos of prototype SWFSMs.

It should be noted that the method proposed in [ZHU09b] is employed for the measurement of on-load static torques. The prototype machine is clamped by the jaws of a lathe and the rotor shaft of the prototype machine is connected to one end of the balance beam. A pre-load weight is added to the other end of the balance beam to make sure the beam bar always contacts the digital scale. During the experiment, the field current is fixed at 15A and the relationship between three-phase armature currents is $i_a = -2i_b = -2i_c$. By rotating the stator in 180 electrical degrees with fixed step, the torque acting on the rotor can be measured and hence the rotor positions of d -axis and q -axis can be identified. The torques versus q -axis armature currents of the prototype machines are shown in Fig. 2.21. It is revealed that the test results are lower than the FEA simulations since the flux-leakage in end region is not accounted in 2D FEA calculations. Overall, a good agreement between the FEA and measured results can be observed.

It is difficult to accurately measure the excitation winding induced EMF if the excitation current is applied. Therefore, a ‘detective excitation winding’ with only one turn is wound on the stator for accurately measuring the actual induced EMF since the current in the detective winding is zero. The actual induced EMF can then be easily obtained by multiplying the measured EMF in the detective winding by the number of turns since the detective winding has only one turn.



(a) Waveforms



(b) Spectra

Fig. 2.20. Armature winding back-EMFs of prototype SWFSMs at open-circuit ($I_{dc}=15A$).

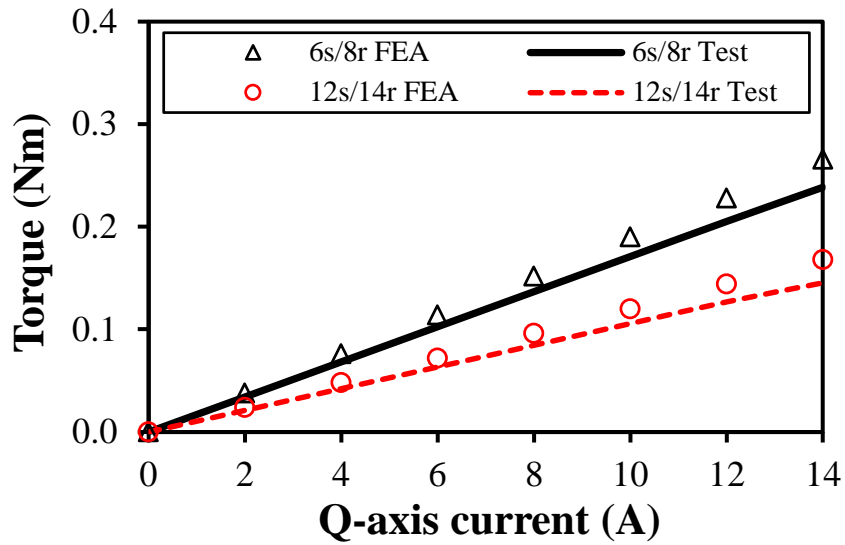
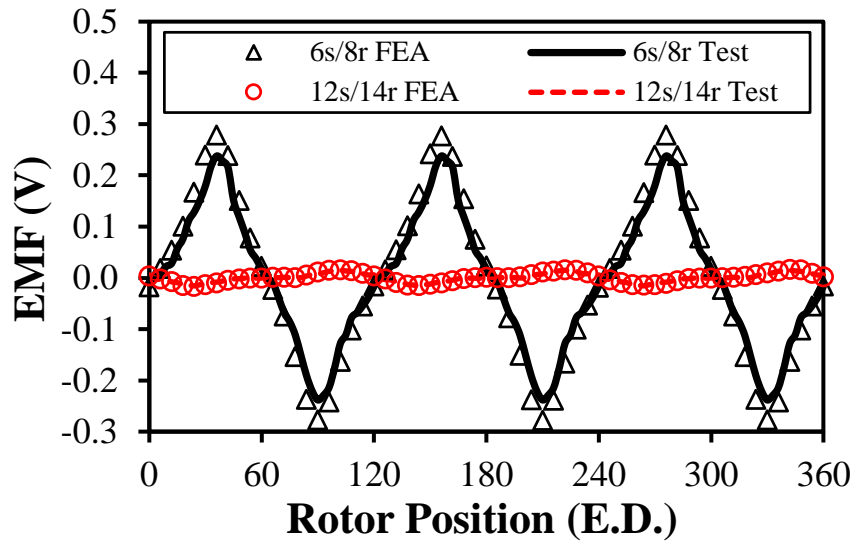
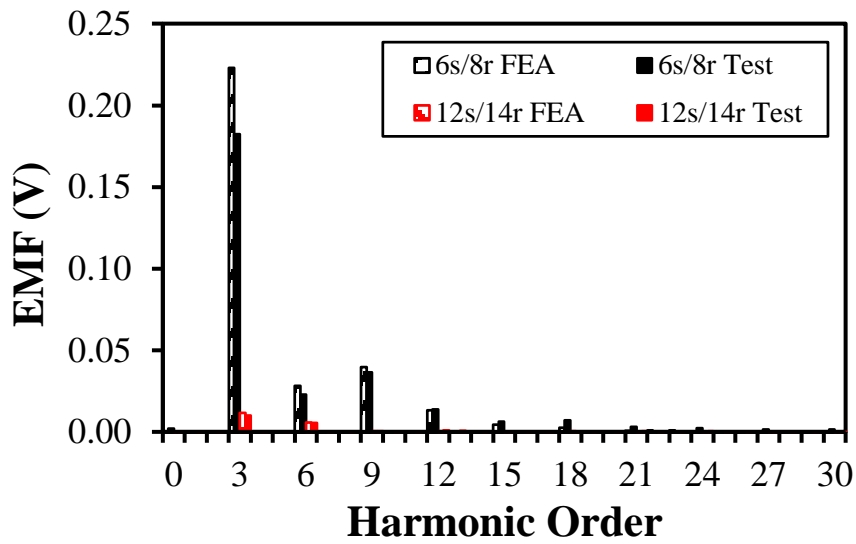


Fig. 2.21. Torque against q -axis current ($I_{dc}=15A$).

The FEA simulated and measured induced EMFs at open-circuit and on-load are comparatively shown in Figs. 2.22 and 2.23, respectively. It is revealed that the FEA predictions agree well with the measured results. Moreover, the induced EMFs at on-load are slightly larger than open-circuit since the EMFs at on-load consist of two components, as aforementioned. Similarly, the differences between the FEA and test results are because of end-effect, manufacturing, and test tolerances.

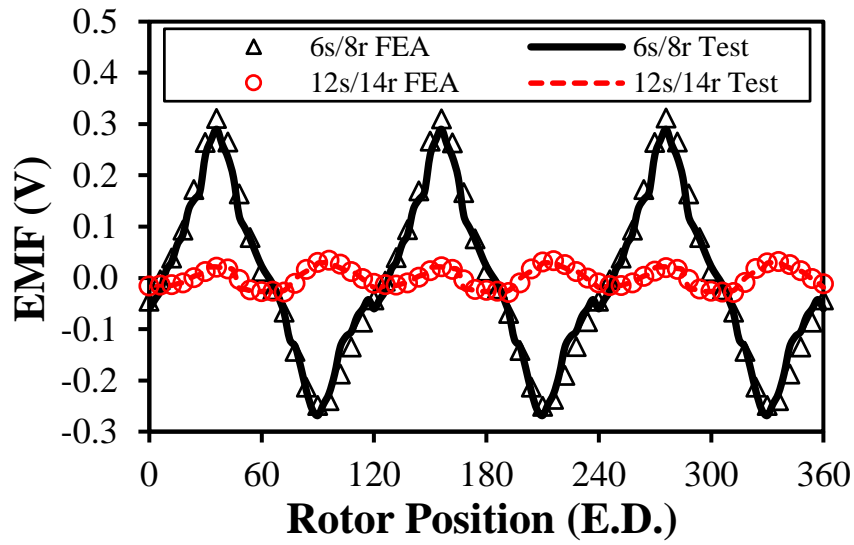


(a) Waveforms

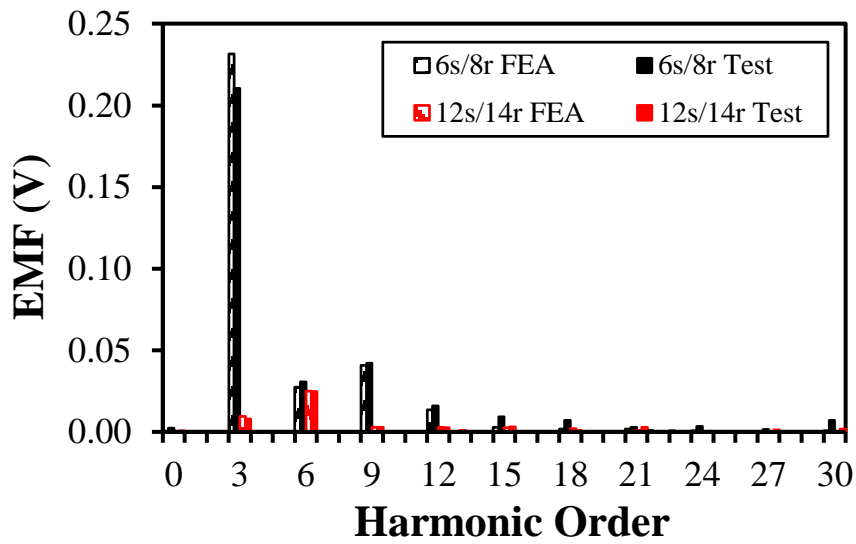


(b) Spectra

Fig. 2.22. Excitation winding EMFs of prototype SWFSMs at open-circuit ($I_{dc}=15A$).



(a) Waveforms



(b) Spectra

Fig. 2.23. Excitation winding EMFs of prototype SWFSMs at on-load ($I_{ac}=4A$, $I_{dc}=15A$).

2.5 Conclusion

This chapter investigates the excitation winding induced EMFs in three-phase non-overlapped SWFSMs. It has revealed that the induced EMF harmonics are different for different slot-pole combinations under different cases. Using suitable slot-pole combinations, the excitation winding EMF can be effectively suppressed by eliminating low-order induced EMF harmonics. Two prototype non-overlapped SWFSMs are fabricated and tested to validate the FEA predictions.

CHAPTER 3

Investigation of DC Winding Induced Voltage in Hybrid Excited Switched Flux Permanent Magnet Machine

The DC winding induced voltage in hybrid excited machines can lead to DC winding current ripple and hence fluctuating field excitation. It may also challenge the DC power source and increase the difficulty of machine control, especially at high speed. The DC winding induced voltage in a hybrid-excited switched-flux permanent magnet (HESFPM) machine is investigated in this chapter. The phenomenon and mechanism of the DC winding induced voltages under both open-circuit and on-load conditions are analyzed, with particular emphasis on on-load operation which consists of open-circuit induced voltage and armature current induced voltage, respectively. Two techniques, i.e., rotor step skewing and unequal rotor teeth, are proposed and comparatively investigated by the finite element analysis (FEA) method to suppress the DC winding induced voltage under on-load condition. FEA results show that the peak-to-peak value of on-load DC winding induced voltage can be effectively suppressed by 96.15% or 89.05% by rotor step skewing or unequal rotor teeth, respectively, whilst the average on-load electromagnetic torque can be maintained at 89.4% or 87.8%. A prototype HESFPM machine is built and tested to verify the FEA results.

This chapter is based on the paper [SUN20a] published in IEEE Transactions on Industry Applications.

3.1 Introduction

Thanks to the rapid development of rare-earth permanent magnet (PM) materials, electrical machines equipped with rare-earth PMs have drawn considerable research interest in recent decades [ZHU07] [CHA07]. PM machines exhibit high torque density and high efficiency due to the replacement of field excitation coils (FECs) by PMs in electrical-excited machines. Nevertheless, the air-gap magnetic field in PM machines is difficult to be regulated due to the fixed excitation of PMs, which restricts their applications in some variable-speed drive systems, such as electrical vehicles, more electrical aircrafts and spindle drives etc. Excellent flux-weakening capability is always required in variable-speed applications for a wide constant power speed range (CPSR). The flux-weakening of PM machines is generally achieved by injecting a negative d -axis armature current ($-i_d$) to counteract the PM flux and reduce the back electromotive force (back-EMF) [SOO94]. However, the flux-weakening with $-i_d$ has the potential to irreversibly demagnetize the PMs. In addition, the available q -axis armature current is decreased due to limited armature current capacity and the torque density may be reduced [ELR10]. Wound field synchronous machines (WFSMs) are desirable for variable-speed applications due to controllable air-gap field. Nonetheless, the torque density and efficiency of WFSMs may be reduced because of the employment of FECs [CHU14a]. Consequently, hybrid excited (HE) PM machines are proposed to inherit the synergies of high torque density and high efficiency from PM machines as well as excellent flux-controllability from WFSMs [AMA11] [HEN94] [ZHA12] [AFI15].

There are a variety of HEPM machine topologies due to flexible combination of two excitation sources, i.e., PMs and FEC excitations. The HE concept is firstly applied to the conventional rotor-PM machines, in which both PMs and field coils are in rotor side [FOD07]. Consequently, the slip rings and brushes are required to conduct the field winding current, which reduces the reliability of the system. In order to realize brushless operation, the HEPM machines with PMs in rotor side while field coils in stator side are proposed. In [TAP03] and [BAR15], the air-gap field is controlled by a toroidal DC field winding located in the center of

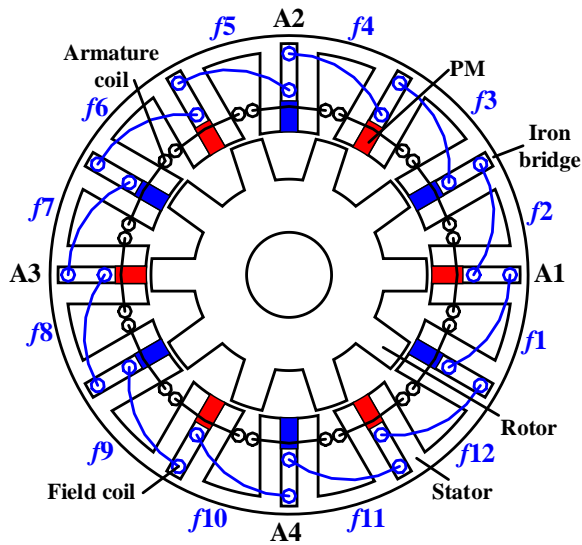
stator yoke. The DC field winding is arranged at the axial extremity of stator in [AMA09] to achieve brushless operation. Nevertheless, all these machines feature three-dimensional (3-D) flux path, which leads to complicated structures, significant flux-leakage, and hence reduced torque density.

In recent years, a multitude of investigations have been carried out on stator excitation HEPM machines, in which the PMs and field coils are both allocated in stator side [CHE11a]. Consequently, the sliding contacts are eliminated and the brushless operation is achieved. Furthermore, stator-excited HEPM machines also benefit from simple rotor structure and easy thermal management. HE switched-flux PM (HESFPM) machines are attracting increasing research interest due to high torque density, sinusoidal back-EMF, and hence low torque ripple. The first HESFPM machine is proposed in [AKE01], in which half of the PMs are simply replaced by FECs. In [HOA07], an extra iron ring is attached to a conventional SFPM machine to accommodate the FECs, which reduces the slot area for both armature windings and PMs. Moreover, a HESFPM machine is proposed in [HUA09] based on the conventional SFPM machine, in which the PM height is reduced to arrange the FECs in the saved space. Furthermore, the HESFPM machine equipped with an iron bridge is introduced in [OWE10] to enhance the flux-controllability. A comprehensive review of hybrid excited machines is provided in [ZHU19a]. DC winding induced voltage in HE machines can lead to DC winding current ripple and hence fluctuating field excitation. In addition, DC winding induced voltage may challenge the DC power source and increase the difficulty of machine control, especially at high speed. The DC winding induced voltage in a WFSM is studied in [WU19] and [WU20]. However, the analysis and reduction of DC winding induced voltage pulsation in HE machines have not been reported in literature. The open-circuit DC winding induced voltage is previously analyzed and suppressed in [SUN19a]. As an extension to [SUN19a], this chapter aims to analyze and minimize the on-load DC winding induced voltage, i.e., both open-circuit and on-load conditions are considered. Moreover, a prototype machine is manufactured and tested to verify the FEA predicted results.

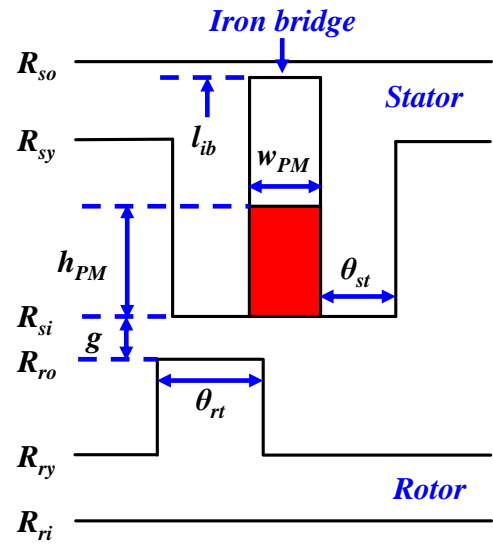
On-load DC winding induced voltage in the HESFPM machine consists of two parts, which are the open-circuit induced voltage and the armature current induced voltage, respectively. In this chapter, the DC winding induced voltage under both open-circuit and on-load conditions are comparatively illustrated and analyzed. This chapter is organized as follows. In section 3.2, a 12-stator-slot and 10-rotor-pole HESFPM machine is illustrated. In section 3.3, the phenomenon and mechanism of the DC winding induced voltage under both open-circuit and on-load conditions are presented and explained, respectively. In section 3.4, rotor step skewing and unequal rotor teeth are comparatively investigated by the FEA method to minimize the on-load DC winding induced voltage. In section 3.5, a prototype machine is manufactured and tested to validate the FEA analysis, followed by conclusions in section 3.6.

3.2 Machine Topology

A 12-stator-slot and 10-rotor-pole HESFPM machine shown in Fig. 3.1(a) [OWE10] is employed to investigate the DC winding induced voltage in the following sections. The HESFPM machine consists of a 12-slot-stator, three-phase non-overlapping concentrated AC armature windings, non-overlapping concentrated DC field excitation winding, 12 pieces circumferentially magnetized PM and a salient 10-pole-rotor. In addition, the iron flux bridge adjacent to the DC field winding slots is utilized as well to enhance the flux-controllability. The HESFPM machine is globally optimized by the genetic algorithm under zero d -axis armature current control due to negligible reluctance torque. The global optimization is carried out for the maximum average on-load electromagnetic torque under the constrains of 20W armature winding copper loss, $5A/mm^2$ DC winding slot current density and 0.5 slot packing factors for the armature winding and DC field winding slots. Key geometric parameters of the optimized machine are listed in Table 3.1, which can be referred to Fig. 3.1(b). It should be mentioned that the geometric parameters from l_a to R_{ri} are fixed while the rest are globally optimized parameters.



(a) Cross section



(b) Linear illustration

Fig. 3.1. Topology of the 12-slot/10-pole HESFPM machine [OWE10].

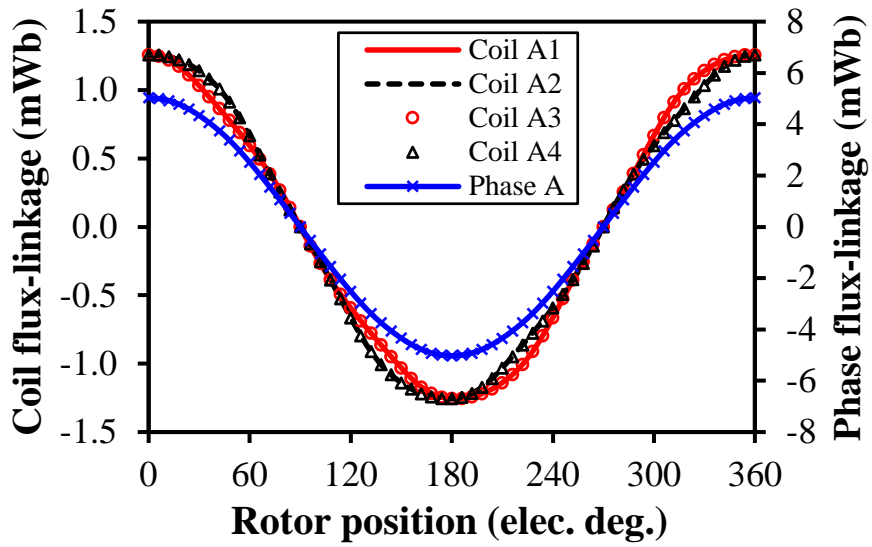
Table 3.1 Key Design Parameters of HESFPM Machine

Items	Value	Items	Value
Stator slot number, N_s	12	PM height, h_{PM}	5.6mm
Rotor pole number, N_r	10	Stator tooth arc, θ_{st}	8.5deg
Active axial length, l_a	25mm	Rotor outer radius, R_{ro}	28.5mm
Stator outer radius, R_{so}	45mm	Rotor yoke radius, R_{ry}	18mm
Iron bridge thickness, l_{ib}	0.5mm	Rotor outer pole arc, θ_{rt}	13.5deg
Air-gap length, g	0.5mm	Slot packing factor, k_{pf}	0.5
PM remanence, B_r	1.23T	Rated DC winding slot current density, J_{dc}	5A/mm ²
PM relative permeability, μ_{rpm}	1.10	Number of turns per DC coil, N_{dc}	90
Rotor inner radius, R_{ri}	10.4mm	Rated DC winding current, I_{dc}	0.41A
Stator yoke radius, R_{sy}	42.5mm	Rated armature winding copper loss, P_{cua}	20W
Stator inner radius, R_{si}	29mm	Number of turns per AC coil, N_{ac}	18
PM thickness, w_{PM}	3mm	Rated armature winding phase RMS current, I_{ac_rms}	12.15A

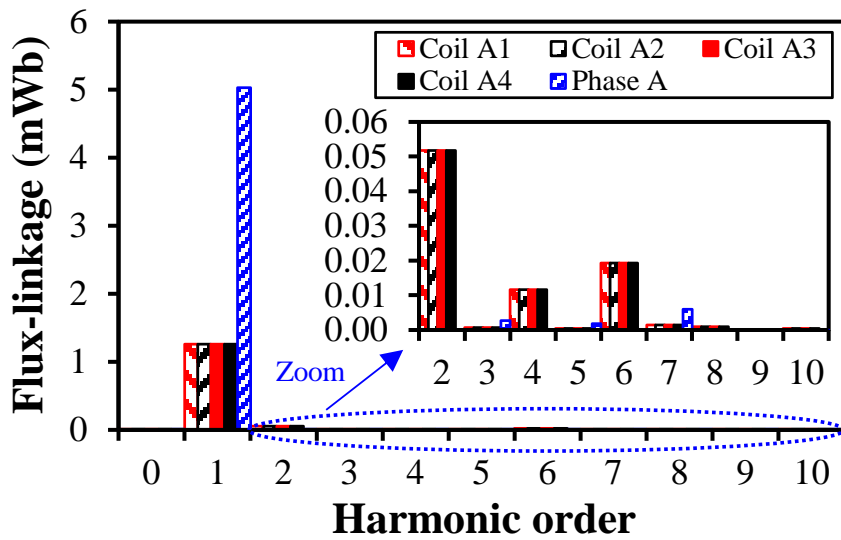
3.3 DC Winding Induced Voltage

3.3.1 Phenomenon

As shown in Fig. 3.1, the HESFPM machine employs salient-pole stator and rotor, i.e., doubly salient structure. When the rotor rotates, the open-circuit armature coil and winding flux-linkages are variable, and therefore voltage is induced in each phase of armature windings, i.e., phase back-EMF, as shown in Figs. 3.2 and 3.3, respectively. When the armature windings are injected with three-phase sinusoidal currents, i.e., BLAC drive, the electromagnetic torque will be produced. Therefore, it can be perceived that the doubly salient structure is essential for the operation of the HESFPM machine. Nevertheless, the doubly salient structure inevitably leads to some parasitic effects. Due to the doubly salient structure and flux modulation effect [WU15], the HESFPM machine has abundant air-gap field harmonics, as shown in Fig. 3.4. Therefore, the open-circuit flux-linkages and induced voltages suffer from a lot of harmonics as shown in Figs. 3.2(b) and 3.3(b), which result in higher torque ripple.

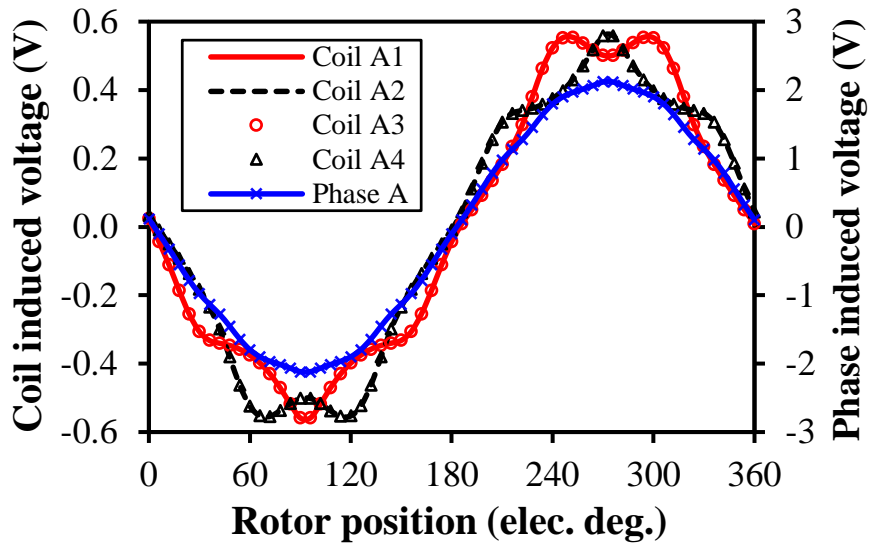


(a) Waveforms

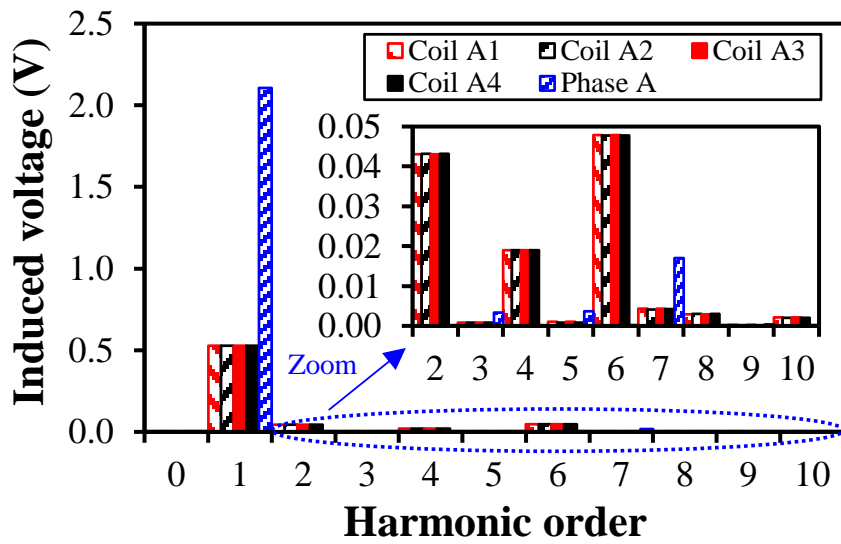


(b) Spectra

Fig. 3.2. Open-circuit phase A armature coil and winding flux-linkages of the 12-slot/10-pole HESFPM machine (with PMs and rated I_{dc}).

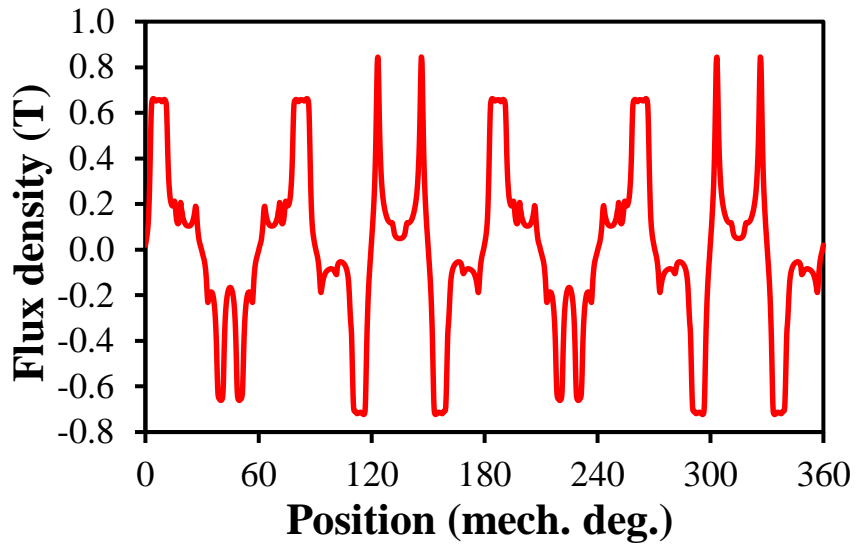


(a) Waveforms

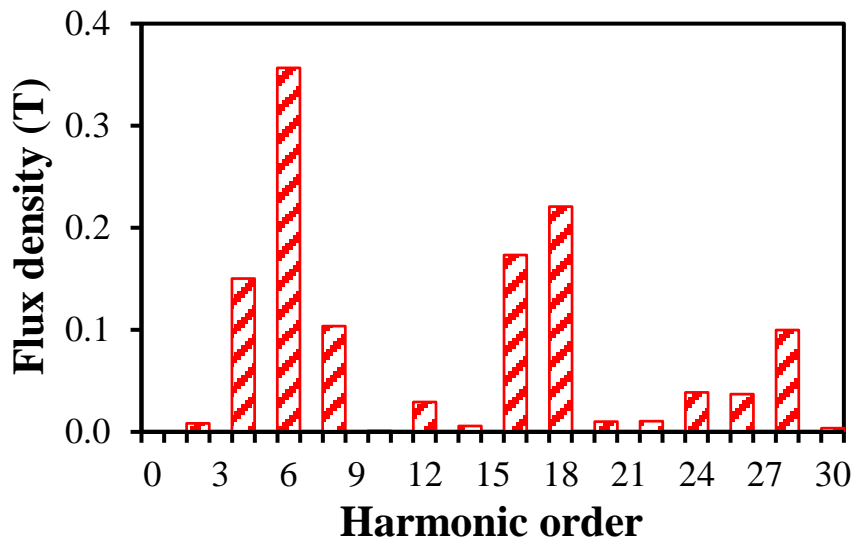


(b) Spectra

Fig. 3.3. Open-circuit phase A armature coil and winding induced voltages of the 12-slot/10-pole HESFPM machine at 400r/min (with PMs and rated I_{dc}).



(a) Waveform



(b) Spectrum

Fig. 3.4. Open-circuit radial air-gap flux density of the 12-slot/10-pole HESFPM machine (with PMs and rated I_{dc}).

As shown in Fig. 3.5, a pulsating voltage is induced in the DC winding under both open-circuit and on-load conditions when the rotor rotates at 400rpm. The peak-to-peak values of the DC winding induced voltages (E_{PP}) are 0.33V and 0.51V under open-circuit (E_{PP_OC}) and on-load (E_{PP_OL}) conditions, respectively. To indicate the effect of the DC winding induced voltage, induced voltage ratio (IVR) is defined in (3.1) as the ratio of E_{PP} to the DC winding resistance voltage drop (V_{RF}). Consequently, the DC winding IVRs are 7.32% and 11.13% for the open-circuit and on-load operations, respectively. A high IVR reveals that the DC winding induced voltage has a higher influence on machine performances. On the contrary, a low IVR indicates that the influence of the induced voltage is lower.

In HESFPM machines, constant DC winding current is desirable as the salient pole rotor rotates, especially when the closed-loop DC winding current control is implemented. The DC winding flux-linkage in HE machines is generally considered as constant if the DC winding current is constant. As a consequence, there will be no induced voltage pulsation in the DC winding according to Faraday's law shown in (3.2). However, as shown in Fig. 3.6, the DC winding flux-linkages are not constant under both open-circuit and on-load conditions and suffer from many harmonics, i.e., 6th, 12th, 18th, etc. Consequently, voltages will be induced in DC winding due to the variation of the DC winding flux-linkages.

$$\text{IVR} = \frac{E_{PP}}{V_{RF}} \times 100\% \quad (3.1)$$

$$E_f = \frac{d(\psi_f)}{d(t)} = \frac{d(\psi_f)}{d(\theta_e)} \times \frac{d(\theta_e)}{d(t)} = p\Omega_m \times \frac{d(\psi_f)}{d(\theta_e)} \quad (3.2)$$

where E_f is the DC winding induced voltage. ψ_f is the DC winding flux-linkage. θ_e is the rotor electric position. p is the rotor pole-pair number. Ω_m is the rotor mechanical speed.

In equation (3.1), E_{PP} can be further expressed as

$$E_{PP} = E_1 \times N_{dc} \quad (3.3)$$

where E_1 is the peak-to-peak DC winding induced voltage for one turn. N_{dc} is the number of turns for each DC coil.

If the end-winding length of the DC winding is not considered, V_{RF} in equation (3.1) can be expressed as

$$V_{RF} = R_{dc} \times I_{dc} = \frac{2N_s \rho_{cu} l_a N_{dc}^2}{S_b k_{pf}} \times I_{dc} \quad (3.4)$$

where R_{dc} is the DC winding resistance. I_{dc} is the DC winding current. N_s is the stator slot number. ρ_{cu} is the electrical resistivity of copper. l_a is the machine active axial length. S_b is the DC winding slot area for coil side. k_{pf} is the slot packing factor.

In equation (3.4), I_{dc} can be further expressed as

$$I_{dc} = \frac{S_b k_{pf} J_{dc}}{N_{dc}} \quad (3.5)$$

where J_{dc} is the DC winding slot current density.

Therefore, V_{RF} can be rewritten as

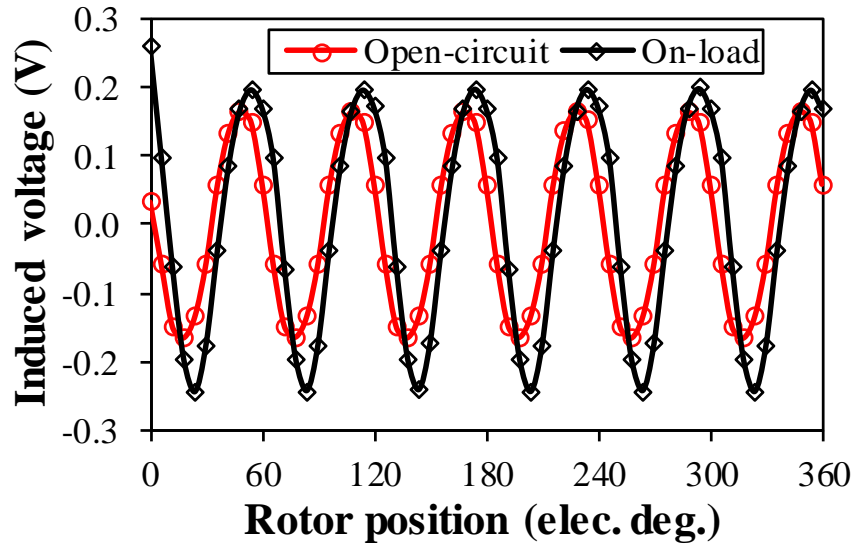
$$V_{RF} = 2N_s \rho_{cu} l_a N_{dc} J_{dc} \quad (3.6)$$

IVR in equation (3.1) can then be simplified as

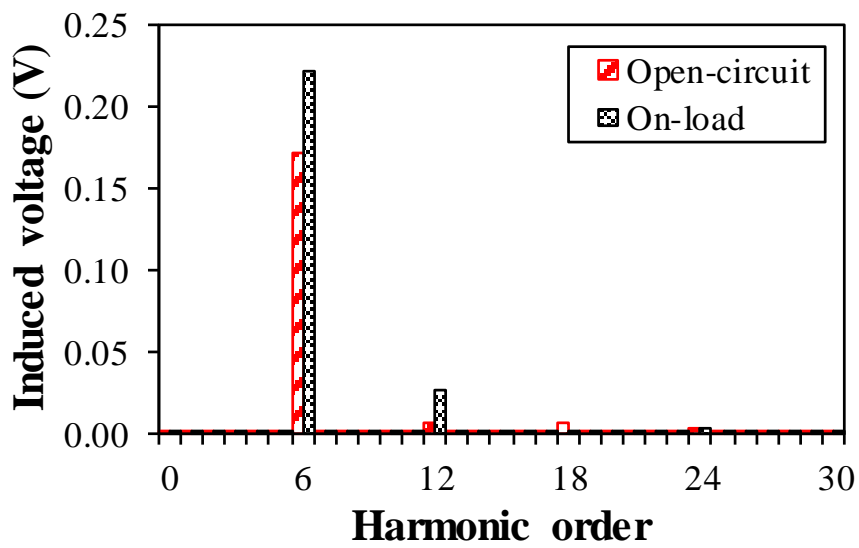
$$\text{IVR} = \frac{E_{PP}}{V_{RF}} = \frac{E_1}{2N_s \rho_{cu} l_a J_{dc}} \quad (3.7)$$

Based on (3.7), it can be found that IVR cannot be reduced with fixed J_{dc} , i.e., fixed MMF of DC winding. Although E_{PP} can be reduced by reducing the number of turns of DC winding, IVR is independent of N_{dc} with fixed DC winding MMF. It reveals that the influence of the DC winding induced voltage cannot be mitigated by just reducing the DC winding number of turns.

Therefore, it is important to study the production mechanism of the induced voltage and apply appropriate methods to suppress it.

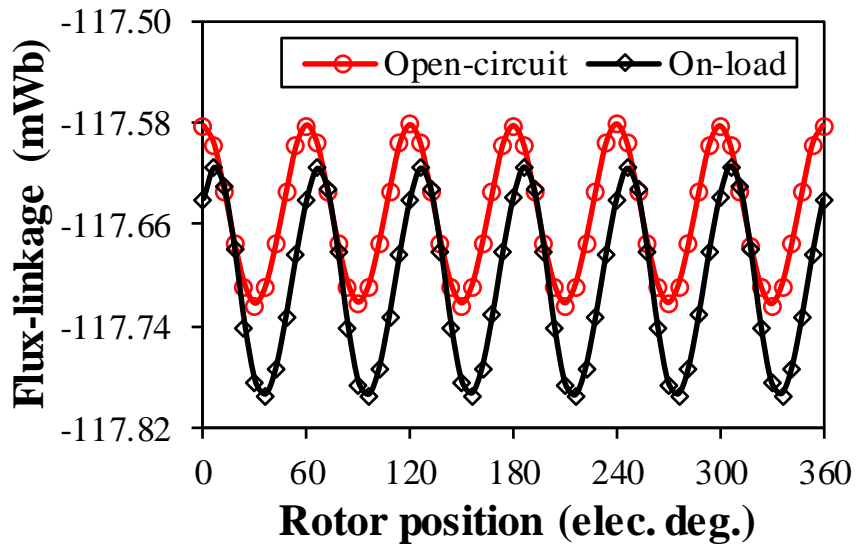


(a) Waveforms

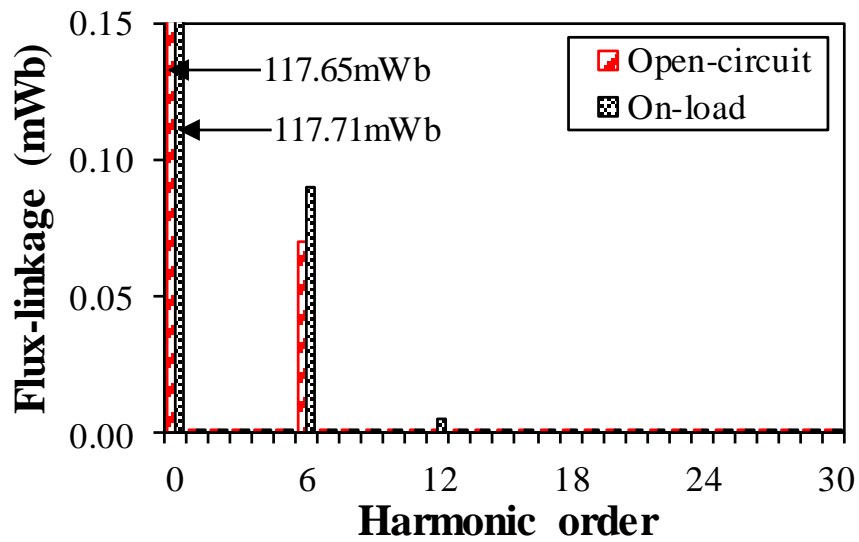


(b) Spectra

Fig. 3.5. DC winding induced voltages of the 12-slot/10-pole HESFPM machine at 400r/min with non-linear core material.



(a) Waveforms



(b) Spectra

Fig. 3.6. DC winding flux-linkages of the 12-slot/10-pole HESFPM machine with non-linear core material.

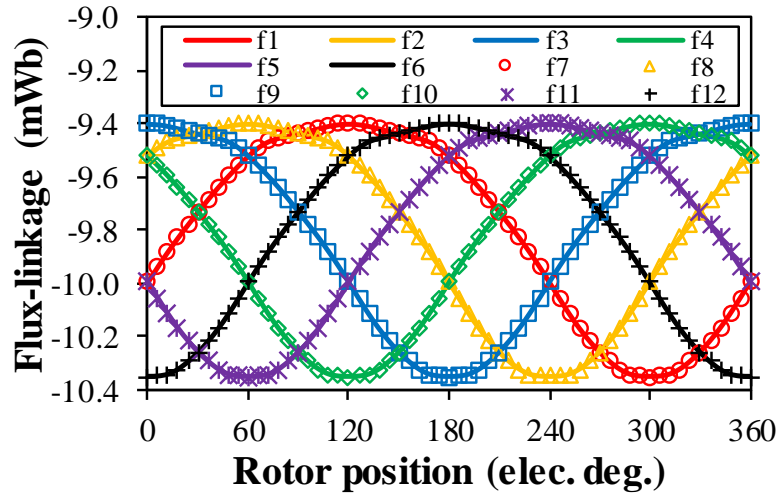
3.3.2 Open-Circuit Induced DC Winding Voltage

When the machine operates under open-circuit condition, i.e., with PMs and field coils excitations, the DC coil flux-linkages vary with the rotor position as shown in Fig. 3.7(a). It is found that the open-circuit DC coil flux-linkage waveforms for different DC coils are the same and the only difference is the 60 electric degrees phase shift between any two adjacent DC coils. Consequently, they share the same harmonic spectrum as shown in Fig. 3.7(b). Similarly, the open-circuit DC coil induced voltages inherently share the same waveforms and spectra except for the phase angle as shown in Fig. 3.8(a) and Fig. 3.8(b), respectively. The open-circuit DC winding flux-linkage is the summation of the open-circuit DC coil flux-linkages due to series connection between different DC coils. The 6th harmonic and its multiples ($6k$, $k=1, 2, 3, \dots$) may exist in the open-circuit DC winding flux-linkage and hence the induced voltage as shown in Figs. 3.5(b) and 3.6(b), since the harmonics of $6k$ cannot be cancelled due to the initial phase angle shown in Figs. 3.7(c) and 3.8(c). Other harmonics are cancelled out due to the 60 electric degrees phase angle (θ_L) between any two adjacent DC coils, which can be expressed by (3.8) for other slot and pole number combinations of the HESFPM machine in Fig. 3.1.

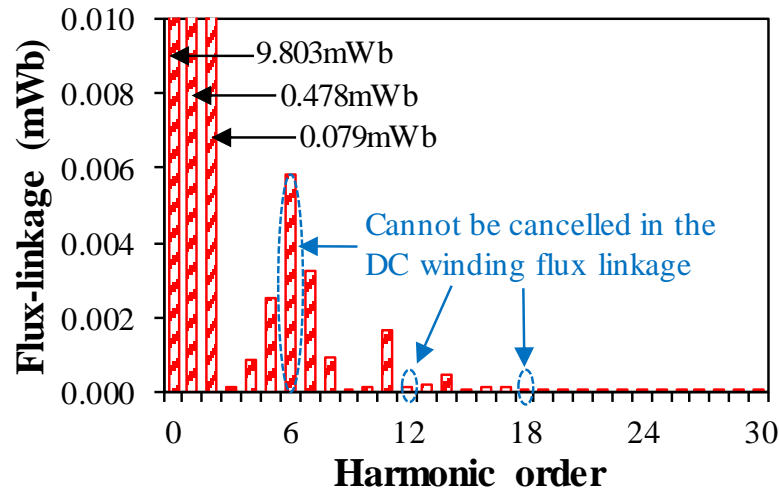
$$\theta_L = 2\pi - \left(\frac{2\pi}{N_s} \times N_r\right) \quad (3.8)$$

where N_s is the stator slot number. N_r is the rotor pole number.

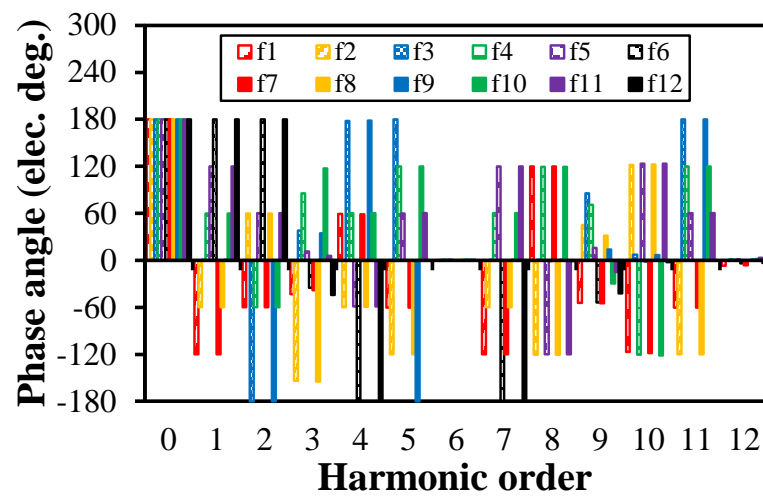
The open-circuit DC coil flux-linkage variation is caused by the variation of the equivalent air-gap magnetic reluctance when the rotor rotates. Taking the DC coil f_l as an example, the open-circuit DC coil f_l flux-linkage ψ_{f_l} varies with the rotor electric position (θ_e) as shown in Fig. 3.7(a). When $\theta_e=120^\circ$, ψ_{f_l} reaches its minimum value 9.39mWb while ψ_{f_l} reaches its maximum value 10.35mWb at $\theta_e=300^\circ$. Consequently, the magnetic reluctance of the DC coil's (f_l) magnetic circuit is maximum at $\theta_e=120^\circ$ and minimum at $\theta_e=300^\circ$ due to the variation of the equivalent air-gap reluctance as the rotor rotates, as shown in Fig. 3.9. Fig. 3.10 shows the open-circuit flux density distributions at those two rotor positions. In fact, the variation of the air-gap reluctance is due to the doubly salient structure of the HESFPM machine.



(a) Waveforms

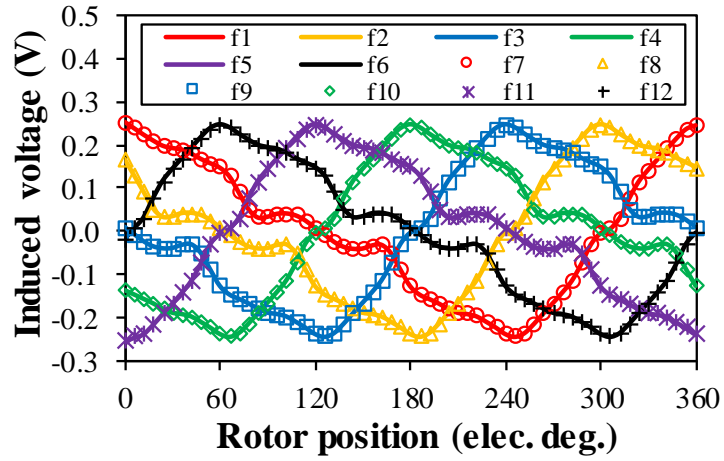


(b) Spectra for all DC coils

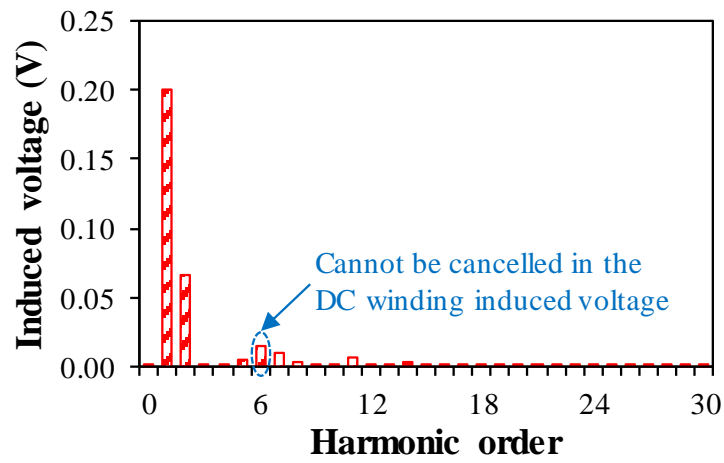


(c) Initial phase

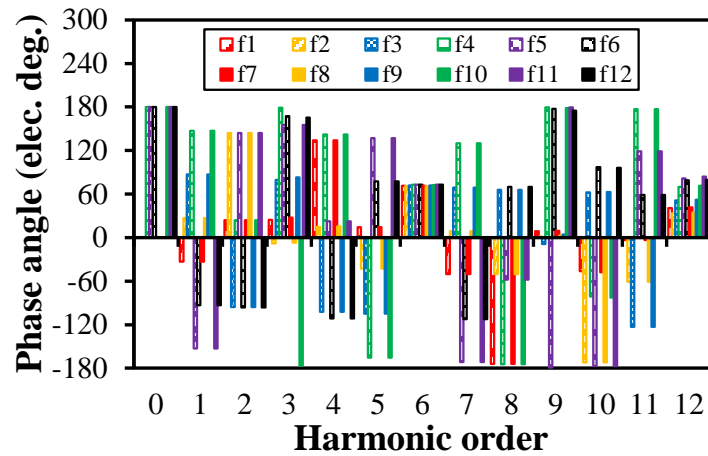
Fig. 3.7. Open-circuit DC coil flux-linkages of the 12-slot/10-pole HESFPM machine.



(a) Waveforms

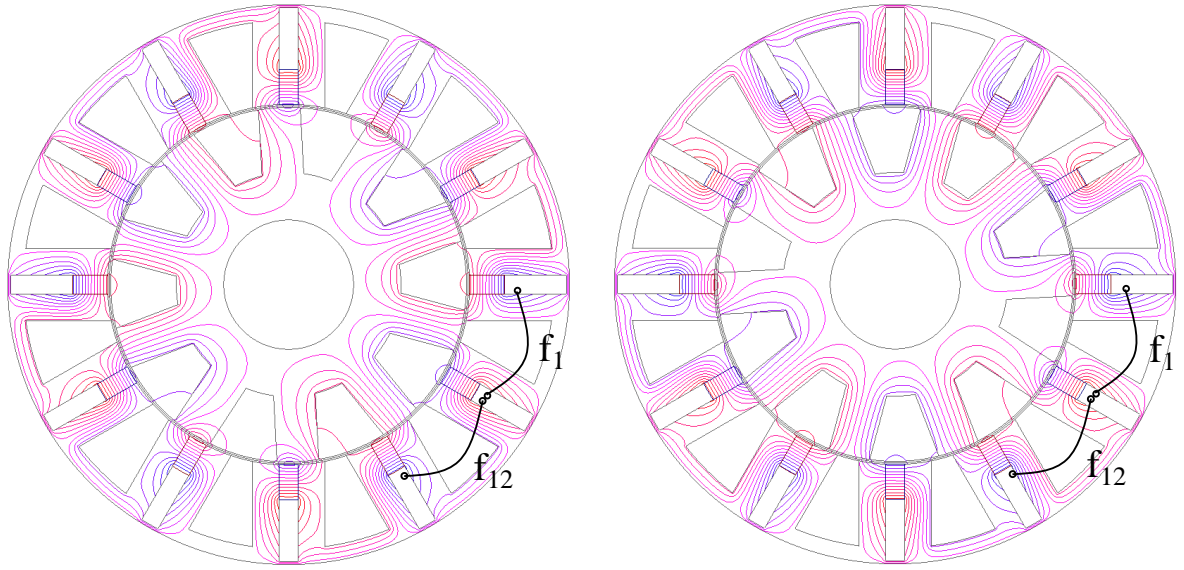


(b) Spectra for all DC coils



(c) Initial phase

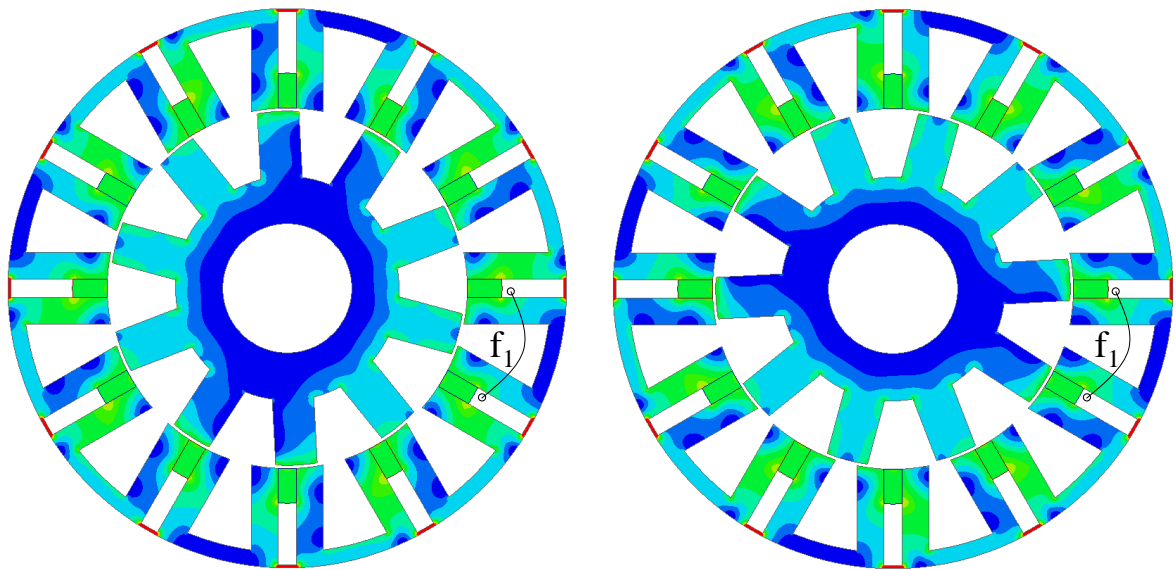
Fig. 3.8. Open-circuit DC coil induced voltages of the 12-slot/10-pole HESFPM machine at 400r/min.



(a) Minimum ($\theta_e=120^\circ$)

(b) Maximum ($\theta_e=300^\circ$)

Fig. 3.9. Open-circuit flux distributions of the 12-slot/10-pole HESFPM machine when ψ_{f1} is minimum and maximum.

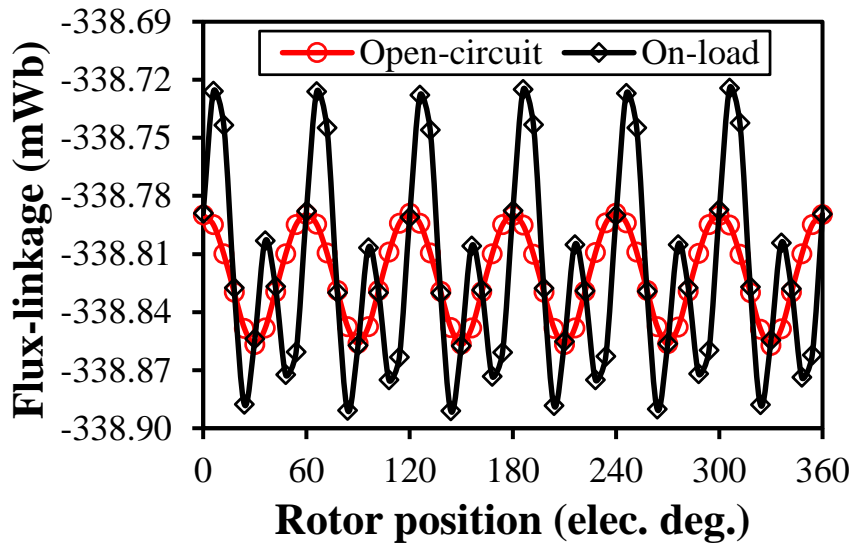


(a) Minimum ($\theta_e=120^\circ$)

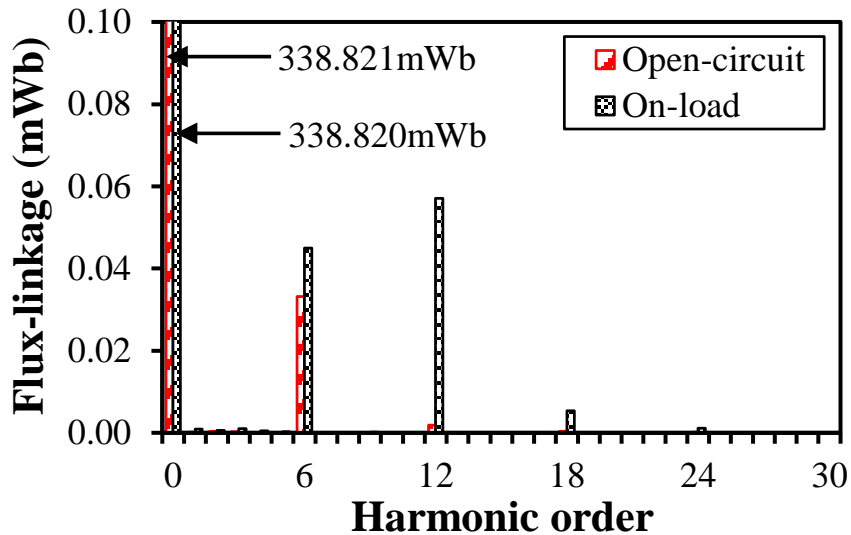
(b) Maximum ($\theta_e=300^\circ$)

Fig. 3.10. Open-circuit flux density distributions of the 12-slot/10-pole HESFPM machine when ψ_{f1} is minimum and maximum.

Figs. 3.11 and 3.12 show the DC winding flux-linkages and induced voltages with linear core material. For the linear core material, the relative permeability μ_r has been assumed a constant, i.e., 10000. It can be found that there are still pulsating flux-linkages and induced voltages in DC winding under both open-circuit and on-load conditions. It reveals that the DC winding induced voltage is not caused by the magnetic saturation but the variation of the air-gap permeance.

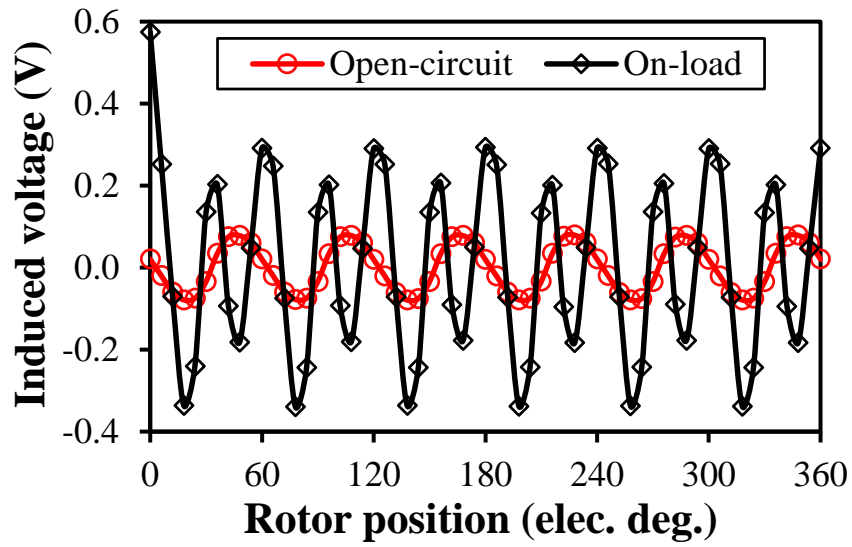


(a) Waveforms

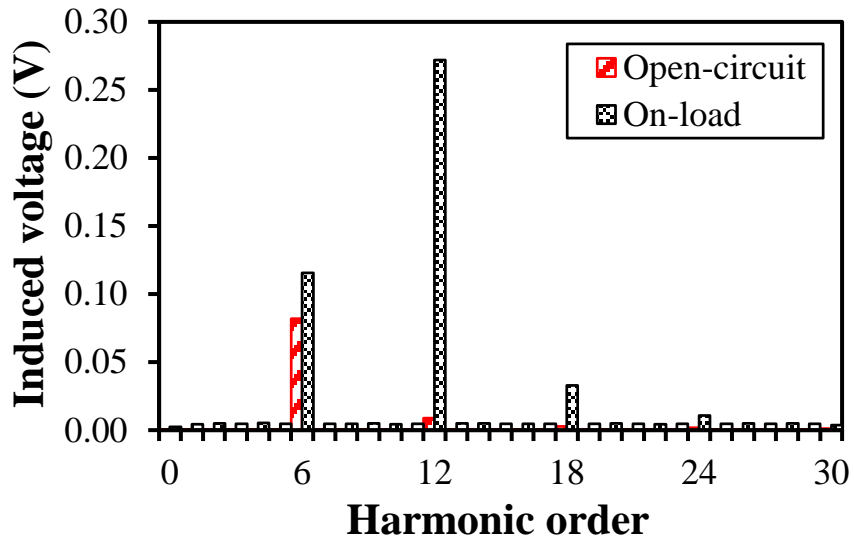


(b) Spectra

Fig. 3.11. DC winding induced voltages of the 12-slot/10-pole HESFPM machine at 400r/min with linear core material ($\mu_r=10000$).



(a) Waveforms

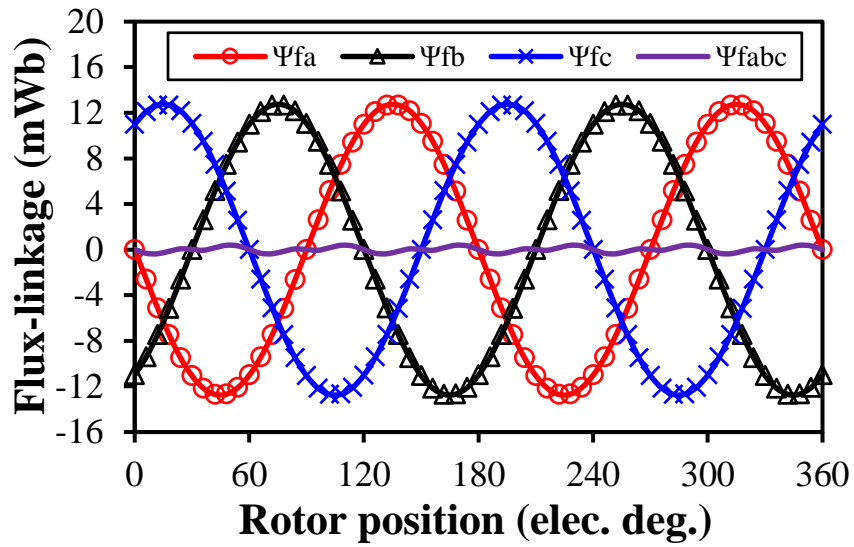


(b) Spectra

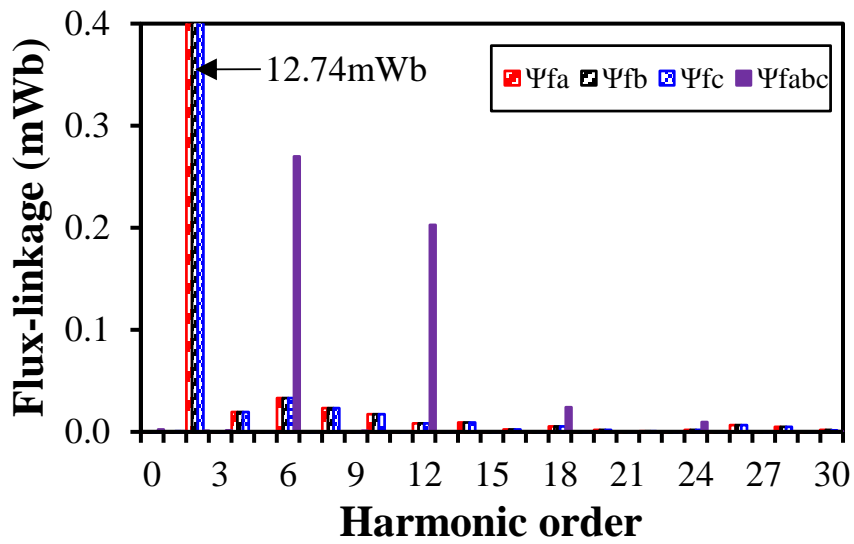
Fig. 3.12. DC winding induced voltages of the 12-slot/10-pole HESFPM machine at 400r/min with linear core material ($\mu_r=10000$).

3.3.3 Armature Current Induced DC Winding Voltage

Fig. 3.13 shows the DC winding flux-linkages due to the sole excitation of the phase A-, B-, and C-currents, i.e., Ψ_{fa} , Ψ_{fb} , and Ψ_{fc} , respectively, in which the PMs and DC excitations are removed. It shows that these waveforms share the same spectra and suffer from a lot of harmonics. In fact, these flux-linkage harmonics are mainly caused by the mutual inductance harmonics between AC and DC windings since the armature currents are pure sinusoidal currents and free from harmonics. When the machine is supplied by three-phase armature currents simultaneously, i.e., Ψ_{fabc} , other flux-linkage harmonics are cancelled out but with the harmonics of $6k$ left in the DC winding. Therefore, a voltage pulsation exists in the DC winding as the rotor rotates as shown in Fig. 3.14(a). As shown in Fig. 3.14(b), the harmonic orders of the induced voltage are $6k$, in which k is a positive integer. This part is the armature current induced DC winding voltage, which is due to the interaction between the armature currents and the mutual inductances between AC and DC windings. When the machine operates under on-load condition as shown in Fig. 3.5(a), the induced voltage is the on-load DC winding induced voltage, which consists of the open-circuit induced voltage and the armature current induced voltage, respectively. Consequently, the on-load DC winding induced voltage harmonic orders are $6k$ as well ($k=1, 2, 3, \dots$) as shown in Fig. 3.5(b) due to the effect of the open-circuit and armature current induced voltages.

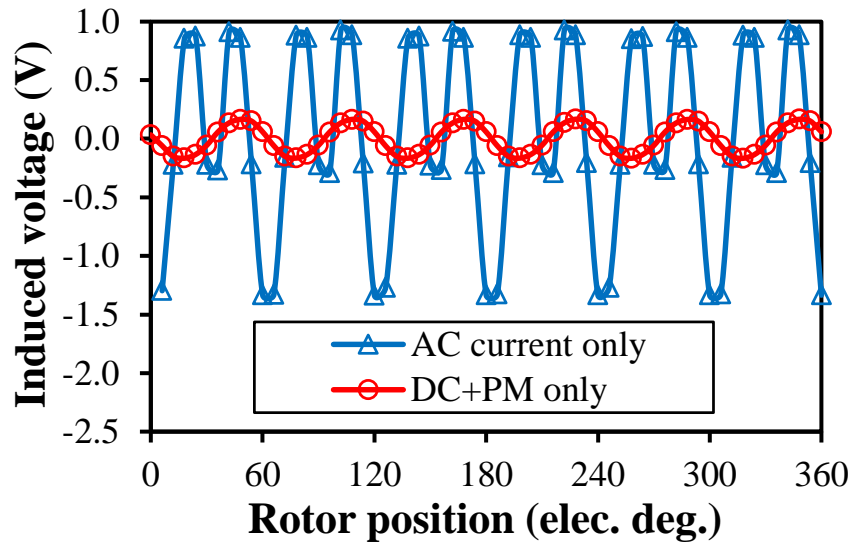


(a) Waveforms

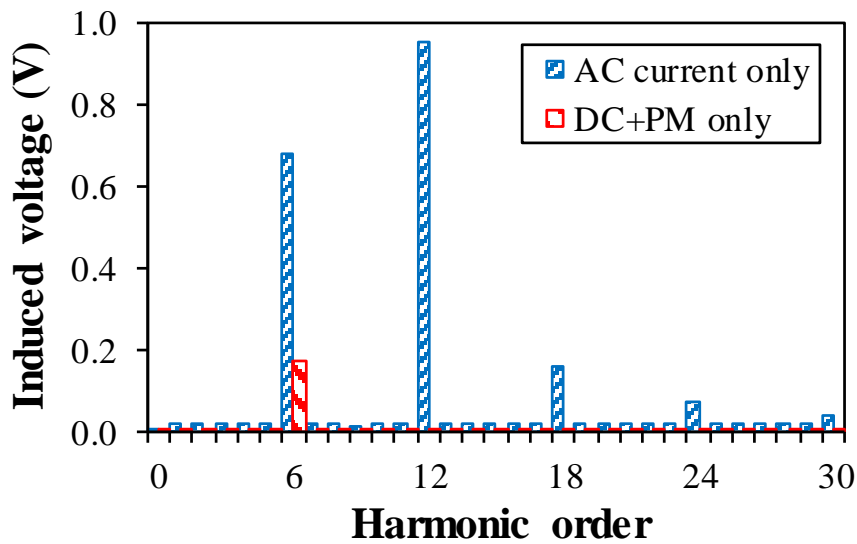


(b) Spectra

Fig. 3.13. DC winding flux-linkages of the 12-slot/10-pole HESFPM machine due to the sole excitation of the phase A-, B-, and C-currents, respectively.



(a) Waveforms



(b) Spectra

Fig. 3.14. Armature current induced DC winding voltages of the 12-slot/10-pole HESFPM machine at 400r/min.

As shown in Fig. 3.15, the peak-to-peak values of the on-load DC winding induced voltages vary against the current advance angle and hence the varied induced voltage ratio. It should be emphasized that the DC winding resistive voltage drop is constant as the current advance angle varies. Consequently, the waveforms of the induced voltage and the induced voltage ratio are the same. When the current angle changes, the permeability of the lamination

steel varies as well. Consequently, both the open-circuit and armature current induced voltages are affected by the current angle and hence the on-load induced voltage. As shown in Fig. 3.16, the maximum torque of the machine occurs at around 0° current angle, which indicates negligible reluctance torque for the machine topology.

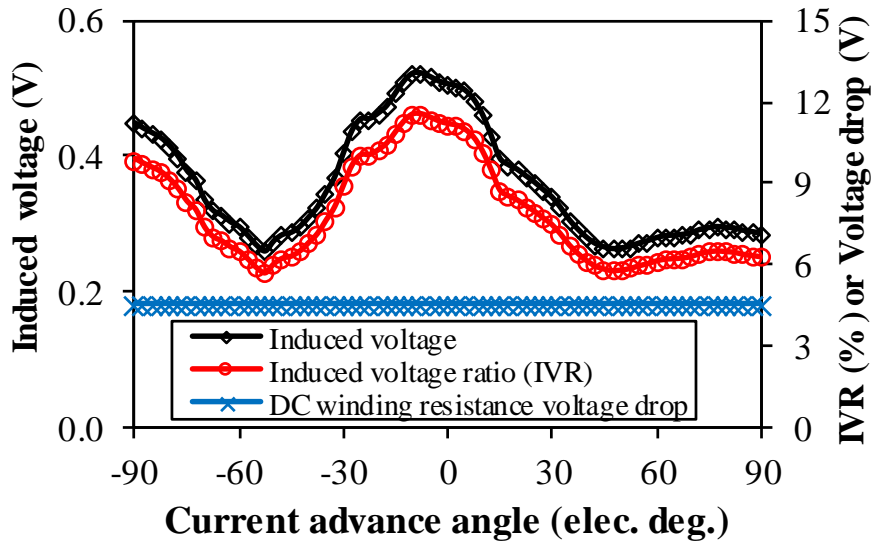


Fig. 3.15. Influence of current advance angle on on-load DC winding induced voltage of the 12-slot/10-pole HESFPM machine at 400r/min.

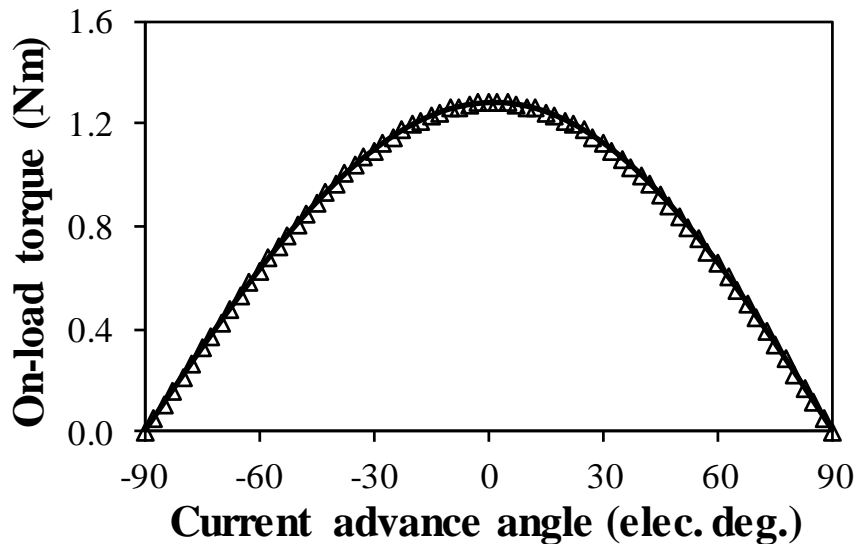


Fig. 3.16. Influence of current advance angle on average torque of the 12-slot/10-pole HESFPM machine.

3.4 Reduction of On-Load DC Winding Induced Voltage

3.4.1 Rotor Step Skewing

Skewing is widely used in electrical machines for cogging torque, back-EMF harmonics and hence torque ripple reductions. Continuous skewing is not preferred in practice due to high manufacturing difficulty, although it has favorable performance. Step skewing is an alternative method to reduce the manufacturing difficulty while maintaining comparable performance compared with continuous skewing. In this section, rotor step skewing illustrated in Fig. 3.17 is firstly employed to reduce the on-load DC winding induced voltage.

As aforementioned, the 6th harmonic and its multiples may exist in the on-load DC winding flux-linkage and hence the induced voltage. As shown in Fig. 5(b), the 6th and 12th harmonics are the dominant on-load DC winding induced voltage harmonics. The amplitudes of the 6th and 12th harmonics are both influenced by the skewing angle (θ_{sk}) as shown in Fig. 3.18. As a consequence, the on-load DC winding induced voltage may be suppressed by the reduction of the 6th and 12th harmonics.

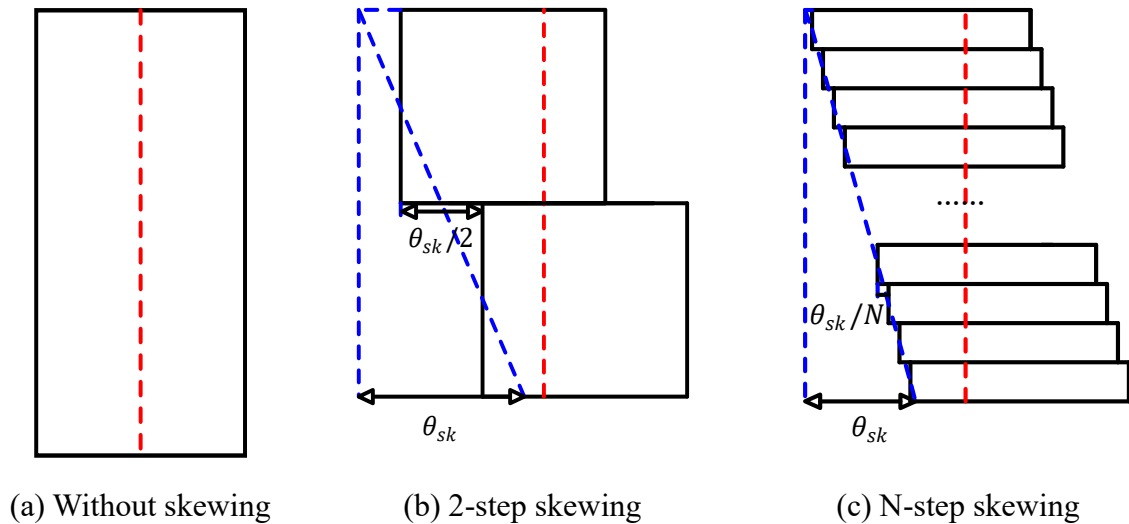


Fig. 3.17. Illustration of rotor step skewing with skewing angle θ_{sk} in electric degree.

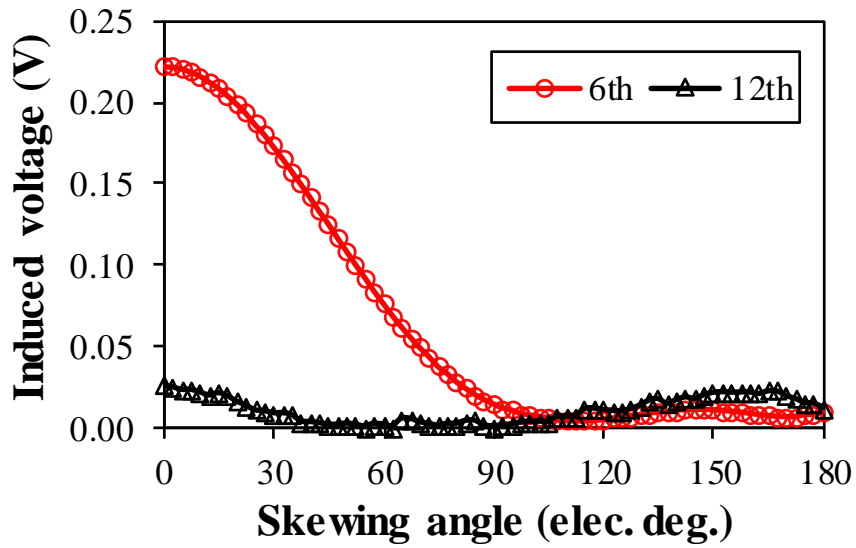


Fig. 3.18. Influence of skewing angle on on-load DC winding induced voltage harmonics ($N=5$).

In order to minimize the on-load DC winding induced voltage, different skewing angles are calculated by the FEA method under 5-step skewing ($N=5$) as shown in Fig. 3.19. It is shown that the on-load DC winding induced voltage is minimized with $\theta_{sk}=110^\circ$ and hence $\theta_{sk}=110^\circ$ is used for rotor step skewing in the following analysis. However, the average on-load torques are slightly reduced by rotor step skewing under different skewing angles as shown in Fig. 3.20.

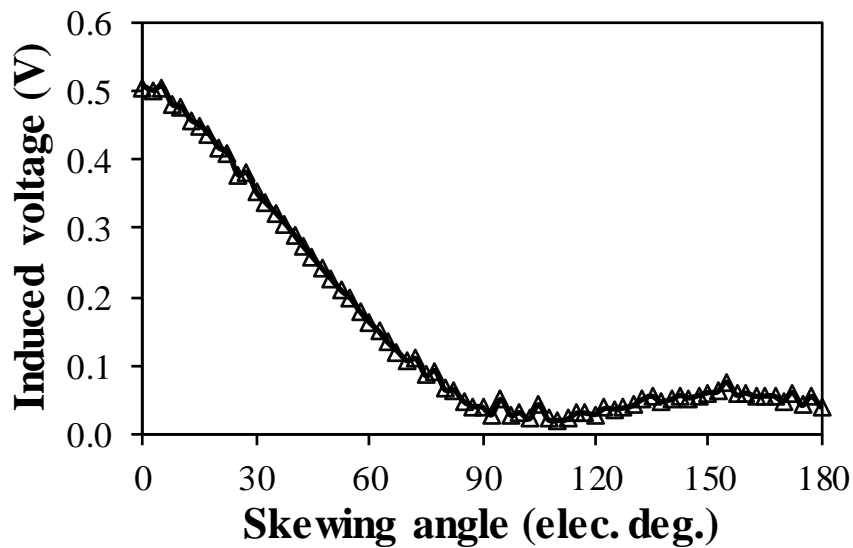


Fig. 3.19. Influence of skewing angle on peak to peak on-load DC winding induced voltage ($N=5$).

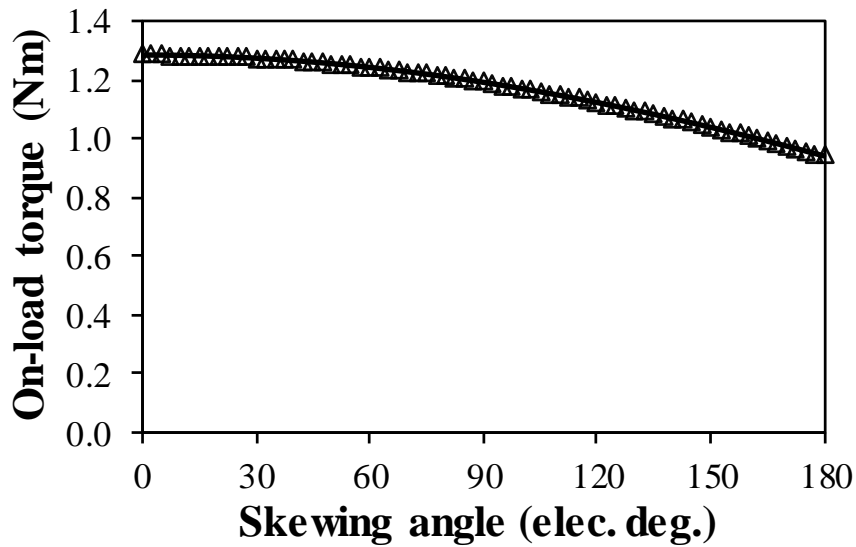


Fig. 3.20. Influence of skewing angle on average torque ($N=5$).

As shown in Figs. 3.21 and 3.22, the on-load DC winding induced voltage has been effectively reduced by rotor step skewing. The peak-to-peak values of the on-load DC winding induced voltages (E_{PP_OL}) are 0.51V, 0.28V, 0.14V, 0.05V, and 0.02V for the skewing step numbers from 1 to 5, respectively. It should be emphasized that the rotor is non-skewed when $N=1$. Consequently, E_{PP_OL} reduction ratios are 44.01%, 71.63%, 89.28%, and 96.15% for the machine with 2-step, 3-step, 4-step, and 5-step skewing, respectively. E_{PP_OL} reduction ratio is maximum when 5-step skewing is employed, i.e., 96.15%, due to the suppression of the 6th and 12th voltage harmonics as shown in Fig. 3.23.

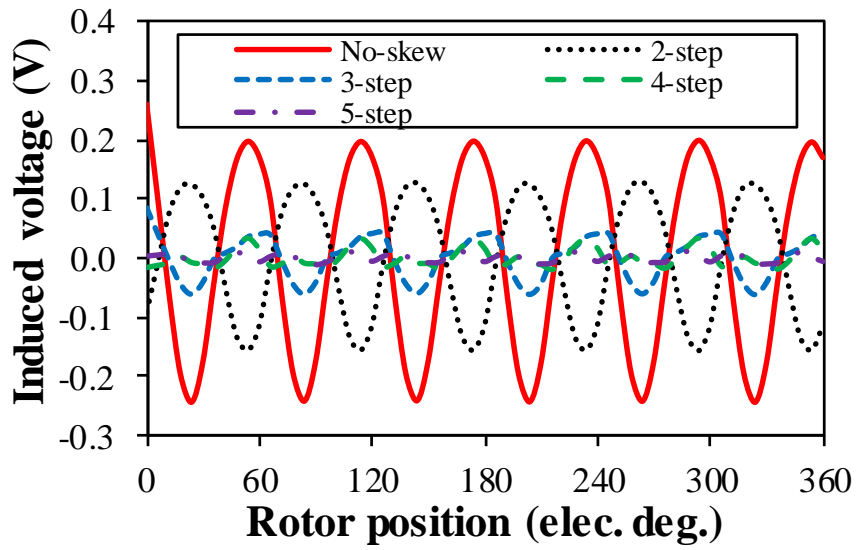


Fig. 3.21. On-load DC winding induced voltage against rotor step-skewing number ($\theta_{sk}=110^\circ$).

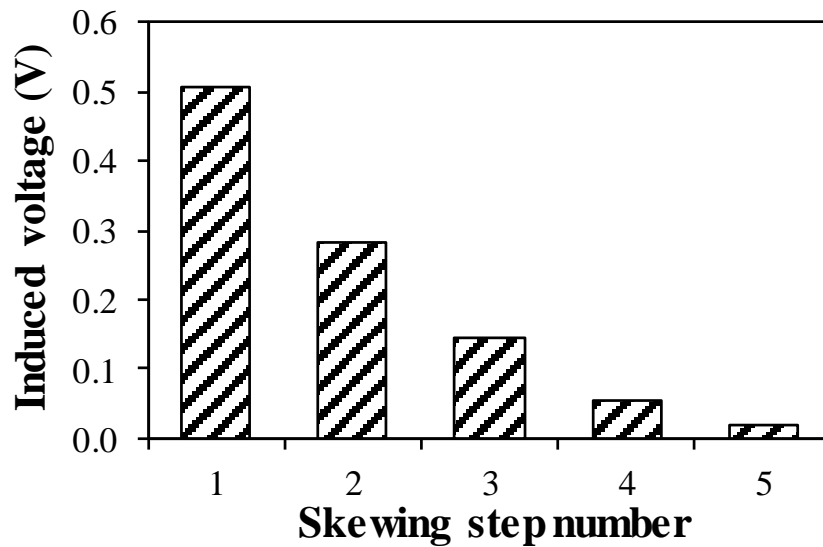
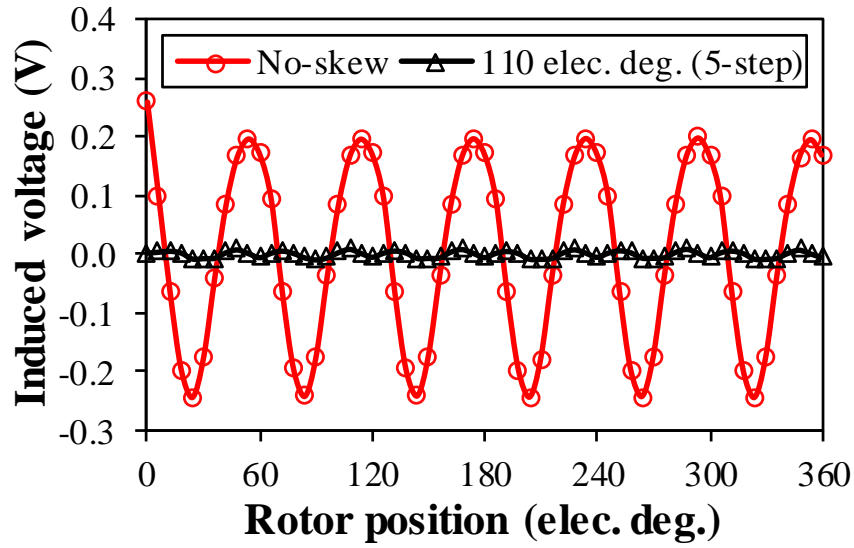
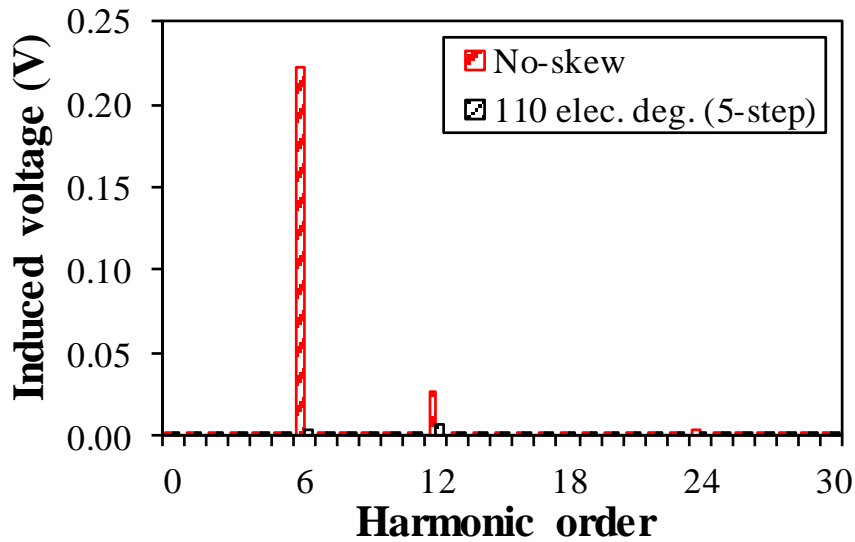


Fig. 3.22. Peak to peak value of on-load DC winding induced voltage against rotor step-skewing number ($\theta_{sk}=110^\circ$).



(a) Waveforms



(b) Spectra

Fig. 3.23. On-load DC winding induced voltage with 5-step rotor skewing ($\theta_{sk}=110^\circ$).

As shown in Figs. 3.24 and 3.25, the average on-load electromagnetic torques (T_{ave}) are slightly reduced by rotor step skewing, i.e., 1.29Nm, 1.14Nm, 1.16Nm, 1.16Nm, and 1.15Nm for the skewing numbers from 1 to 5, respectively. As a consequence, T_{ave} reduction ratios are 11.3%, 9.9%, 10.2%, and 10.6%, respectively. Likewise, the torque ripples (T_{rip}) shown in equation (3.9) are suppressed as well by rotor step skewing, i.e., 12.27%, 10.51%, 3.07%, 1.49%, and 1.25% for the machine with 2-step, 3-step, 4-step, and 5-step skewing, respectively.

Consequently, T_{rip} reduction ratios are 14.3%, 75.0%, 87.8%, and 89.8%, respectively. As shown in Fig. 3.26, it reveals that the armature winding phase fundamental back-EMF is slightly reduced while the 6th back-EMF harmonic is greatly reduced by 5-step rotor skewing ($\theta_{sk}=110^\circ$). Consequently, T_{rip} reduction ratio is much higher than that of T_{ave} . The characteristics of the HESFPM machine by rotor step skewing are listed in Table 3.2.

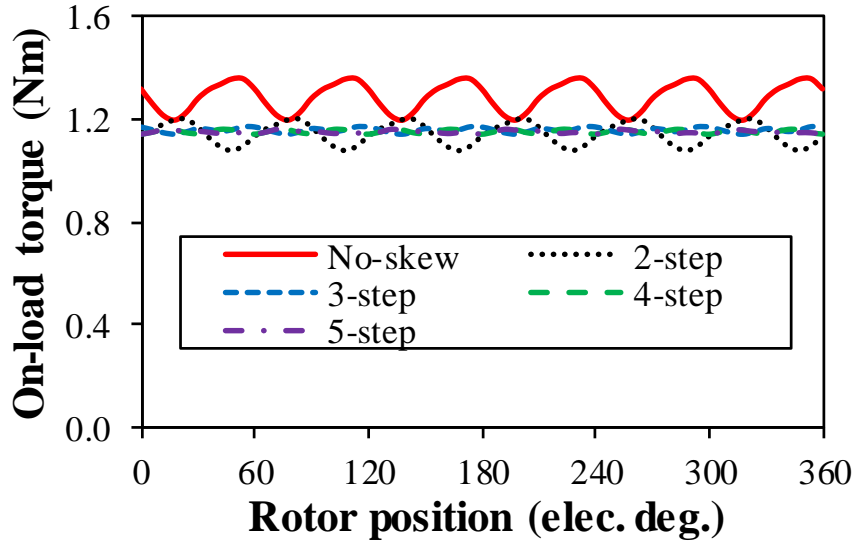


Fig. 3.24. On-load torque against rotor step-skewing number ($\theta_{sk}=110^\circ$).

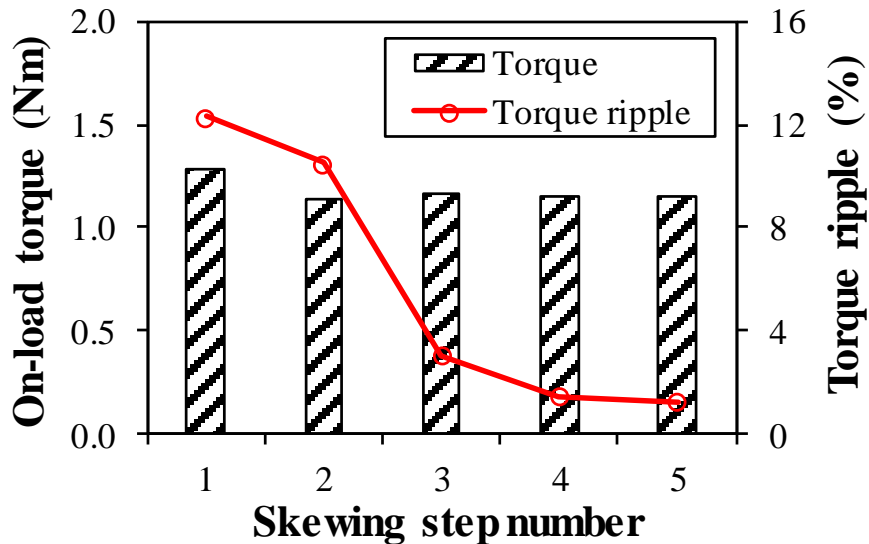
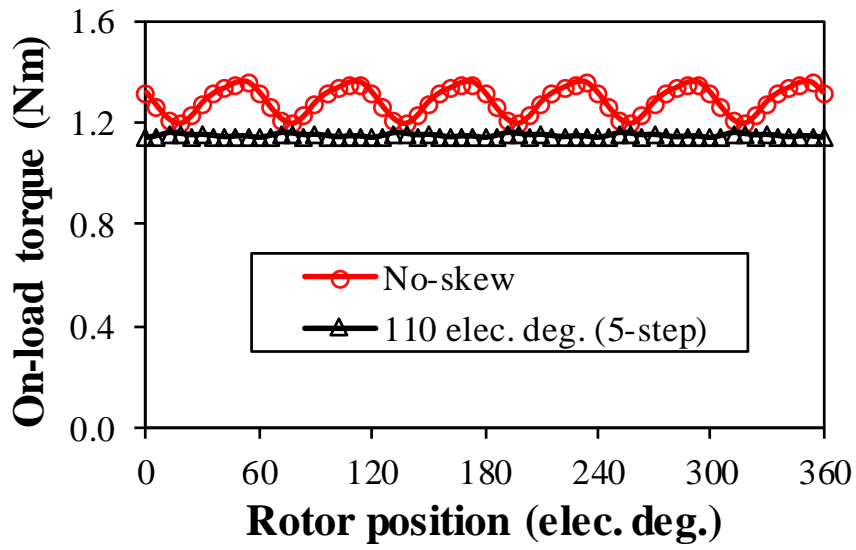
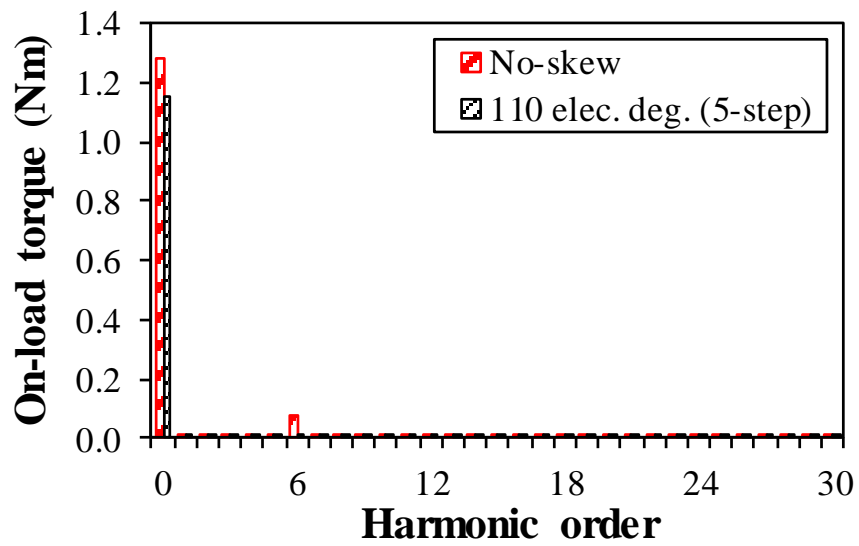


Fig. 3.25. Average on-load torque and torque ripple against rotor step-skewing number ($\theta_{sk}=110^\circ$).



(a) Waveforms



(b) Spectra

Fig. 3.26. On-load torque with 5-step rotor skewing ($\theta_{sk}=110^\circ$).

Table 3.2 Characteristics of HESFPM Machine by Rotor Step Skewing

Item	Unit	Value				
		1	2	3	4	5
N	-	1	2	3	4	5
E_{PP_OL}	V	0.51	0.28	0.14	0.05	0.02
E_{PP_OL} reduction ratio	%	-	44.01	71.63	89.28	96.15
T_{ave}	Nm	1.29	1.14	1.16	1.16	1.15
T_{ave} reduction ratio	%	-	11.3	9.9	10.2	10.6
T_{rip}	%	12.27	10.51	3.07	1.49	1.25
T_{rip} reduction ratio	%	-	14.3	75.0	87.8	89.8

3.4.2 Unequal Rotor Teeth

It is shown in Fig. 3.27 that the peak-to-peak value of the on-load DC winding induced voltage (E_{PP_OL}) varies with the rotor outer pole arc. As aforementioned, the 6th harmonic and its multiples may exist in the on-load DC winding induced voltage, in which the 6th and 12th are dominant harmonics as shown in Fig. 3.5(b). Both the amplitude and initial phase of the 6th and 12th harmonics are affected by the rotor outer pole arc as shown in Figs. 3.28 and 3.29. Consequently, it is expected that the on-load DC winding induced voltage may be suppressed by designing a rotor with unequal teeth. Consequently, unequal rotor teeth method illustrated in Fig. 3.30 is subsequently employed to reduce the on-load DC winding induced voltage. The mechanism behind this method is to cancel the corresponding on-load DC winding induced voltage harmonics by a pair of rotor outer pole arcs.

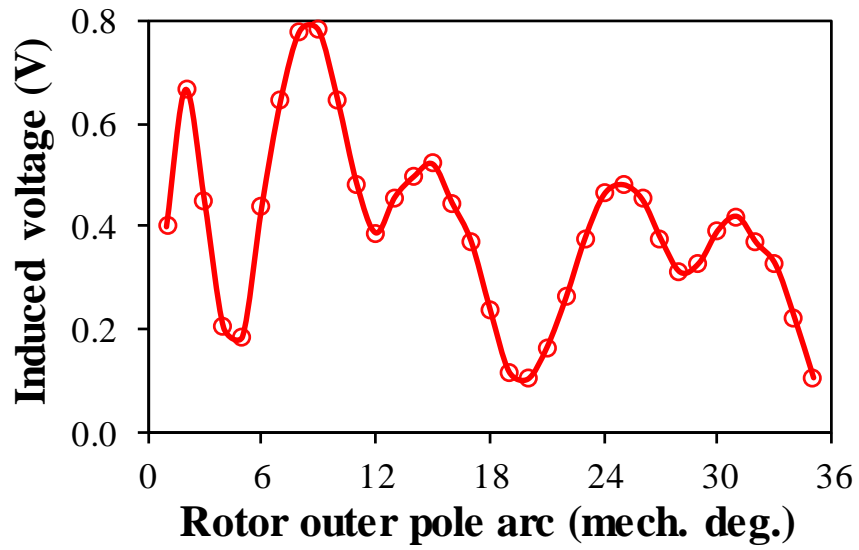


Fig. 3.27. Peak to peak value of on-load DC winding induced voltage against rotor outer pole arc.

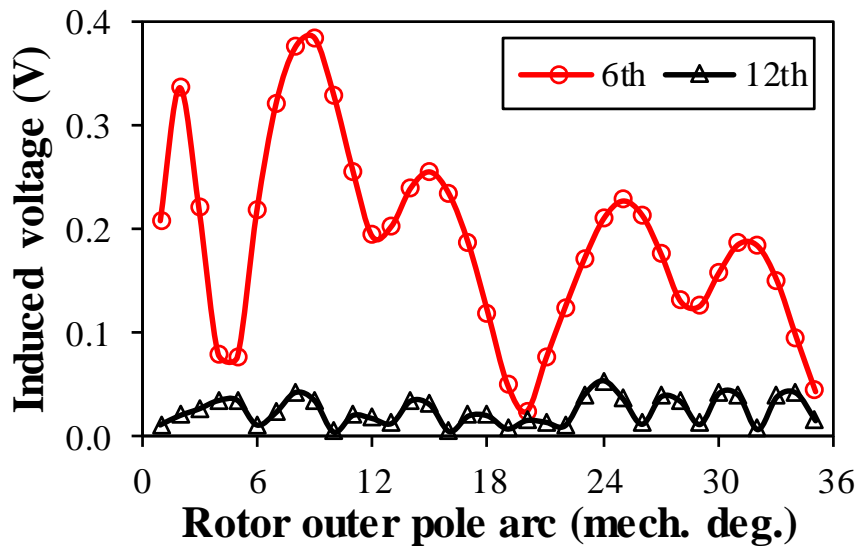


Fig. 3.28. Amplitude of on-load DC winding induced voltage harmonics against rotor outer pole arc.

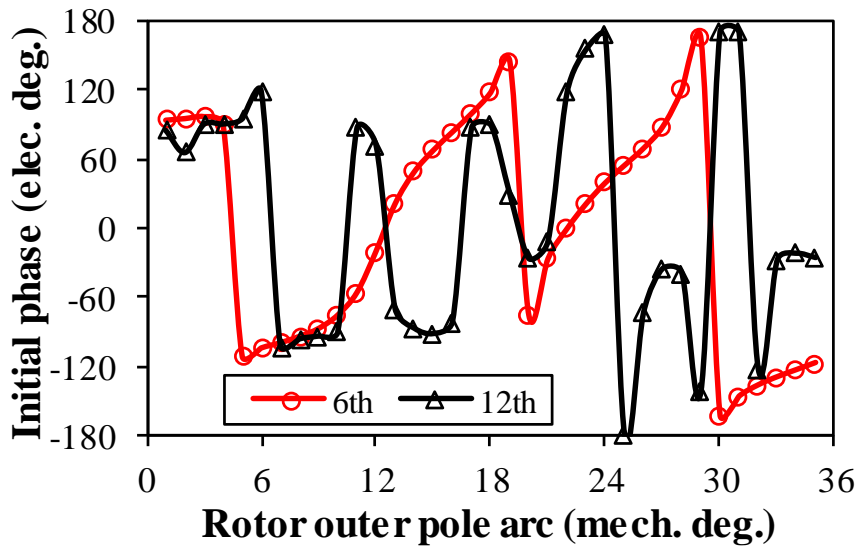


Fig. 3.29. Initial phase of on-load DC winding induced voltage harmonics against rotor outer pole arc.

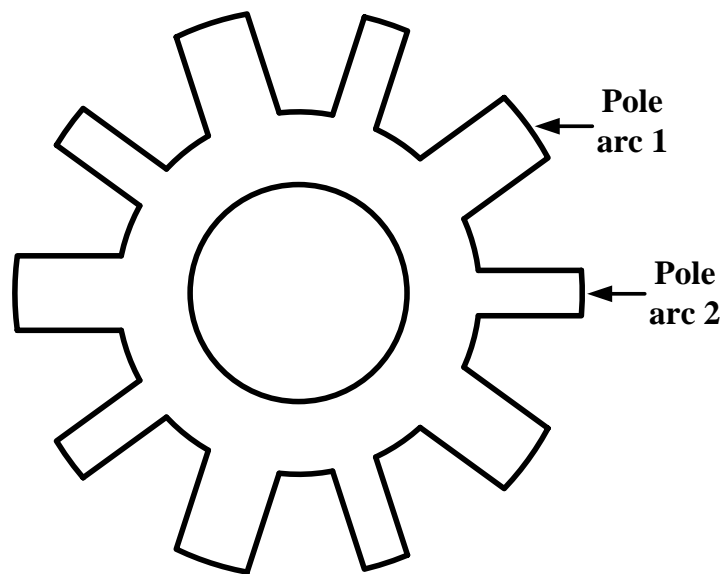


Fig. 3.30. Illustration of unequal rotor teeth.

In order to minimize E_{PP_OL} , all available combinations of rotor outer pole arcs 1 and 2 are calculated by the FEA method. E_{PP_OL} and T_{ave} are plotted against rotor outer pole arcs 1 and 2 as shown in Figs. 3.31 and 3.32. It is shown in Fig. 3.31 that a smaller E_{PP_OL} can be achieved by designing the rotor with unequal teeth. It is found that the combination of $\theta_{r1}=19^\circ$ and $\theta_{r2}=20^\circ$ shown in Fig. 3.33 has the highest E_{PP_OL} reduction, i.e., 0.51V and 0.06V for the HESFPM

machines without and with unequal rotor teeth, respectively, as shown in Fig. 3.34(a). Consequently, E_{PP_OL} reduction ratio is 89.05% by unequal rotor teeth, which is mainly due to the reduction of the 6th and 12th harmonics as shown in Fig. 3.34(b).

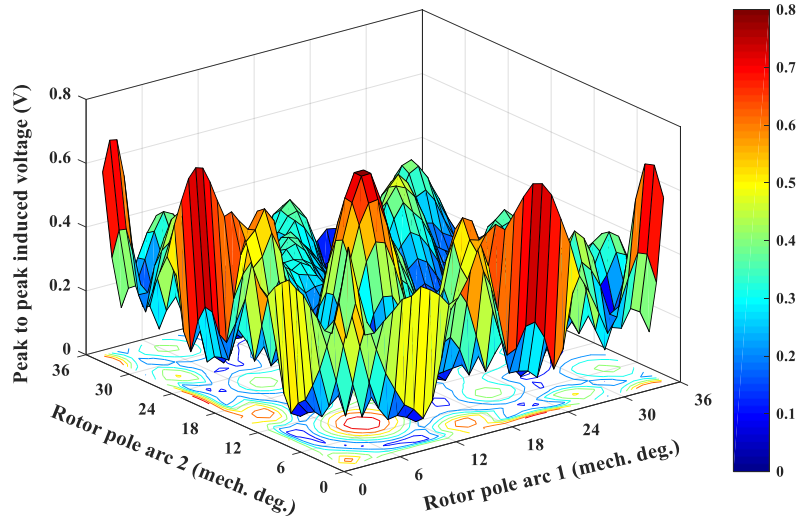


Fig. 3.31. Influence of unequal rotor pole arcs on peak-to-peak value of on-load DC winding induced voltage.

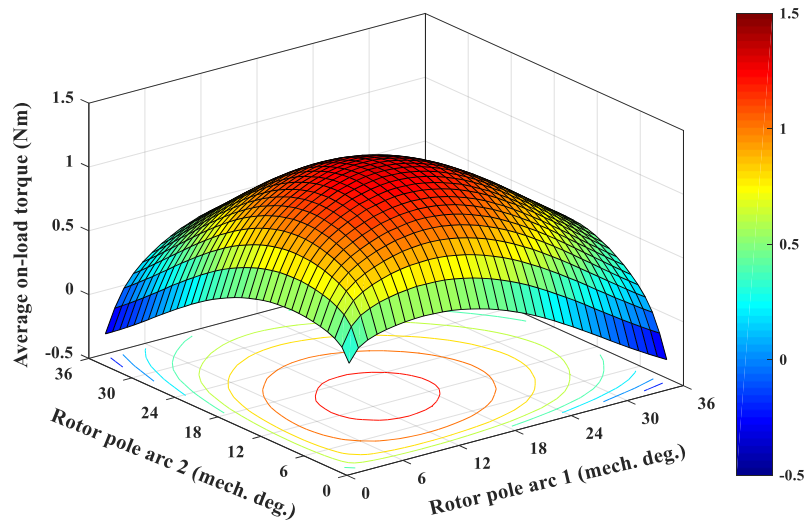
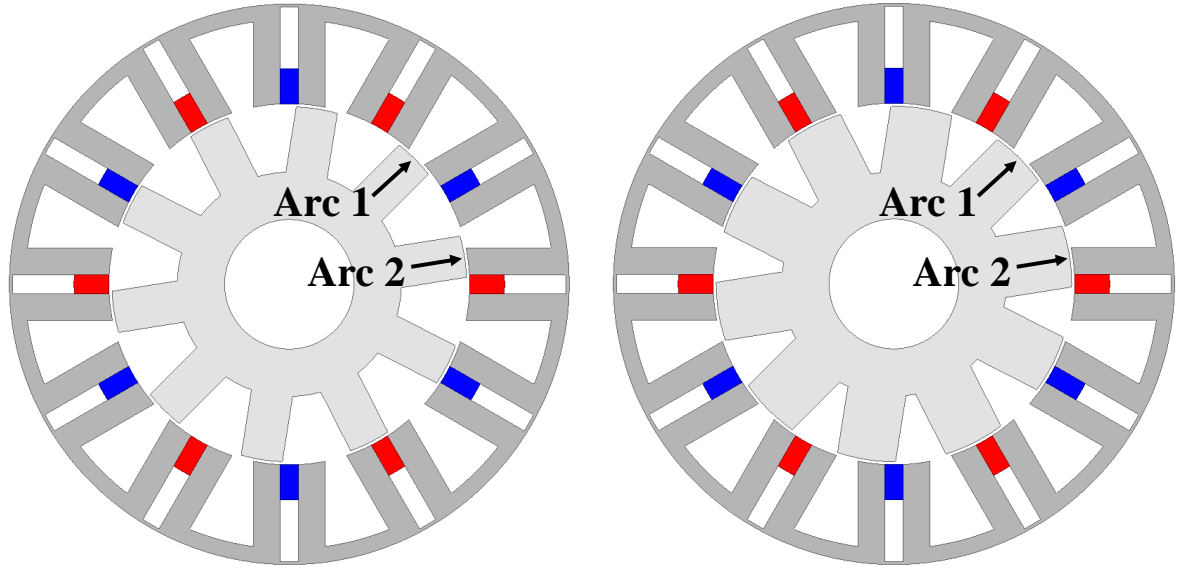


Fig. 3.32. Influence of unequal rotor pole arcs on average on-load electromagnetic torque.

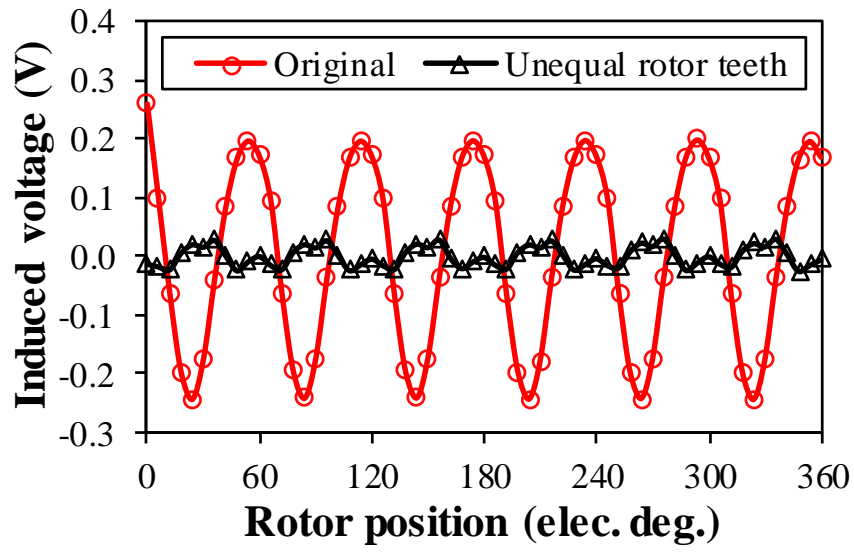


(a) Original ($\theta_{r1}=13.5^\circ$, $\theta_{r2}=13.5^\circ$)

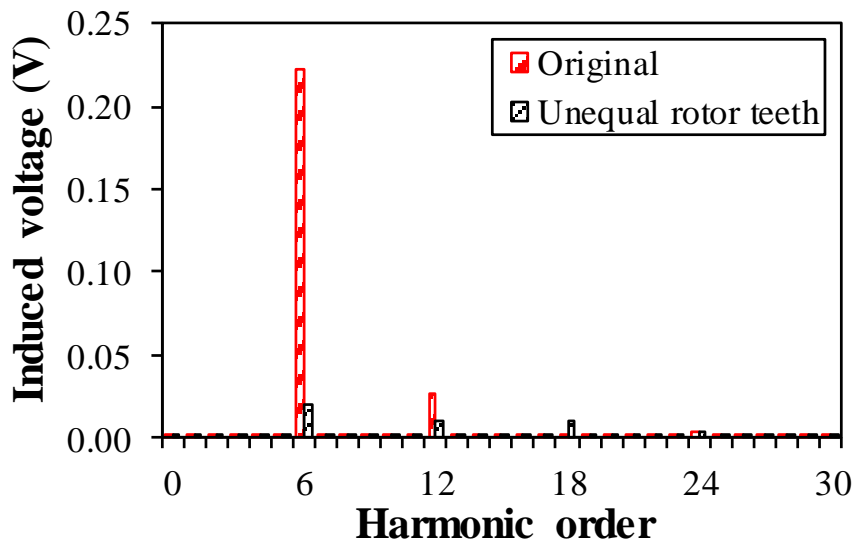
(b) Unequal rotor teeth ($\theta_{r1}=19^\circ$, $\theta_{r2}=20^\circ$)

Fig. 3.33. Optimal machine with unequal rotor teeth.

As shown in Fig. 3.35, T_{ave} of the optimal machine with unequal rotor teeth is slightly decreased, i.e., 1.13Nm due to a lower phase fundamental back-EMF compared with the original machine. Therefore, T_{ave} reduction ratio is 12.20% by unequal rotor teeth. However, T_{rip} is suppressed from 12.27% to 8.17% due to the reduction of the 6th armature winding phase back-EMF harmonic by unequal rotor teeth. Table 3.3 summarizes the characteristics of the HESFPM machine by unequal rotor teeth.

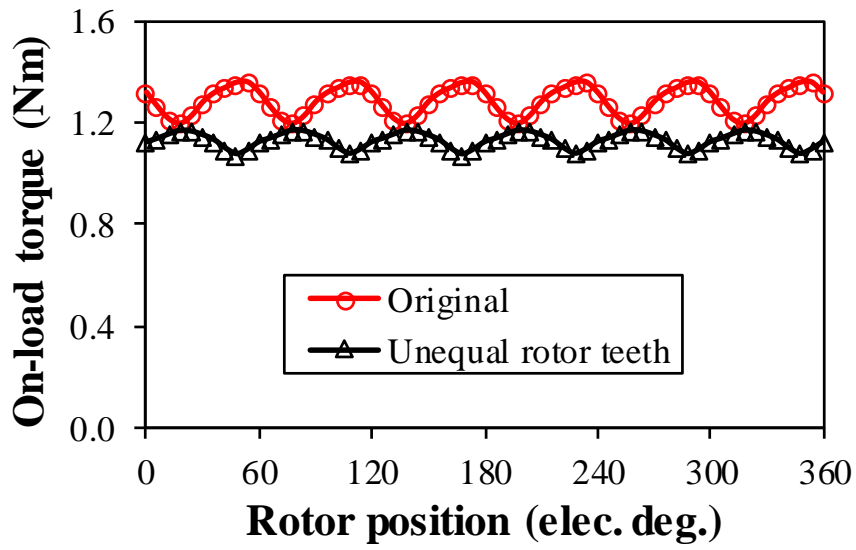


(a) Waveforms

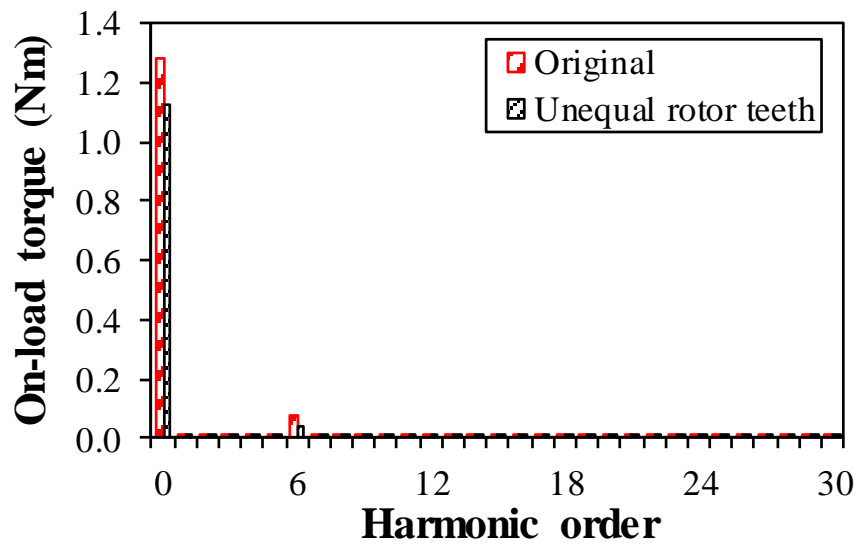


(b) Spectra

Fig. 3.34. On-load DC winding induced voltage with unequal rotor teeth.



(a) Waveforms



(b) Spectra

Fig. 3.35. On-load torque with unequal rotor teeth.

Table 3.3 Characteristics of HESFPM Machine by Unequal Rotor Teeth

Item	Unit	Value
Machine	-	Original Unequal rotor teeth
E_{PP_OL}	V	0.51 0.06
E_{PP_OL} reduction ratio	%	- 89.05
T_{ave}	Nm	1.29 1.13
T_{ave} reduction ratio	%	- 12.20
T_{rip}	%	12.27 8.17
T_{rip} reduction ratio	%	- 33.41

$$T_{rip} = \frac{T_{max} - T_{min}}{T_{ave}} \quad (3.9)$$

where T_{max} , T_{min} and T_{ave} are the maximum, minimum and average on-load electromagnetic torque, respectively.

3.5 Experimental Validation

3.5.1 Prototype and Test Rig

An existing 12-slot and 10-pole prototype machine from the previous research is employed and tested to verify the foregoing finite element analyses (FEA). Table 3.4 lists the specification of the prototype machine. Fig. 3.36 shows its stator and rotor. It should be emphasized that a 1mm thick iron flux bridge is employed adjacent to the DC field winding slots to facilitate the flux regulation. As illustrated in Fig. 3.1(a), the DC field excitation winding consists of 12 DC coils that are connected in series and they are marked as $f_1, f_2, f_3, \dots, f_{12}$, respectively. The prototype machine is tested on the test rig shown in Fig. 3.37. The three-phase armature winding back-EMFs due to PM excitation only are measured and compared with the FEA results at 400r/min as shown in Fig. 3.38. The measured three-phase back-EMFs are symmetrical and slightly lower than the FEA predicted results due to end-effect.

Table 3.4 Specification of the Prototype HESFM

Parameters	Value	Parameters	Value
Stator pole number, N_s	12	Rotor pole number, N_r	10
Outer stator radius, R_{so}	45mm	Stack length, l_s	25mm
Air-gap length, g	0.5mm	Iron bridge length, l_{ib}	1mm
Rotor shaft radius, R_{ri}	6mm	Stator yoke radius, R_{sy}	41.5mm
Stator inner radius, R_{si}	27mm	PM volume	7950mm ³
PM remanence	1.2T	PM relative permeability	1.05
PM width, w_{PM}	3.5mm	PM length, h_{PM}	7.5mm
Arc of stator tooth, θ_{st}	7.5°	Rotor outer radius, R_{ro}	26.5mm
Rotor yoke radius, R_{ry}	20mm	Rotor tooth arc, θ_{rt}	8.2°
Turns per phase of AW	72	Turns per FC	10



(a) Stator



(b) Rotor

Fig. 3.36. Prototype of the 12-slot/10-pole HESFPM machine.

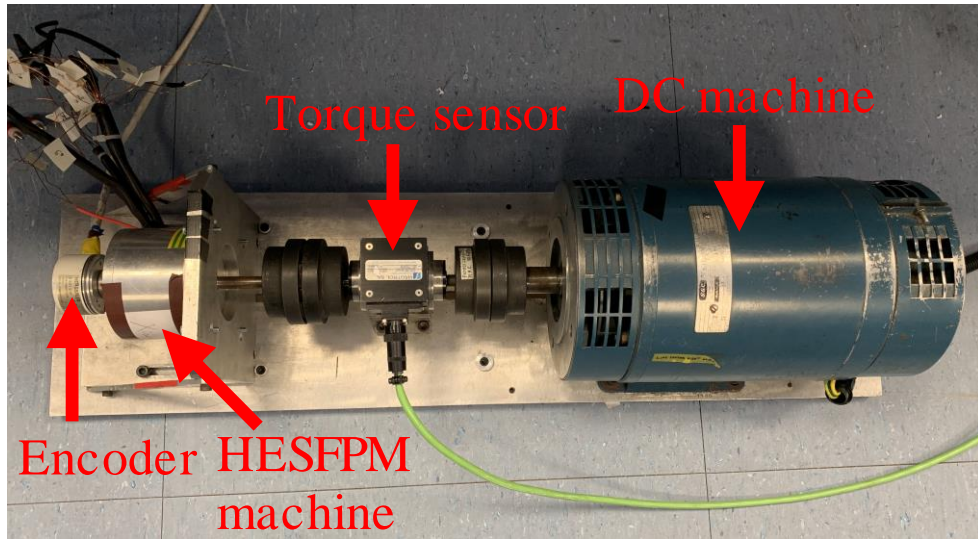
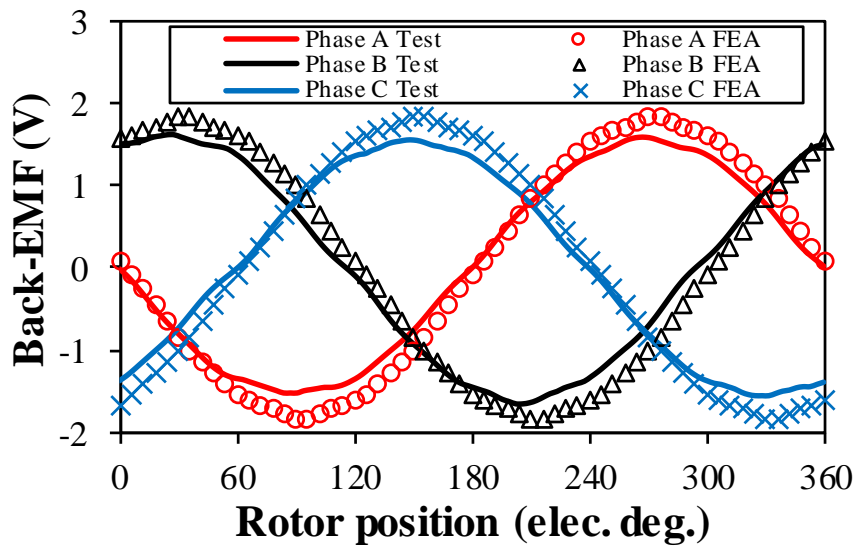


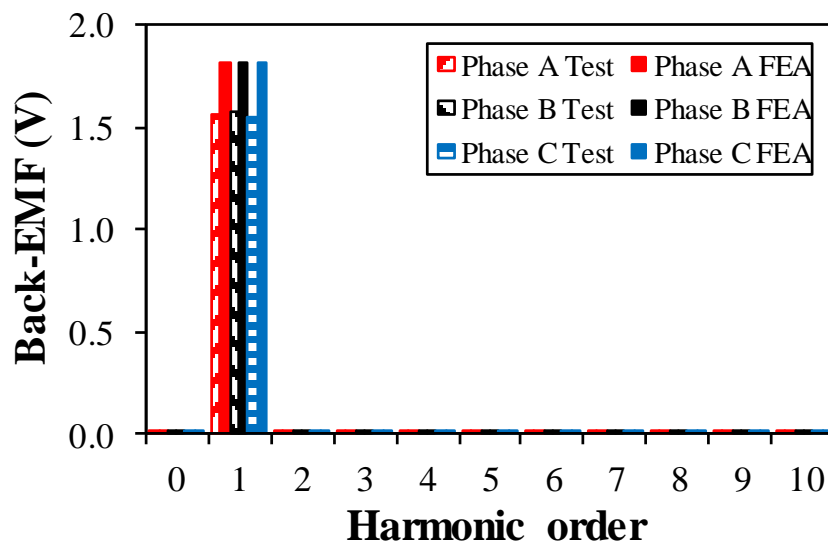
Fig. 3.37. Test rig of the 12-slot/10-pole HESFPM machine.

3.5.2 Back-EMF

The peak phase fundamental back-EMF against DC field winding current (I_f) is measured and compared with the FEA prediction as shown in Fig. 3.39. In this test, the DC field winding consists of all 12 DC coils that are connected in series as shown in Fig. 3.1(a). It shows that the peak phase fundamental back-EMF can be effectively regulated by the DC field winding current, which indicates good flux-controllability. The measured results are lower than the FEA predictions due to end-effect as aforementioned.



(a) Waveforms



(b) Spectra

Fig. 3.38. Back-EMF under PM excitation only at 400r/min.

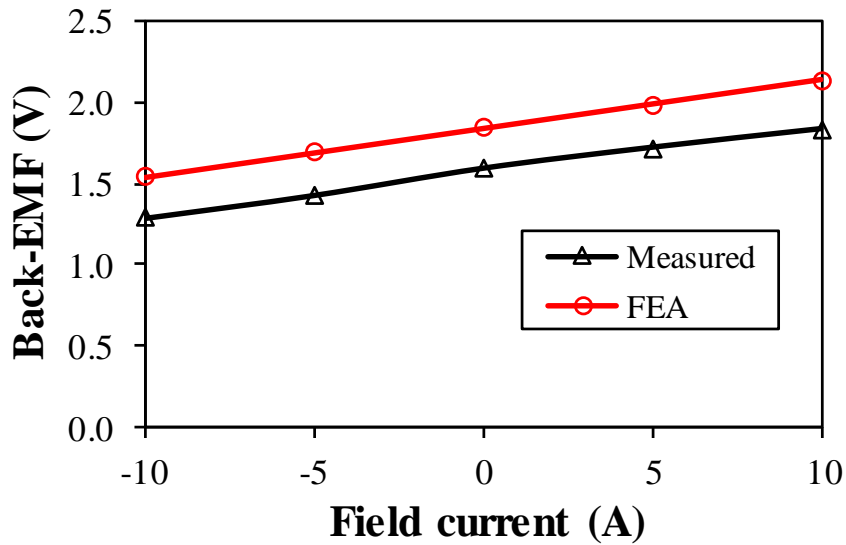
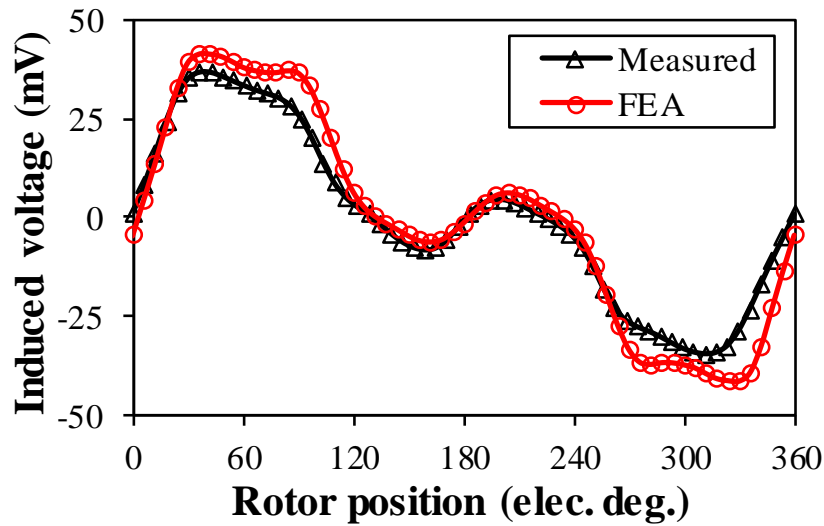


Fig. 3.39. Peak phase fundamental back-EMF against field excitation current at 400r/min.

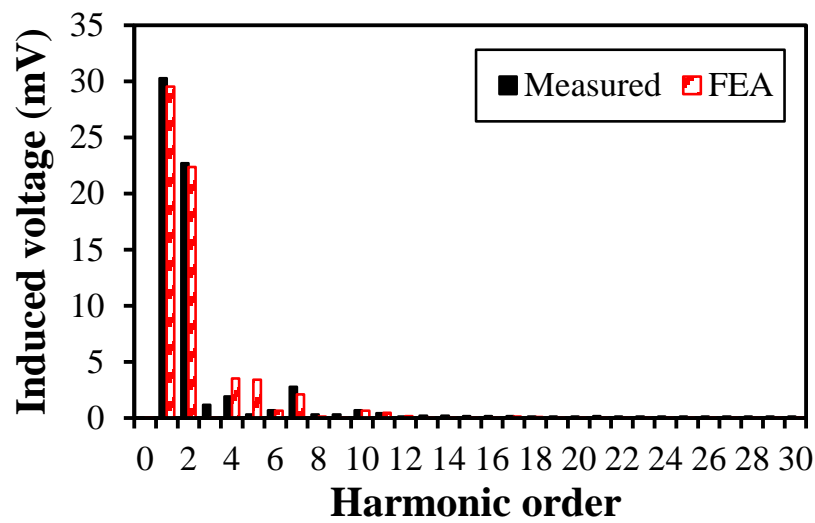
3.5.3 Open-Circuit DC Winding Induced Voltage

When the DC field winding is loaded, the DC winding induced voltage cannot be measured due to the influence of the current in DC field winding. Consequently, the DC coils $f_2, f_4, f_6, f_8, f_{10}$, and f_{12} shown in Fig. 3.1(a) are connected in series and supplied by $2I_f = 4A$ to generate the same DC field winding magneto motive force (MMF) as the conditions that all 12 DC coils are connected together and supplied by $I_f = 2A$. It should be emphasized that the DC coils f_1, f_3, f_5, f_7, f_9 , and f_{11} are open-circuits. The induced voltage of the DC coil f_1 is measured under both open-circuit and on-load conditions, in which the DC coil f_1 will not be influenced by the DC winding current as it is open-circuit. In theory, the induced voltages of DC coils f_3, f_5, f_7, f_9 , and f_{11} can be measured as well because they are also open-circuits.

As shown in Fig. 3.40, the measured open-circuit DC coil f_1 induced voltage agrees well with the FEA prediction. It should be emphasized that the measured open-circuit DC winding induced voltage shown in Fig. 3.41 is calculated based on the measured open-circuit DC coil f_1 induced voltage shown in Fig. 3.40 according to the relationships between different open-circuit DC coil induced voltage waveforms shown in Fig. 3.8. It should be noted that Figs. 3.40 and 3.41 show the open-circuit (with DC current and PM excitations only) induced DC coil f_1 (in one DC coil) and DC winding (in all DC winding coils) voltages, which only consist of open-circuit induced voltage component.

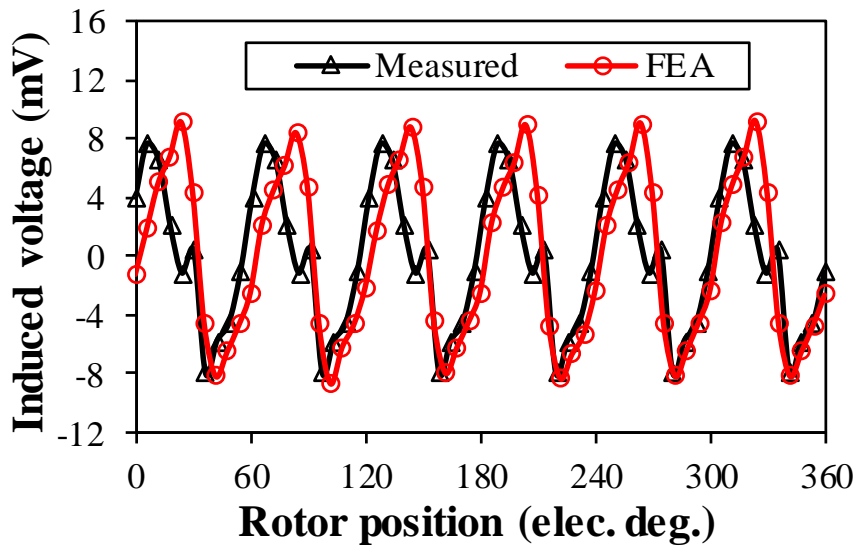


(a) Waveforms

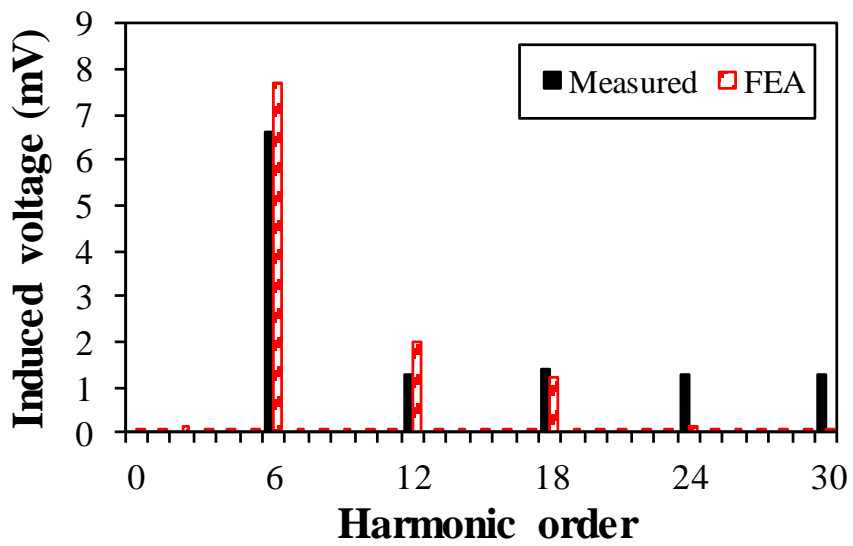


(b) Spectra

Fig. 3.40. Open-circuit DC coil f_1 induced voltage at 400r/min ($I_f=2A$).



(a) Waveforms

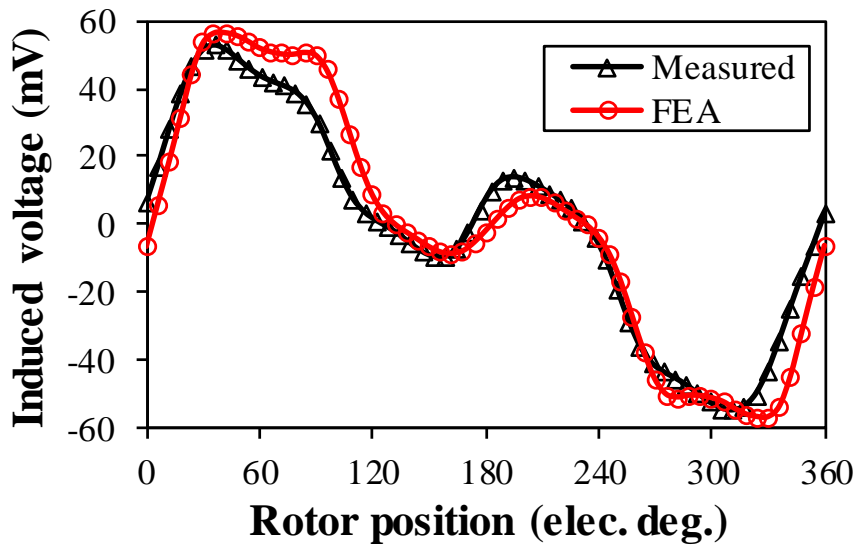


(b) Spectra

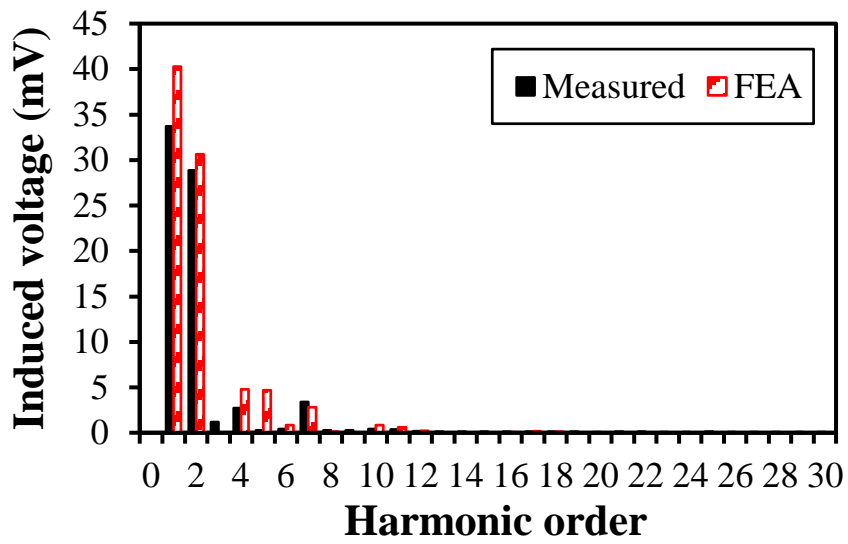
Fig. 3.41. Open-circuit DC winding induced voltage at 400r/min ($I_f=2A$).

3.5.4 On-Load DC Winding Induced Voltage

Similarly, the relationships shown in Fig. 3.8 also apply to different DC coil induced voltage waveforms under on-load condition. Therefore, the measured on-load DC coil f_1 induced voltage shown in Fig. 3.42 is employed to calculate the measured on-load DC winding induced voltage shown in Fig. 3.43. The measured and FEA-predicted on-load DC coil f_1 and DC winding induced voltages have good agreement, as shown in Figs. 3.42 and 3.43, respectively, in which the HESFPM machine is operated under motoring mode. It should be noted that Figs. 3.42 and 3.43 show the on-load (with AC current, DC current and PM excitations) induced DC coil f_1 (in one DC coil) and DC winding (in all DC winding coils) voltages, which consist of both open-circuit induced voltage component and armature current induced voltage component. The minor differences between the measured and FEA predicted results shown in Figs. 3.40 to 3.43 are due to end-effect, imperfect manufacturing and measuring errors.

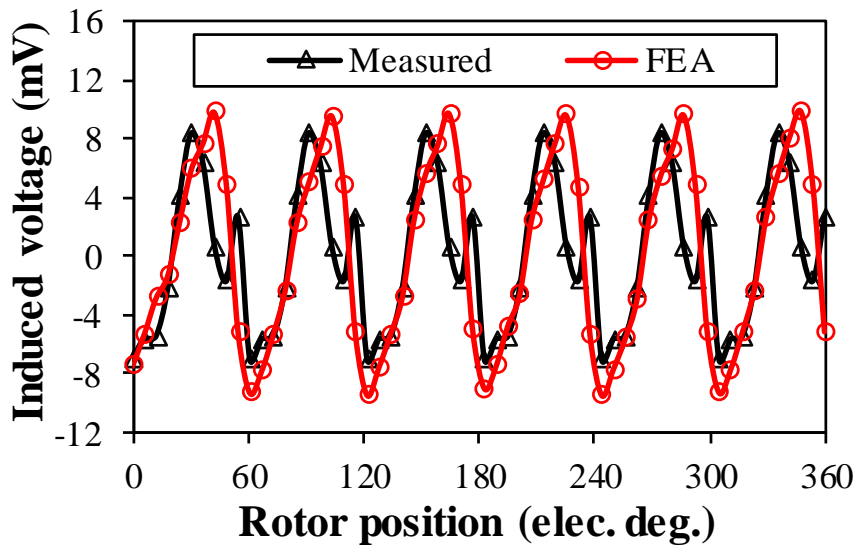


(a) Waveforms

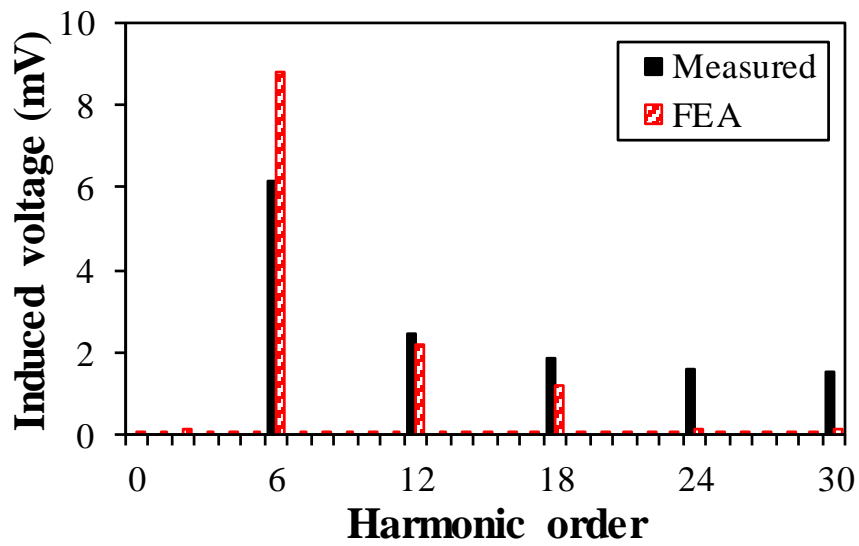


(b) Spectra

Fig. 3.42. On-load DC coil f_1 induced voltage at 400r/min ($I_{ac_rms}=2A$, $I_f=2A$).



(a) Waveforms



(b) Spectra

Fig. 3.43. On-load DC winding induced voltage at 400r/min ($I_{ac_rms}=2A$, $I_f=2A$).

3.6 Conclusion

The DC winding induced voltages in a HESFPM machine under both open-circuit and on-load conditions are investigated in this chapter. The on-load DC winding induced voltage consists of two components, i.e., the open-circuit induced voltage and the armature current induced voltage, respectively. The open-circuit DC winding induced voltage is caused by the variation of the equivalent air-gap magnetic reluctance when the rotor rotates. The armature current induced voltage is due to the interaction between the armature currents and the mutual inductances between AC and DC windings. By way of example, two methods, i.e., rotor step skewing and unequal rotor teeth, are comparatively investigated by the FEA method to suppress the on-load DC winding induced voltage. FEA results show that the peak-to-peak value of the on-load DC winding induced voltage can be suppressed by 96.15% by 5-step rotor skewing, whilst the average torque can be maintained at 89.4%. For unequal rotor teeth, the peak-to-peak value of the on-load induced voltage can be reduced by 89.05%, whilst the average torque can be maintained at 87.8%. The torque ripples are reduced as well by these two techniques due to the reduction of the 6th armature winding phase back-EMF harmonic. The proposed methods can also be applied to other hybrid excited PM machine topologies.

CHAPTER 4

Influence of Stator Slot and Rotor Pole Number Combination on Field Winding Induced Voltage Ripple in Hybrid Excitation Switched Flux Machine

The induced voltage ripple in DC field windings can cause many problems in hybrid excitation machines (HEMs). It can generate ripple current in field winding, thus causing unsteady magnetic field excitation and hence additional torque ripple and losses. Besides, the torque and power density of hybrid excitation machines may be deteriorated as a result of the influence of the induced voltage ripple on field winding's excitation circuit, particularly under high-speed conditions. Based on a hybrid excitation switched flux machine (HESFM), the influence of stator slot and rotor pole number combination on no-load and on-load field winding induced voltage ripples are studied and compared by the finite element analysis (FEA) method. It reveals that the harmonic content and thus the peak-to-peak value of the field winding induced voltage ripple are closely related to the stator slot and rotor pole number combination at both no-load and on-load operating conditions. The FEA calculations are verified by experiments on a prototype HESFM.

This chapter is based the paper [SUN21a] published in IEEE Transactions on Energy Conversion.

4.1 Introduction

Permanent magnet synchronous machines (PMSMs) are characterized by high torque density, high efficiency, and high-power factor, thanks to high energy-product rare-earth PMs [BIA06a]. PMSMs have been applied to a variety of applications, ranging from electrical vehicles/hybrid electrical vehicles (EVs/HEVs), wind power generation, to aerospace, etc. [LIU10] [CHE05] [PAT08]. However, the flux-weakening performance of PMSMs is relatively poor, as the PM excitation is fixed. In order to operate beyond the base speed, the armature current of PMSMs needs to be controlled. By applying a negative d -axis armature current, the PM flux can be counteracted in flux-weakening region [JAH86] [SOO94]. Nevertheless, the flux-weakening technique by means of d -axis armature current can bring the disadvantages of reduced torque and power density, additional copper loss and degraded efficiency, and even uncontrolled voltage problem at high speed [SOO02] [RAM11].

Another method for extending the operating region of PM machines is to integrate the conventional PM machines with magnetic gears, i.e., magnetically geared (MGd) machines. MGd machines are initially developed from a coaxial magnetic gear [ATA01], which is capable of transmitting torque and speed by using PMs without any mechanical contacts. In theory, all three parts of a magnetic gear can be movable, i.e., high-speed element, low-speed element, and magnetic modulation ring. Alternatively, one part can be fixed to work in a way like a mechanical gear with a fixed gear ratio between the other two parts for contactless torque and speed transmission. There are many different ways to achieve MGd machines by integrating the conventional PM machines with magnetic gears, e.g., mechanically coupled MGd machines, pseudo MGd machines, and vernier machines, etc. [ZHU18a]. As such, MGd machines inherit many advantages from magnetic gears, such as no lubrication required, little or no maintenance, low noise and vibration, inherent overload protection, high reliability and efficiency, and high torque transmission, etc. However, they also suffer from complicated mechanical structures, high cost due to rare-earth PMs, torque ripple, iron loss, and PM eddy current loss, etc., especially at the higher speed [WAN19].

Wound field synchronous machines (WFSMs) possess excellent flux-controllability due to the variable air-gap magnetic field excited by DC field winding (FW), but with the demerits of low efficiency, low torque, and power density compared with PMSMs. Hybrid excitation machines (HEMs) having both PMs and FWs can be an alternative option to tackle the aforementioned issues that are concerned with PMSMs and WFSMs. HEMs exhibit high torque density and high efficiency compared to WFSMs while possessing better flux-control capability compared to PMSMs, which are ideal for variable-speed applications, e.g., EVs/HEVs [ZHU19a] [ZHU19b] [POT19].

The HEM topologies are diverse, which are mainly derived from the conventional rotor-PM and stator-PM machines by simply replacing a part of PMs with field coils (FCs) or directly integrating FCs into the existing machine topologies [LUO00] [CHA03]. Amongst multitudes of HEM topologies, stator-PM HEMs with both PMs and FCs on the stator side, are of great interest and have been comprehensively developed over many years [CHE14] [GAO18] [AFI15] [CAI19]. This is due to the simple and robust rotor structure, good heat management, and the absence of slip rings and brushes.

Among various stator-PM HEMs, HE switched flux machines (HESFMs), which are developed from the conventional SFPM machines are attracting much attention among scholars in recent years owing to the utilization of flux focusing effect and hence high torque density. Many HESFM topologies have been developed and evaluated [HOA07] [OWE10] [ZHA15a] [HUA16a]. In addition, the parasitic effects, such as cogging torque, back electromotive force (back-EMF) harmonics, torque ripple, unbalance magnetic force, and losses, etc., also have been studied in different HEMs [XU16] [HUA16a] [CAI20]. However, another significant parasitic effect in HEMs, i.e., the induced voltage ripple in DC field winding has not been perceived and studied in depth.

The FW induced ripple voltage inevitably causes a lot of problems to HEMs, such as ripple current in FW, unsteady excitation field, additional torque ripple and losses, and even reduced

torque and power density, particularly at high speed. The phenomenon, fallout, and reduction of FW induced voltage ripple are firstly investigated in WFSMs [WU19] [WU20] [WU18], and then extended to HEMs [SUN20a]. In [SUN20a], the phenomenon of FW induced ripple voltage and the way of its suppression are presented based on a 12-slot/10-pole (12/10) HESFM. In this chapter, the influence of stator slot and rotor pole number combination on field winding induced voltage ripple in the HESFM is analyzed by considering both no-load and on-load conditions. The main purpose of this chapter is to provide guidance for the selection of suitable slot and pole number combination with a low field winding induced voltage ripple for certain machine design, without using any other passive reduction methods.

This chapter is organized as follows. In section 4.2, the machine topology, operating principle, and feasible stator slot and rotor pole number combinations of the investigated HESFM are presented. Then, the FW induced voltage ripple under no-load, three-phase armature currents only, and on-load are evaluated and compared by the finite element analysis (FEA) method for different slot/pole number combinations in section 4.3. Next, FEA predicted results are verified by experiments on a prototype HEM in section 4.4. Finally, some general conclusions are provided in section 4.5.

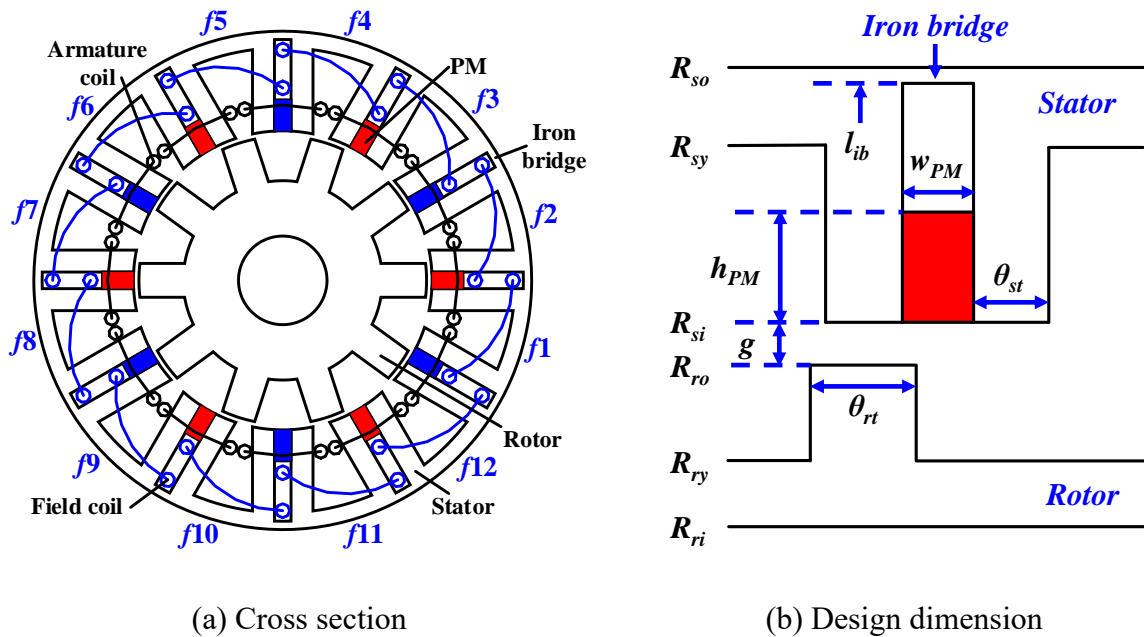


Fig. 4.1. HESFM with 12-stator-slot and 10-rotor-pole [OWE10].

4.2 Hybrid Excitation Switched Flux Machine

4.2.1 Machine Topology and Operation Principle

Fig. 4.1 shows a three-phase HESFM with 12-slot and 10-pole, which is developed from the conventional three-phase SFPM machine by replacing a part of PMs with FCs and adding an outer iron bridge for improved flux-controllability [HOA97] [OWE10]. The stator is utilized to accommodate armature winding (AW), FW, and PMs. The salient rotor is iron cored without any PMs and coils, which is robust and ideal for high-speed operation. The AW and FW consist of concentrated non-overlapping coils, which feature short end-winding, high fault-tolerant capability, low copper loss, and thus high efficiency. The PMs are tangentially magnetized and placed in the middle of each stator pole. Moreover, magnetic iron bridges are utilized to provide additional flux path for FCs, which can help to mitigate the potential irreversible demagnetization of PMs and improve the flux-controllability of the HESFM. It is worth mentioning that a thick iron bridge can lead to high flux-leakage and hence reduced PM excited torque while a thin iron bridge would restrict the flux regulation capability due to magnetic saturation, as illustrated in Fig. 4.2. Consequently, a 0.5-mm-thick iron bridge is selected in this chapter to balance the PM excited torque capability and the flux regulation capability. The flux regulation ratio δ is defined as

$$\delta = \frac{E_e - E_w}{E_{PM}} \quad (4.1)$$

where E_e , E_w , and E_{PM} are the open-circuit phase fundamental back-EMFs under positive field current, negative field current, and sole PM excitations, respectively.

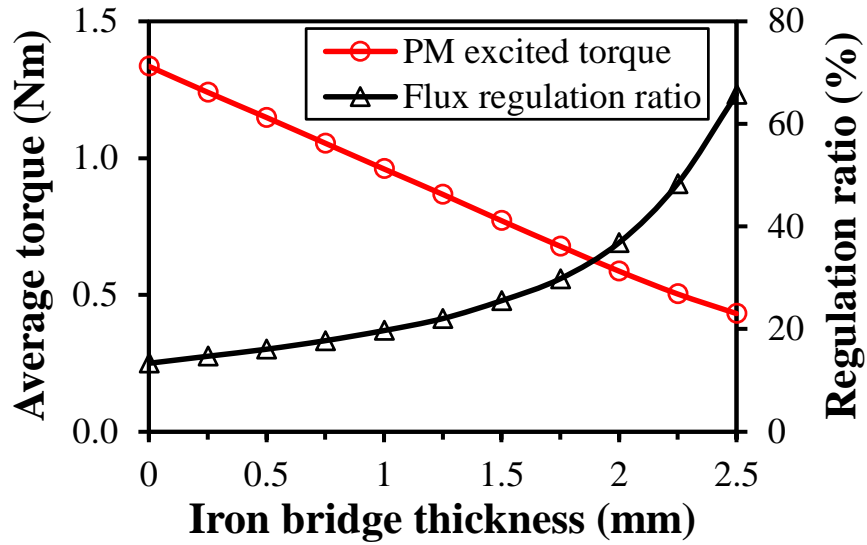


Fig. 4.2. Influence of iron bridge thickness on average torque and flux regulation ratio.

In the HESFM, the induced open-circuit back-EMF in each phase is nearly sinusoidal [OWE10]. Therefore, the armature windings are excited by sinusoidal currents for stable output torque, i.e., brushless AC (BLAC) excitation. The PM flux is constant while the FW flux is variable. Therefore, the air-gap field can be regulated by changing the polarity and magnitude of the DC current in FW. The phase flux-linkage, induced back-EMF, and hence output torque can be varied, depending on operating conditions. At low speed, a positive DC current can be injected into the FW to improve the air-gap field and thus the starting torque. At high speed, a negative DC current is applied to weaken the PM field, thus reducing the induced back-EMF [OWE10].

4.2.2 Feasible Stator Slot and Rotor Pole Number Combination

Similar to the conventional SFPM machine [CHE10c], many stator slot and rotor pole number combinations are feasible for the HESFM shown in Fig. 4.1, which can be expressed by

$$N_s = k_1 m \quad k_1 = 1, 2, \dots \quad (4.2)$$

$$N_r = N_s \pm k_2 \quad k_2 = 1, 2, \dots \quad (4.3)$$

where N_s and N_r are the stator slot and rotor pole numbers, respectively, and m is the AW phase number. In HESFMs, N_s must be an even number. Therefore, k_1 should be a positive integer if m is an even number while k_1 should be an even number if m is an odd number, and k_2 is a positive integer.

For a three-phase HESFM, the stator slot number $N_s=3k_1$, where $m=3$ and k_1 is an even number. For the HESFM with different N_s -stator-slot/ N_r -rotor-pole (N_s/N_r), the coil pitch factor k_{pv} of the v^{th} back-EMF harmonic can be obtained by

$$k_{pv} = \cos \left[v\pi \left(\frac{N_r}{N_s} - 1 \right) \right] \quad (4.4)$$

In order to obtain a larger fundamental coil pitch factor and hence a higher output torque, N_r should be close to N_s based on (4.4). For a three-phase HESFM with 6-stator-slot ($m=3$, $k_1=2$), the potential N_r are 4, 5, 7, and 8, respectively, while for a three-phase HESFM with 12-stator-slot ($m=3$, $k_1=4$), the preferred N_r are 10, 11, 13, and 14, respectively. Consequently, the three-phase HESFMs having $N_s=6$, $N_r=4, 5, 7, \text{ and } 8$ as well as $N_s=12$, $N_r=10, 11, 13, \text{ and } 14$ are utilized for analysis.

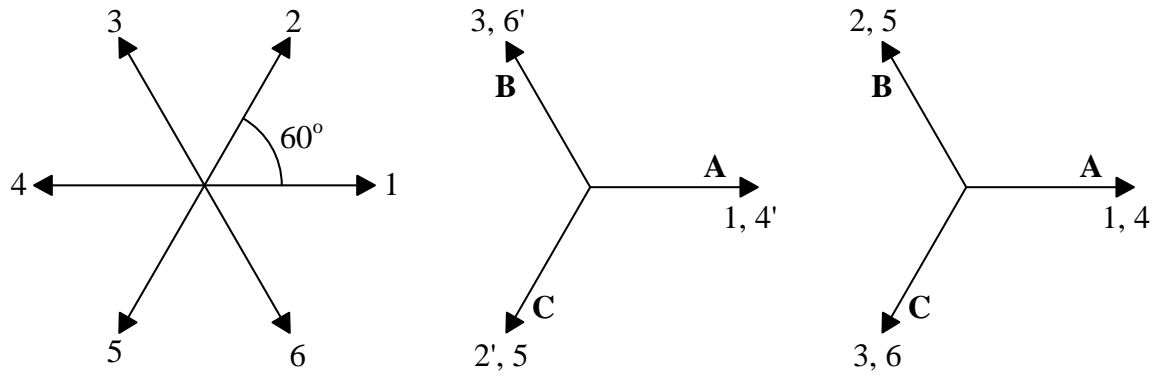
4.2.3 Armature Winding Connection

The connection of each phase can be obtained by coil back-EMF phasors. The electrical degrees θ_e between coil back-EMF phasors can be calculated by

$$\theta_e = N_r \times \theta_m \quad (4.5)$$

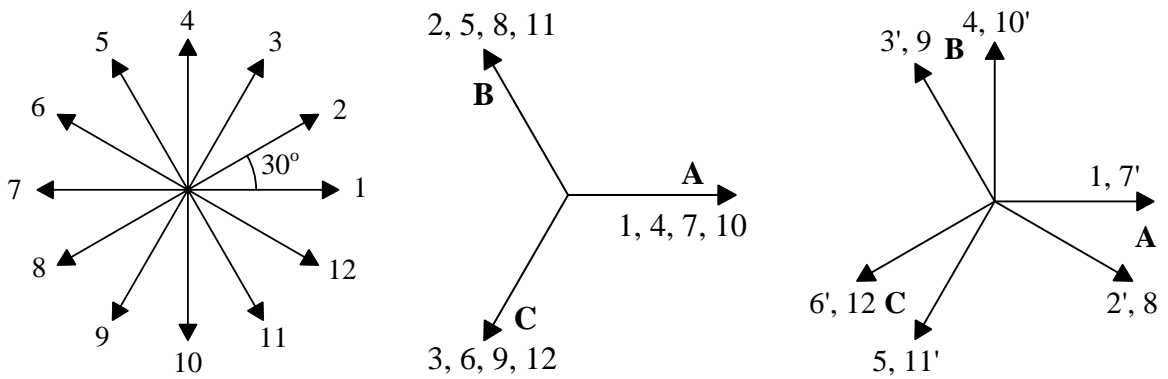
where θ_m is the mechanical degrees between coil back-EMF phasors.

Fig. 4.3(a) shows the mechanical position of armature coils of the 6-slot stator. For different rotor pole numbers, the electrical position of armature coils can be obtained by (4.5). In order to obtain symmetrical and higher three-phase back-EMFs, the connections between armature coils for 6/4 and 6/5 HESFMs are shown in Figs. 4.3(b) and 4.3(c), respectively. It should be noted that the polarities of coils n and n' are opposite due to alternate magnetized PMs in tangential direction. The armature coil connections for 6/7 and 6/8 machines are similar to those of 6/4 and 6/5 machines, respectively, and the only difference is the interchange of phases B and C. The mechanical position of armature coils of the 12-slot stator is shown in Fig. 4.4(a). The armature coil connections for 12/10 and 12/11 machines are shown in Figs. 4.4(b) and 4.4(c), respectively. Similarly, the armature coil connections for 12/13 and 12/14 machines can be obtained by interchanging phase B with phase C in 12/10 and 12/11 machines, respectively. The winding layout and configuration of the HESFM with different slot and pole number combinations are illustrated in Fig. 4.5. It can be found that the connection between field coils remains the same for different slot and pole number combinations, whereas the connection between armature coils changes.



(a) Mechanical position of the 6-slot stator (b) Connection of the 6/4-pole machine (c) Connection of the 6/5-pole machine

Fig. 4.3. Mechanical position and connection of armature coils of the 6-slot stator with different rotor pole numbers.



(a) Mechanical position of the 12-slot stator (b) Connection of the 12/10-pole machine (c) Connection of the 12/11-pole machine

Fig. 4.4. Mechanical position and connection of armature coils of 12-slot stator with different rotor pole numbers.

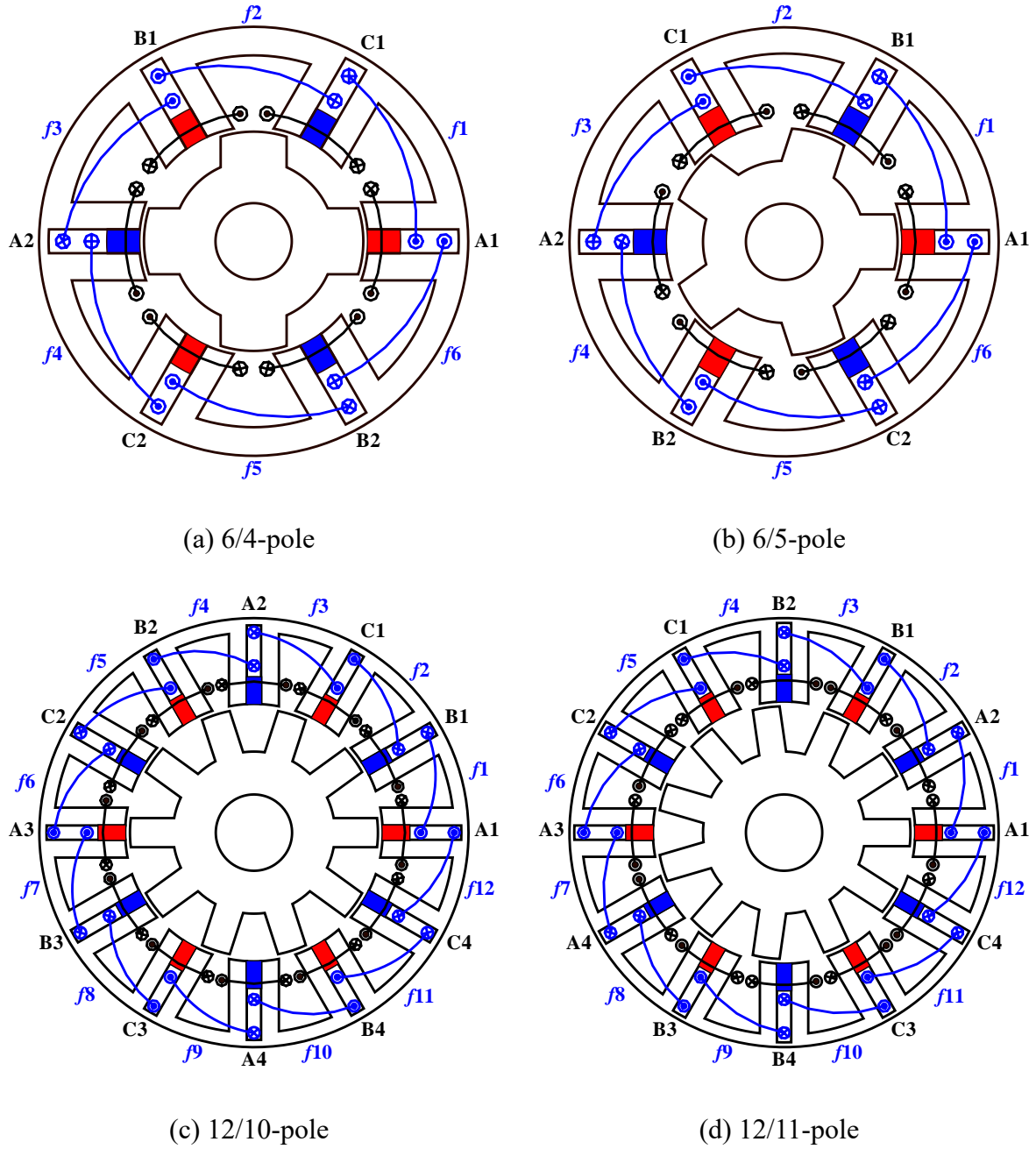


Fig. 4.5. Winding layout and configuration of HESFM with different slot/pole number combinations.

The HESFM with different N_s/N_r are firstly optimized by the genetic algorithm embedded in the FEA software (ANSYS/Maxwell), and the optimization goal is the highest average electromagnetic torque. During optimization, the stator outer diameter, the stack length, the air-gap length, the length of the iron bridge, the rotor shaft diameter, the PM volume, the AW copper loss, the current density in FW slot (J_{dc}), and the slot filling factor for AW and FW slots remain

the same and constant. At low speed, the iron loss and AC loss are not the main loss. Consequently, only a fixed copper loss of 20W in AW is considered during optimization, as the rated rotor speed is only 400rpm. Besides, the HESFMs are optimized by applying zero d -axis current control and flux-enhancing current in FW of 5A/mm². The main parameters after optimization can be found in Table 4.1.

Table 4.1 Main Parameters of HESFMs After Optimization

Parameters	Unit	Value							
Number of stator slots, N_s	-	6	6	6	6	12	12	12	12
Number of rotor poles, N_r	-	4	5	7	8	10	11	13	14
Stator outer radius, R_{so}	mm	45							
Stack length, l_a	mm	25							
Air-gap length, g	mm	0.5							
Iron-bridge length, l_{ib}	mm	0.5							
PM remanence	T	1.2							
PM coercivity	kA/m	890							
Rotor shaft radius, R_{ri}	mm	10.4							
Stator yoke radius, R_{sy}	mm	40.5	40.9	41.6	42.1	42.5	42.7	43.1	43.2
Stator inner radius, R_{si}	mm	27.5	27.7	28.3	28.6	29	29.2	29.8	30.1
PM width, w_{PM}	mm	5	4.6	3.9	3.6	3	2.8	2.6	2.5
PM length, h_{PM}	mm	6.7	7.3	8.6	9.3	5.6	5.9	6.5	6.7
Stator tooth arc, θ_{st}	°	14	13.4	12.6	11.8	8.5	8.2	7.6	7.4
Rotor outer radius, R_{ro}	mm	27	27.4	27.9	28.3	28.5	28.7	29.3	29.5
Rotor yoke radius, R_{ry}	mm	19.4	19.4	19.4	19.4	18	18	18	18
Rotor tooth arc, θ_{rt}	°	35	28.2	19.5	17.1	13.5	12.4	10.3	9.8
Slot filling factor, k_f	-	0.5							
Turns per armature coil	-	18							
Turns per field coil	-	90							

4.2.4 Torque Performance

Fig. 4.6 shows the on-load torque waveforms of the 12-slot/10-pole machine under flux-enhancing ($J_{dc}=+20\text{A/mm}^2$), flux-weakening ($J_{dc}=-20\text{A/mm}^2$), and sole PM excitations ($J_{dc}=0$), respectively, in which the AC winding copper loss is fixed at 20W. Water cooling or oil cooling techniques are recommended for this machine since the current density is quite high. It can be seen that the DC current is able to effectively regulate the on-load torque of the HESFM machine. As shown in Fig. 4.7, the average torque can be changed in a wide range by changing the polarity and magnitude of the DC current. Fig. 4.8 shows the average torque versus AC winding copper loss with different current densities in the DC slot. It can be observed that the average torque increases with the increase of AC winding copper loss with different current densities in DC slot, although magnetic saturation may be severe under higher copper loss. Besides, the torques with positive DC current are higher than those without DC current or with negative DC current over the whole range of copper loss.

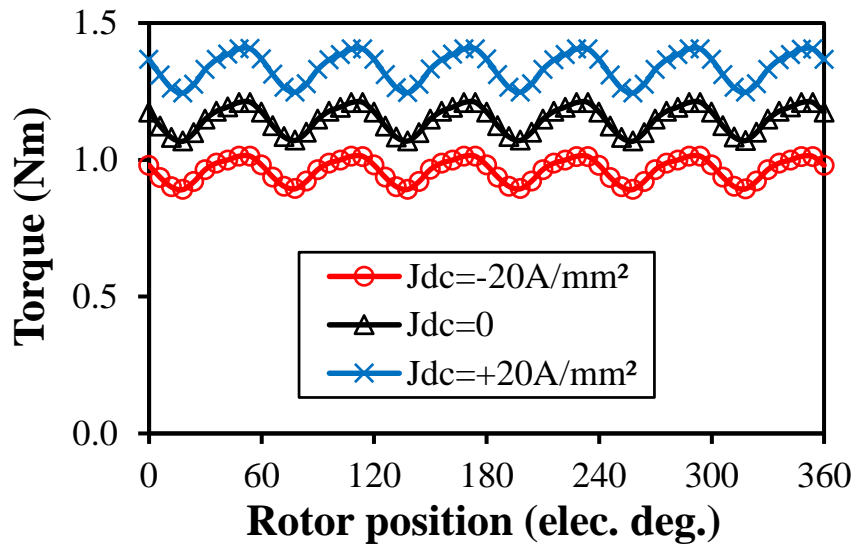


Fig. 4.6. Torque waveforms of 12-slot/10-pole HESFM with different current densities in DC slot and 20W copper loss in AC winding.

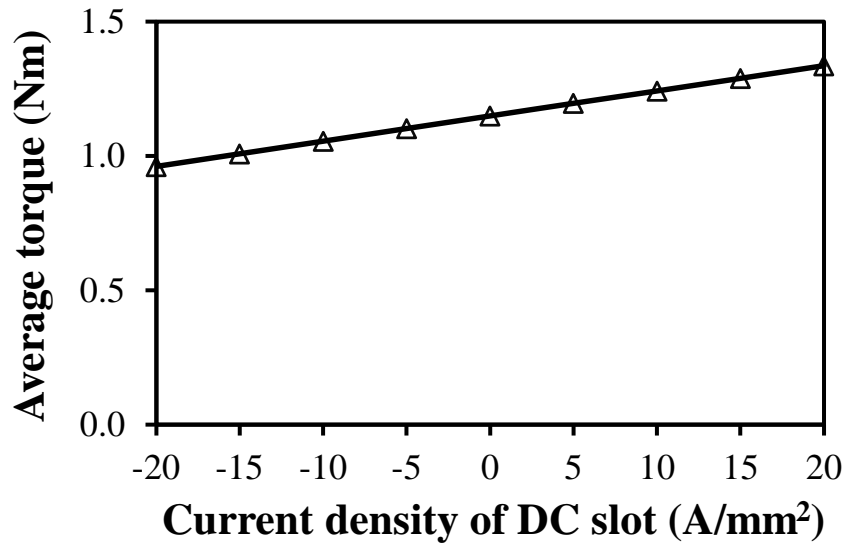


Fig. 4.7. Average torques of 12-slot/10-pole HESFM with different current densities in DC slot and 20W copper loss in AC winding.

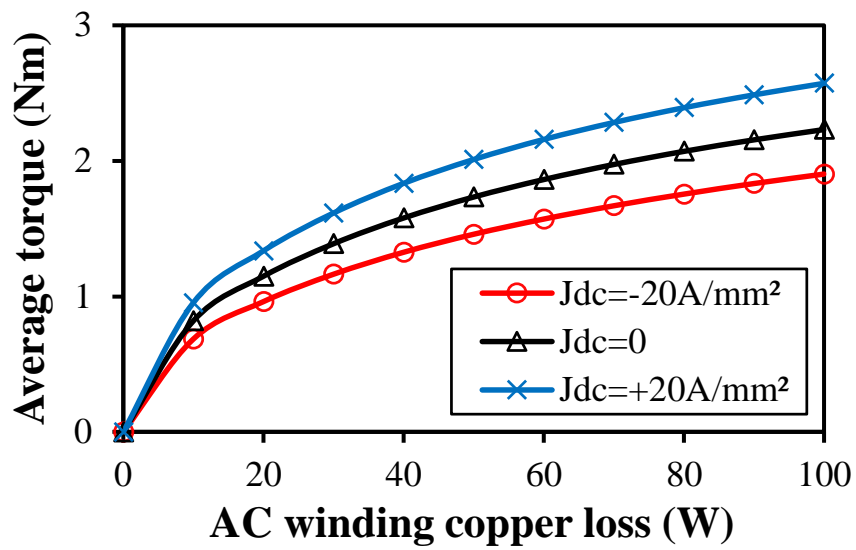
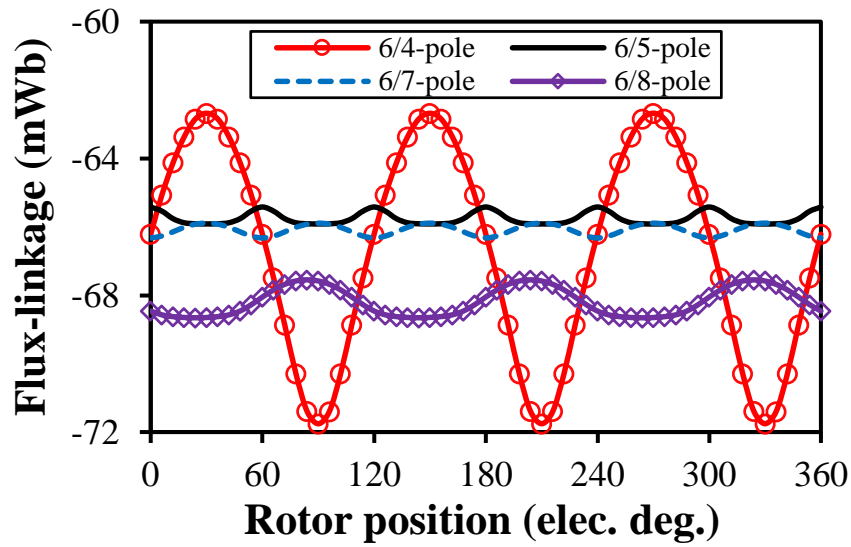


Fig. 4.8. Average torques of 12-slot/10-pole HESFM versus armature winding copper loss with different current densities in DC slot.

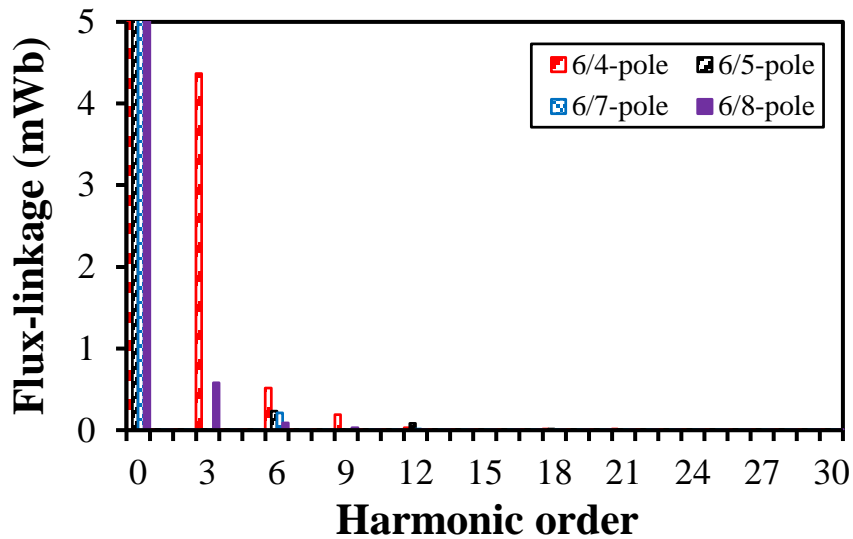
4.3 Field Winding Induced Voltage Ripple

4.3.1 No-Load Induced Voltage

For the 6-stator-slot HESFMs having 4-, 5-, 7-, and 8-rotor-pole, the DC field winding (FW) on the stator side contains 6 individual DC field coils (FCs) and they are connected in series. While for the 12-stator-slot HESFMs having 10-, 11-, 13-, and 14-rotor-pole, the DC FW contains 12 individual DC FCs as illustrated in Fig. 4.1(a) and they are connected in series as well. Fig. 4.9 shows the FW flux-linkage waveforms and their harmonic spectra of the 6-slot HESFMs having 4-, 5-, 7-, and 8-pole at no-load, in which the AWs are open-circuited while the PMs and FWs coexist for field excitation. As shown in Fig. 4.9(a), the FW flux-linkage waveforms vary periodically versus rotor position and the number of periods is different for the 6-slot HESFMs having different rotor poles within one electric period of rotor position. As can be seen from Fig. 4.9(b), the predominant FW flux-linkage harmonic order (HO) is 3 for 6/4 and 6/8 machines, while it is 6 for 6/5 and 6/7 machines.



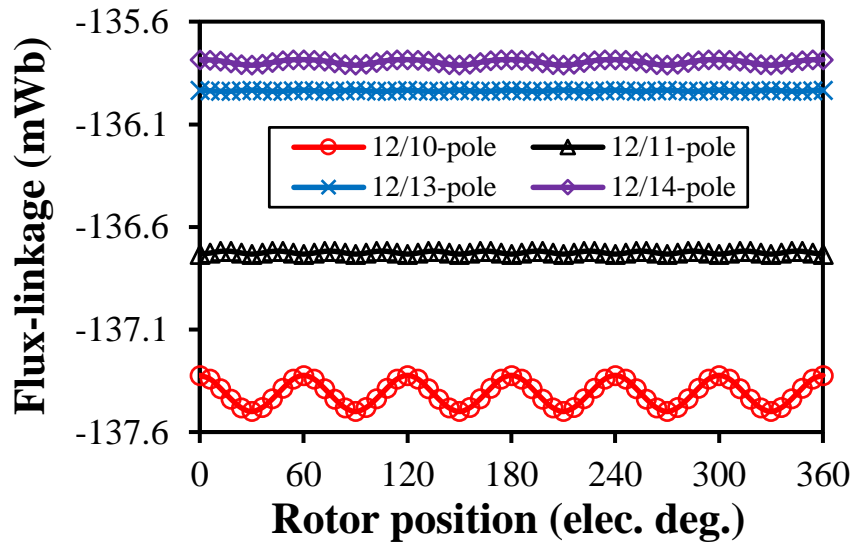
(a) Waveforms



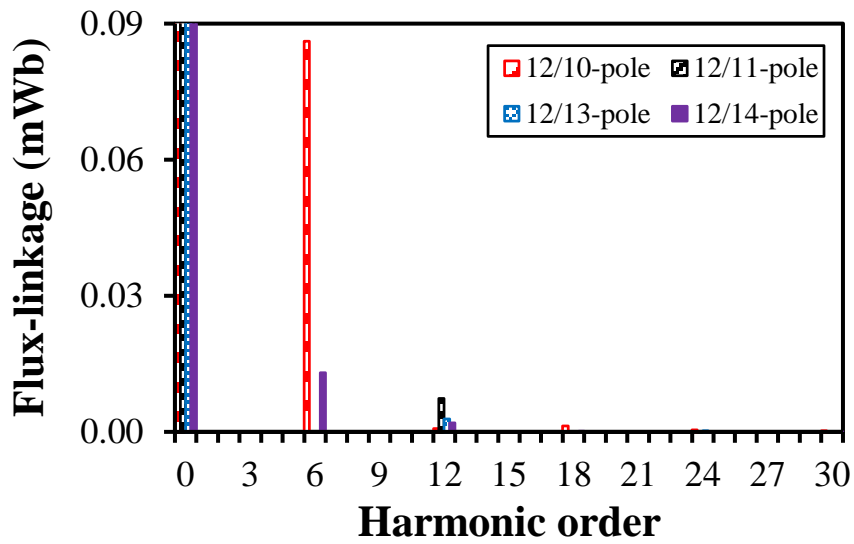
(b) Spectra

Fig. 4.9. No-load FW flux-linkages of the 6-stator-slot HESFMs having 4-, 5-, 7-, and 8-rotor-pole.

Fig. 4.10 shows the no-load FW flux-linkage waveforms and their harmonic spectra of the 12-slot HESFMs having 10-, 11-, 13-, and 14-pole. Similarly, the FW flux-linkage waveforms are periodic against the rotor electric position as shown in Fig. 4.10(a). However, the dominant FW flux-linkage harmonic orders of the 12-slot HESFMs are different from the 6-slot counterparts. For 12/10 and 12/14 machines, the dominant harmonic order is 6, while it is 12 for 12/11 and 12/13 machines, as shown in Fig. 4.10(b).



(a) Waveforms



(b) Spectra

Fig. 4.10. No-load FW flux-linkages of the 12-stator-slot HESFMs having 10-, 11-, 13-, and 14-rotor-pole.

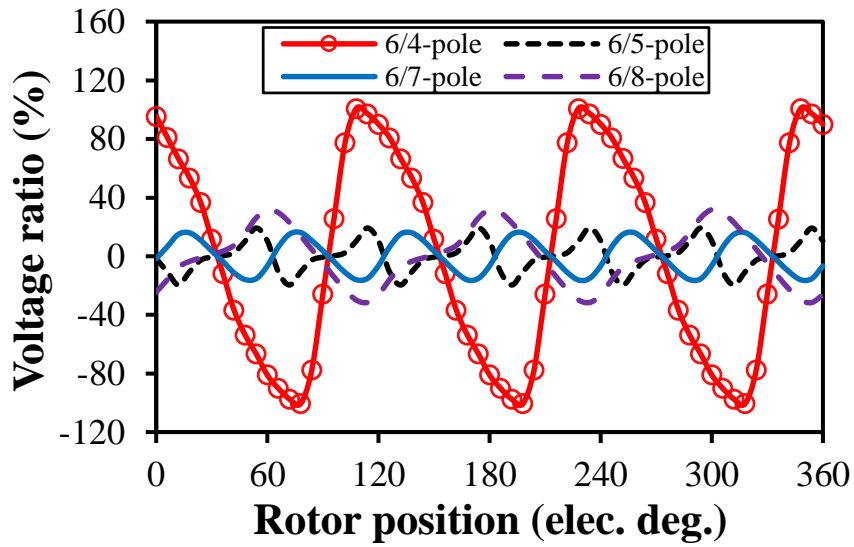
Based on Faraday's law of electromagnetic induction, the voltage ripple will be generated in the FW owing to the fluctuant FW flux-linkage. In order to quantify the influence of the FW induced voltage ripple, the FW induced voltage ratio (IVR_{FW}) is adopted and defined in (4.6). It should be mentioned that the FW's resistance voltage drop is kept as constant and it does not change against the rotor electric position for each slot and pole number combination in the following analyses.

$$IVR_{FW} = \frac{V_{FW}}{V_R} \times 100\% \quad (4.6)$$

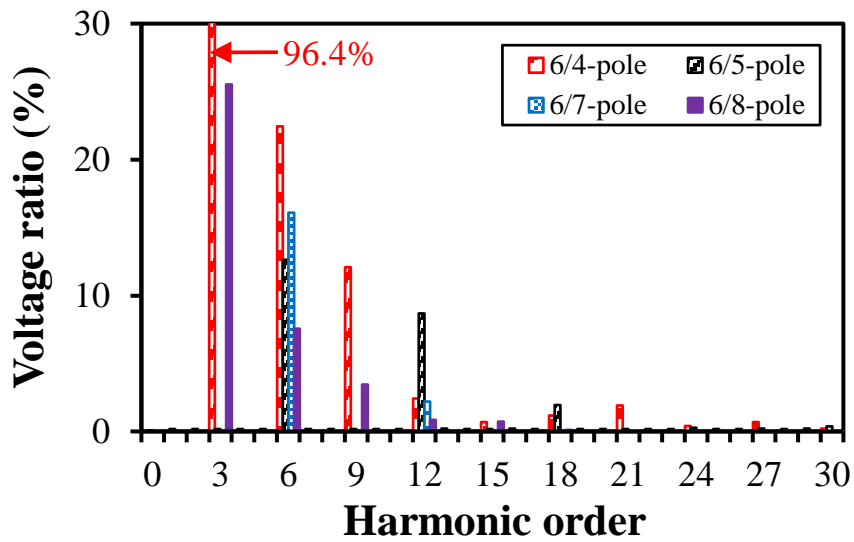
where V_{FW} is the value of the FW induced voltage ripple. V_R is the FW's resistance voltage drop.

The FW induced voltage ratios and their harmonic spectra of the 6-slot HESFMs having 4-, 5-, 7-, and 8-pole at no-load are shown in Fig. 4.11. Similar to the no-load FW flux-linkages shown in Fig. 4.9, the dominating no-load FW induced voltage harmonic order is 3 for 6/4 and 6/8 machines, but 6 for 6/5 and 6/7 machines. For 12/10 and 12/14 machines, the main no-load FW induced voltage harmonic order is 6, while for 12/11 and 12/13 machines, the main harmonic order is 12, as shown in Fig. 4.12.

Among the 6-slot HESFM counterparts, 6/4 and 6/8 machines have relatively higher peak-to-peak no-load FW induced voltage ratio (IVR_{FW_PP}) than that of 6/5 and 6/7 machines due to higher amplitude of low order harmonics. As for the 12-slot HESFM counterparts, the peak-to-peak no-load FW induced voltage ratio of 12/11 and 12/13 machines is relatively lower than that of 12/10 and 12/14 machines due to lower amplitude of high order harmonics.

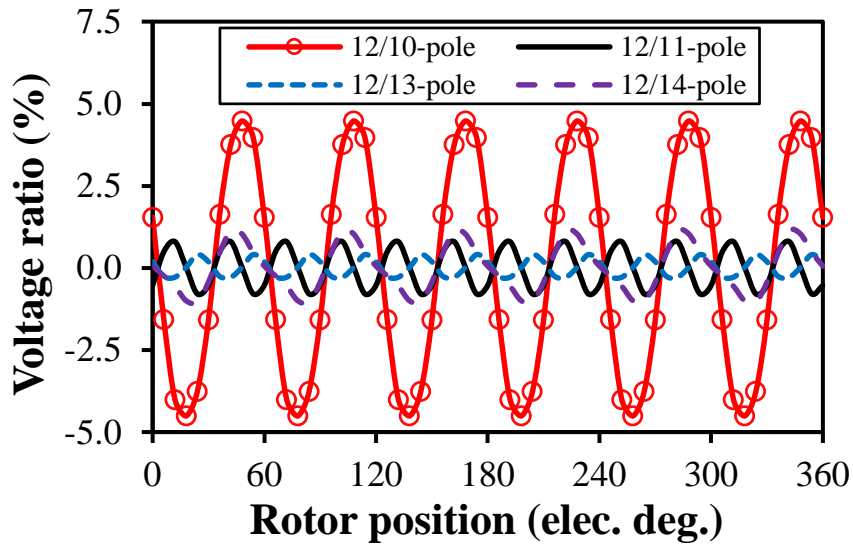


(a) Waveforms

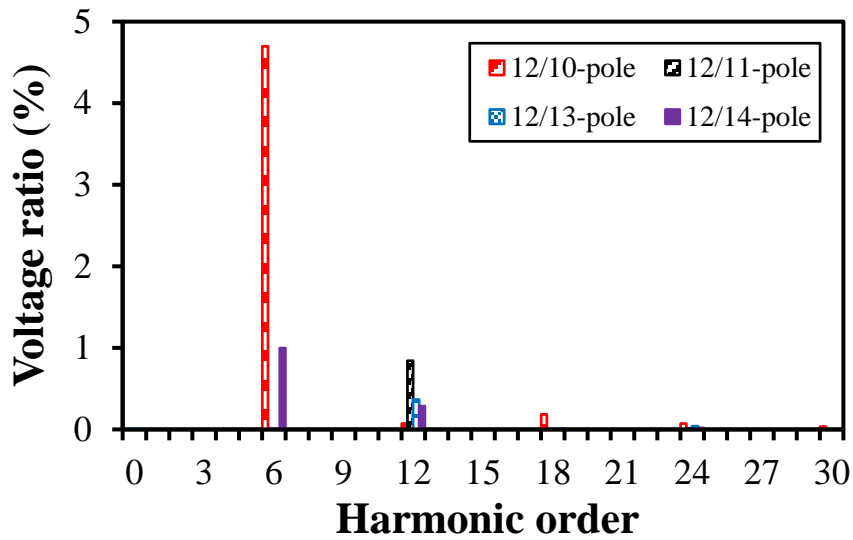


(b) Spectra

Fig. 4.11. No-load FW induced voltage ratios of the 6-stator-slot HESFMs having 4-, 5-, 7-, and 8-rotor-pole at 400rpm.



(a) Waveforms



(b) Spectra

Fig. 4.12. No-load FW induced voltage ratios of the 12-stator-slot HESFMs having 10-, 11-, 13-, and 14-rotor-pole at 400rpm.

In order to understand the difference in harmonic orders and hence the peak-to-peak values of the no-load FW induced voltage ripple (V_{FW_PP}) for different stator slot and rotor pole number combinations, the no-load field coil flux-linkage waveforms of the HESFMs having different stator slot and rotor pole numbers are given in Figs. 4.13 and 4.14. As aforementioned, the DC FW of the 6-slot HESFMs has 6 FCs, which are denoted here as f_1, f_2, f_3, f_4, f_5 , and f_6 , respectively,

for convenience. Similarly, 12 FCs in the DC FW of the 12-slot HESFMs are denoted as f_1 , f_2 , ..., and f_{12} , respectively. In the HESFM shown in Fig. 4.1, the doubly salient structure, i.e., salient stator and rotor, is employed to generate variable flux-linkage and thus induced back-EMF in the AWs for torque production. However, this inevitably leads to the fluctuating FC flux-linkages at no-load, owing to the change of the air-gap magnetic field with the rotation of the salient rotor.

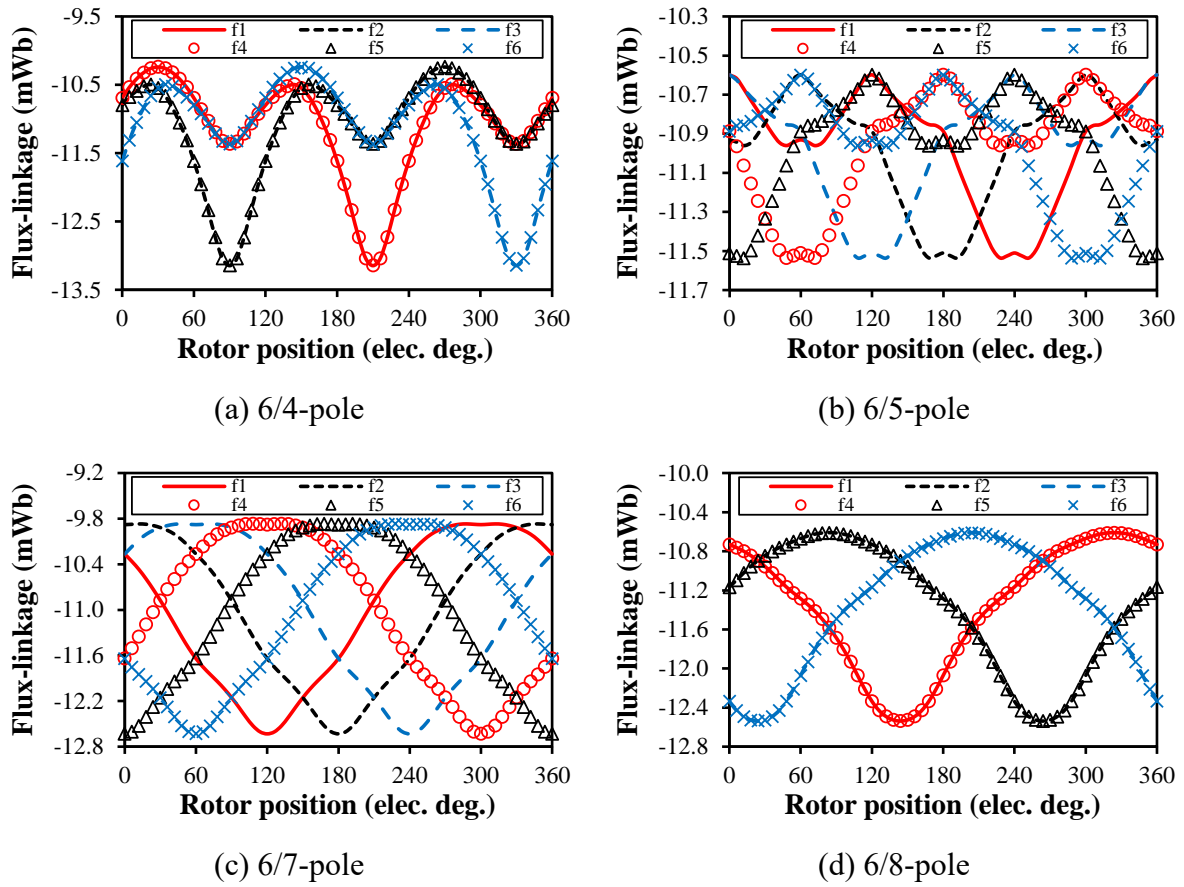


Fig. 4.13. No-load FC flux-linkages of the 6-stator-slot HESFMs having 4-, 5-, 7-, and 8-rotor-pole.

As shown in Figs. 4.13 and 4.14, for a specific stator slot and rotor pole number combination, the no-load flux-linkage waveforms of different FCs are the same apart from the phase difference. For the 6-slot HESFMs having 4-, 5-, 7-, and 8-pole, the phase differences (θ_s) between the no-load flux-linkage waveforms of two adjacent FCs are 120° , 60° , 60° , and 120° , respectively. As for the 12-slot HESFMs having 10-, 11-, 13-, and 14-pole, θ_s of the no-load

flux-linkages between two adjacent FCs are 60° , 30° , 30° , and 60° , respectively. The relation between the rotor electric position (θ_e) and mechanical position (θ_m) can be described by (4.5). For the HESFM with N_s/N_r -pole, θ_s can be given by (4.7).

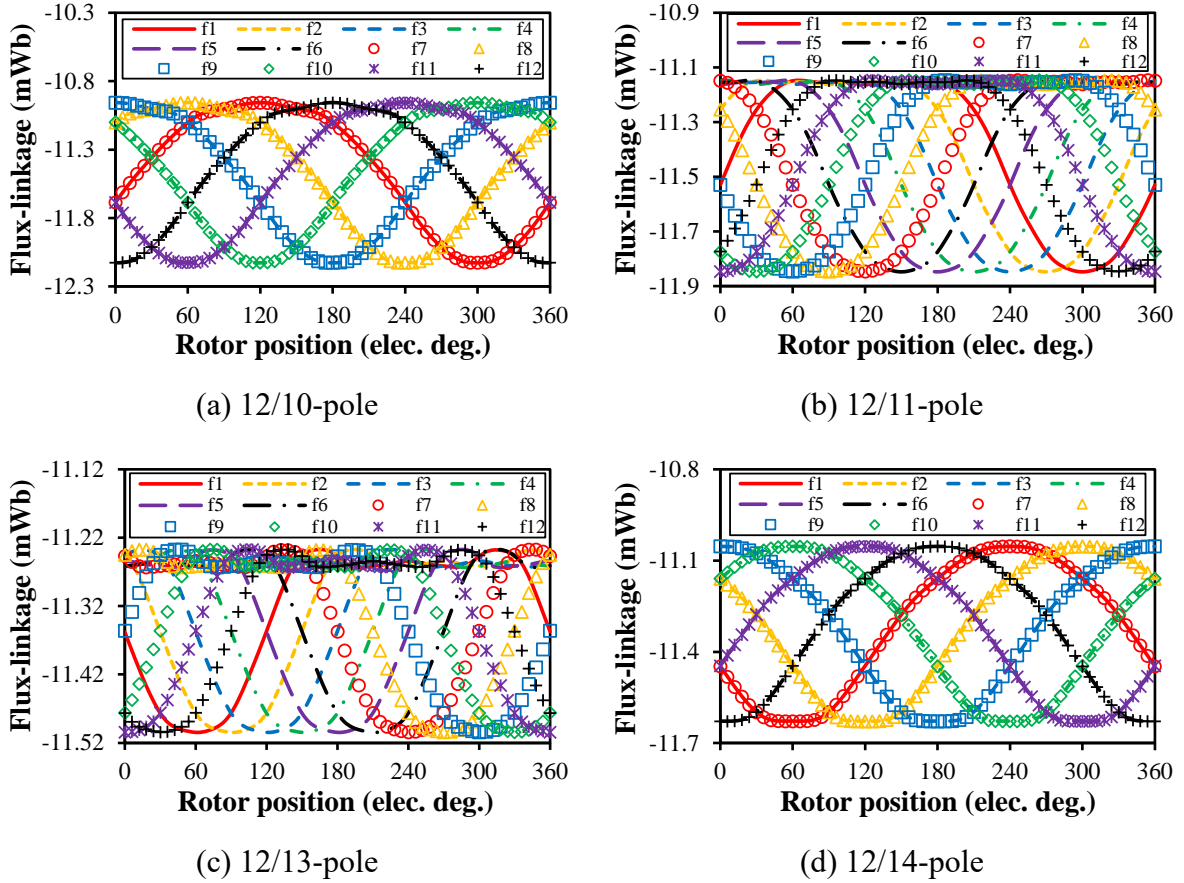
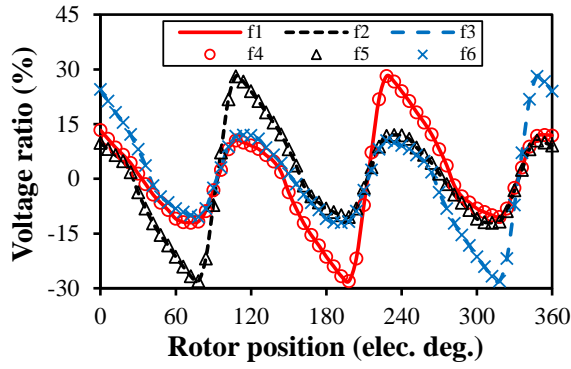


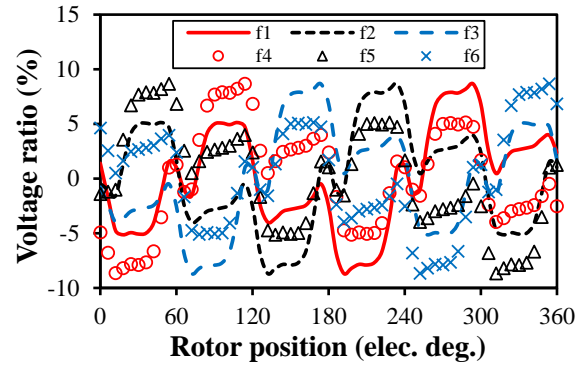
Fig. 4.14. No-load FC flux-linkages of the 12-stator-slot HESFMs having 10-, 11-, 13-, and 14-rotor-pole.

$$\theta_s = 2\pi - \left(\frac{2\pi}{N_s} \times N_r\right) \quad (4.7)$$

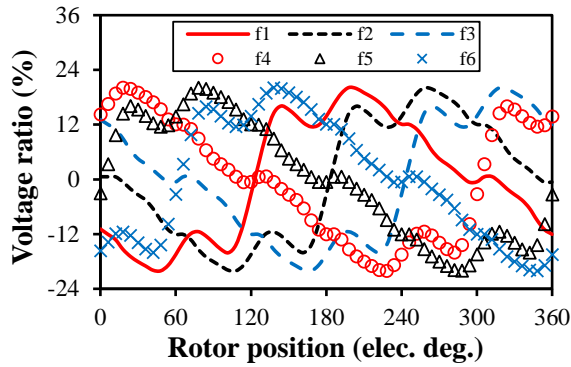
Figs. 4.15 and 4.16 show the no-load FC induced voltage ratios of the HESFMs having different stator slot and rotor pole number combinations. As can be seen from Figs. 4.15 and 4.16, voltage ripples are generated in the FCs owing to the unstable FC flux-linkages shown in Figs. 4.13 and 4.14 for different stator slot and rotor pole number combinations.



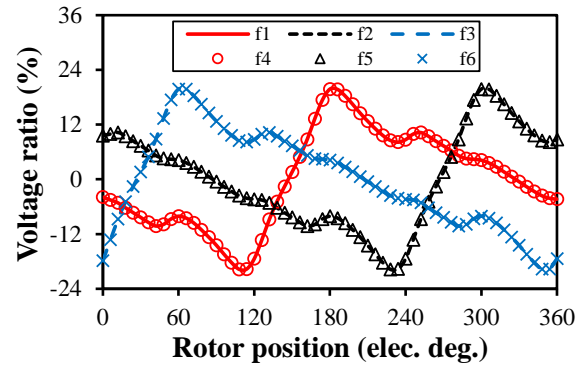
(a) 6/4-pole



(b) 6/5-pole



(c) 6/7-pole



(d) 6/8-pole

Fig. 4.15. No-load FC induced voltage ratios of the 6-stator-slot HESFMs having 4-, 5-, 7-, and 8-rotor-pole at 400rpm.

For a specific stator slot and rotor pole number combination, the phase differences between the no-load induced voltages of two adjacent FCs are the same as θ_s of the no-load flux-linkages between two adjacent FCs, and can be described by (4.7) as well. Therefore, for the 6-slot HESFMs having 4-, 5-, 7-, and 8-pole, θ_s of the induced voltages between two adjacent FCs are 120° , 60° , 60° , and 120° , respectively. As for the 12-slot HESFMs having 10-, 11-, 13-, and 14-pole, θ_s of the induced voltages between two adjacent FCs are 60° , 30° , 30° , and 60° , respectively.

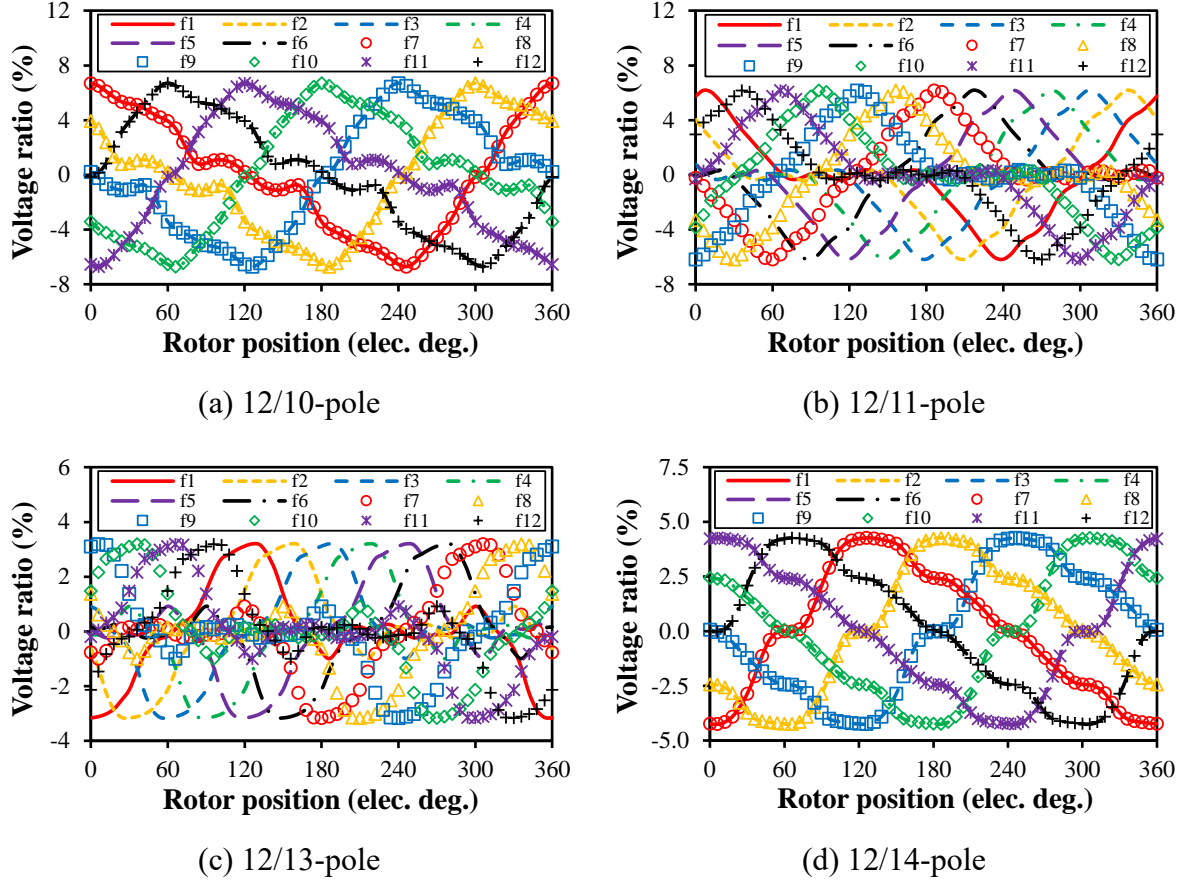


Fig. 4.16. No-load FC induced voltage ratios of the 12-stator-slot HESFMs having 10-, 11-, 13-, and 14-rotor-pole at 400rpm.

$$i = \frac{\text{LCM}(N_s, N_r)}{N_r} k \quad (4.8)$$

In the HESFM, the FW is made up of different FCs via the series connection. Consequently, the FW flux-linkage and induced voltage are the sum of different FC flux-linkages and induced voltages, respectively. By way of example, for the 6/4-pole machine, θ_s of the no-load flux-linkages and induced voltages between two adjacent FCs are 120° as shown in Figs. 4.13(a) and 4.15(a), which results in the compensation of other harmonics in the no-load FW flux-linkage and induced voltage waveforms apart from the harmonic orders of $3k$, where k is a positive integer. In other words, for the 6/4-pole machine, the FW flux-linkage and induced voltage waveforms are free from other harmonics except for the harmonic order of $3k$ (3^{rd} , 6^{th} , 9^{th} , ...).

The harmonic compensation phenomenon also occurs in the HESFMs having other stator slot and rotor pole number combinations. As can be seen from Figs. 4.9 and 4.11, the no-load FW flux-linkage and induced voltage harmonic orders are $3k$, $6k$, $6k$, and $3k$ for the 6-slot HESFMs having 4-, 5-, 7-, and 8-pole. While for the 12-slot HESFMs having 10-, 11-, 13-, and 14-pole, the no-load FW flux-linkage and induced voltage harmonic orders are $6k$, $12k$, $12k$, and $6k$, respectively, as shown in Figs. 4.10 and 4.12. For the HESFM with N_s/N_r -pole, the harmonic order (i) of the no-load FW flux-linkage and induced voltage can be described by (4.8), as derived in Appendix B. The properties of the no-load FW induced voltage ripple for the HESFMs with different N_s/N_r -pole are listed in Table 4.2.

Table 4.2 Properties of No-Load Induced Field Winding Voltage Ripple

N_s/N_r	6/4	6/5	6/7	6/8	12/10	12/11	12/13	12/14
HO	$3k$	$6k$	$6k$	$3k$	$6k$	$12k$	$12k$	$6k$
V_{FW_PP} (V)	4.57	0.88	0.73	1.43	0.42	0.11	0.08	0.13
IVR_{FW_PP} (%)	201	39	32	63	9.2	2.5	1.7	2.9

4.3.2 Armature Current Induced Voltage

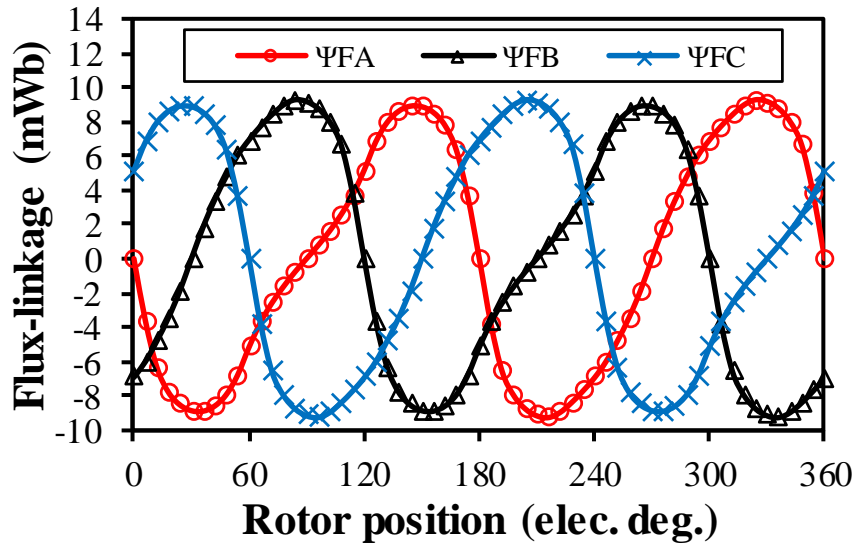
If the magnetic saturation in stator and rotor laminations is neglected, the flux-linkage captured by the FW due to the three-phase AW currents (Ψ_{FAW}) can be expressed by,

$$\begin{aligned}\Psi_{FAW}(\theta_e) &= \Psi_{FA}(\theta_e) + \Psi_{FB}(\theta_e) + \Psi_{FC}(\theta_e) \\ &= M_{AF}(\theta_e)I_a(\theta_e) + M_{BF}(\theta_e)I_b(\theta_e) + M_{CF}(\theta_e)I_c(\theta_e)\end{aligned}\quad (4.9)$$

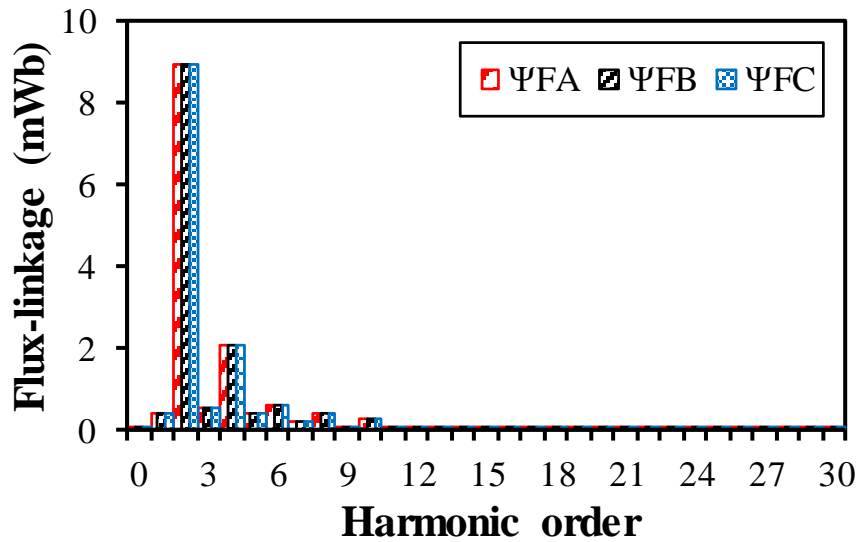
where Ψ_{FA} , Ψ_{FB} , and Ψ_{FC} are the flux-linkages captured by the FW due to the phase A-, B-, and C-currents, respectively. M_{AF} , M_{BF} , and M_{CF} are the mutual inductances between the three-phase AWs and the FW, respectively. I_a , I_b , and I_c are the three-phase AW currents, respectively, which can be given by

$$\begin{aligned}
 I_a &= I_p \cos(\theta_e + \theta_a) \\
 I_b &= I_p \cos(\theta_e - \frac{2\pi}{3} + \theta_a) \\
 I_c &= I_p \cos(\theta_e - \frac{4\pi}{3} + \theta_a)
 \end{aligned}
 \tag{4.10}$$

where I_p is the peak phase current. θ_a is the phase current angle.

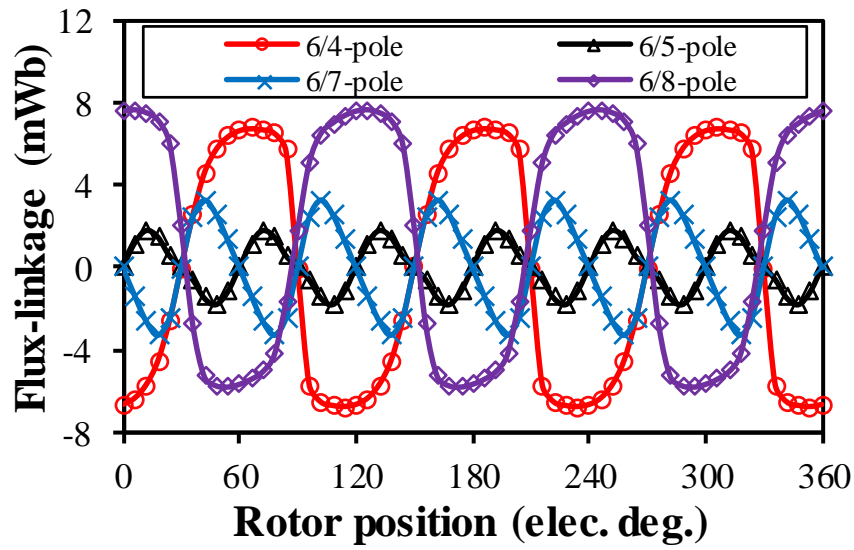


(a) Waveforms

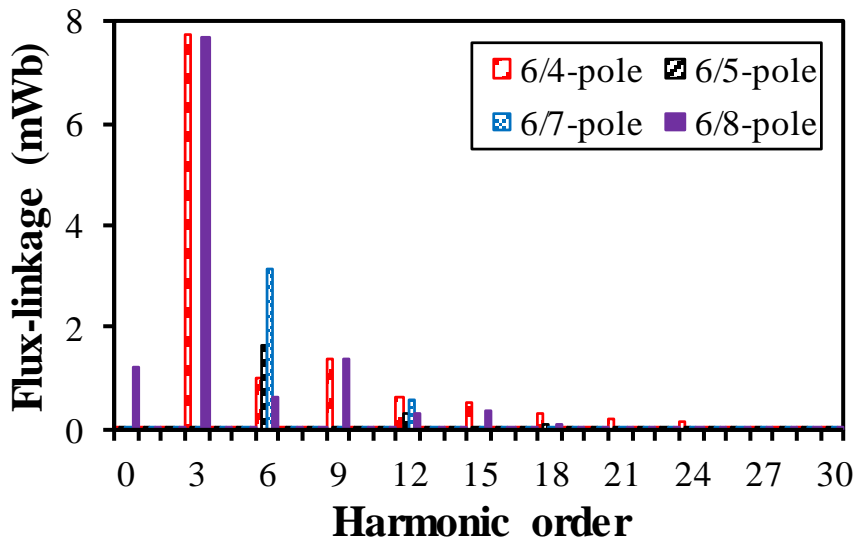


(b) Spectra

Fig. 4.17. FW flux-linkages of the 6/4-pole HESFM due to the sole excitation of the phase A-, B-, and C-currents, respectively.



(a) Waveforms

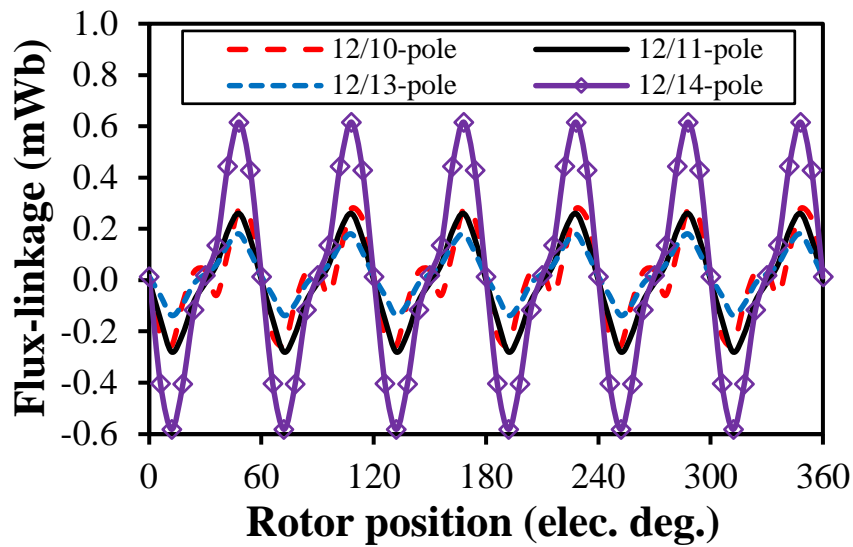


(b) Spectra

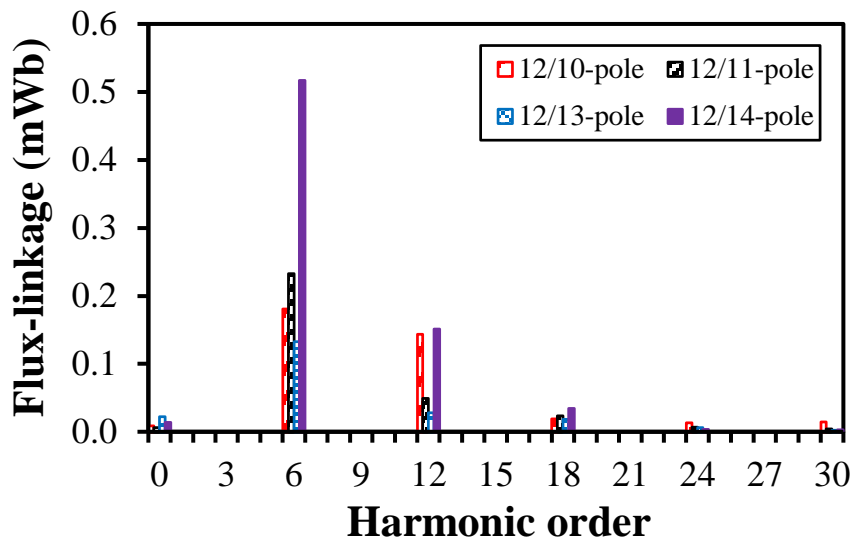
Fig. 4.18. FW flux-linkages of the 6-stator-slot HESFMs having 4-, 5-, 7-, and 8-rotor-pole under three-phase armature currents excitation only.

By way of example, the flux-linkages captured by the FW due to the sole excitation of the phase A-, B-, and C-currents of the 6/4 machine, i.e., Ψ_{FA} , Ψ_{FB} , and Ψ_{FC} , respectively, are shown in Fig. 4.17. Ψ_{FA} , Ψ_{FB} , and Ψ_{FC} are obtained by injecting the phase A-, B-, and C-currents separately, in which the PMs are set as air and the FW excitation is absent. It clearly shows that there are abundant harmonics in Ψ_{FA} , Ψ_{FB} , and Ψ_{FC} , owing to the doubly salient machine

structure and the modulation effect of the salient rotor pole. It can also be observed from Fig. 4.17 that the harmonic spectra of Ψ_{FA} , Ψ_{FB} , and Ψ_{FC} are the same, and the difference lies in the 120° phase angle between two adjacent waveforms. When the symmetrical three-phase sinusoidal currents are simultaneously injected into the AWs, i.e., the HESFM is free from PMs and FW excitations, the FW flux-linkage of the 6/4-pole machine only suffers from the harmonic orders of $3k$, as other harmonics are compensated as shown in Fig. 4.18.

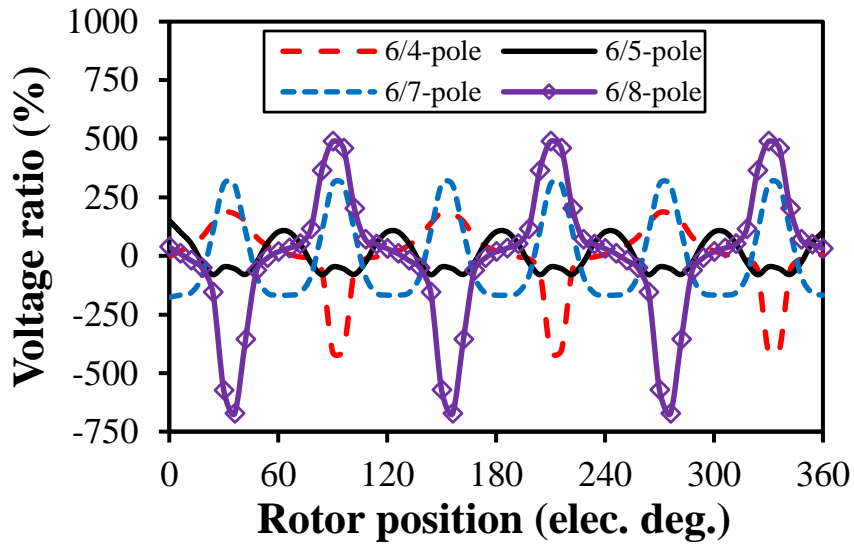


(a) Waveforms

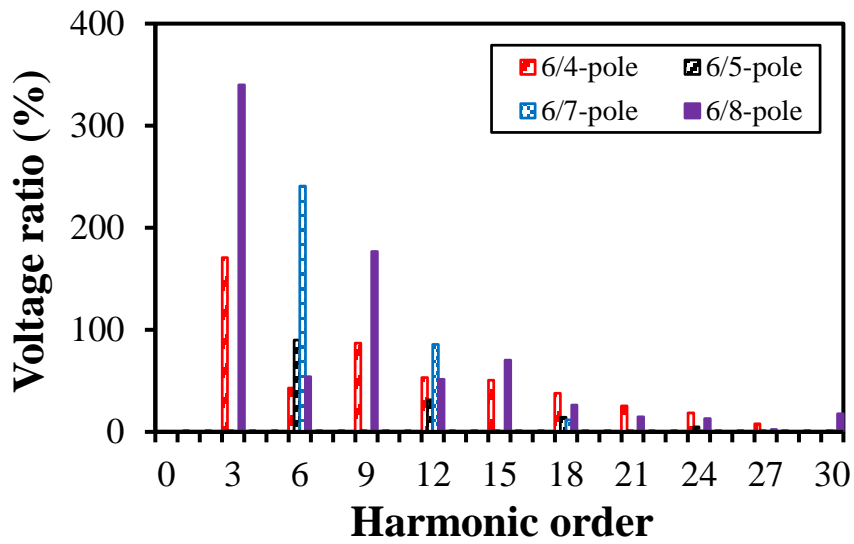


(b) Spectra

Fig. 4.19. FW flux-linkages of the 12-stator-slot HESFMs having 10-, 11-, 13-, and 14-rotor-pole under three-phase armature currents excitation only.

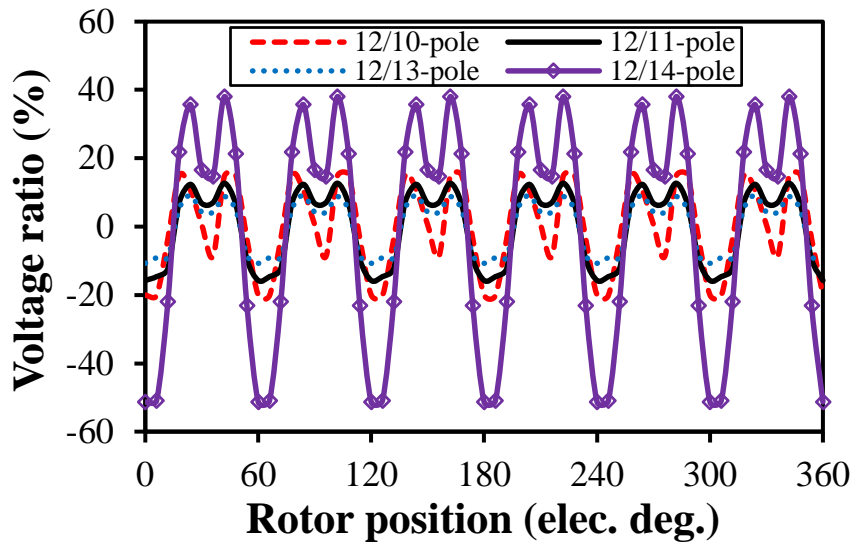


(a) Waveforms

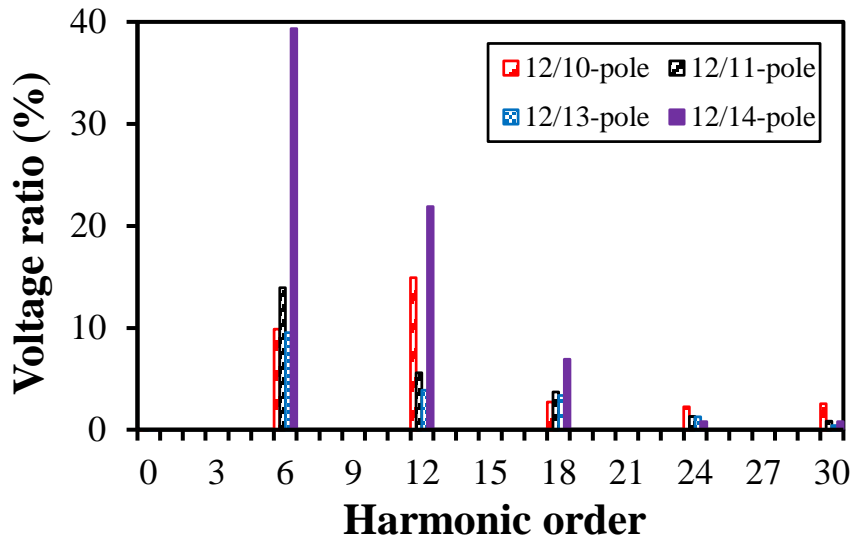


(b) Spectra

Fig. 4.20. FW induced voltage ratios of the 6-stator-slot HESFMs having 4-, 5-, 7-, and 8-rotor-pole under three-phase armature currents excitation only at 400rpm.



(a) Waveforms



(b) Spectra

Fig. 4.21. FW induced voltage ratios of the 12-stator-slot HESFMs having 10-, 11-, 13-, and 14-rotor-pole under three-phase armature currents excitation only at 400rpm.

As shown in Figs. 4.18 to 4.21, the stator slot and rotor pole number combinations significantly influence the harmonic orders of the FW flux-linkages and induced voltages caused by the three-phase armature currents. In order to further explain the difference in harmonic contents, the FC induced voltage ratios of the HESFMs having different stator slot and rotor pole numbers under three-phase armature currents excitation only are provided in Figs. 4.22 and 4.23.

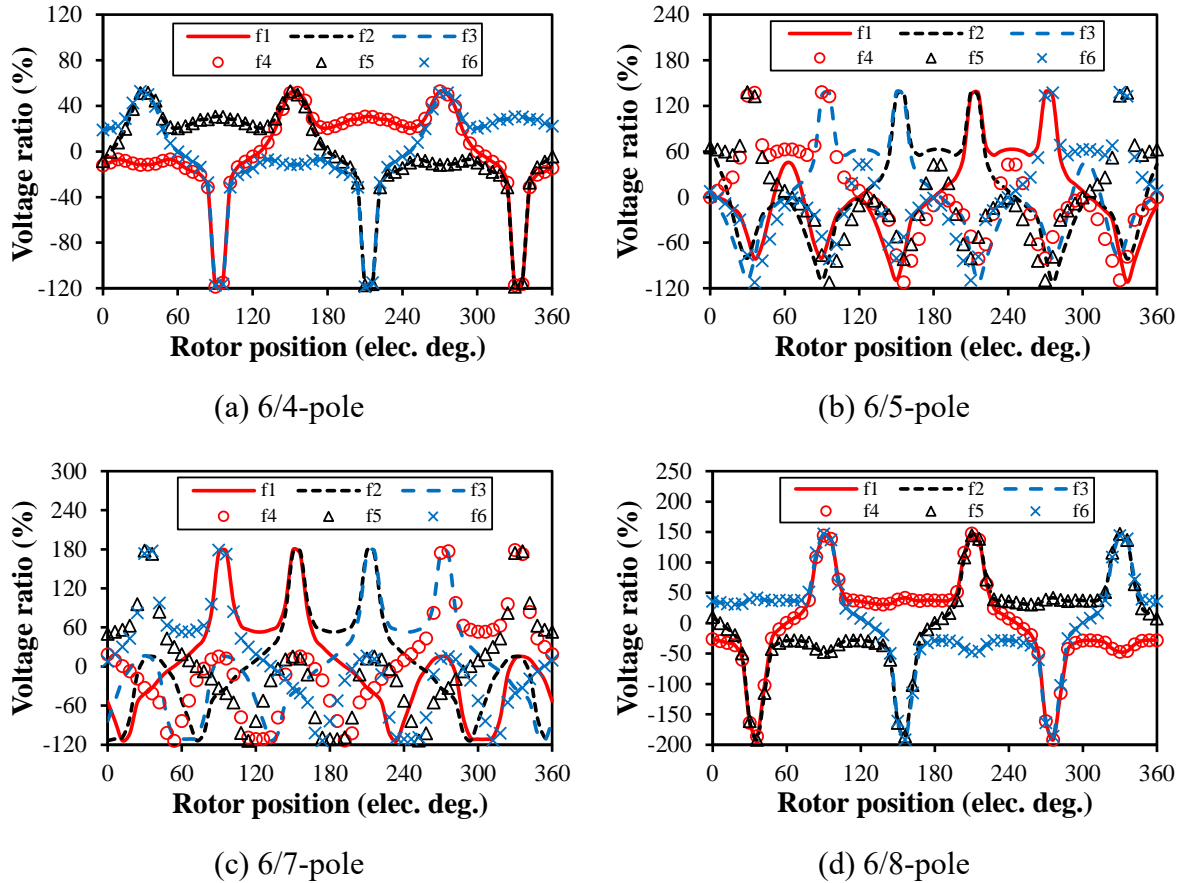


Fig. 4.22. FC induced voltage ratios of the 6-stator-slot HESFMs having 4-, 5-, 7-, and 8-rotor-pole under three-phase armature currents excitation only at 400rpm.

For the 6-slot HESFMs having 4-, 5-, 7-, and 8-pole, the relationships between different FC flux-linkages and induced voltages under armature currents excitation only are similar to those at no-load. In other words, for the 6-slot HESFM counterparts, the waveforms and spectra of different FC flux-linkages and induced voltages are the same under no-load and armature currents excitation only, respectively, in a specific machine. In addition, the phase differences between two adjacent FC induced voltages are also the same as those of the no-load, i.e., 120° , 60° , 60° , and 120° for the 6/4-, 6/5-, 6/7-, and 6/8-pole machines, respectively, as shown in Fig. 4.22. Therefore, the harmonic orders of the FW flux-linkages and induced voltages caused by three-phase armature currents are $3k$, $6k$, $6k$, and $3k$ for the 6/4-, 6/5-, 6/7-, and 6/8-pole machines, respectively, as shown in Figs. 4.18 and 4.20.

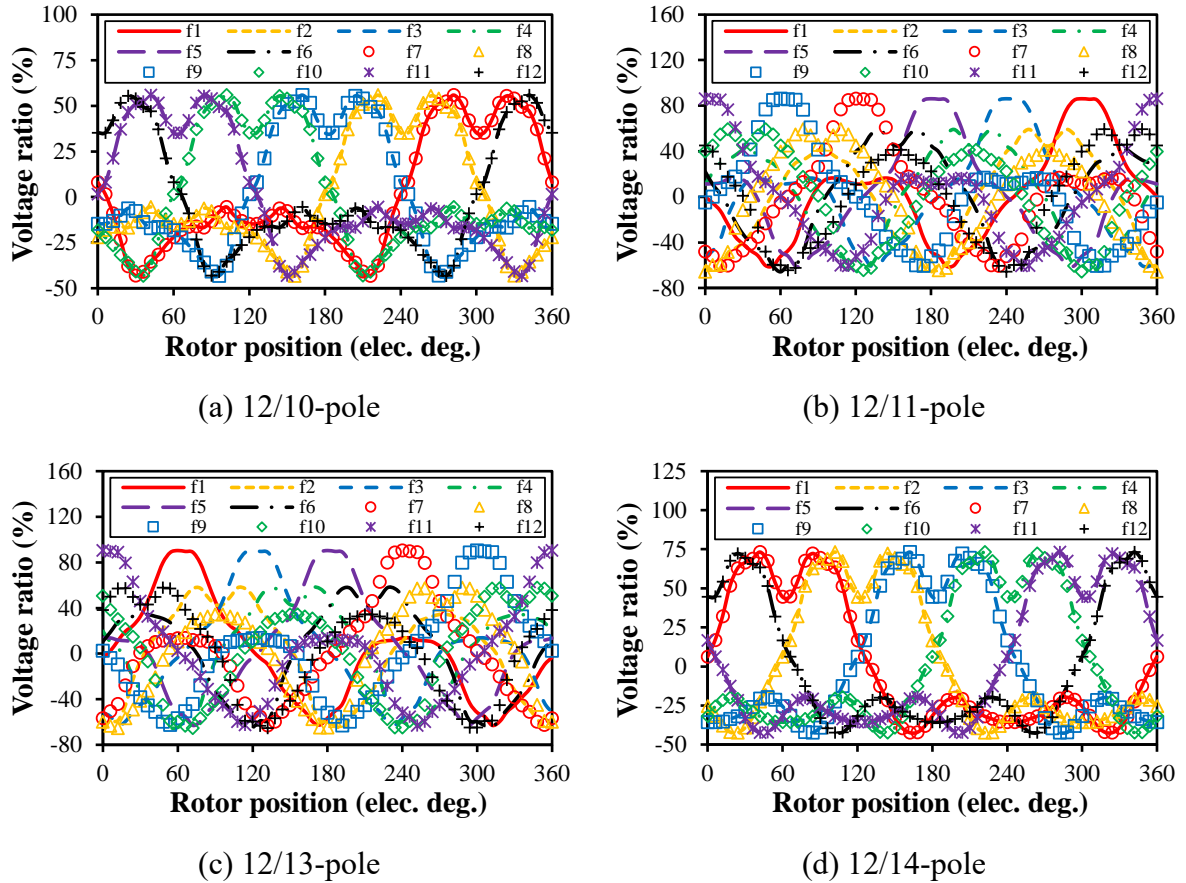


Fig. 4.23. FC induced voltage ratios of the 12-stator-slot HESFMs having 10-, 11-, 13-, and 14-rotor-pole under three-phase armature currents excitation only at 400rpm.

As for the 12-slot HESFM counterparts, the waveforms and spectra of different FC induced voltages are the same for the 12/10- and 12/14-pole machines as shown in Figs. 4.23(a) and 4.23(d). Moreover, the phase angles between two adjacent FC induced voltages are the same as those at no-load, i.e., 60° for the 12/10- and 12/14-pole machines. Consequently, the armature current induced voltage harmonics of the 12/10- and 12/14-pole machines are $6k$, which are the same as the no-load FW induced voltage harmonics. While for the 12/11- and 12/13-pole machines, the FC induced voltages caused by armature currents are distorted as shown in Figs. 4.23(b) and 4.23(c). This means that the waveforms and harmonic spectra of two adjacent FCs are not the same. In the 12/11- and 12/13-pole machines, the induced voltage waveforms of FCs f_1, f_3, f_5, f_7, f_9 , and f_{11} are the same other than the 60° phase difference between two adjacent FCs, whilst the FCs $f_2, f_4, f_6, f_8, f_{10}$, and f_{12} have the same induced voltage waveform and the phase difference is 60° as well. Consequently, the armature current induced voltage

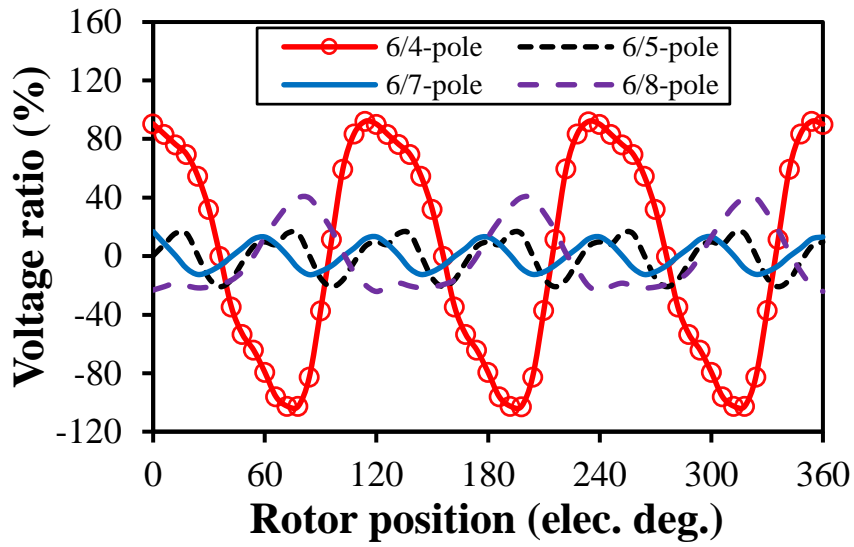
harmonic orders of the 12/11- and 12/13-pole machines are $6k$, which are different from their corresponding no-load induced voltage harmonic orders, i.e., $12k$, as the harmonic orders of $6k$ cannot be cancelled anymore. The characteristics of the armature current induced FW voltage ripple are summarized in Table 4.3.

Table 4.3 Properties of Armature Current Induced Field Winding Voltage Ripple

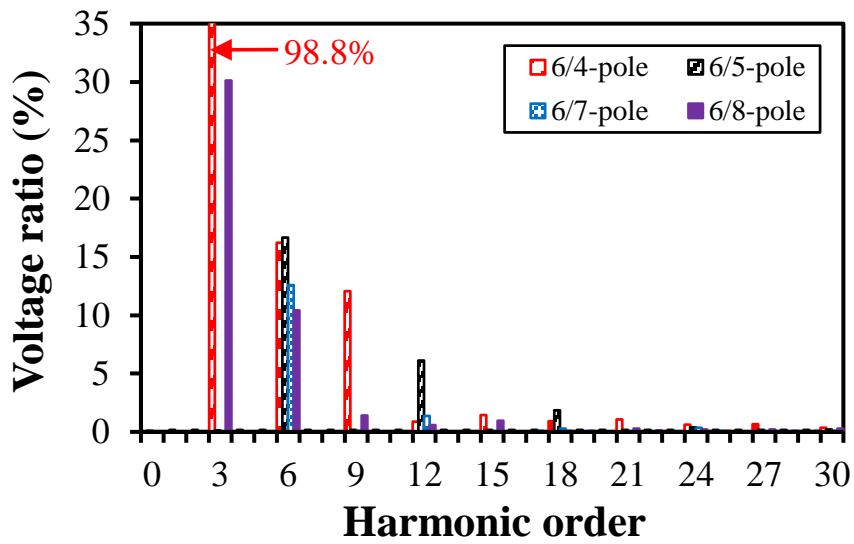
N_s/N_r	6/4	6/5	6/7	6/8	12/10	12/11	12/13	12/14
HO	$3k$	$6k$	$6k$	$3k$	$6k$	$6k$	$6k$	$6k$
V_{FW_PP} (V)	13.5	5.2	10.9	26.3	2.4	10.3	11.2	2.7
IVR_{FW_PP} (%)	595	230	482	1161	52	227	247	60

4.3.3 On-Load Induced Voltage

On-load induced FW voltage ripple contains the no-load induced voltage component and the armature current induced voltage component at the same time. Consequently, the on-load FW induced voltage harmonics essentially depend on the FW induced voltage harmonics caused by the no-load and the armature currents. As discussed above, the no-load FW flux-linkage and induced voltage harmonic orders of the 6-slot HESFMs having 4-, 5-, 7-, and 8-pole are $3k$, $6k$, $6k$, and $3k$, respectively. While for the 12-slot HESFMs having 10-, 11-, 13-, and 14-pole, the no-load FW flux-linkage and induced voltage harmonic orders are $6k$, $12k$, $12k$, and $6k$, respectively. The armature current induced FW voltage harmonic orders of the 6-slot HESFMs having 4-, 5-, 7-, and 8-pole are the same as those of the no-load, i.e., $3k$, $6k$, $6k$, and $3k$, respectively. While for the 12-slot HESFMs having 10-, 11-, 13-, and 14-pole, the armature current induced FW voltage harmonic orders are all the same, i.e., $6k$. Therefore, under on-load condition, the FW induced voltage harmonic orders are $3k$, $6k$, $6k$, and $3k$, for the 6/4-, 6/5-, 6/7-, and 6/8-pole HESFMs, respectively, as shown in Fig. 4.24. While for the 12/10-, 12/11-, 12/13-, and 12/14-pole HESFMs, the on-load FW induced voltage harmonic orders are $6k$, as shown in Fig. 4.25.

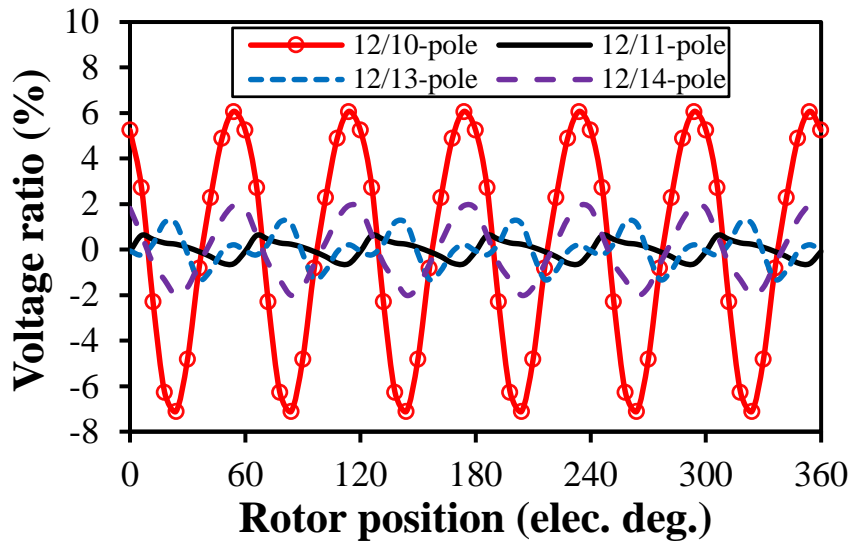


(a) Waveforms

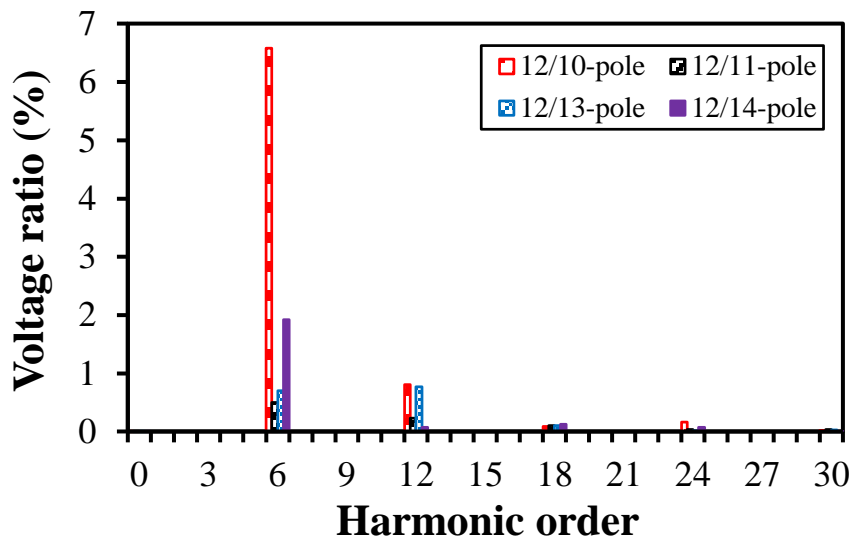


(b) Spectra

Fig. 4.24. On-load FW induced voltage ratios of the 6-stator-slot HESFMs having 4-, 5-, 7-, and 8-rotor-pole at 400rpm.



(a) Waveforms



(b) Spectra

Fig. 4.25. On-load FW induced voltage ratios of the 12-stator-slot HESFMs having 10-, 11-, 13-, and 14-rotor-pole at 400rpm.

Table 4.4 Properties of On-Load Induced Field Winding Voltage Ripple

N_s/N_r	6/4	6/5	6/7	6/8	12/10	12/11	12/13	12/14
HO	3k	6k	6k	3k	6k	6k	6k	6k
V_{FW_PP} (V)	4.42	0.82	0.67	1.46	0.68	0.09	0.16	0.22
IVR_{FW_PP} (%)	195	36.3	29.4	64.2	14.9	1.9	3.5	4.9

The on-load FC induced voltages for the HESFMs with different slot/pole number combinations are not shown to avoid duplication. However, it should be mentioned that the relationships between different on-load FC induced voltages for the 6/4-, 6/5-, 6/7-, 6/8-, 12/10-, and 12/14-pole HESFMs are the same as those of their corresponding no-load conditions. While for the 12/11- and 12/13-pole HESFMs, the relationships between different FC induced voltages at on-load are different from those at no-load, but are the same as those under armature currents excitation only, owing to the distortion caused by armature currents as shown in Figs. 4.23(b) and 4.23(c).

Fig. 4.26 shows the on-load induced field winding voltage ratios of the 6-slot/4-pole machine under different loading levels, i.e., 25%, 50%, 75%, 100%, and 125% of the full load (FL) condition. It can be found that the on-load induced voltage ripple is influenced by the loading level. When the loading level changes, the permeability of the steel lamination varies. Therefore, both the no-load induced voltage component and the armature current induced voltage component are influenced by the loading level and thus the on-load induced voltage ripple.

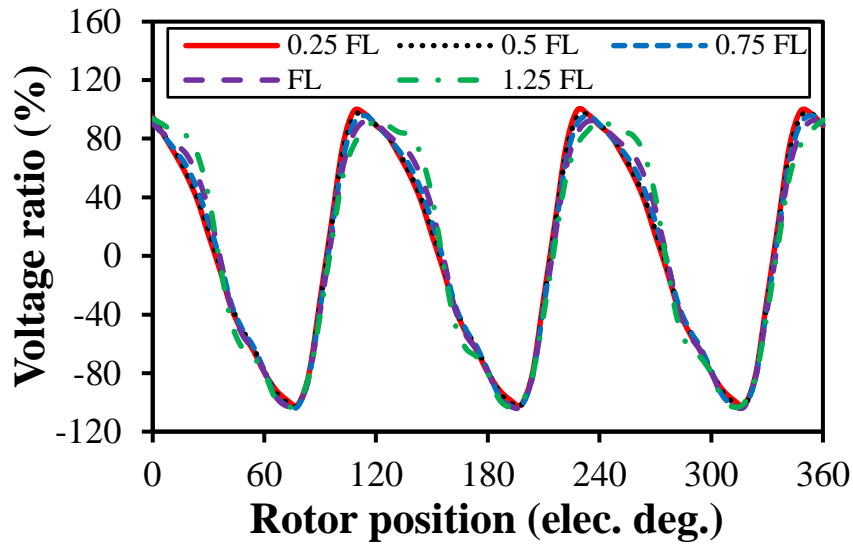


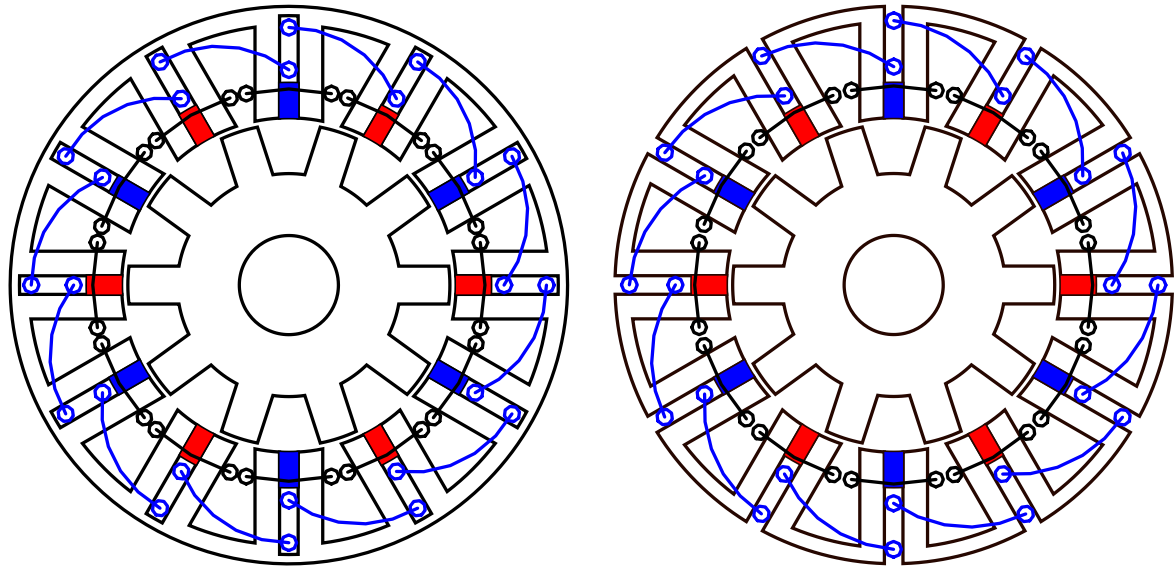
Fig. 4.26. On-load FW induced voltage ratios of the 6-slot/4-pole HESFM under different loading levels at 400rpm.

It is worth noting that the value of the on-load FW induced voltage ripple is not always higher than that of the no-load. Although the on-load FW induced voltage contains two components, i.e., the no-load induced voltage component and the armature current induced voltage component, the values of these two components are very sensitive to magnetic saturation. Table 4.4 lists the properties of the on-load FW induced voltage ripple. Moreover, based on the previous analyses, it can also be found that the HESFMs having an odd number of rotor poles tend to exhibit lower induced voltage ripple in field windings than those having an even number of rotor poles under both no-load and on-load operations, and the reason behind this phenomenon can be explained as follows. In the HESFMs, each field winding consists of the field coils that are connected in series. Therefore, the flux-linkage and induced voltage of each field winding are the sum of the flux-linkage and induced voltage of different field coils, respectively. By way of example, for the 6-stator-slot HESFMs, the no-load induced voltages in different field coils are the same, and the only difference between two adjacent waveforms is the phase differences, which are 120° , 60° , 60° , and 120° for the 6/4, 6/5, 6/7, and 6/8 machines, respectively, as shown in Fig. 4.15. Consequently, the no-load induced voltages in field windings only contain the harmonic orders of $3k$, $6k$, $6k$, and $3k$ for the 6/4, 6/5, 6/7, and

6/8 machines, respectively, as other harmonics are cancelled due to the corresponding phase difference, as shown in Fig. 4.11. The harmonic spectra of the armature current induced voltages in different field coils are the same as well, and the main difference between two adjacent waveforms is still the phase differences, which are 120° , 60° , 60° , and 120° for the 6/4, 6/5, 6/7, and 6/8 machines, respectively, as shown in Fig. 4.22. Similarly, the armature current induced voltages in field windings only contain the harmonic orders of $3k$, $6k$, $6k$, and $3k$ for the 6/4, 6/5, 6/7, and 6/8 machines, respectively, due to the cancellation of others harmonics, as shown in Fig. 4.20. Similar harmonic cancellation phenomena can also be found in the 12-stator-slot HESFM counterparts but with higher harmonic orders, as shown in Figs. 4.16, 4.12, 4.23, and 4.21. Overall, the field winding induced voltages in the HESFMs with an odd number of rotor poles suffer from higher harmonic orders than those in the HESFMs with an even number of rotor poles under both no-load and on-load conditions.

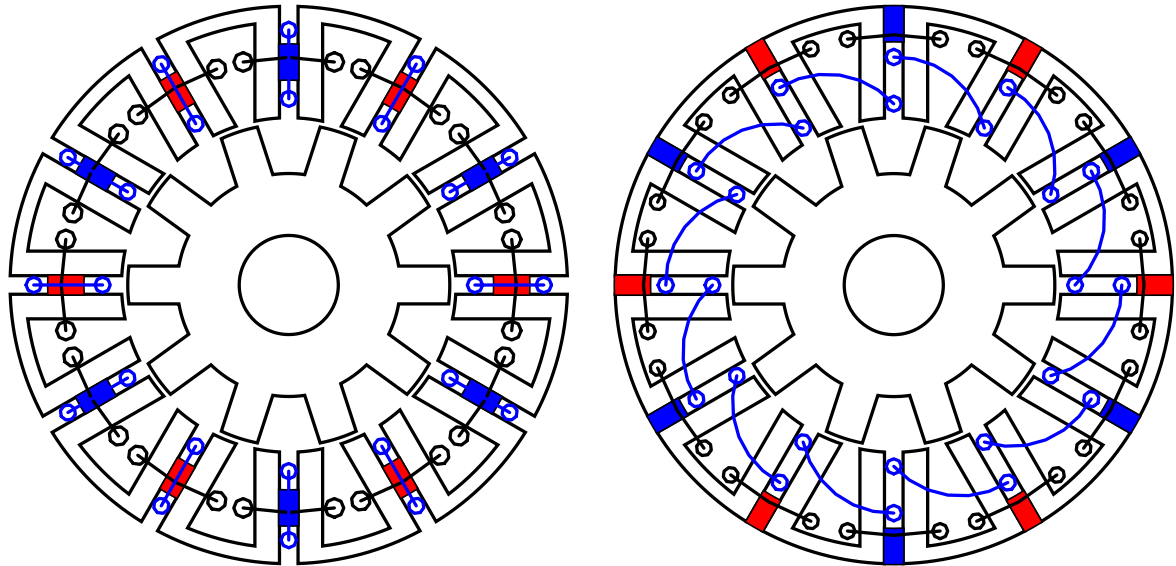
4.3.4 Influence of PM Position

The previous analyses are all based on the HESFM topology shown in Fig. 4.27(a), i.e., PM-bottom with iron bridge. In fact, the position of the PMs is quite flexible and the PMs can be placed in the middle or on top of each slot for the field winding as well. Figs. 4.27(b)-(d) show three variants of the PM-bottom HESFM with iron bridge, i.e., PM-bottom HESFM without iron bridge, PM-middle HESFM, and PM-top HESFM, respectively.



(a) PM-bottom with iron bridge

(b) PM-bottom without iron bridge



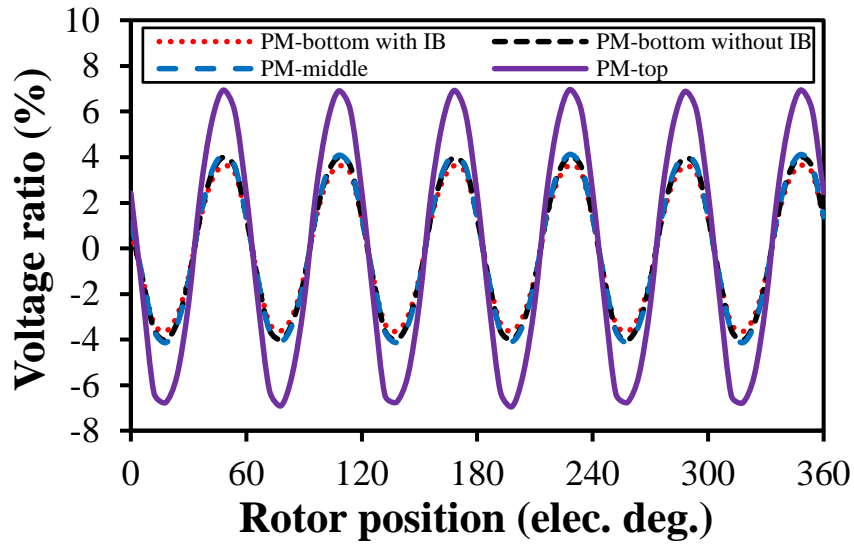
(c) PM-middle

(d) PM-top

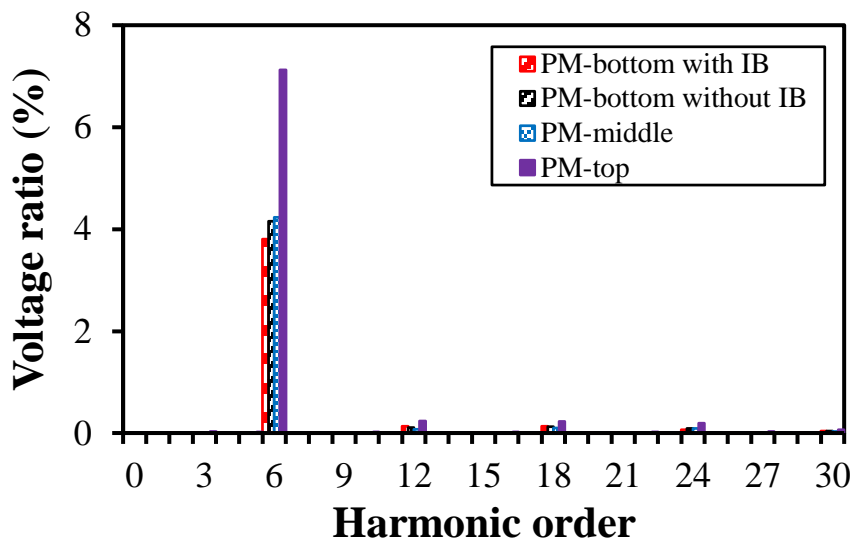
Fig. 4.27. 12-slot/10-pole HESFMs with different PM positions.

The no-load and on-load field winding induced voltage ratios of the 12-slot/10-pole HESFMs with different PM positions are shown in Fig. 4.28 and Fig. 4.29, respectively. It reveals that the PM-top machine exhibits a relatively higher field winding induced voltage ratio than other HESFMs under both no-load and on-load conditions, owing to the high amplitude of the 6th harmonic. More importantly, the position of the PMs and the adoption of the iron bridge (IB) do not influence the harmonic orders of the field winding induced voltage ratios, which is

6k for both the 12/10 PM-bottom machine and its corresponding variants under both no-load and on-load conditions. Essentially, these HESFMs share similar operating principles and machine topologies, and the main difference lies in the position of the PMs [HUA15]. Therefore, the studies and conclusions of the PM-bottom HESFM in this chapter can be equally applied to its variants shown in Figs. 4.27(b)-(d).

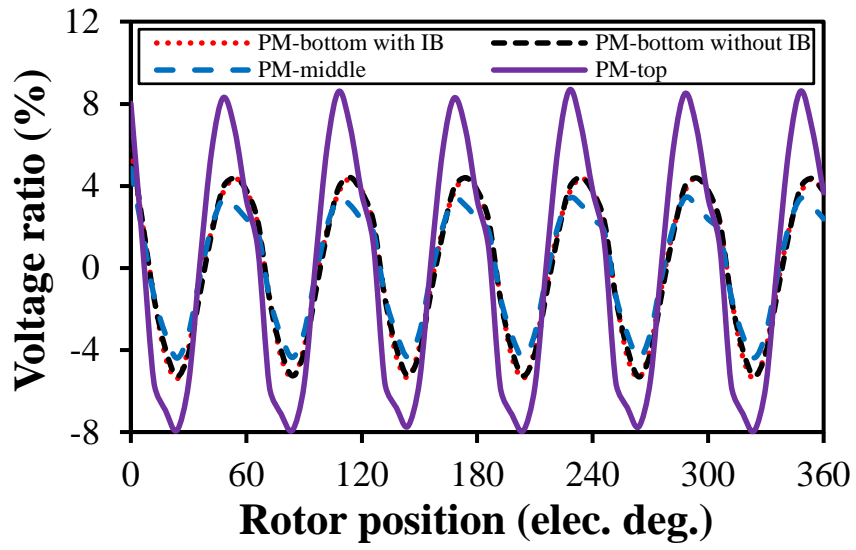


(a) Waveforms

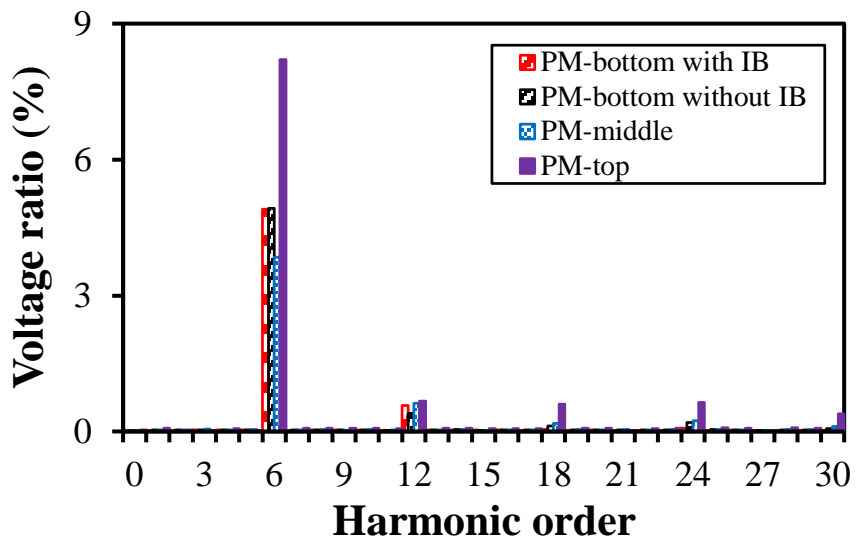


(b) Spectra

Fig. 4.28. No-load FW induced voltage ratios of the 12-slot/10-pole HESFMs with different PM positions at 400rpm.



(a) Waveforms



(b) Spectra

Fig. 4.29. On-load FW induced voltage ratios of the 12-slot/10-pole HESFMs with different PM positions at 400rpm.

4.3.5 Influence of Field Winding Induced Voltage Ripple

In the previous analyses, the field current is considered as constant, e.g., the red line with markers shown in Fig. 4.30. Due to the influence of the induced voltage ripple, the field current suffers from the current ripple, as the black line with markers shown in Fig. 4.30. By applying the field currents shown in Fig. 4.30, the on-load torque waveforms are calculated and presented in Fig. 4.31. Due to the unstable field current, the torque ripple increases by 86.6% from 21.5% to 40.1%, whilst the average torque decreases by 2.4% from 0.88Nm to 0.86Nm. This is due to the fact that the unstable field current can introduce additional back-EMF harmonics and hence significantly change the back-EMF waveform. Apart from the torque and speed oscillations, the field winding induced voltage also brings challenges to the power supply and control system as discussed as follows.

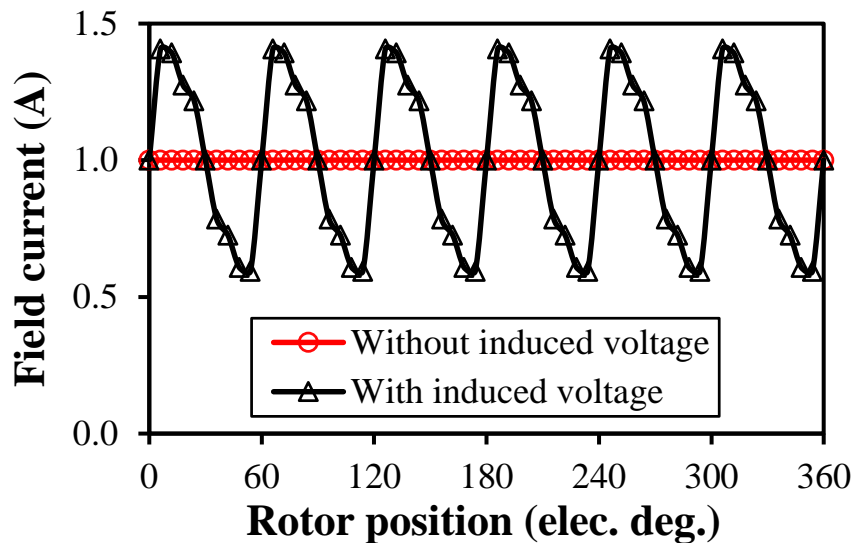


Fig. 4.30. Influence of on-load field winding induced voltage on field current of the 6-slot/5-pole PM-bottom HESFM with iron bridge.

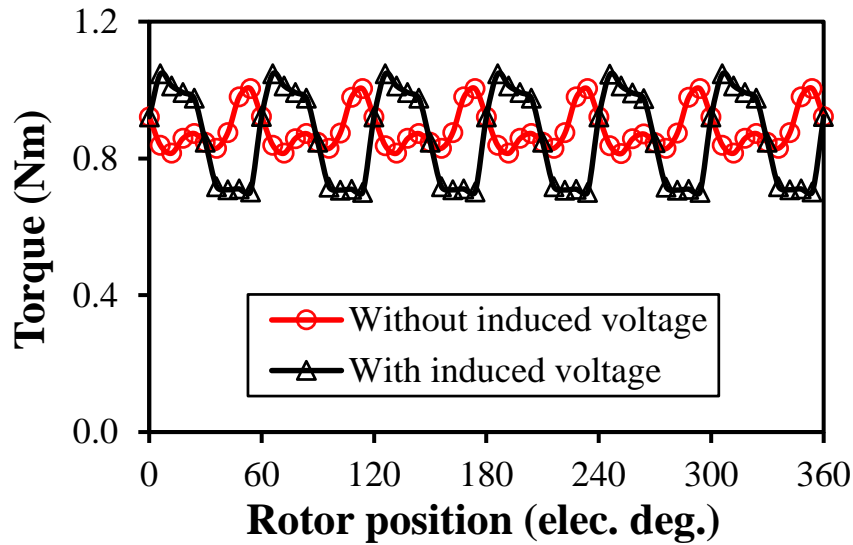


Fig. 4.31. Influence of on-load field winding induced voltage on torque of the 6-slot/5-pole PM-bottom HESFM with iron bridge.

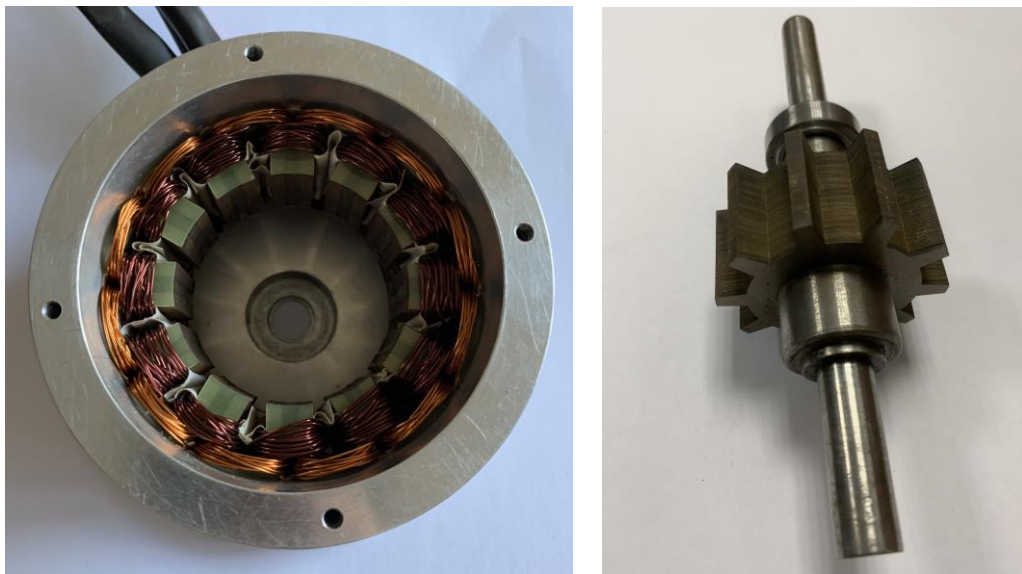
In HEMs, the DC field winding can be either excited by a constant current power supply or H-bridge converters. When the field winding is excited by a constant current power supply, the influence of induced voltage ripple mainly lies in three aspects. Firstly, the compliance voltage of the constant current power supply may be smaller than the required voltage at some rotor positions due to the existence of the field winding induced voltage ripple. Therefore, the actual current in the field winding will be reduced at some rotor positions, which leads to reduced torque and power density, especially at a higher speed. Secondly, a reverse input current may challenge the current power supply if the induced voltage ripple is higher than the compliance voltage over the whole range of rotor positions at a higher speed. Thirdly, the current power supply may also suffer from the challenge of a reverse voltage at higher speed owing to the negative value of the induced voltage ripple, which may lead to the activation of reverse voltage protection mechanism of the current power supply.

When the field winding is excited by a half or full H-bridge converter, the influence of the induced voltage ripple is as follows. In order to obtain a steady DC current in the field winding, the induced voltage ripple needs to be added into the control diagram as a disturbing voltage when applying closed-loop current control, which further complicates the control system. In order to balance the induced voltage, the DC bus voltage of the converter should be much higher, especially at a higher speed. This means that the operation speed of the machine is constrained if the DC bus voltage is of a certain value, owing to the existence of the induced voltage. In order to balance the negative value of the induced voltage at a higher speed, only a full H-bridge converter can be implemented, since the half H-bridge converter cannot provide a reverse output voltage. Consequently, the induced voltage ripple in field windings significantly influences the control system and operating characteristics of the HEMs and it also increases the KVA ratings and thus the cost of the converter feeding it, especially at a higher speed.

4.4 Experimental Validation

4.4.1 Prototype and Test Rig

In order to validate the FEA predictions in previous sections, an existing prototype PM-bottom HESFM having 12-stator-slots, 10-rotor-poles, and iron bridges is employed as shown in Fig. 4.32. The basic design parameters of the prototype HESFM are listed in Table 4.5. The test rig illustrated in Fig. 4.33 is adopted for the experimental validation. It should be noted that the aim of this section is to validate the phenomenon of the no-load and on-load FW induced voltage ripples and the accuracy of FEA predictions. Therefore, the number of turns per FC is reduced to 10 in the prototype machine to reduce the difficulty of the winding process while the number of turns per phase of AW is kept the same as the FEA analysis in previous sections.



(a) Stator

(b) Rotor

Fig. 4.32. Prototype of the PM-bottom HESFM with iron bridge.

Table 4.5 Basic Design Parameters of Prototype HESFM

Parameters	Value	Parameters	Value
Stator pole number, N_s	12	Rotor pole number, N_r	10
Outer stator radius, R_{so}	45mm	Stack length, l_s	25mm
Air-gap length, g	0.5mm	Iron bridge length, l_{ib}	1mm
Rotor shaft radius, R_{ri}	6mm	Stator yoke radius, R_{sy}	41.5mm
Stator inner radius, R_{si}	27mm	PM volume	7950mm ³
PM remanence	1.2T	PM relative permeability	1.05
PM width, w_{PM}	3.5mm	PM length, h_{PM}	7.5mm
Arc of stator tooth, θ_{st}	7.5°	Rotor outer radius, R_{ro}	26.5mm
Rotor yoke radius, R_{ry}	20mm	Rotor tooth arc, θ_{rt}	8.2°
Turns per phase of AW	72	Turns per FC	10

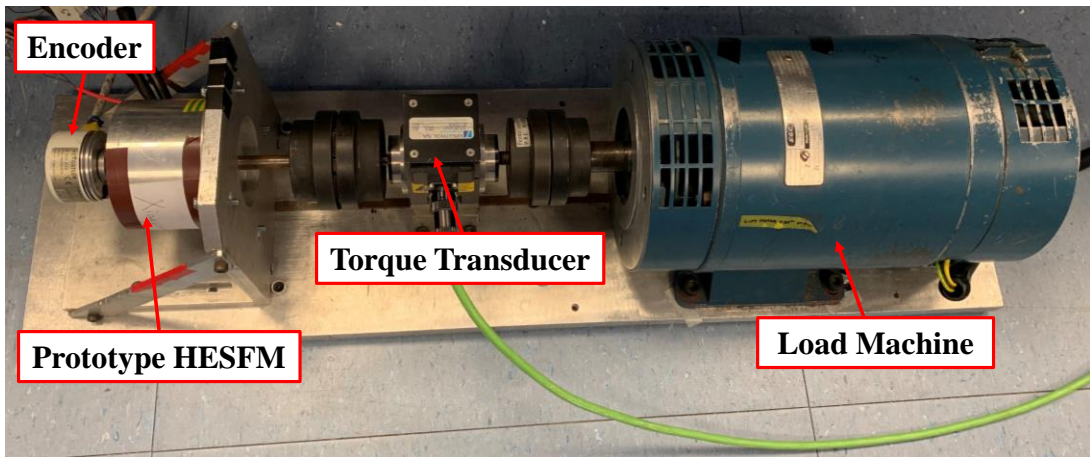
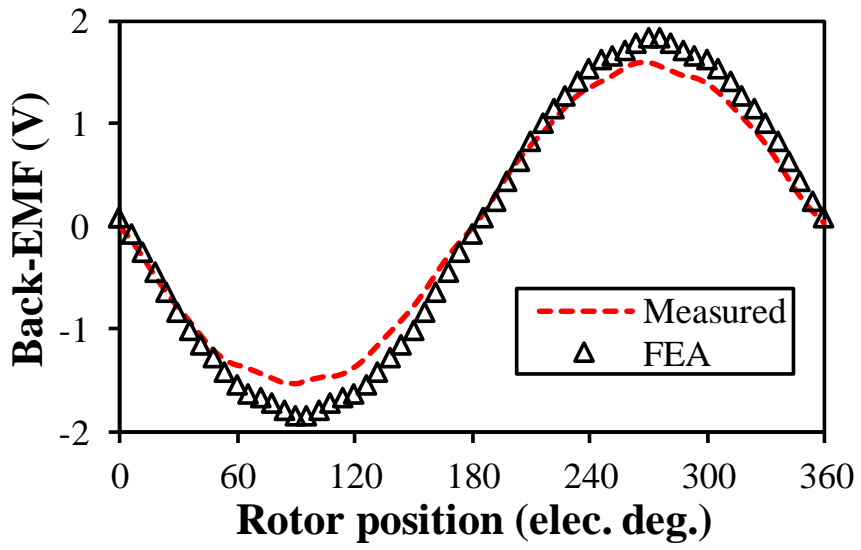


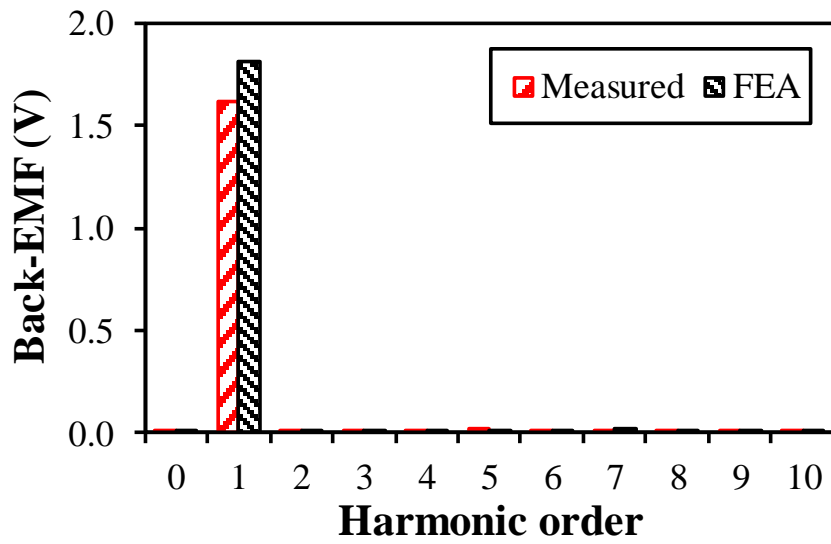
Fig. 4.33. Test rig for the prototype HESFM.

4.4.2 Back-EMF

The no-load phase back-EMF is tested and presented in Fig. 4.34 together with the 2D FEA calculated one at 400rpm, in which the prototype is only excited by PMs. The stack length of the prototype is 25mm, which is relatively short. Therefore, the end effect in the prototype is severe and the flux leakage in the end region will contribute to a large part of the total flux leakage, which results in a much lower measured phase back-EMF compared with the 2D FEA calculated one as shown in Fig. 4.34, since the end region effect is not considered in the 2D FEA calculations. The amplitudes of the no-load fundamental phase back-EMF under different FW excitation currents are tested and calculated by the 2D FEA, as shown in Fig. 4.35. It can be observed that the amplitude of the no-load fundamental phase back-EMF can be flexibly adjusted in a wide range by changing the amplitude and polarity of the FW current. Similarly, the measured phase fundamental back-EMFs are much lower than the 2D FEA predictions under different FW currents, owing to severe end region effect as aforementioned.



(a) Waveforms



(b) Spectra

Fig. 4.34. No-load phase back-EMFs without FW current at 400rpm.

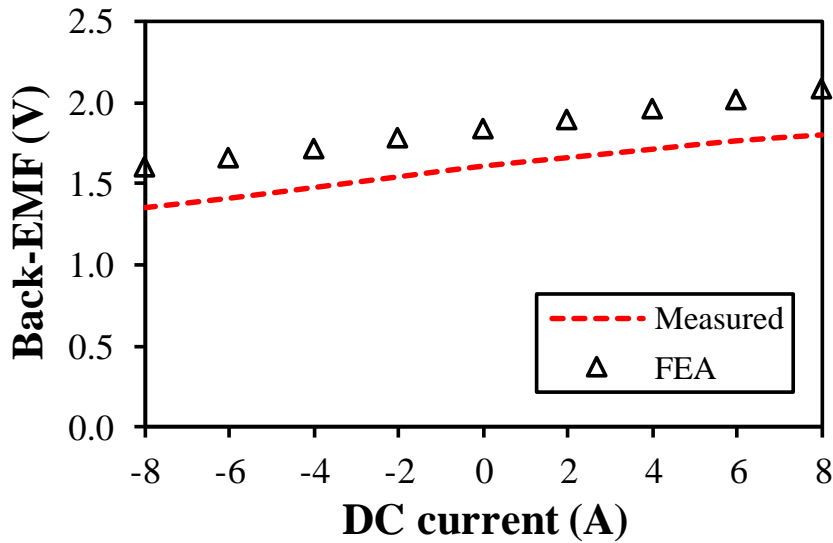
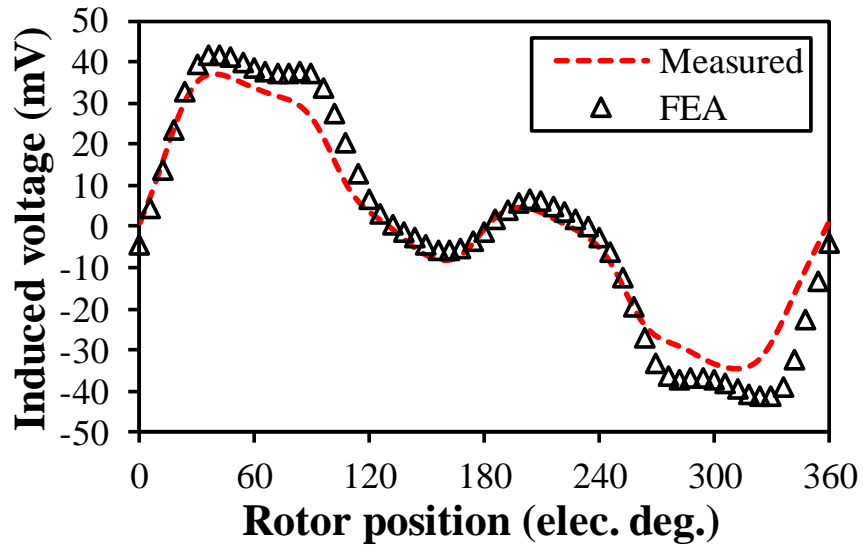


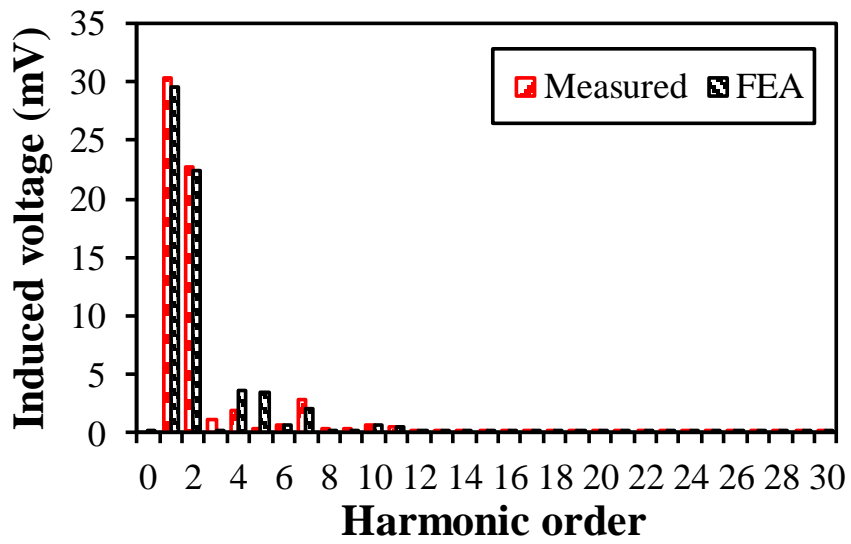
Fig. 4.35. Amplitudes of no-load fundamental phase back-EMF with varying FW currents at 400rpm.

4.4.3 No-Load Induced Voltage

As labelled in Fig. 4.1(a), there are 12 FCs in the 12-slot/10-pole prototype machine and the FW is formed by connecting 12 FCs in series. When the FW is injected with DC current (I_{dc}), the induced voltage in the FW cannot be accurately measured. In order to solve this problem, the FCs f_1, f_3, f_5, f_7, f_9 , and f_{11} are connected in series to form a new FW, while the FCs $f_2, f_4, f_6, f_8, f_{10}$, and f_{12} are left as open-circuits. The no-load and on-load induced voltages of the FC f_2 are measured instead, as it is open-circuited and free from DC current. Fig. 4.36 shows the measured and 2D FEA predicted no-load induced voltage waveforms and harmonic spectra of the FC f_2 , and there is a satisfying agreement between the measured and the 2D FEA simulated results apart from the slight difference that results from the end region effect, manufacturing and measuring tolerances. It is worth mentioning that the new FW (with 6 FCs) is injected with positive 4A I_{dc} at no-load induced voltage test, which is equivalent to applying positive 2A I_{dc} to the original FW (with 12 FCs), as the number of FCs is halved in the new FW and hence the new FW's current needs to be doubled to generate the same magneto-motive force (MMF) as the original FW.



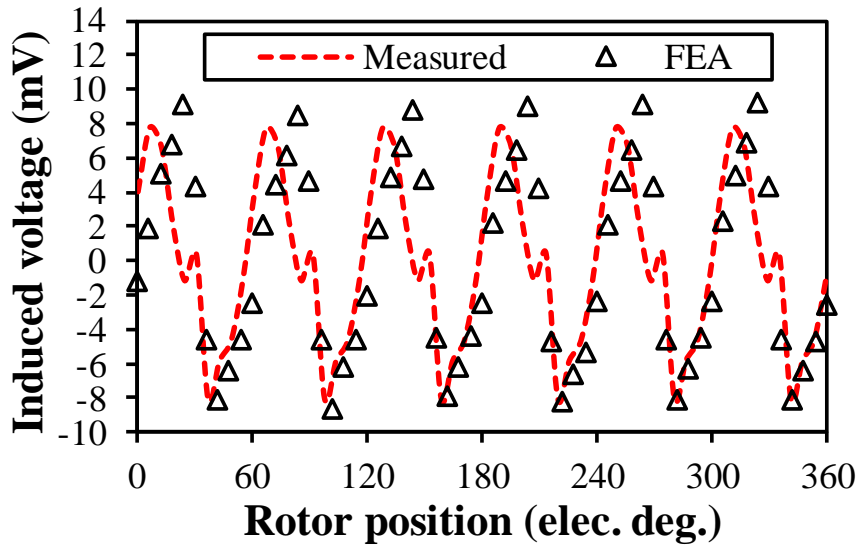
(a) Waveforms



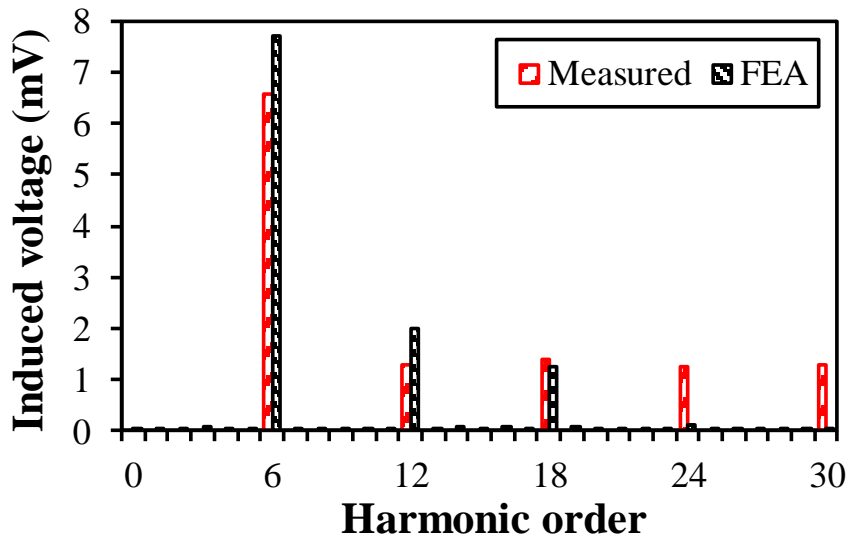
(b) Spectra

Fig. 4.36. No-load field coil f_2 induced voltage at 400rpm ($I_{dc}=4A$).

As aforementioned, the induced voltage in the field winding cannot be directly measured due to the influence of the field winding current. In order to obtain the measured no-load induced field winding voltage, the no-load induced voltages of other field coils are firstly obtained by shifting the measured no-load induced voltage waveform of field coil f_2 shown in Fig. 4.36(a) according to the waveforms illustrated in Fig. 4.16(a). Then, the measured no-load induced field winding voltage can be obtained by adding these waveforms together. As shown in Fig. 4.37, the measured and 2D FEA calculated no-load field winding induced voltages only contain the high order harmonics of $6k$, which verifies the foregoing analyses. It can be found that the low order field coil induced voltage harmonics with high amplitude, e.g., 1st, 2nd..., shown in Fig. 4.36 vanish in the field winding induced voltages shown in Fig. 4.37, due to the harmonic compensation phenomenon illustrated in section 4.3.1. In the prototype machine, the amplitude of high order harmonics, i.e., $6k$, is relatively low and the accuracy of measurement to these harmonics is very sensitive to end region effect, manufacturing, and measuring tolerances. Therefore, there is a relatively large error between the measured and 2D FEA predicted waveforms shown in Fig. 4.37.



(a) Waveforms



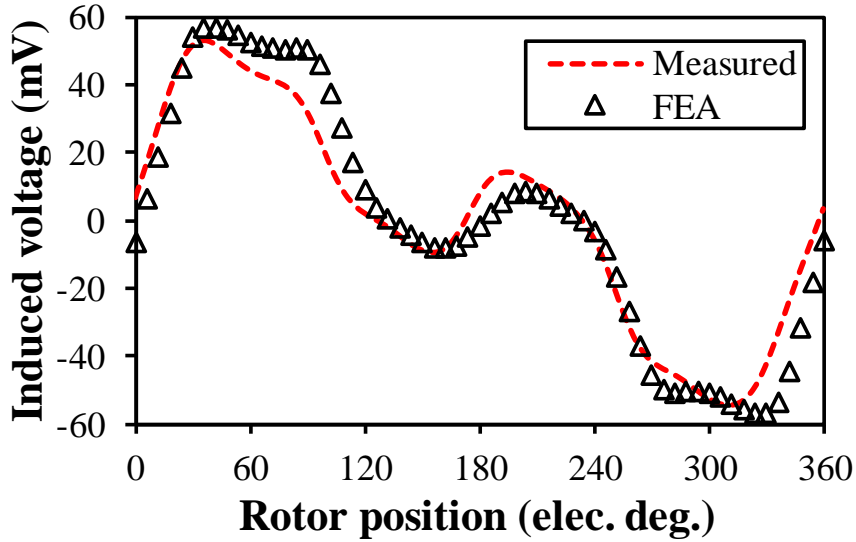
(b) Spectra

Fig. 4.37. No-load field winding induced voltage at 400rpm ($I_{dc}=4A$).

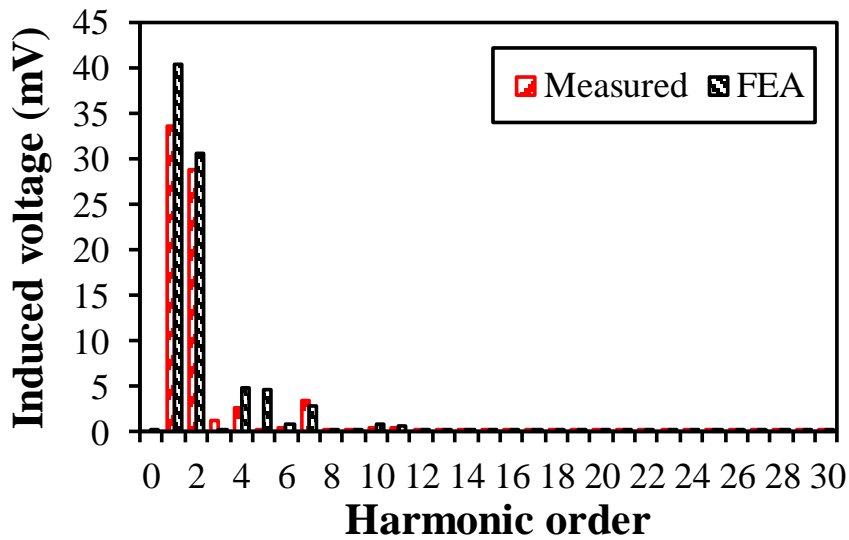
4.4.4 On-Load Induced Voltage

The measured and FEA predicted on-load induced voltages of field coil f_2 are shown in Fig. 4.38, in which good agreement can be found. It is worth mentioning that the on-load induced voltage of field coil f_2 is measured when the machine operates as a motor. Apart from the end region effect, manufacturing and measuring tolerances, the current harmonics in armature winding may also introduce additional on-load induced voltage harmonics in field coil

f_2 , which is another reason for the relatively large errors between the measured and 2D FEA simulated waveforms observed in Figs. 4.38 and 4.39, since the armature winding current harmonics are not considered in the 2D FEA simulations.



(a) Waveforms

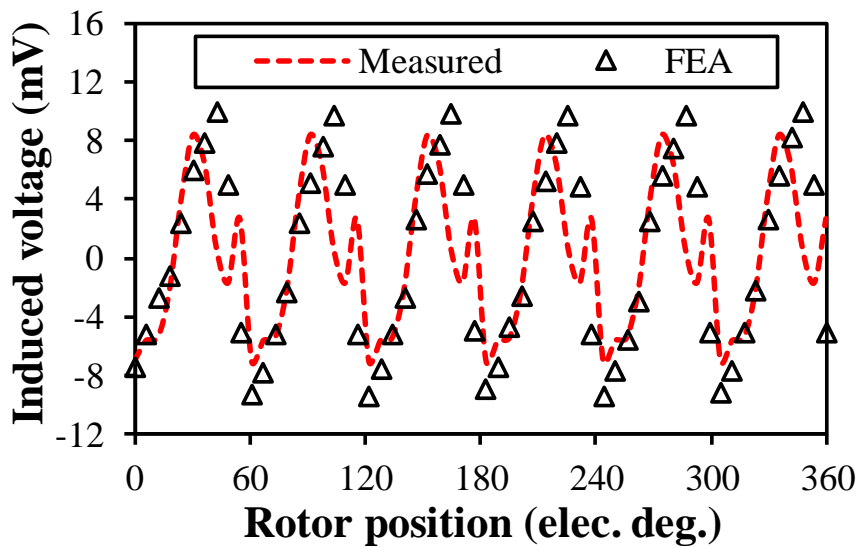


(b) Spectra

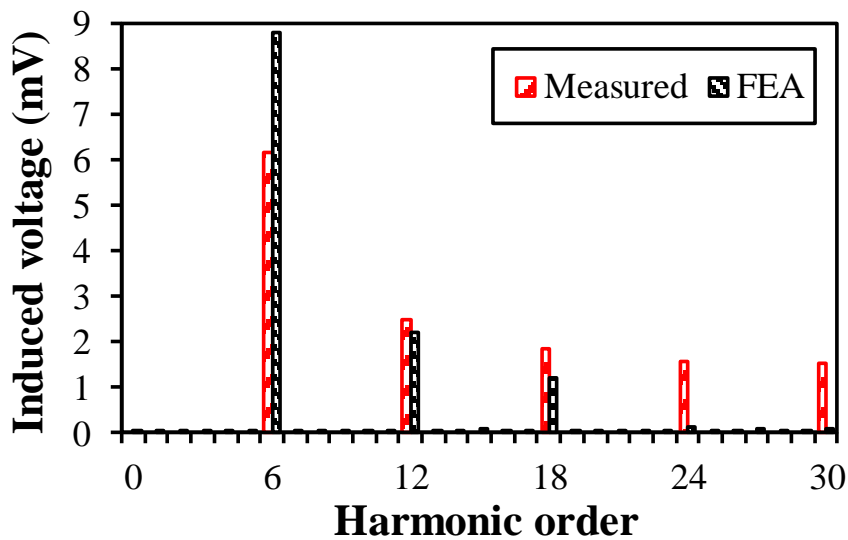
Fig. 4.38. On-load field coil f_2 induced voltage at 400rpm ($I_{dc}=4A$, $I_d=0A$, $I_q=4A$).

Similar to the no-load condition, the measured on-load field winding induced voltage shown in Fig. 4.39(a) is obtained by shifting the measured on-load induced voltage of field coil f_2 shown in Fig. 4.38(a) to obtain other field coils' on-load induced voltage waveforms and then

add them together, as the relationship between different field coils' on-load induced voltages for the 12-slot/10-pole machine is the same as that of the no-load condition shown in Fig. 4.16(a). Therefore, only the harmonic orders of $6k$ exist in the on-load field winding induced voltage, as shown in Fig. 4.39. In fact, other open-circuited field coils, i.e., f_4, f_6, f_8, f_{10} , and f_{12} can be used for the test at no-load and on-load conditions as well, as they are open-circuited and free from DC current.



(a) Waveforms



(b) Spectra

Fig. 4.39. On-load field winding induced voltage at 400rpm ($I_{dc}=4A, I_d=0A, I_q=4A$).

4.5 Conclusion

In this chapter, the influence of stator slot and rotor pole number combination on field winding induced voltage ripple in the PM-bottom HESFM with iron bridge is investigated. The influence of the PM position on the induced voltage ripple in field windings is presented as well. Moreover, the effects of the field winding induced voltage ripple on machine characteristics are also discussed. Based on the analytical derivations and 2D FEA results, it can be found that the harmonic contents and thus the peak-to-peak values of the induced voltage ripple are significantly influenced by the stator slot and rotor pole number combination at both no-load and on-load conditions.

It shows that the HESFMs with high order harmonics in the field winding induced voltage tend to exhibit low peak-to-peak value and thus low effects on machine characteristics. From the perspective of torque production capability, the HESFMs with the stator slot and rotor pole number combination of $N_s/N_r \pm 1$ or $N_s/N_r \pm 2$ are recommended for high torque performance due to high fundamental coil pitch factor. However, from the perspective of diminishing the effects of the field winding induced voltage ripple, it is recommended that the HESFMs with $N_s/N_r \pm 1$ should be employed, since the HESFMs having an odd number of rotor poles tend to exhibit high order induced voltage harmonics in field windings and thus low field winding induced voltages and effects on machine characteristics, as aforementioned. However, the HESFMs with an odd number of rotor poles would suffer from unbalanced magnetic pull, which should also be considered when making selections. Besides, the HESFMs with a high number of rotor poles would suffer from high core loss and PM eddy loss, etc., especially at high speed due to high electrical frequency. In addition, high electrical frequency also leads to high switching loss of the power devices in the control system. Therefore, there is a trade-off between these losses and low field winding induced voltage ripple, which needs to be carefully considered when selecting the stator slot and rotor pole numbers of the HESFM for a specific application.

CHAPTER 5

Analysis and Suppression of DC Winding Induced Voltage in Partitioned Stator Hybrid Excited Switched Flux Machines

This chapter aims to analyze and minimize the DC winding induced voltage in partitioned-stator hybrid-excited switched-flux permanent magnet (PS-HESFPM) machines under both open-circuit and on-load operations. The phenomenon and mechanism of the DC winding induced voltage are illustrated and explained under different conditions. Two techniques are proposed and comparatively analyzed by the finite element analysis (FEA) method to reduce the open-circuit and on-load DC winding induced voltage, i.e., rotor pole arc pairing and unevenly distributed rotor teeth, respectively. At open-circuit, FEA results show that the peak-to-peak value of the DC winding induced voltage can be reduced by 89.89% and 88.73% by using rotor pole arc pairing and unevenly distributed rotor teeth, respectively. At on-load, it shows that by employing rotor pole arc pairing and unevenly distributed rotor teeth, the peak-to-peak value of the DC winding induced voltage can be effectively reduced by 92.81% and 90.57%, whilst the average on-load electromagnetic torque can be maintained at 92.68% and 93.42%. Finally, a prototype 12-slot/11-pole PS-HESFPM machine is tested to verify the FEA analyses.

This chapter is based on the conference papers [SUN19b] [SUN20c] published in EVER 2019 and PEMD 2020.

5.1 Introduction

Permanent magnet (PM) machines have attracted extensive research interest in past few decades due to their high torque density and high efficiency [ZHU07] [CHA08]. Nevertheless, the high cost of PMs and relatively poor flux-weakening capability restrict their applications in some low-cost and variable-speed drive systems. Wound field synchronous machines (WFSMs) are suitable for some low-cost and variable-speed applications thanks to their PM-free structure and controllable air-gap field [CHU14]. Nonetheless, WFSMs have the reduced torque density and efficiency because of the employment of field excitation coils (FECs). Consequently, the hybrid excited (HE) machines having both PMs and FECs are introduced to combine the advantages of high torque density, high efficiency, and excellent flux-control capability.

The HEPM machine topologies are diverse, since the PMs and FECs can be flexibly allocated in stator and/or rotor. Consequently, a multitude of HEPM machine topologies have been investigated [CHE14] [GEN15] [GAU14]. Hybrid-excited switched-flux PM (HESFPM) machines are drawing increasing research interest in recently years, since they exhibit high torque density, sinusoidal back electromotive force (back-EMF) and hence low torque ripple. In addition, the PMs and FECs are both allocated in stator side in HESFPM machines. Consequently, they are beneficial from brushless operation, simple rotor structure and hence easy thermal management.

In [HOA07], a traditional SFPM machine is transformed into a HESFPM machine by adding an additional outermost iron ring to accommodate the concentrated field windings. In addition, a HESFPM with identical lamination to a conventional SFPM machine is proposed in [HUA09], in which the PM volume is reduced to allocate the field windings in the saved place. Furthermore, three HESFPM machine topologies are comparatively investigated in [HUA15], in which the PMs are allocated at the top, middle and bottom of the stator teeth, respectively. Meanwhile, the iron flux bridge can be employed to enhance the flux regulation capability [OWE10]. However, the torque density may be reduced due to partially short-circuited PM flux. In [CHE11], an E-core HESFPM machine is presented, where the field coils are placed in the

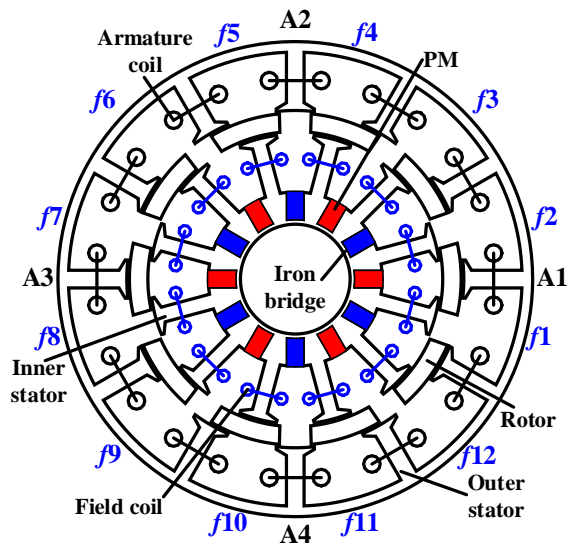
middle teeth of E-core stator. Nevertheless, the flux regulation capability of this machine is limited, since two field coils adjacent to one armature coil can generate fluxes with reversed polarities. The comparison between HESFPM machines with C-core and E-core stator is investigated in [ZHA16]. A partitioned-stator (PS) HESFPM machine is proposed in [HUA17], which exhibits higher torque density and better flux regulation capability than its counterparts due to better inner space utilization. In [WU19] and [WU20], the DC winding induced voltage issue and its reduction methods are investigated based on PS-WFSF machines. PS-HESFPM machines also suffer from DC winding induced voltage issue. However, it has not been reported in literature.

This chapter aims to analyze the DC winding induced voltage issue and its reduction methods in PS-HESFPM machines under both open-circuit and on-load conditions. This chapter is organized as follows. In section 5.2, the machine topology of the PS-HESFPM machine is introduced. Then, in section 5.3, the phenomenon and mechanism of the DC winding induced voltage under both open-circuit and on-load conditions are illustrated. In section 5.4 and section 5.5, two reduction methods, i.e., rotor pole arc pairing and unevenly distributed rotor teeth, are proposed and investigated by the FEA method to reduce the DC winding induced voltage under open-circuit and on-load, respectively. In section 5.6, a prototype 12-slot/11-pole PS-HESFPM machine is tested to verify the FEA predictions, followed by conclusions in section 5.7.

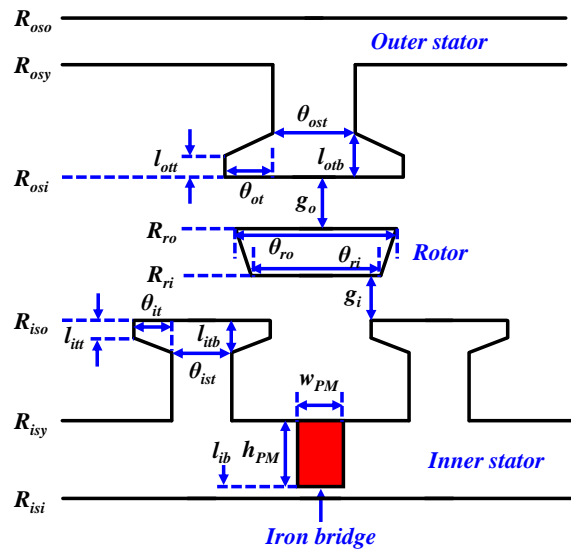
5.2 Machine Topology

The three-phase, 12-stator-slot, and 10-rotor-pole PS-HESFPM machine is shown in Fig. 5.1, which consists of 12-slot outer stator wound by three-phase AC armature windings, 12-slot inner stator wound by DC field winding, a sandwiched 10-pole iron-piece rotor, and 12 pieces PMs, respectively. The AC armature windings and DC field winding are both non-overlapping concentrated windings. The circumferentially magnetized PMs are all inserted in the inner stator yokes. The iron flux bridge is employed to enhance the flux regulation capability. It is worth noting that the outer stator and inner stator have equal stator slot number, whilst the outer stator slots align with the inner stator teeth.

The global optimization of the 12/10 PS-HESFPM machine is carried out for the maximum average electromagnetic torque during one electric period under brushless AC control with zero d -axis current, 20W armature winding copper loss and positive $5\text{A}/\text{mm}^2$ current density in DC field winding slots. It should be mentioned that the packing factor is 0.5 for both AC armature winding and DC field winding slots. The key geometric parameters of the globally optimized machine are listed in Table 5.1, which can be referred to Fig. 5.2. It is worth nothing that the parameters from l_a to l_{ib} are fixed, whilst the rest are globally optimized parameters. In addition, the following analyses are based on the globally optimized PS-HESF machine.



(a) Cross-section



(b) Linear illustration

Fig. 5.1. Topology of the 12-slot/10-pole PS-HESFM [HUA17].

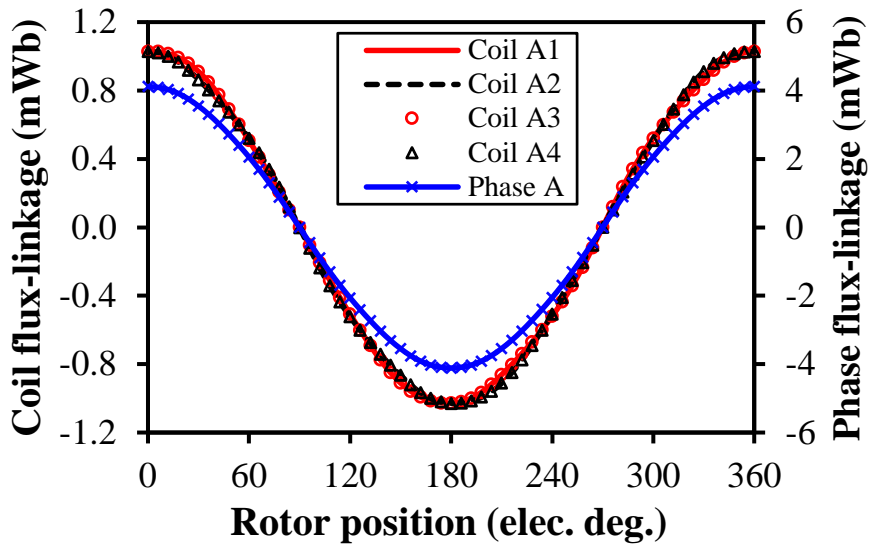
Table 5.1 Key Design Parameters of the PS-HESFPM Machine

Items	Unit	Value	Items	Unit	Value
Stator slot number, N_s	-	12	Outer stator tooth arc, θ_{ost}	deg	6
Rotor pole number, N_r	-	10	Outer stator tooth tip arc, θ_{ot}	deg	3.5
Active axial length, l_a	mm	25	Inner stator outer radius, R_{iso}	mm	27.45
Outer stator outer radius, R_{oso}	mm	45	Inner stator yoke radius, R_{isy}	mm	16.5
Inner stator inner radius, R_{isi}	mm	10.4	Inner stator tooth arc, θ_{ist}	deg	6
Outer air-gap length, g_o	mm	0.5	Inner stator tooth tip arc, θ_{it}	deg	4.5
Inner air-gap length, g_i	mm	0.5	Rotor outer radius, R_{ro}	mm	31.45
Outer stator tip top length, l_{ott}	mm	0.5	Rotor inner radius, R_{ri}	mm	27.95
Outer stator tip bottom length, l_{otb}	mm	1.5	Rotor outer pole arc, θ_{ro}	deg	25
Inner stator tip top length, l_{itt}	mm	0.5	Rotor inner pole arc, θ_{ri}	deg	24
Inner stator tip bottom length, l_{itb}	mm	1.5	Slot packing factor, k_{pf}	-	0.5
PM volume	mm ³	5000	Rated rotor mechanical speed	r/min	400
PM remanence, B_r	T	1.23	Rated DC winding slot current density	A/mm ²	5
PM relative permeability, μ_r	-	1.10	Number of turns per DC coil	-	90
Iron bridge thickness, l_{ib}	mm	0.5	Rated DC winding current	A	1.08
Outer stator yoke radius, R_{osy}	mm	43	Rated AC winding copper loss	W	20
Outer stator inner radius, R_{osi}	mm	31.95	Number of turns per AC coil	-	18
PM thickness, w_{PM}	mm	3	Rated AC winding phase RMS current	A	15.61
PM height, h_{PM}	mm	5.6			

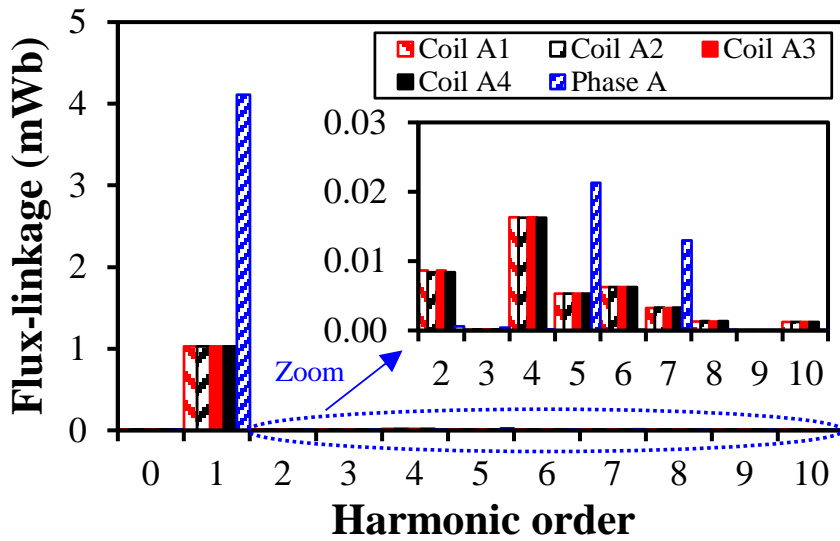
5.3 DC Winding Induced Voltage

5.3.1 Phenomenon

Fig. 5.2 and Fig. 5.3 show the open-circuit armature coil/winding flux-linkages and induced voltages, respectively. It can be found that both the phase flux-linkage and induced voltage waveforms are more sinusoidal. Therefore, BLAC drive is more suitable for this machine to produce steady output torque. Besides, both armature individual coil and armature phase winding suffer from flux-linkage and induced voltage harmonics. Due to the doubly salient structure and flux modulation effect [WU16], the armature coils suffer from both odd and even order harmonics, whereas in phase winding, even order harmonics are cancelled out due to appropriate connection between armature coils, as shown in Figs. 5.2(b) and 5.3(b).

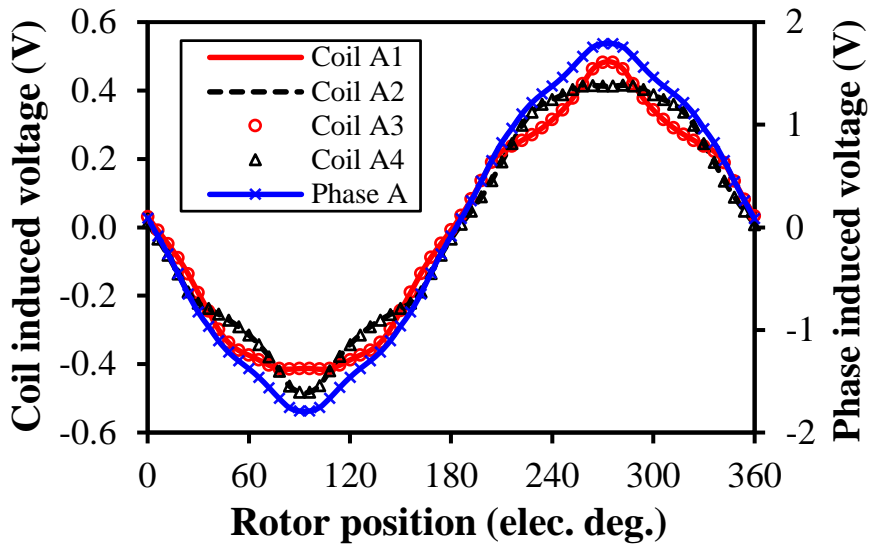


(a) Waveforms

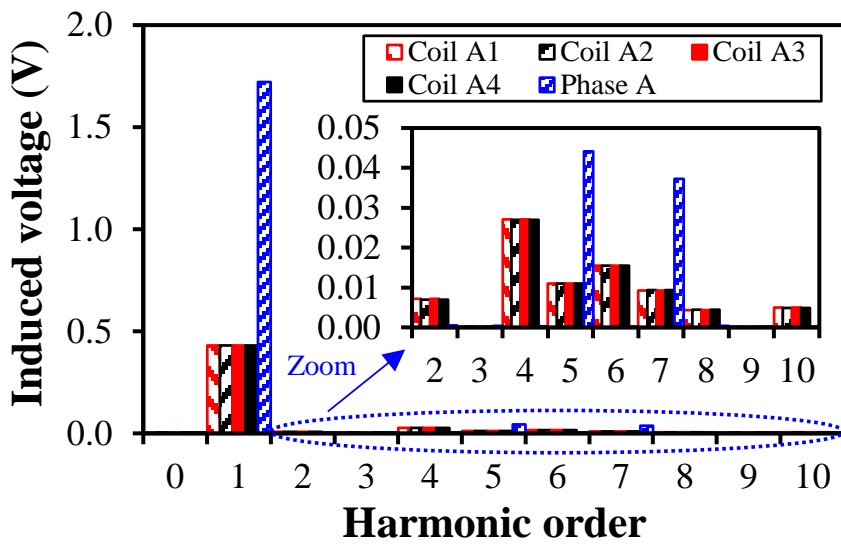


(b) Spectra

Fig. 5.2. Open-circuit armature individual coil/phase winding flux-linkages of the 12-slot/10-pole PS-HESFM.



(a) Waveforms



(b) Spectra

Fig. 5.3. Open-circuit armature individual coil/phase winding induced voltages of the 12-slot/10-pole PS-HESFM.

In the PS-HESF machine, the DC winding current is desirable to be constant from the prospective of closed-loop DC winding current control. Therefore, the DC winding flux-linkage can be considered as constant if the DC winding current is constant. However, this is not the fact in the PS-HESF machine. Similar to the open-circuit phase winding flux-linkage, the flux-linkage of DC winding also suffers from a lot of harmonics, i.e., 6th, 12th, 18th and so on, as shown in Fig. 5.4. Therefore, voltage pulsation will be induced in the DC winding due to the variation of the DC winding flux-linkage according to Faraday's law in equation (5.1), as shown in Fig. 5.5.

It can be found from Fig. 5.5(a) that a fluctuating voltage (red line with markers) is induced in the DC field winding when the rotor rotates at 400rpm mechanical speed under open-circuit condition, in which the DC field winding is supplied by a rated constant current $I_{dc}=1.08\text{A}$. The peak-to-peak value (E_{pp}) of the open-circuit DC winding induced voltage is 0.63V, which is 13.87% of the DC winding resistance voltage drop V_{rf} . Consequently, the DC winding induced voltage ratio (IVR) at open-circuit is 13.87%, which is defined as the ratio of E_{pp} to V_{rf} as shown in (5.2). The DC winding induced voltage ratio is used to reflect the influence of the DC winding induced voltage on the machine performance. A higher IVR indicates a higher effect of the DC winding induced voltage and vice versa.

When the AC armature windings and DC field winding are supplied by three-phase sinusoidal currents ($I_{ac_rms}=15.61\text{A}$) and constant DC current ($I_{dc}=1.08\text{A}$), respectively, a pulsating voltage (black line with markers) is induced in the DC field winding under motoring mode as shown in Fig. 5.5(a). The peak-to-peak value of the on-load DC winding induced voltage is 0.72V when the rotor rotates at 400rpm and the IVR at on-load is 15.82%, which is 14.09% higher than that under open-circuit condition ($E_{pp}=0.63\text{V}$). This is due to the influence of the armature current induced DC winding voltage, which will be discussed in detail later.

$$E_f = \frac{d(\psi_f)}{d(t)} = \frac{d(\psi_f)}{d(\theta_e)} \times \frac{d(\theta_e)}{d(t)} = \Omega_e \times \frac{d(\psi_f)}{d(\theta_e)} \quad (5.1)$$

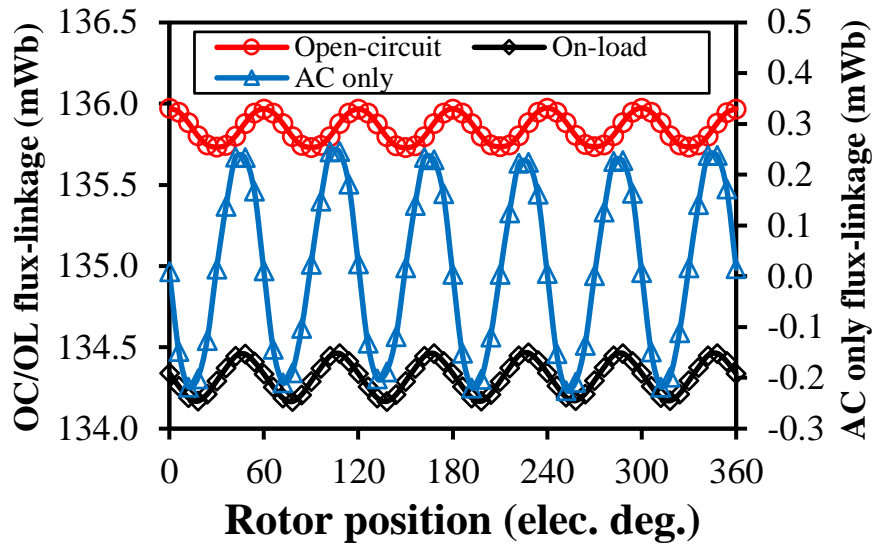
$$\text{IVR} = \frac{E_{pp}}{V_{rf}} \times 100\% \quad (5.2)$$

where E_f is the DC winding induced voltage. ψ_f is the DC winding flux-linkage. θ_e is the rotor electric position. Ω_e is the rotor electrical speed.

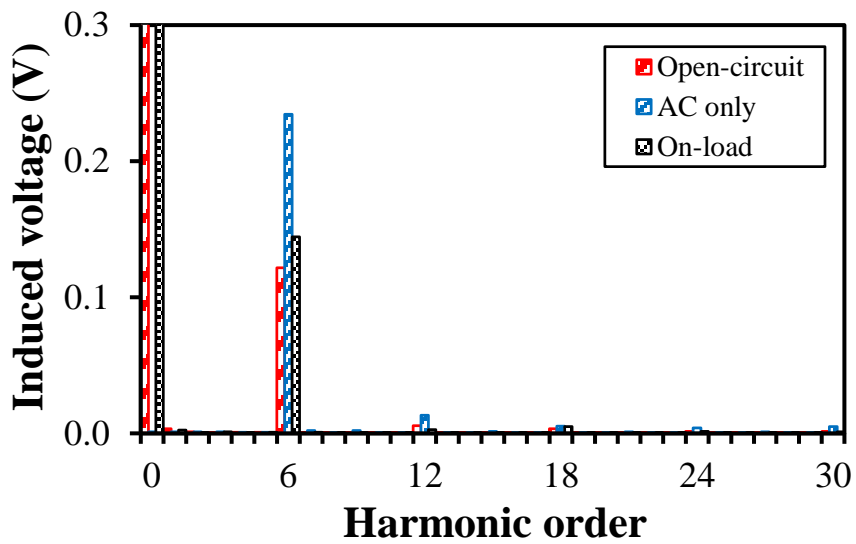
Fig. 5.4 and Fig. 5.5 show the DC winding flux-linkages and induced voltages under different operating conditions. When the machine operates under open-circuit condition, i.e., only with PM and DC excitations, the peak-to-peak value of the induced voltage is 0.63V and the induced voltage ratio is 13.87%. The induced voltage harmonics with $6k$ ($k=1, 2, 3 \dots$) may exist in the DC winding and other harmonics are cancelled out due to series connection between all DC coils. This part is so called open-circuit DC winding induced voltage, which is due to the variable reluctance in the air-gap caused by the modulation effect of the salient rotor. When the machine is only supplied by three-phase AC armature currents, i.e., the PM and DC excitations are removed, the induced voltage harmonic orders are $6k$ as shown in Fig. 5.5(b), which indicates that the DC winding induced voltage harmonic orders caused by the armature currents only are $6k$. This voltage pulsation in the DC winding is referred as the armature current induced voltage. When the machine operates under on-load condition, i.e., PMs, DC field current, and AC armature currents co-exist, the DC winding induced voltage is defined as the on-load DC winding induced voltage. Consequently, the on-load DC winding induced voltage harmonic orders are $6k$ due to the co-existence of the open-circuit and armature current induced voltages. As can be found from Fig. 5.5 that the armature winding only voltage ripple is higher than that of on-load condition due to the magnetic saturation caused by PMs and DC currents under on-load. It can also be found that the peak-to-peak value of the on-load induced voltage is higher than that of the open-circuit due to the influence of the armature current induced voltage and the increase ratio is 14.09%.

The DC winding induced voltage results from the variation of the DC winding flux-linkage. There are two induced voltage components in the DC winding at on-load, i.e., the open-circuit induced voltage and the armature current induced voltage, respectively. The open-circuit induced DC winding voltage is caused by the variation of the air-gap permeance. Whereas, the armature current induced DC winding voltage results from the interaction between the three-phase AC currents and the mutual inductances between the DC field winding and AC armature windings.

Due to the existence of the DC winding induced voltage, the DC winding suffers from current ripple and hence fluctuating excitation field, which is not desirable in PS-HESF machines. Meanwhile, the DC winding induced voltage will challenge the DC power supply and the control performance as well. Consequently, it is important to investigate the mechanism of the DC winding induced voltage and the techniques to reduce it.

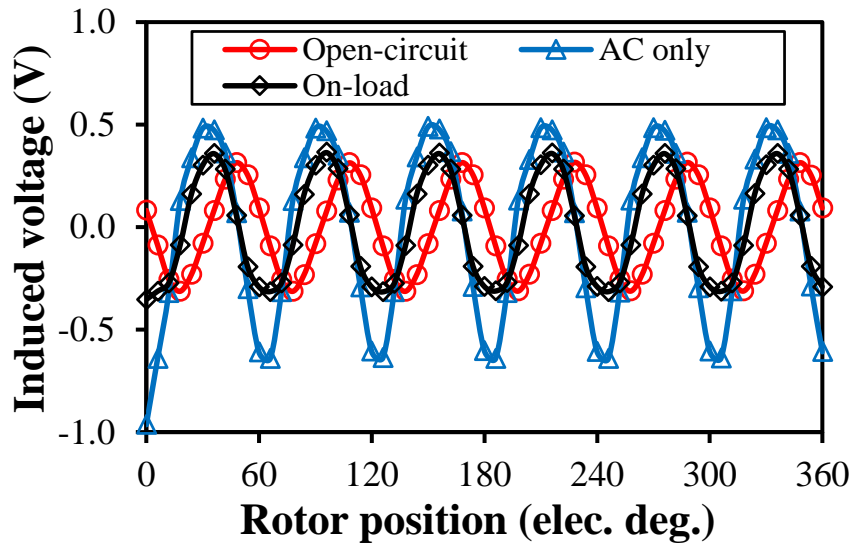


(a) Waveforms

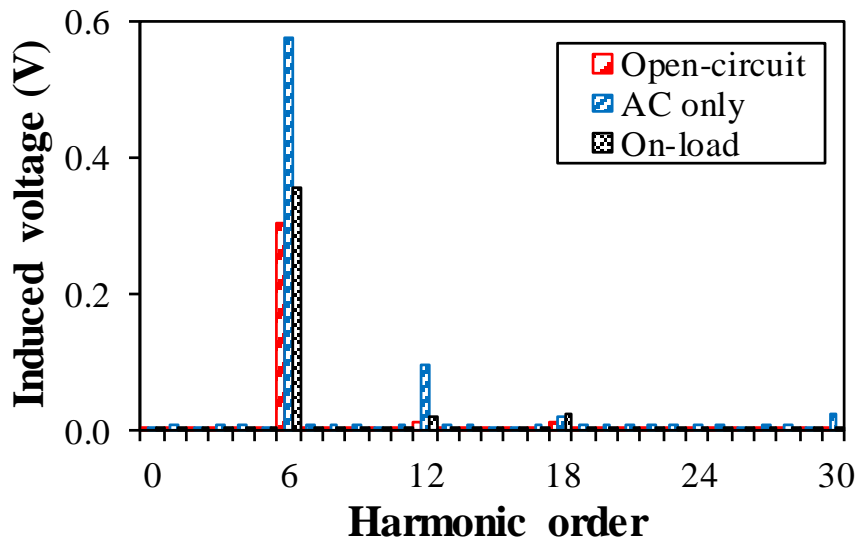


(b) Spectra

Fig. 5.4. DC winding flux-linkages of the 12-slot/10-pole PS-HESFM under different conditions.



(a) Waveforms



(b) Spectra

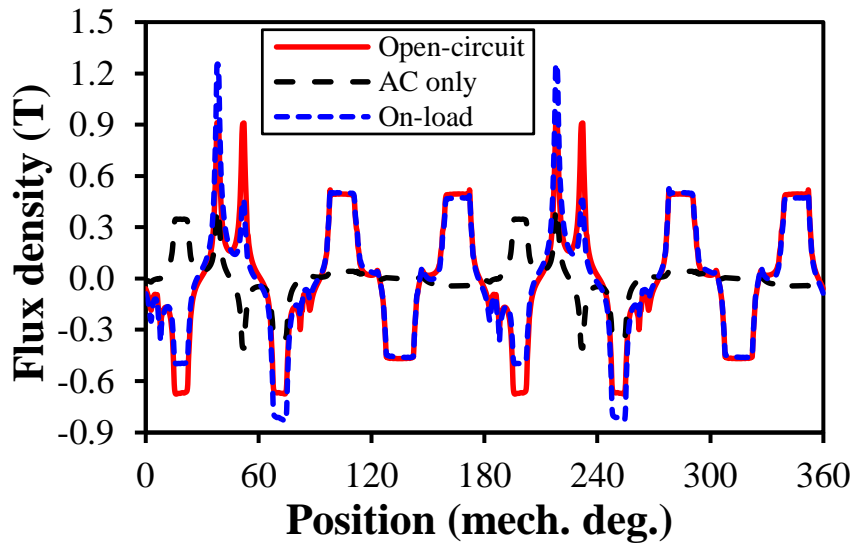
Fig. 5.5. DC winding induced voltages of the 12-slot/10-pole PS-HESFM under different conditions.

5.3.2 Mechanism

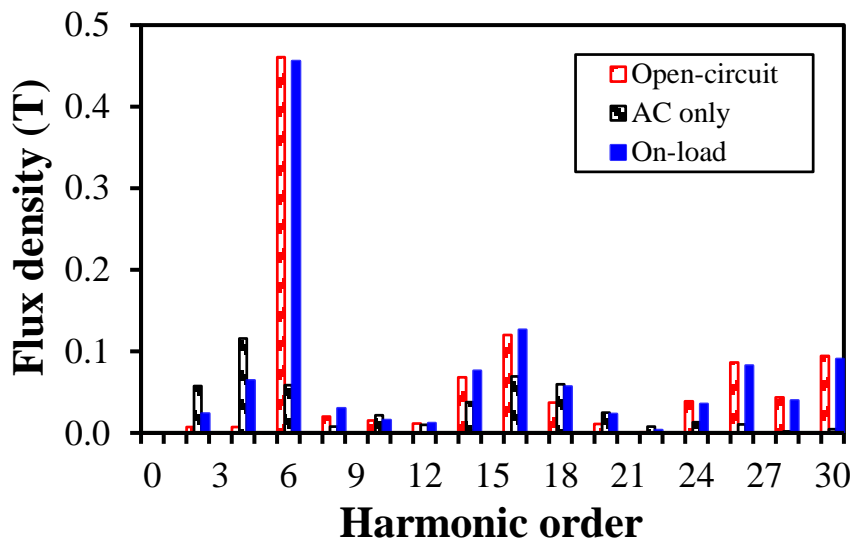
As aforementioned, the open-circuit DC winding induced voltage is caused by the variation of the open-circuit DC winding flux-linkage. Consequently, it is necessary to analyze the reason that leads to the variation of the open-circuit DC winding flux-linkage. The DC field winding consists of 12 non-overlapping concentrated coils and these coils are connected in series. Therefore, the DC winding flux-linkage is the summation of all 12 DC coil flux-linkages. In the PS-HESF machine, there are abundant air-gap field harmonics due to the modulation effect of the salient-pole rotor to the excitation field and armature field, as illustrated in Figs. 5.6 and 5.7. Therefore, the DC coil flux-linkages vary with rotor electric position and suffer from many harmonics, as shown in Fig. 5.8. In fact, they share the same flux-linkage waveforms and harmonic spectra, the only difference is the 60 electric degrees phase shift between adjacent flux-linkage waveforms. The phase shift for the 12-slot/10-pole PS-HESF machine is 60 electric degrees while for other slot and pole number combinations, the phase shift (θ_l) in electric degrees can be given by equation (5.3).

$$\theta_l = 2\pi - \left(\frac{2\pi}{N_s} \times N_r\right) \quad (5.3)$$

where N_s is the stator slot number. N_r is the rotor pole number.

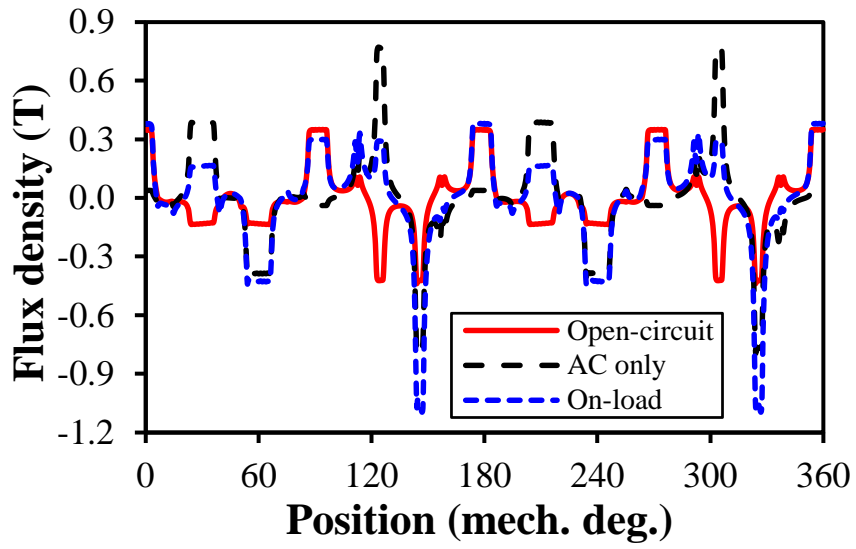


(a) Waveforms

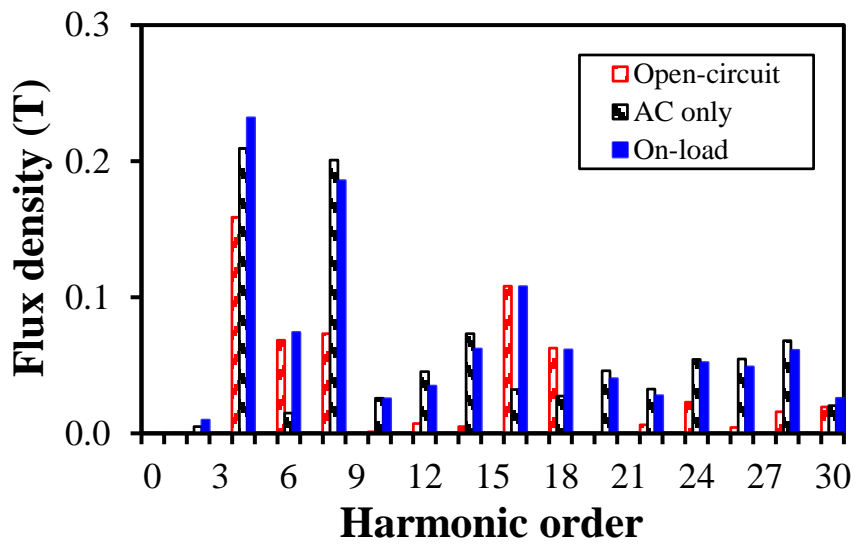


(b) Spectra

Fig. 5.6. Inner air-gap radial flux densities of the 12-slot/10-pole PS-HESFM under different conditions.



(a) Waveforms

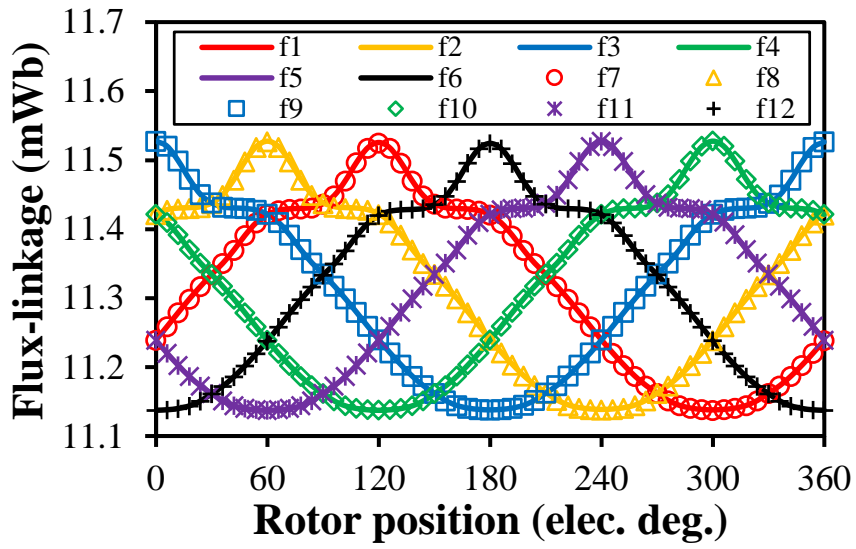


(b) Spectra

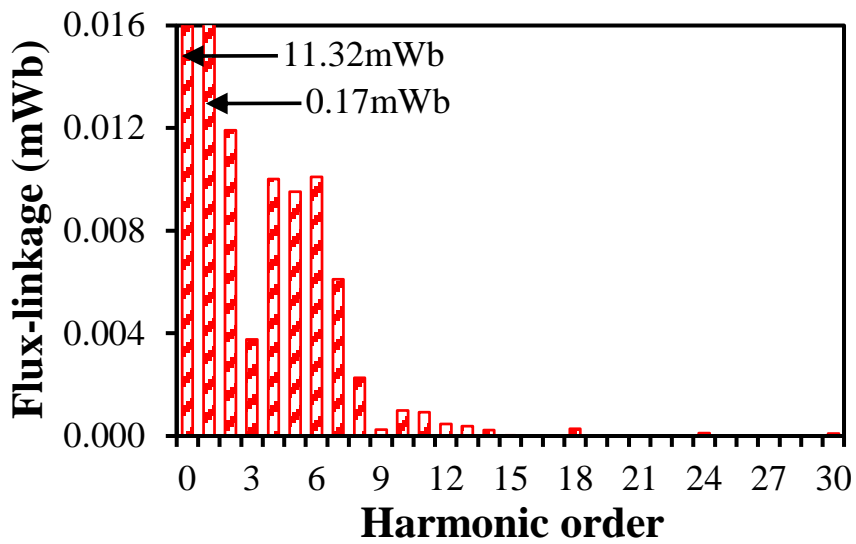
Fig. 5.7. Outer air-gap radial flux densities of the 12-slot/10-pole PS-HESFM under different conditions.

For the 12-slot and 10-pole PS-HESFPM machine, all other harmonics are cancelled out and only the 6th harmonic and its multiples, i.e., 6th, 12th, 18th, 24th... can exist in the open-circuit DC winding flux-linkage and hence the induced voltage.

The variation of the DC coil flux-linkage results in the variation of the DC winding flux-linkage and hence the DC winding voltage pulsation. The variation of the DC coil flux-linkage is caused by the variation of the equivalent air-gap magnetic reluctance when the rotor rotates. It can be found from Fig. 5.8 and Fig. 5.9 that the flux-linkage of the DC coil f_l reaches its maximum value 11.53mWb at $\theta_e=120^\circ$ and minimum value 11.14mWb at $\theta_e=300^\circ$, respectively. At $\theta_e=120^\circ$, the main flux of the DC coil f_l passes the inner stator tooth f_1 , inner air-gap and inner stator tooth f_2 , respectively. Consequently, the magnetic reluctance of the DC coil f_l flux-linkage is minimum at $\theta_e=120^\circ$. At $\theta_e=300^\circ$, the main flux of the DC coil f_l passes the inner stator tooth f_1 , inner air-gap, outer air-gap and inner stator tooth f_2 , respectively. Therefore, the magnetic reluctance of the DC coil f_l flux-linkage is maximum at $\theta_e=300^\circ$. Consequently, it has been proved that the variation of the equivalent air-gap reluctance leads to the variation of the DC coil flux-linkage and hence the DC winding flux-linkage. As a result, a voltage pulsation is induced in the DC winding under open-circuit condition.

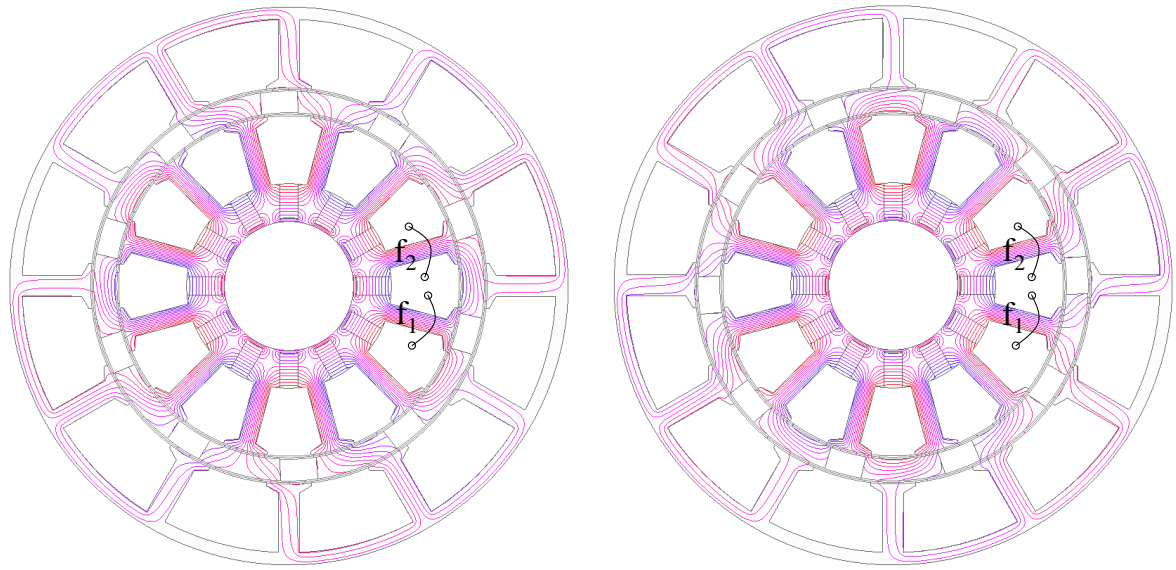


(a) Waveforms



(b) Spectra for all DC coils

Fig. 5.8. Open-circuit DC coil flux-linkages of the 12-slot/10-pole PS-HESF machine.



(a) Maximum ($\theta_e=120^\circ$)

(b) Minimum ($\theta_e=300^\circ$)

Fig. 5.9. Open-circuit flux distributions of the 12-slot/10-pole PS-HESF machine when ψ_{f1} is maximum and minimum.

5.3.3 Influence of Current Advance Angle

As shown in Fig. 5.10, the peak-to-peak value of the on-load DC winding induced voltage varies with the current advance angle (θ_e , the phase angle between the phase current vector and the open-circuit back-EMF) and hence, the on-load induced voltage ratio is varied as well. This is because the permeability of the lamination steel changes with the variation of the current advance angle. The air-gap permeance and the mutual inductances between AC and DC windings are both affected by the current advance angle. Consequently, both the open-circuit induced voltage and the armature current induced voltage vary with the current advance angle and hence, the on-load DC winding induced voltage is varied as well. When the current angle equals to zero, the machine operates under zero d -axis current control, where E_{pp} is 0.72V and IVR is 15.82%. Fig. 5.11 shows the average torque variation against the current advance angle. As can be found that the maximum average torque is achieved with $\theta_e=10^\circ$. It is revealed that the saliency ratio (L_q/L_d) is very close to 1 and therefore the reluctance torque component is negligible in the PS-HESFM.

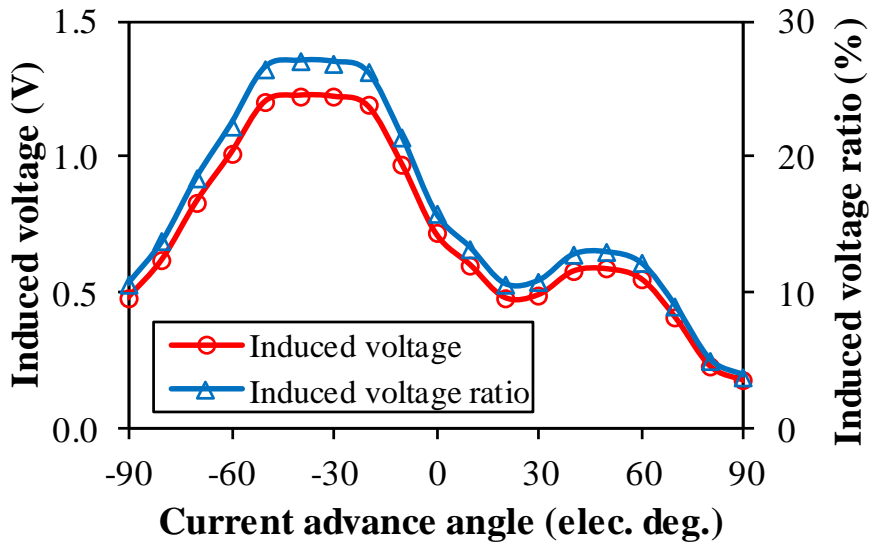


Fig. 5.10. Influence of current advance angle on peak-to-peak on-load DC winding induced voltage of the 12-slot/10-pole PS-HESFM.

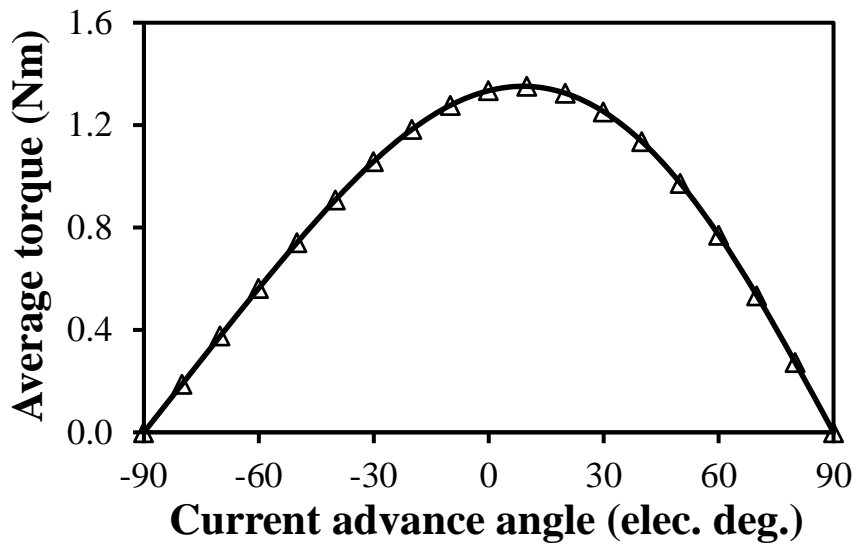


Fig. 5.11. Influence of current advance angle on average torque of the 12-slot/10-pole PS-HESFM.

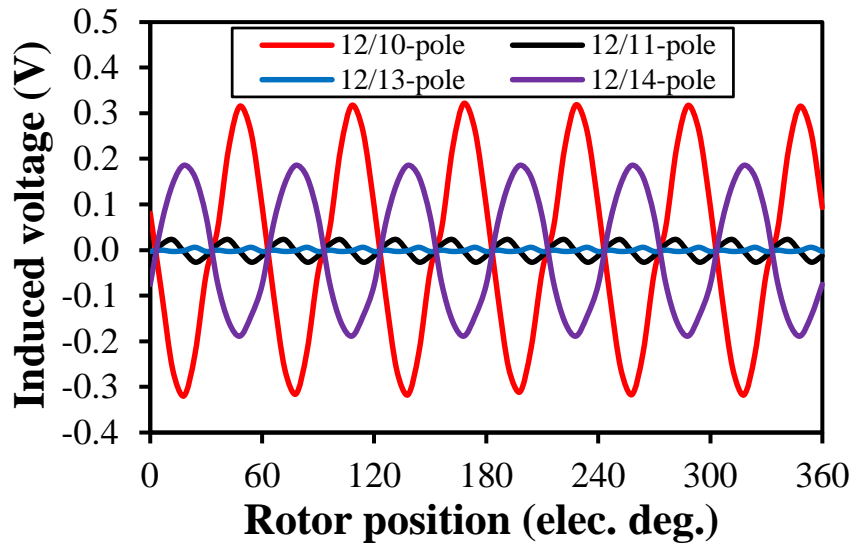
5.3.4 Influence of Slot/Pole Number Combination

The previous analyses are restricted to a specific slot/pole number combination, i.e., 12-slot/10-pole. In this sub-section, the influence of the slot/pole number combination on the DC winding induced voltage will be illustrated. Fig. 5.12 shows the open-circuit DC winding induced voltages of the PS-HESFM with different slot/pole combinations. It can be found that the 12/10-pole and 12/14-pole machines exhibit relatively higher induced voltages than the 12/11-pole and 12/13-pole machines. This is because the 12/10-pole and 12/14-pole machines contain the induced voltage harmonics of $6k$, e.g., 6th, 12th, 18th ..., while the induced voltage harmonic orders of the 12/11-pole and 12/13-pole machines are $12k$, e.g., 12th, 24th, etc. Fig. 5.13 shows the armature current induced DC winding voltages of the PS-HESFM with different slot/pole combinations. It shows that the harmonic orders of the armature induced DC winding voltage are the same for these four machines, i.e., $6k$. As aforementioned, the on-load induced voltage contains the open-circuit induced voltage component and the armature current induced voltage component simultaneously. Therefore, the harmonic orders of the on-load induced voltage are the same for these four machines as well, i.e., $6k$, as shown in Fig. 5.14. At on-load, the 12/10-pole and 12/14-pole machines still exhibit relatively higher induced voltages than the 12/11-pole and 12/13-pole machines, which is mainly attributed to the higher amplitude of the 6th voltage harmonic. Table 5.2 lists the induced voltage harmonic orders of different slot-pole combinations under different conditions. Fig. 5.15 shows the peak-to-peak values of the DC winding induced voltage under different conditions.

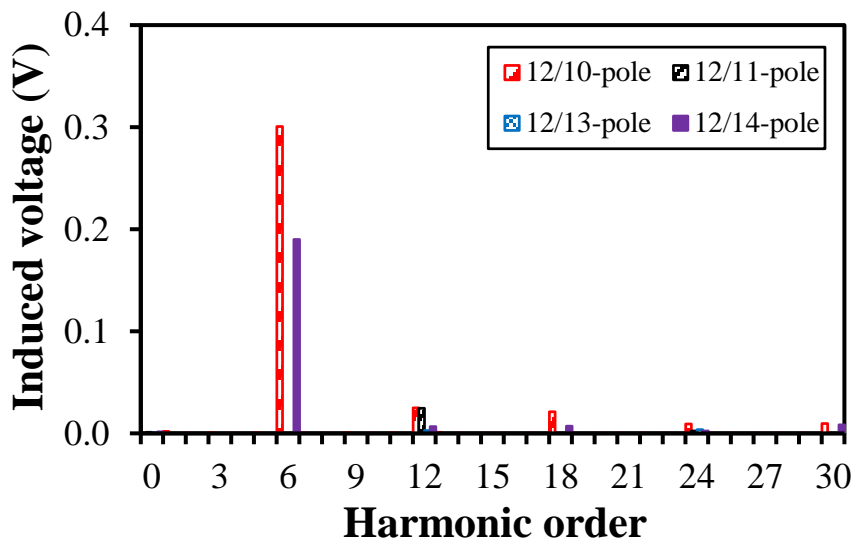
For other slot and pole number combinations of the PS-HESF machine, the open-circuit DC winding flux-linkage, and hence the induced voltage cycles per electric period N_{pe} can be given by equation (5.4).

$$N_{pe} = \frac{\text{LCM}(N_s, N_r)}{N_r} \quad (5.4)$$

where LCM is the least common multiple.

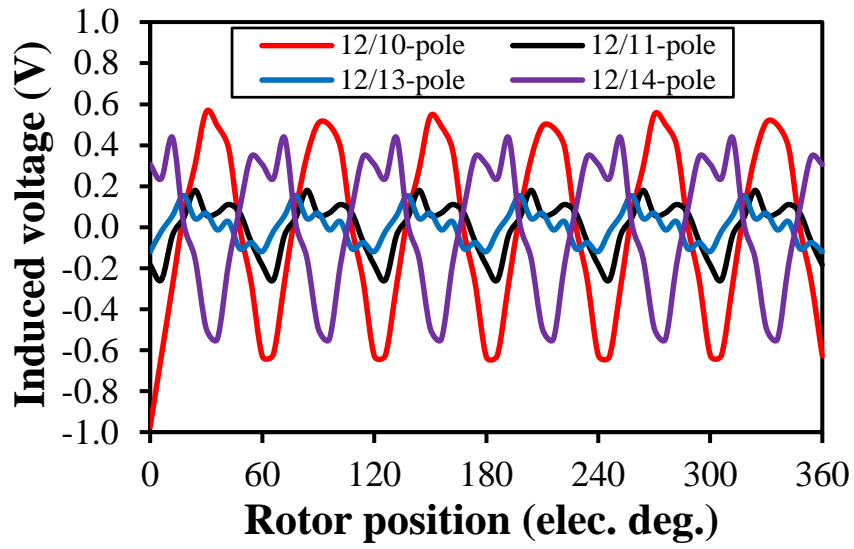


(a) Waveforms

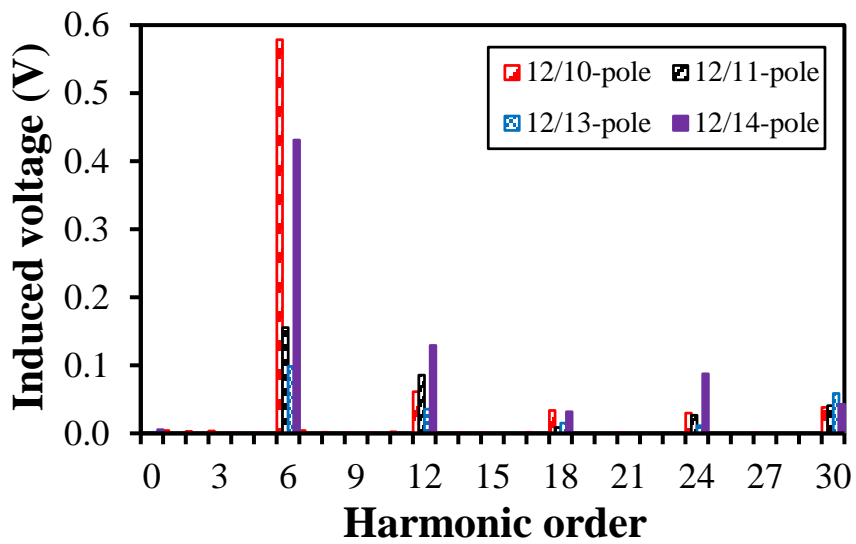


(b) Spectra

Fig. 5.12. Open-circuit DC winding induced voltages of the PS-HESFM with different slot/pole combinations.

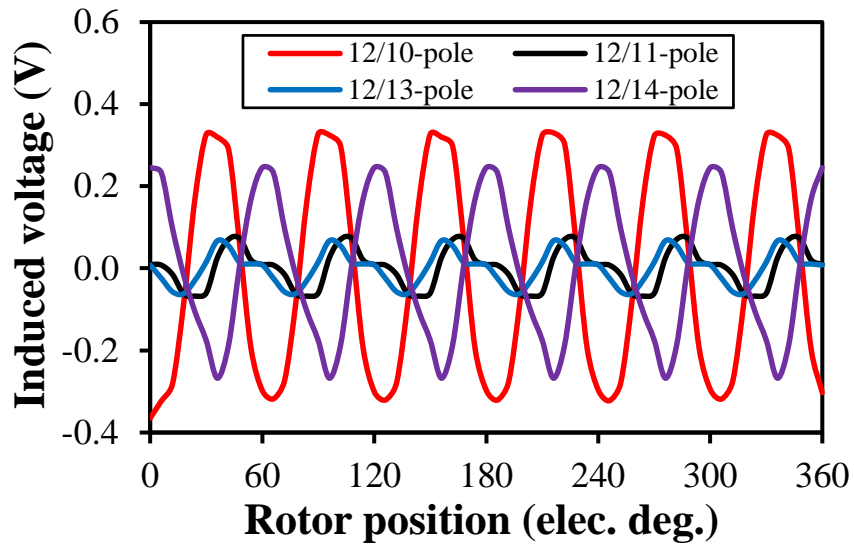


(a) Waveforms

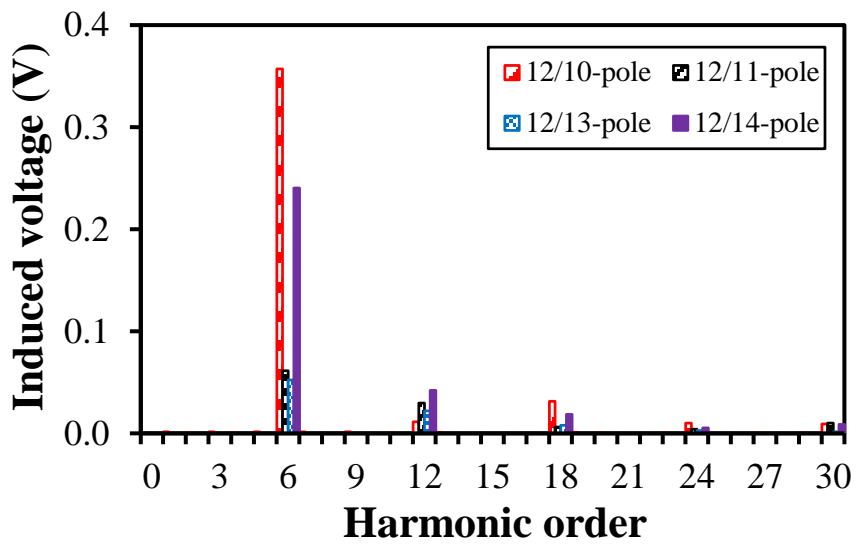


(b) Spectra

Fig. 5.13. Armature current induced DC winding voltages of the PS-HESFM with different slot/pole combinations.



(a) Waveforms



(b) Spectra

Fig. 5.14. On-load DC winding induced voltages of the PS-HESFM with different slot/pole combinations.

Table 5.2 Harmonic Orders of DC Winding Induced Voltage

Slot/pole	Open-circuit	Armature current induced	On-load
12/10	6k	6k	6k
12/11	12k	6k	6k
12/13	12k	6k	6k
12/14	6k	6k	6k

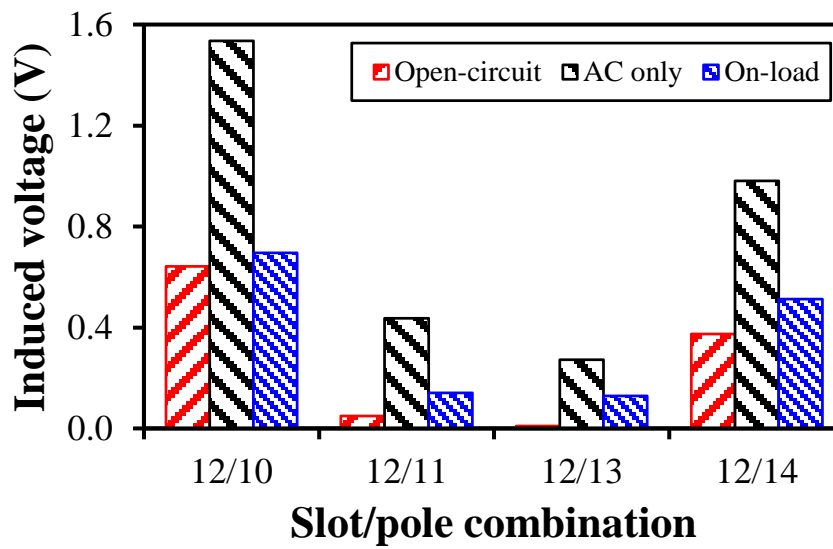


Fig. 5.15. Peak-to-peak DC winding induced voltages of the PS-HESFM with different slot/pole combinations under different conditions.

5.4 Reduction of Open-Circuit DC Winding Induced Voltage

5.4.1 Rotor Pole Arc Pairing

Pairing is widely used in electrical machines for reducing cogging torque, back-EMF harmonics and hence torque ripple. The mechanism behind pairing is to cancel the corresponding harmonics by a pair of machine components, e.g., PM width pairing, teeth width pairing and pole width pairing [FEI10] [PET15] [KIM05]. As aforementioned, the open-circuit DC winding induced voltage is essentially caused by the variation of the equivalent air-gap reluctance when the rotor rotates. By altering the rotor outer pole arc and inner pole arc, the reluctance of the outer air-gap and inner air-gap both can be affected. Consequently, it is expected that the open-circuit DC winding induced voltage can be reduced by rotor pole arc pairing, i.e., the combination of rotor outer pole arc and inner pole arc as shown in Fig. 5.16. Rotor pole arc pairing is firstly employed to reduce the open-circuit DC winding induced voltage.

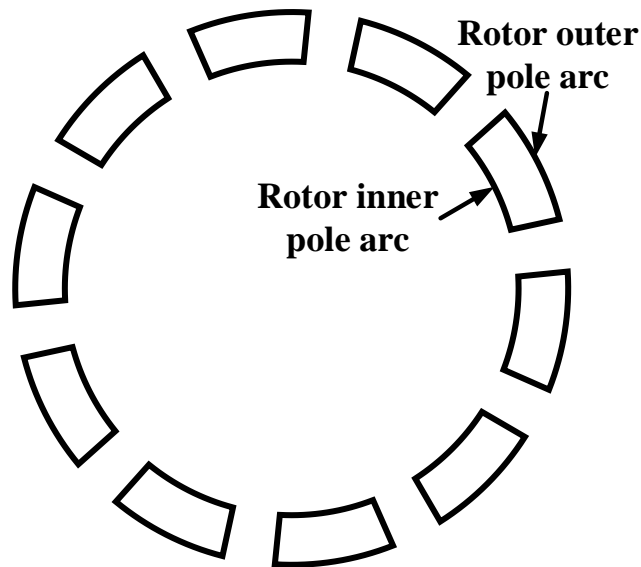


Fig. 5.16. Illustration of rotor pole arc pairing.

All feasible combinations of rotor inner pole arc and outer pole arc are calculated by the FEA method for the peak-to-peak values of the open-circuit DC winding induced voltages and the armature winding phase fundamental back-EMFs as shown in Figs. 5.17 and 5.18. In order to minimize the open-circuit DC winding induced voltage, whilst keeping the average on-load electromagnetic torque as higher as possible, the following two steps are employed.

Step 1, if the armature winding phase fundamental back-EMF of a combination of θ_{ri} and θ_{ro} is smaller than 95% armature winding phase fundamental back-EMF of the original machine, i.e., the globally optimized machine for the maximum average torque, this combination is ignored. Step 2, find the optimal combination of θ_{ri} and θ_{ro} with the highest E_{pp} reduction among the rest combinations and the armature winding phase fundamental back-EMF of which is greater than or equal to 95% armature winding phase fundamental back-EMF of the original machine. By following these two steps, the optimal combination of θ_{ri} and θ_{ro} ($\theta_{ri}=22^\circ$, $\theta_{ro}=28^\circ$) for the 12-slot/10-pole PS-HESFPM machine is obtained as shown in Fig. 5.19.

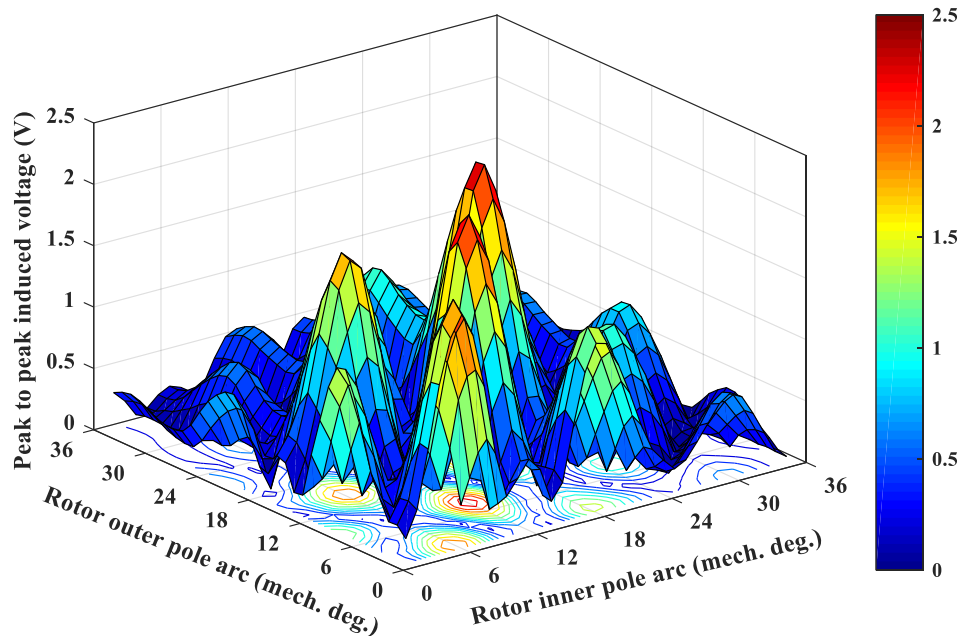


Fig. 5.17. Influence of rotor pole arc pairing on peak-to-peak values of the open-circuit DC winding induced voltage.

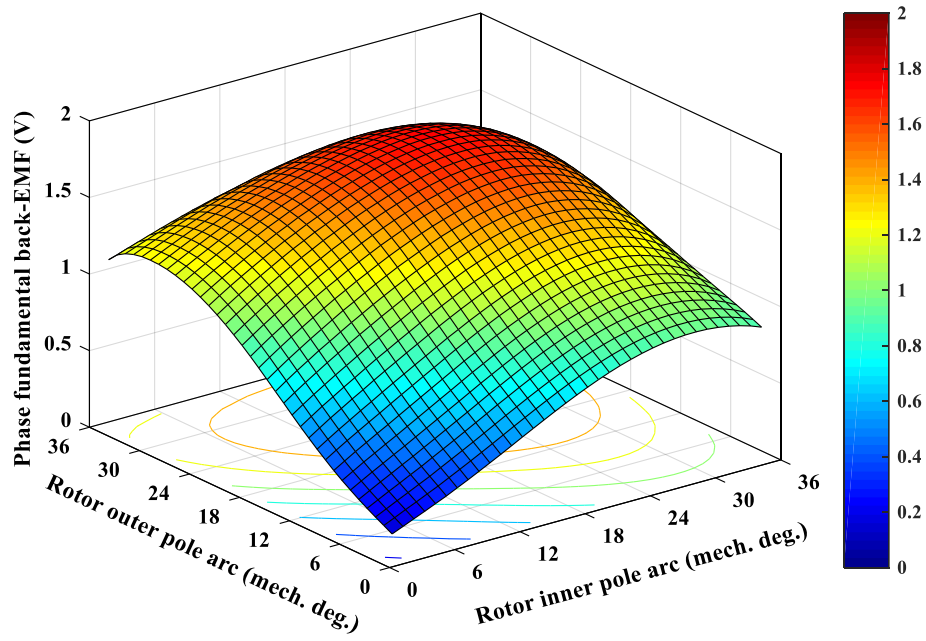


Fig. 5.18. Influence of rotor pole arc pairing on armature winding phase fundamental back-EMFs.

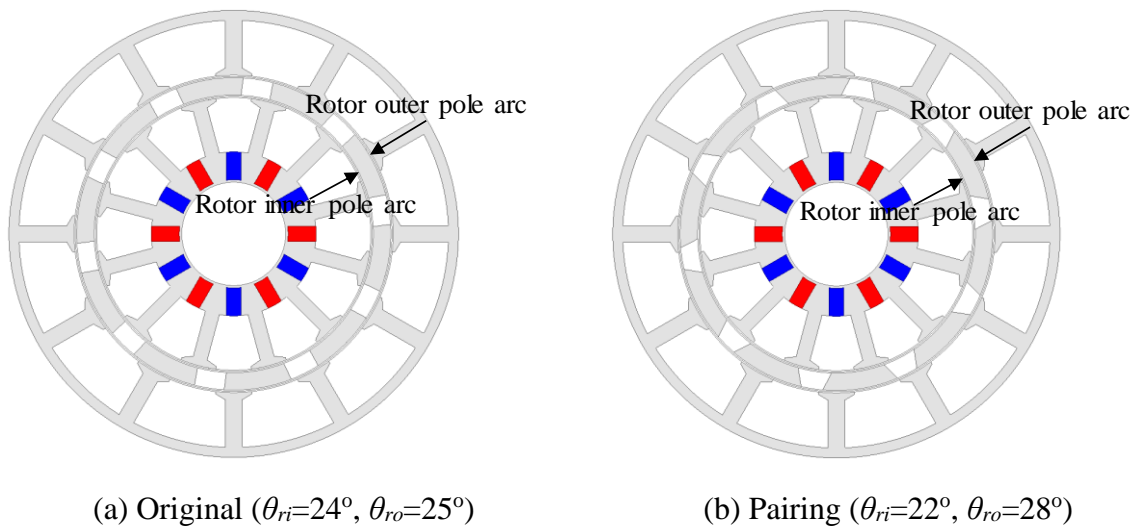
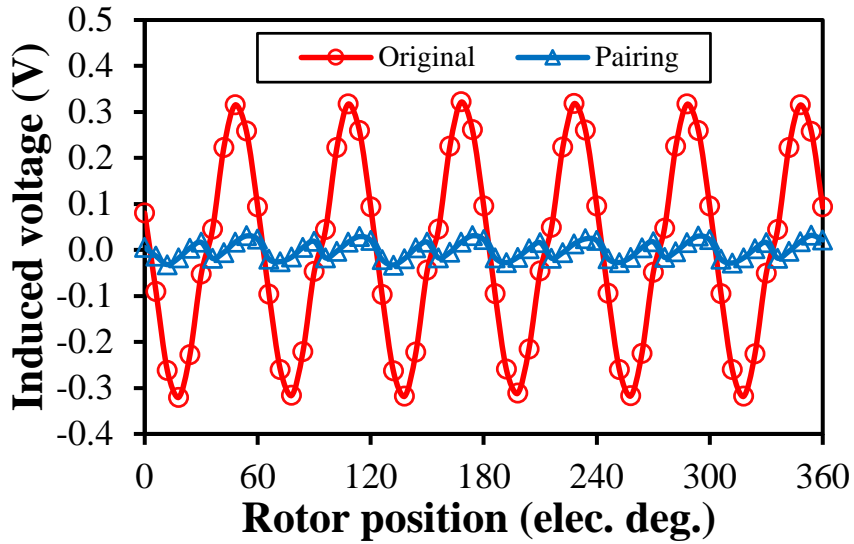
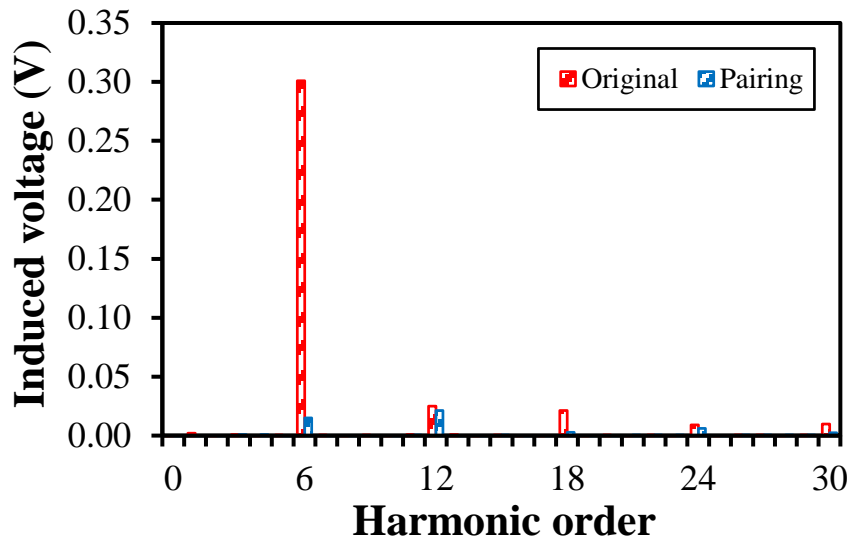


Fig. 5.19. Optimal machines with rotor pole arc pairing.

It can be found from Fig. 5.20 that the peak-to-peak values of the open-circuit DC winding induced voltages (E_{PP}) are 0.64V and 0.06V for the original machine and the optimal machine with pairing, respectively. Consequently, the peak-to-peak induced voltage reduction ratio is 89.89% with rotor pole arc pairing.



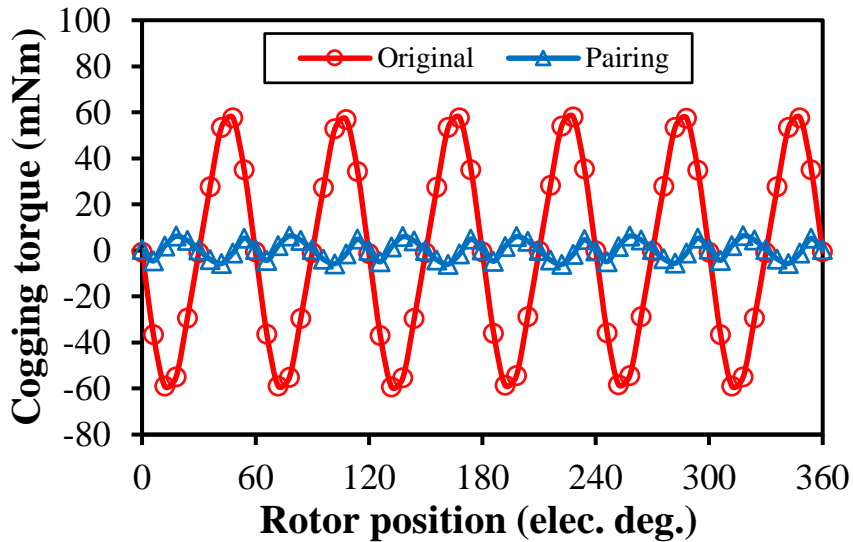
(a) Waveforms



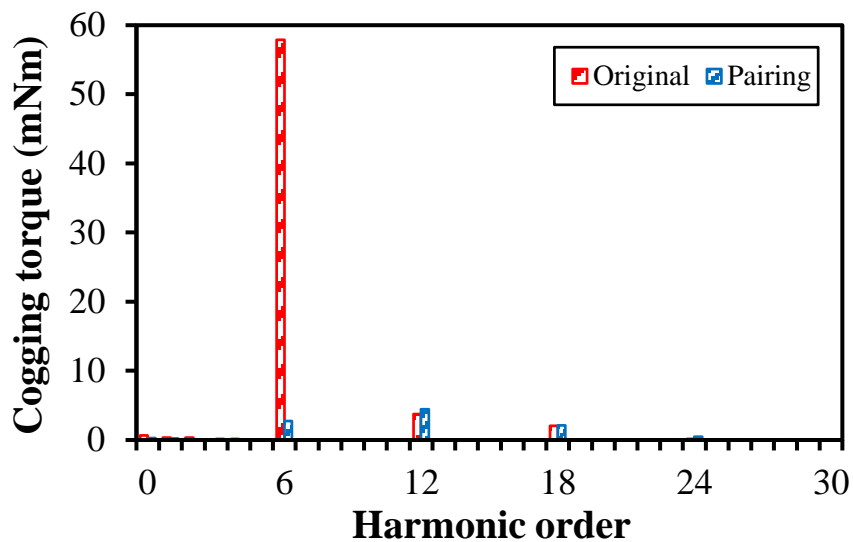
(b) Spectra

Fig. 5.20. Open-circuit DC winding induced voltage with rotor pole arc pairing.

It can be seen from Fig. 5.21 that the peak-to-peak values of the cogging torques (T_{cog}) can also be effectively reduced by rotor pole arc pairing, i.e., 117.55mNm and 12.51mNm for the original machine and the optimal machine with pairing, respectively. Therefore, the peak-to-peak cogging torque reduction ratio by rotor pole arc pairing is 89.36%. Table 5.3 lists the characteristics of the 12/10 PS-HESF machine with rotor pole arc pairing at open-circuit.



(a) Waveforms



(b) Spectra

Fig. 5.21. Cogging torque with rotor pole arc pairing.

Table 5.3 Characteristics of PS-HESF Machine with Rotor Pole Arc Pairing at Open-Circuit

Items	Unit	Values	
Machine	-	Original	Pairing
E_{pp}	V	0.64	0.06
E_{pp} reduction ratio	%	-	89.89
T_{cog}	mNm	117.55	12.51
T_{cog} reduction ratio	%	-	89.36

5.4.2 Unevenly Distributed Rotor Teeth

Unevenly distributed rotor teeth shown in Fig. 5.22 is subsequently employed for the reduction of the open-circuit DC winding induced voltage. By shifting half the number of the rotor iron pieces with a shift angle θ_s , it can be found that both the amplitude and initial phase of the 6th induced voltage harmonic can be affected as shown in Figs. 5.23 and 5.24. In addition, the initial phase waveform of the 6th harmonic is bipolar. As aforementioned, the 6th harmonic is the dominant harmonic in the open-circuit DC winding flux-linkage and hence the induced voltage for the 12-slot/10-pole PS-HESFPM machine. Consequently, it is expected that the open-circuit DC winding induced voltage can be reduced by unevenly distributed rotor teeth due to the variation of the 6th induced voltage harmonic with the shift angle θ_s .

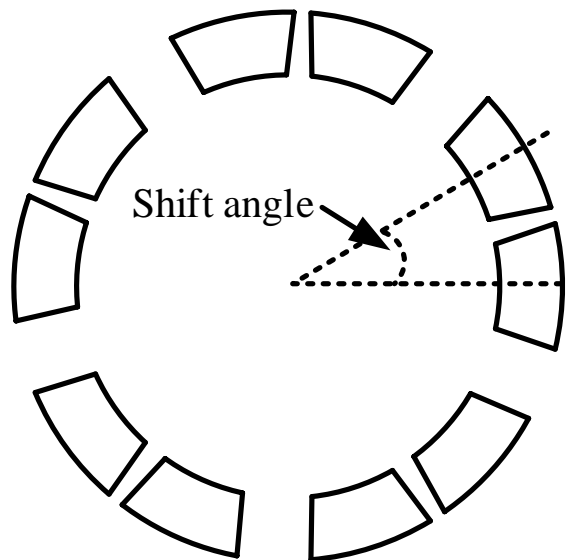


Fig. 5.22. Illustration of unevenly distributed rotor teeth.

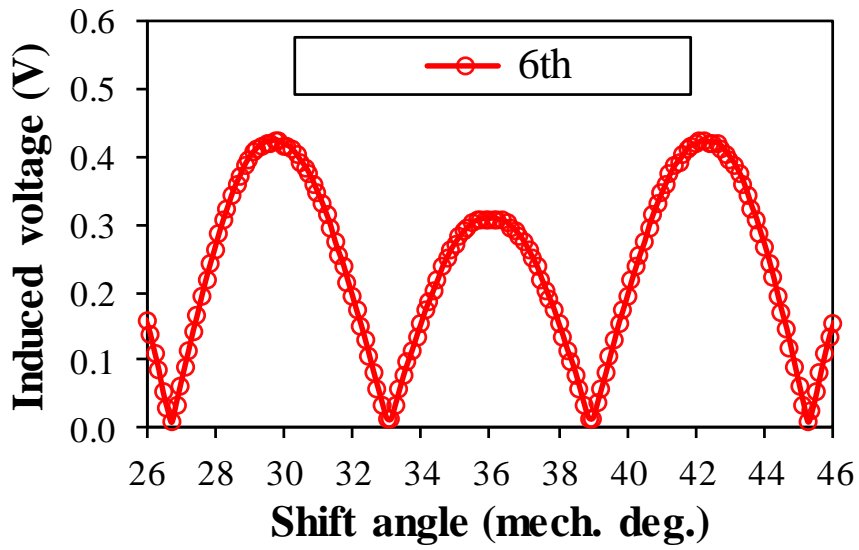


Fig. 5.23. Influence of shift angle on amplitude of the 6th open-circuit DC winding induced voltage harmonic.

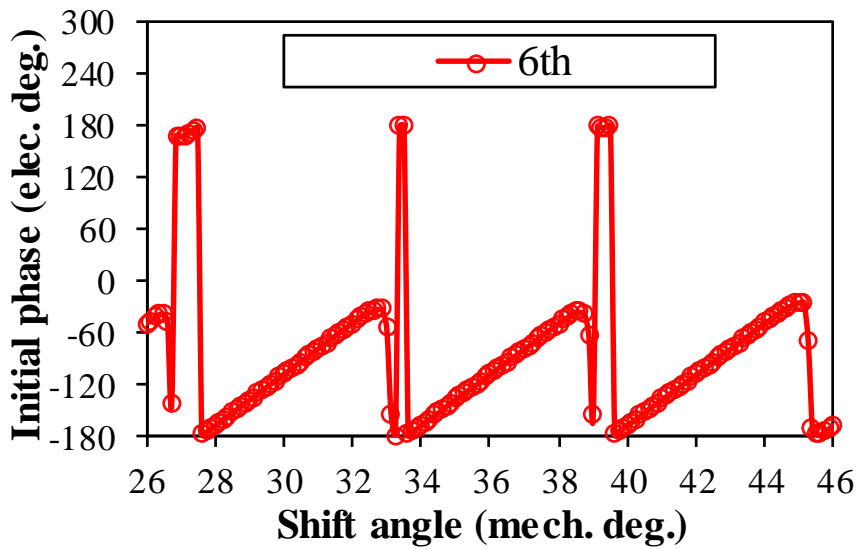


Fig. 5.24. Influence of shift angle on initial phase of the 6th open-circuit DC winding induced voltage harmonic.

All possible values of the shift angle θ_s are calculated by the FEA method for the peak-to-peak values of the open-circuit DC winding induced voltages and the armature winding phase fundamental back-EMFs as shown in Figs. 5.25 and 5.26, respectively. It can be observed from Fig. 5.25 that the peak-to-peak values of the open-circuit DC winding induced voltages vary with the shift angle, which is mainly due to the variation of the 6th induced voltage harmonic with the shift angle as shown in Fig. 5.23. Similarly, the armature winding phase fundamental back-EMFs vary with the shift angle as well as shown in Fig. 5.26. In order to find the optimal shift angle with the highest open-circuit DC winding induced voltage reduction while maintaining the average on-load torque as higher as possible, two similar steps are followed.

Step 1, if the armature winding phase fundamental back-EMF of a shift angle θ_s is smaller than 95% armature winding phase fundamental back-EMF of the original machine, this combination is ignored. Step 2, find the optimal value of θ_s with the highest E_{pp} reduction among the rest values and the armature winding phase fundamental back-EMF of which is greater than or equal to 95% armature winding phase fundamental back-EMF of the original machine. By following these two steps, the optimal shift angle θ_s ($\theta_s=33.13^\circ$) for the 12-slot/10-pole PS-HESFPM machine is obtained as shown in Fig. 5.27.

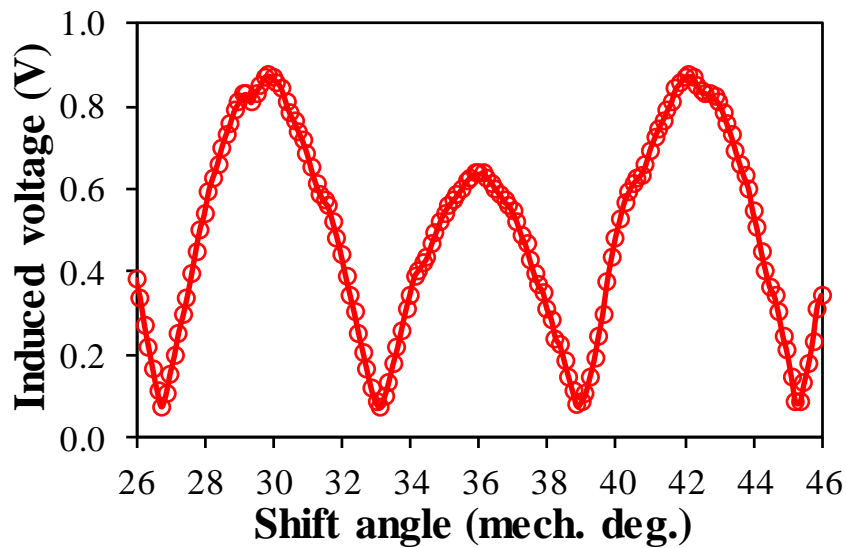


Fig. 5.25. Influence of shift angle on peak-to-peak value of the open-circuit DC winding induced voltage.

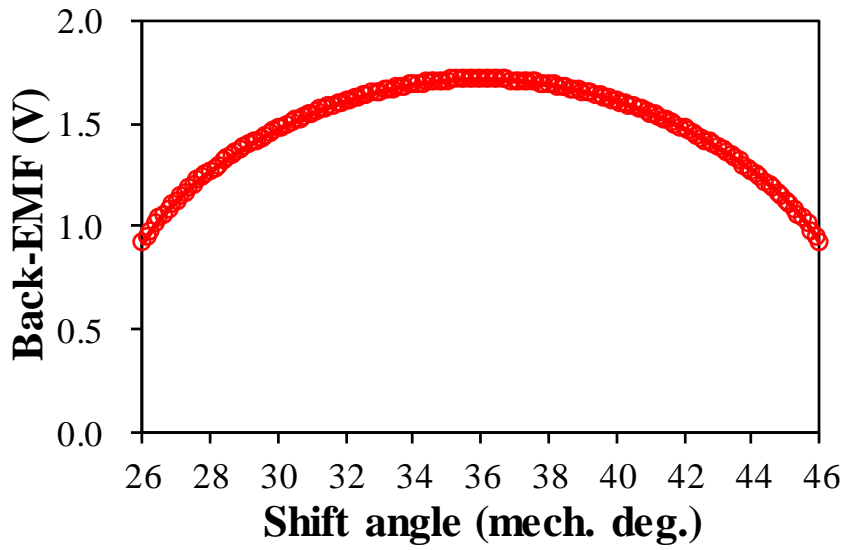


Fig. 5.26. Influence of shift angle on amplitude of the armature winding phase fundamental back-EMF.

It can be found from Fig. 5.28 that the peak-to-peak values of the open-circuit DC winding induced voltages (E_{PP}) are 0.64V and 0.07V for the original machine and the optimal machine with uneven teeth, respectively. Consequently, the peak-to-peak induced voltage reduction ratio is 88.73% with unevenly distributed rotor teeth.

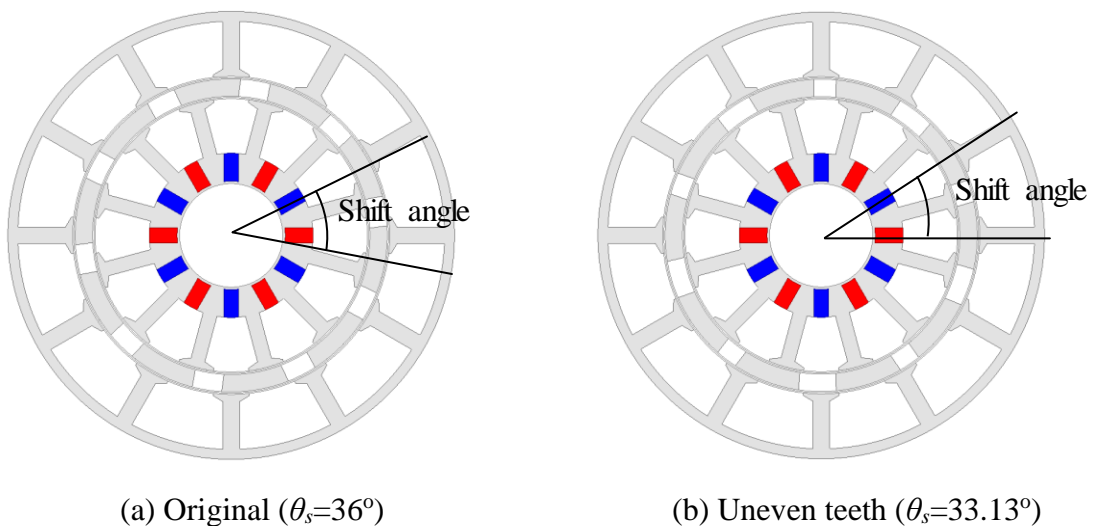
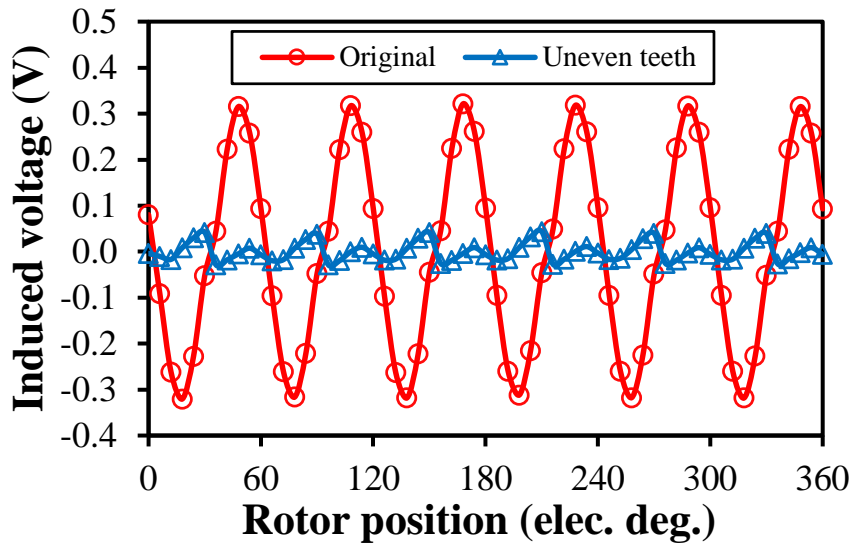
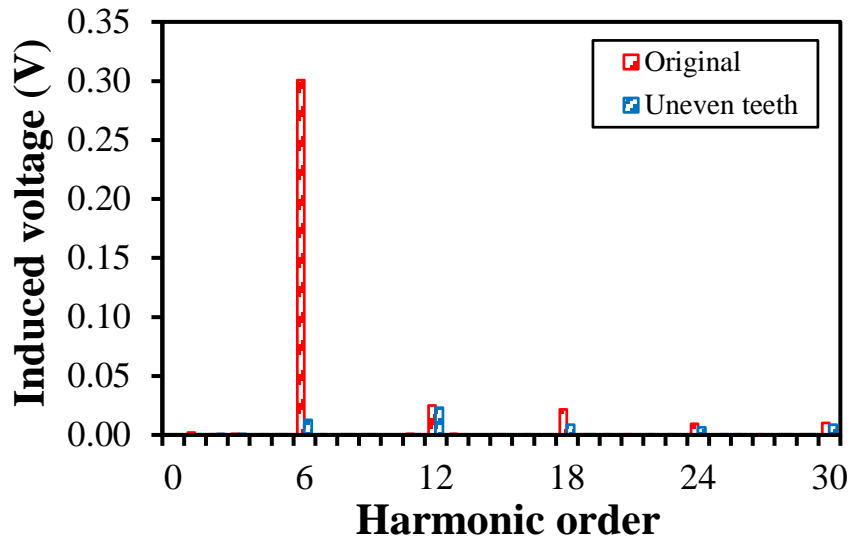


Fig. 5.27. Optimal machines with unevenly distributed rotor teeth.



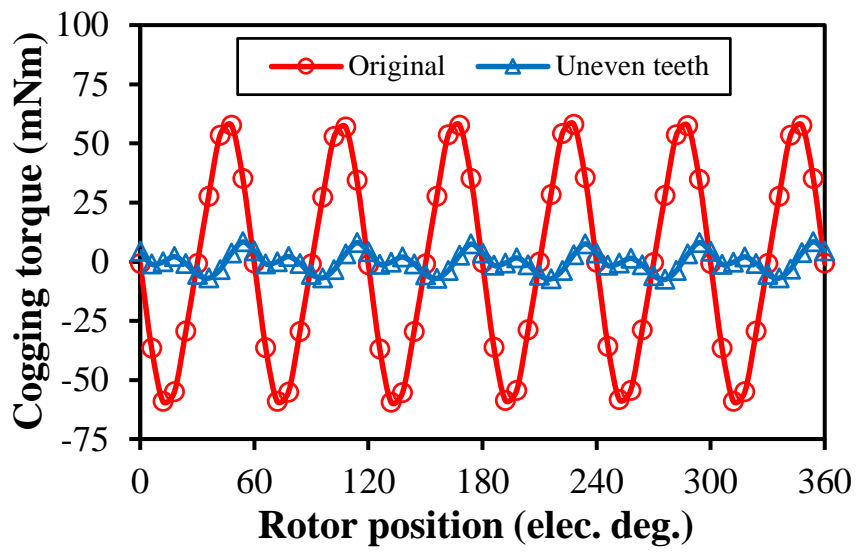
(a) Waveforms



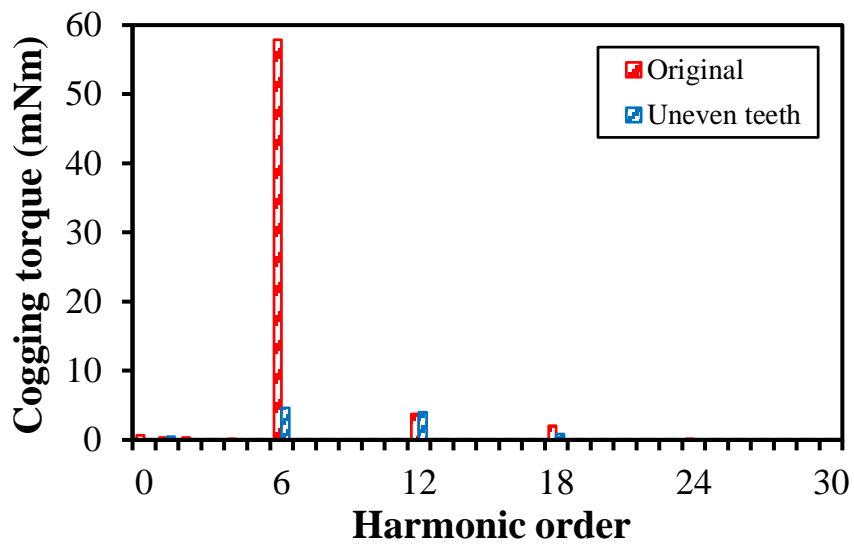
(b) Spectra

Fig. 5.28. Open-circuit DC winding induced voltage with unevenly distributed rotor teeth.

It can be seen from Fig. 5.29 that the peak-to-peak values of the cogging torques (T_{cog}) can also be effectively reduced by unevenly distributed rotor teeth, i.e., 117.55mNm and 15.89 mNm for the original machine and the optimal machine with uneven teeth, respectively. Therefore, the peak-to-peak cogging torque reduction ratio by unevenly distributed rotor teeth is 86.49%. Table 5.4 presents a summary of the characteristics of the 12/10 PS-HESFPM machine with unevenly distributed rotor teeth at open-circuit.



(a) Waveforms



(b) Spectra

Fig. 5.29. Cogging torque with unevenly distributed rotor teeth.

Table 5.4 Characteristics of PS-HESF Machine with Unevenly Distributed Rotor Teeth at
Open-Circuit

Items	Unit	Values	
Machine	-	Original	Pairing
E_{pp}	V	0.64	0.07
E_{pp} reduction ratio	%	-	88.73
T_{cog}	mNm	117.55	15.89
T_{cog} reduction ratio	%	-	86.49

5.5 Reduction of On-Load DC Winding Induced Voltage

5.5.1 Rotor Pole Arc Pairing

As aforementioned, the 6th harmonic is the dominant harmonic among the on-load DC winding induced voltage harmonics. Consequently, it is expected that the peak-to-peak value of the on-load induced voltage can be suppressed by reducing the amplitude of the 6th harmonic. When the iron piece rotor inner and outer pole arcs are changed, the amplitude of the 6th harmonic at on-load varies as well, as shown in Fig. 5.30. There are two air-gaps in the PS-HESF machine, in which the rotor outer pole arc (θ_{ro}) mainly affects the permeance of the outer air-gap while the rotor inner pole arc (θ_{ri}) mainly influences the inner air-gap. By changing θ_{ri} and θ_{ro} simultaneously, the equivalent air-gap permeance varies compared with the original optimized PS-HESF machine. Consequently, both the open-circuit and armature current induced voltage components are different with different combinations of θ_{ri} and θ_{ro} and hence the on-load induced voltages are different as well. Therefore, rotor pole arc pairing in Fig. 5.16 is again employed in this sub-section to suppress the DC winding induced voltage at on-load.

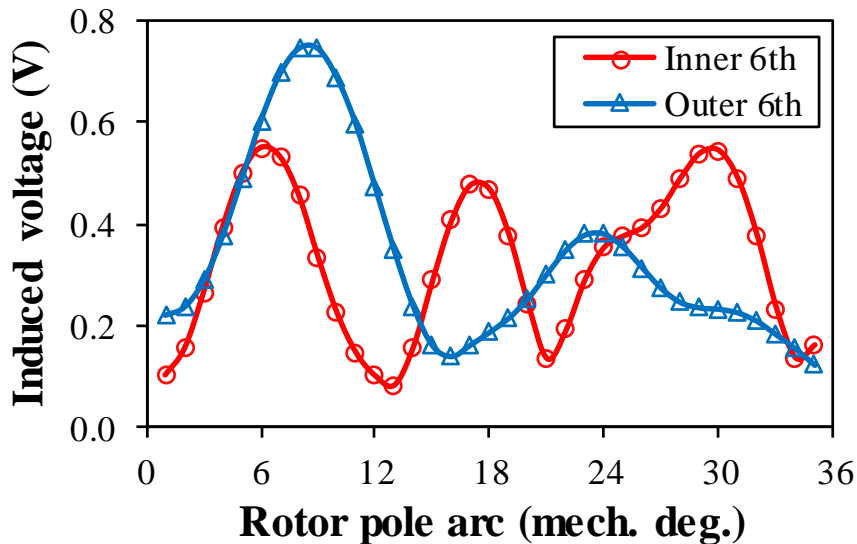


Fig. 5.30. Influence of rotor pole arcs on amplitude of the 6th on-load DC winding induced voltage harmonic.

In order to suppress the pulsating on-load DC winding induced voltage while maintaining the average on-load electromagnetic torque, the FEA method is employed to calculate different combinations of the iron piece rotor outer and inner pole arcs within the possible ranges of θ_{ri} and θ_{ro} . The peak-to-peak values of the on-load DC winding induced voltages (E_{pp}) and the average on-load electromagnetic torques (T_{ave}) are drawn against θ_{ri} and θ_{ro} as shown in Figs. 5.31 and 5.32. In order to minimize the on-load DC winding induced voltage pulsation, the combination of θ_{ri} and θ_{ro} ($\theta_{ri}=13^\circ$, $\theta_{ro}=27^\circ$) with the minimum value of E_{pp} is employed among all possible combinations.

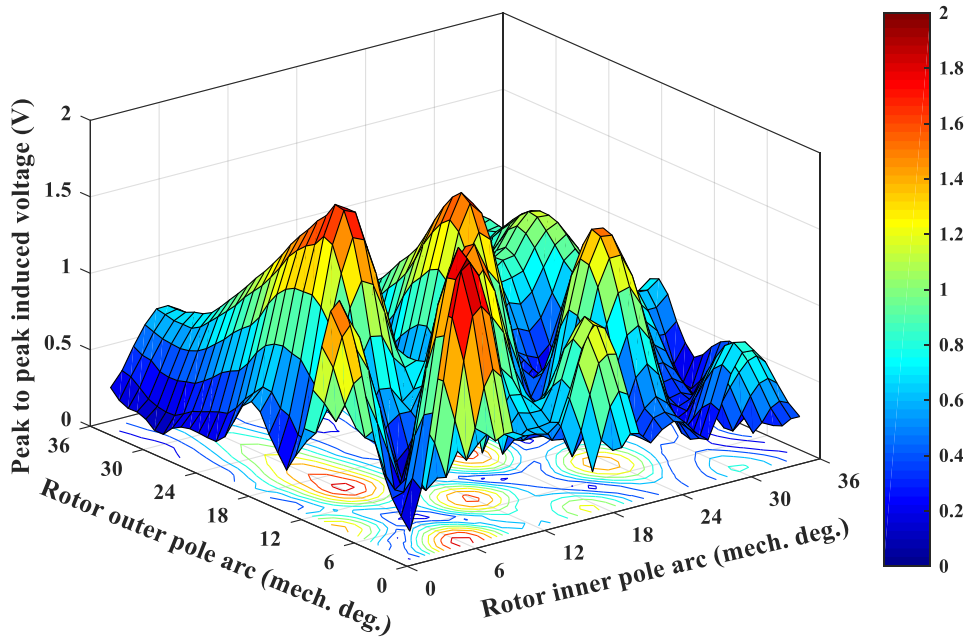


Fig. 5.31. Influence of rotor pole arcs pairing on peak to peak value of the on-load DC winding induced voltage.

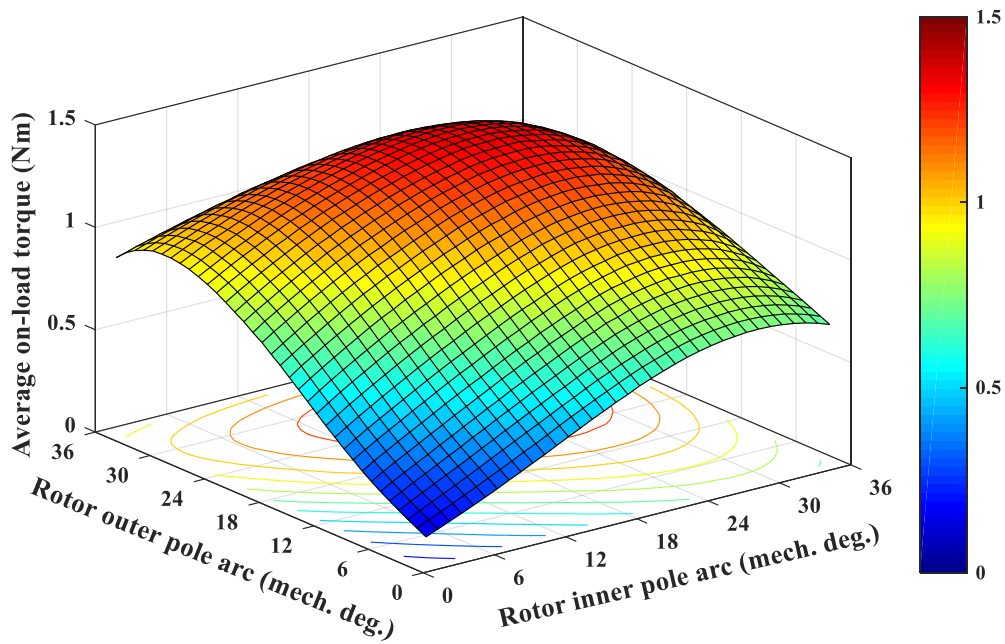
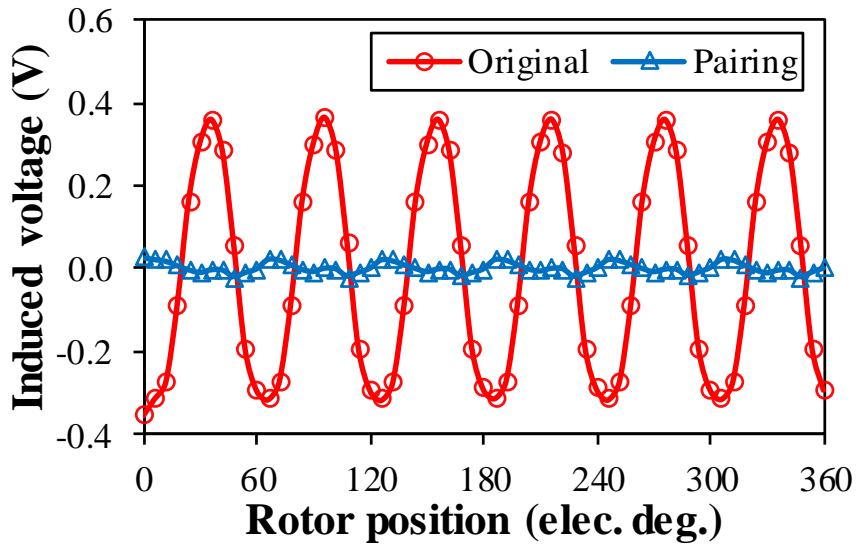
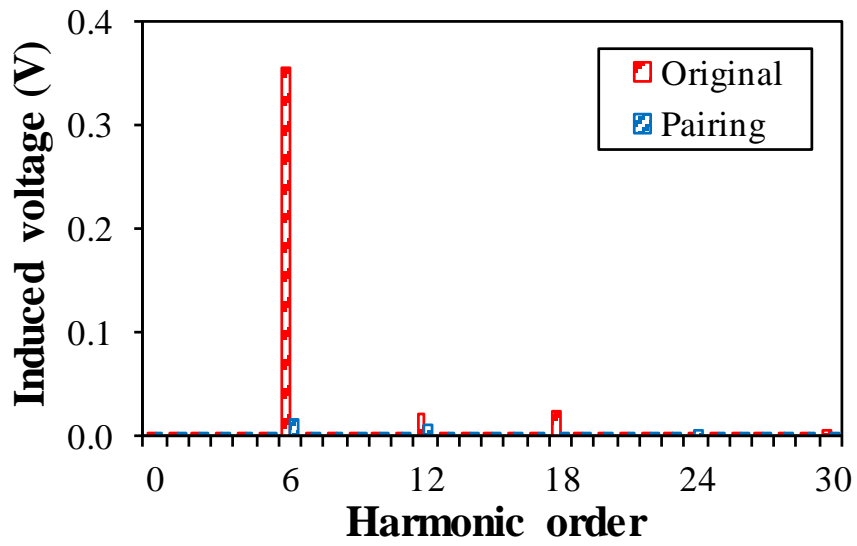


Fig. 5.32. Influence of rotor pole arcs pairing on average on-load electromagnetic torque.

As shown in Fig. 5.33(a) the peak-to-peak value of the on-load DC winding induced voltage E_{pp} has been significantly suppressed by employing the technique of rotor pole arc pairing, i.e., 0.05V and 0.72V for the optimized machines with and without pairing, respectively. Consequently, E_{pp} reduction ratio is 92.81% due to the suppression of the 6th on-load DC winding induced voltage harmonic as shown in Fig. 5.33(b), in which the amplitude of the 6th harmonic is reduced from 0.36V to 0.02V. It should be noted that the original machine is the global optimized 12-slot/10-pole PS-HESF machine with the highest T_{ave} while the machine with pairing is the optimized machine with the highest E_{pp} reduction ratio.



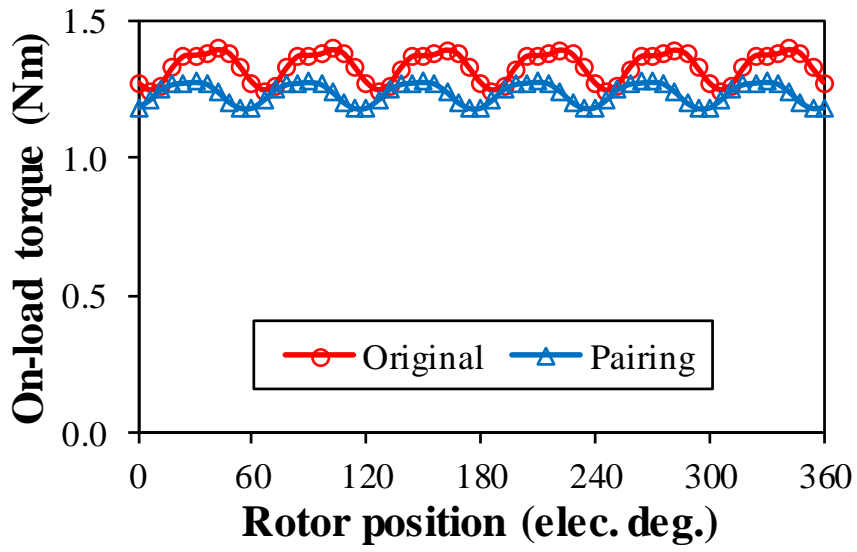
(a) Waveforms



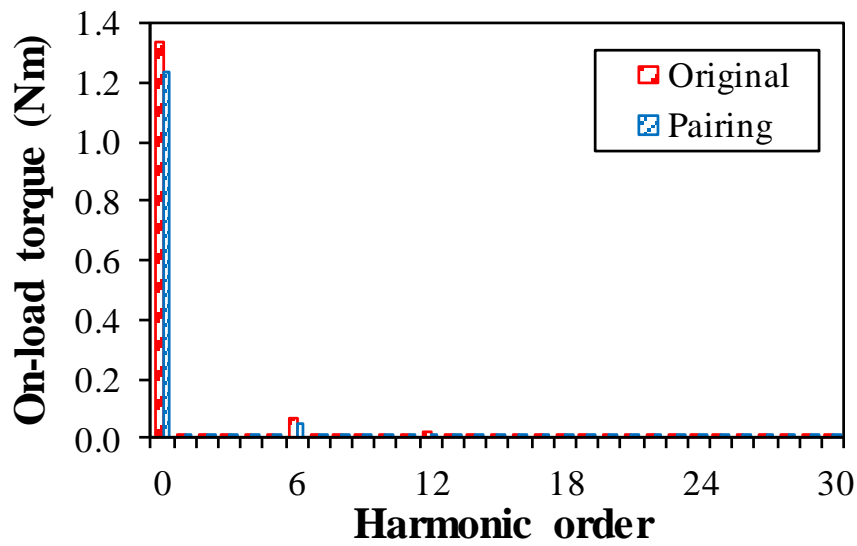
(b) Spectra

Fig. 5.33. On-load DC winding induced voltages of the 12-slot/10-pole PS-HESFM with rotor pole arc pairing.

As shown in Fig. 5.34(a), the average on-load torque (T_{ave}) is slightly reduced by rotor pole arc pairing, i.e., 1.24Nm and 1.33Nm for the machines with and without pairing, respectively, due to the reduction of the fundamental back-EMF of AC armature winding. Consequently, T_{ave} reduction ratio is 7.32%. Furthermore, the torque ripple T_{rip} is reduced from 11.46% to 8.10% for the original machine and the machine with pairing, respectively, which is mainly due to the suppression of the 6th back-EMF harmonic in armature winding as shown in Fig. 5.34(b). Table 5.5 summaries the main characteristics of the 12-slot/10-pole PS-HESF machine with rotor pole arc pairing at on-load.



(a) Waveforms



(b) Spectra

Fig. 5.34. On-load torques of the 12-slot/10-pole PS-HESFM with rotor pole arc pairing.

Table 5.5 Characteristics of PS-HESFM with Rotor Pole Arc Pairing at On-Load

Items	Unit	Values	
		Original	Pairing
Machine	-		
E_{pp}	V	0.72	0.05
E_{pp} reduction ratio	%	-	92.81
T_{ave}	Nm	1.33	1.24
T_{ave} reduction ratio	%	-	7.32
T_{rip}	%	11.46	8.10
T_{rip} reduction ratio	%	-	29.31

5.5.2 Unevenly Distributed Rotor Teeth

By shifting half the number of rotor iron pieces by a mechanical angle θ_s , the amplitude of the dominant 6th induced voltage harmonic at on-load varies with the angle θ_s as well as shown in Fig. 5.35. Both the open-circuit and armature current induced voltages vary with the shift angle θ_s due to the variation of the equivalent air-gap permeance and hence the on-load induced voltage is varied as well. Consequently, E_{pp} may be suppressed by selecting an appropriate value of θ_s . Moreover, when the shift angle varies, the current advance angle to achieve the maximum torque per ampere (MTPA) changes as well. As shown in Fig. 5.10, the current advance angle also influences E_{pp} . Consequently, both the shift angle θ_s and the current advance angle θ_e are scanned by the FEA method to calculate E_{pp} and T_{ave} as shown in Figs. 5.36 and 5.37, respectively.

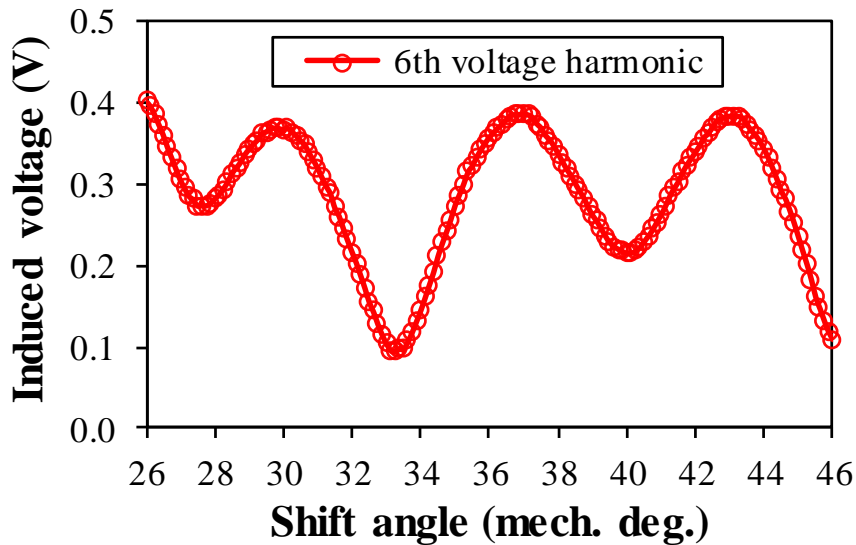


Fig. 5.35. Influence of shift angle on amplitude of the 6th on-load DC winding induced voltage harmonic.

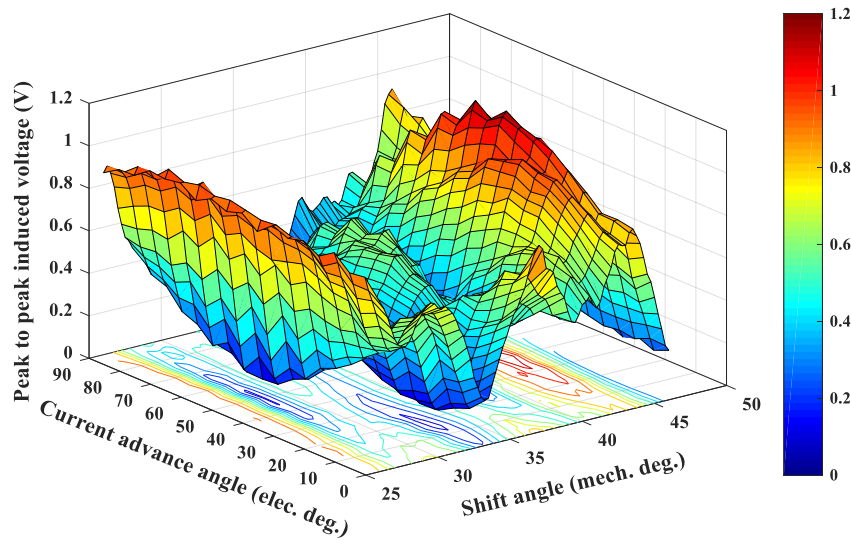


Fig. 5.36. Influence of current and shift angles on peak-to-peak values of the on-load DC winding induced voltages.

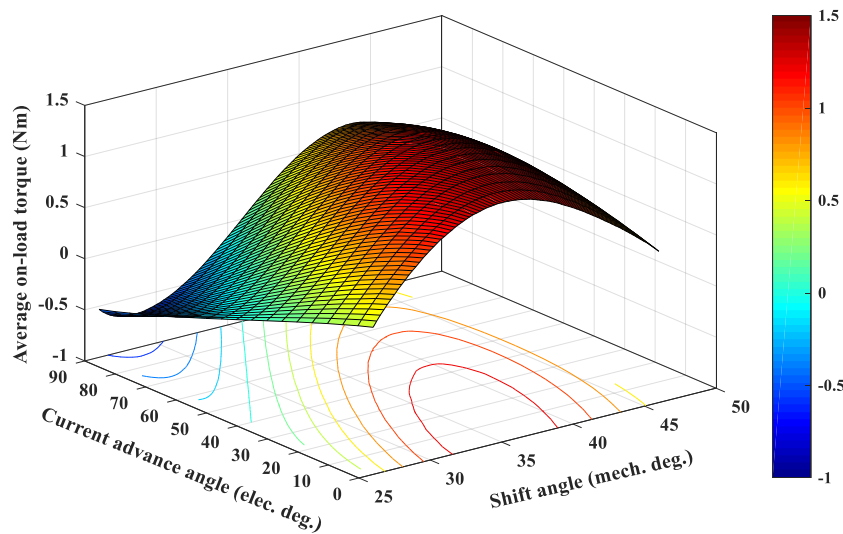
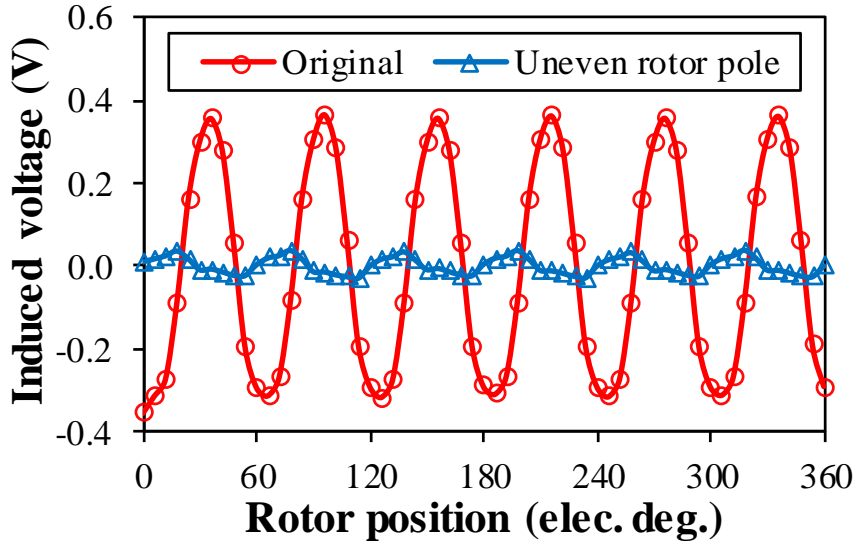


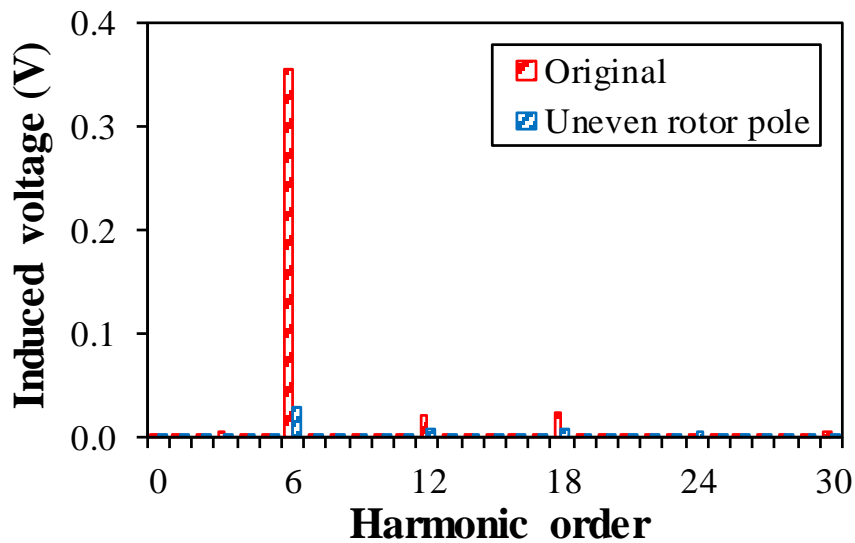
Fig. 5.37. Influence of current and shift angles on average on-load torques.

In order to minimize E_{pp} , the combination of θ_s and θ_e with the maximum E_{pp} reduction ratio is selected, where $\theta_s=38.75^\circ$ and $\theta_e=40^\circ$. As shown in Fig. 5.38(a), the peak-to-peak value of the on-load DC winding induced voltage (E_{pp}) can be effectively reduced by adopting the method of unevenly distributed rotor teeth, i.e., 0.07V and 0.72V for the optimized machines with and without uneven rotor teeth, respectively. Consequently, E_{pp} reduction ratio for this

technique is 90.57%. Likewise, the reduction of E_{pp} is mainly based on the suppression of the 6th on-load DC winding induced voltage harmonic as shown in Fig. 5.38 (b).



(a) Waveforms

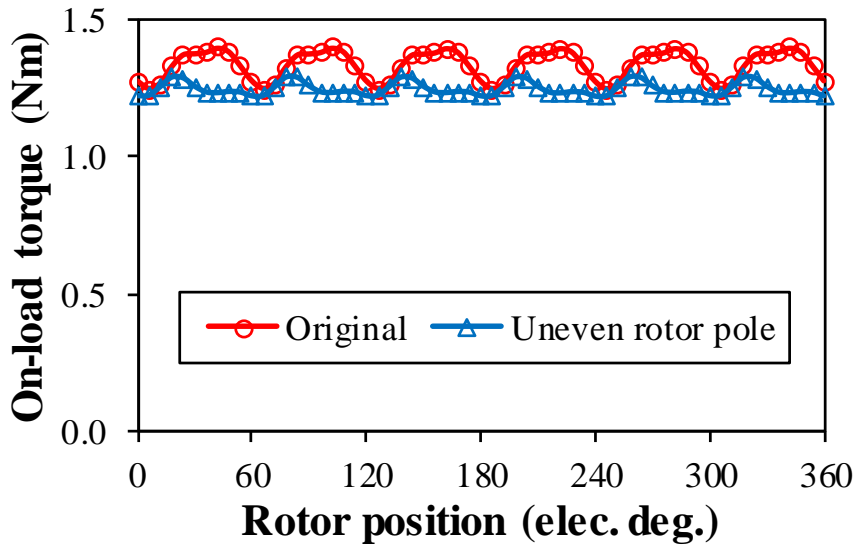


(b) Spectra

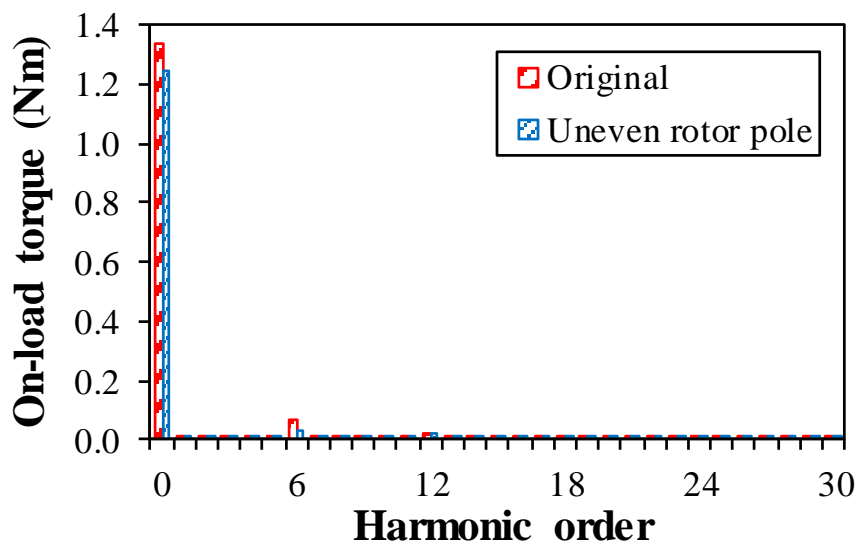
Fig. 5.38. On-load DC winding induced voltage of the 12-slot/10-pole PS-HESFM with unevenly distributed rotor teeth.

As shown in Fig. 5.39, T_{ave} of the optimized machine by adopting unevenly distributed rotor pole is slightly lower than the original machine, i.e., 1.25Nm and 1.33Nm, respectively,

due to a lower phase fundamental back-EMF in armature winding. Therefore, T_{ave} reduction ratio of this method is 6.58%. In addition, the torque ripple T_{rip} is also reduced from 11.46% to 5.77%, i.e., 49.61% T_{rip} reduction ratio, owing to the suppression of the 6th back-EMF harmonic. The main characteristics of the 12-slot/10-pole PS-HESF machine by employing unevenly distributed iron piece rotor pole are listed in Table 5.6.



(a) Waveforms



(b) Spectra

Fig. 5.39. On-load torques of the 12-slot/10-pole PS-HESFM with unevenly distributed rotor teeth.

Table 5.6 Characteristics of PS-HESFM with Unevenly Distributed Rotor Teeth at On-Load

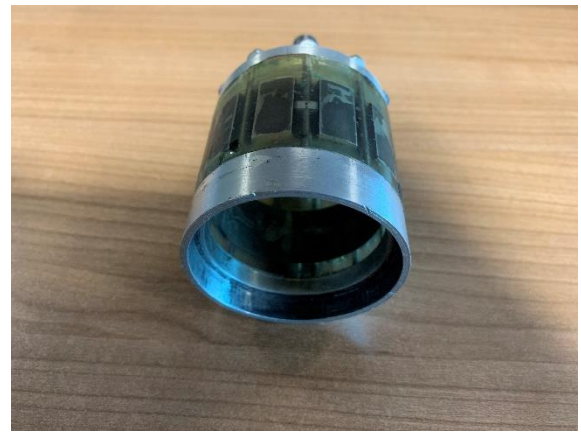
Items	Unit	Values	
		Original	Uneven rotor pole
Machine	-		
E_{pp}	V	0.72	0.07
E_{pp} reduction ratio	%	-	90.57
T_{ave}	Nm	1.33	1.25
T_{ave} reduction ratio	%	-	6.58
T_{rip}	%	11.46	5.77
T_{rip} reduction ratio	%	-	49.61

5.6 Experimental Validation

To validate the foregoing analyses, an existing prototype 12-slot/11-pole PS-HESF machine from the previous research is employed and tested, as shown in Fig. 5.40. Fig. 5.41 shows the FEA predicted and measured phase back-EMFs of the prototype machine. It can be found that a good agreement between the FEA and measured results can be observed. Fig. 5.42 shows the peak phase fundamental back-EMF against DC winding current. It is revealed that the PS-HESF machine exhibits good flux-regulation capability. The measured results are slightly lower than the FEA calculations due to end-effect.



(a) Outer and inner stators



(b) Cup rotor

Fig. 5.40. Prototype of the 12-slot/11-pole PS-HESF machine.

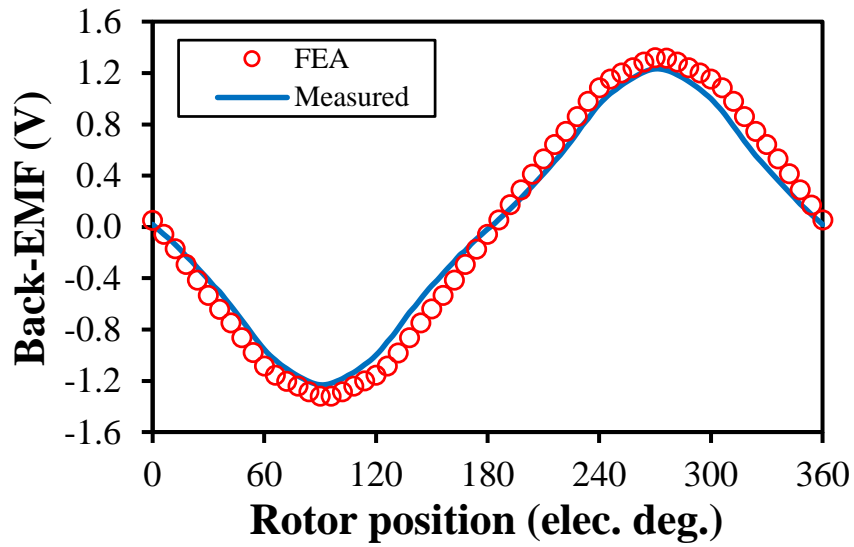


Fig. 5.41. Phase back-EMF under PM excitation only at 400r/min ($I_{dc}=0$).

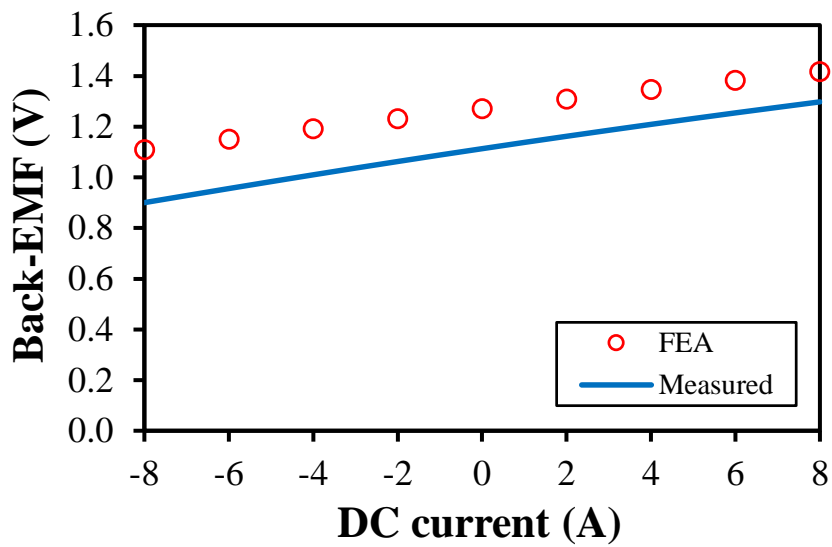
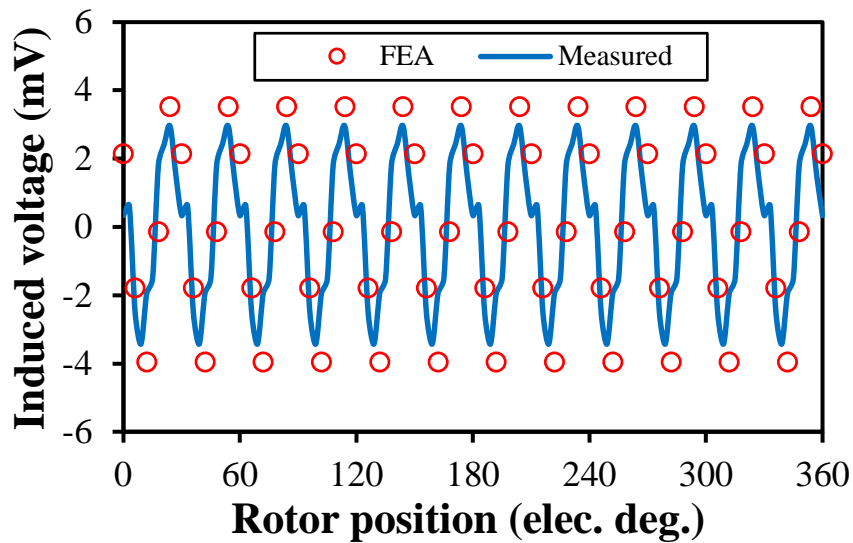
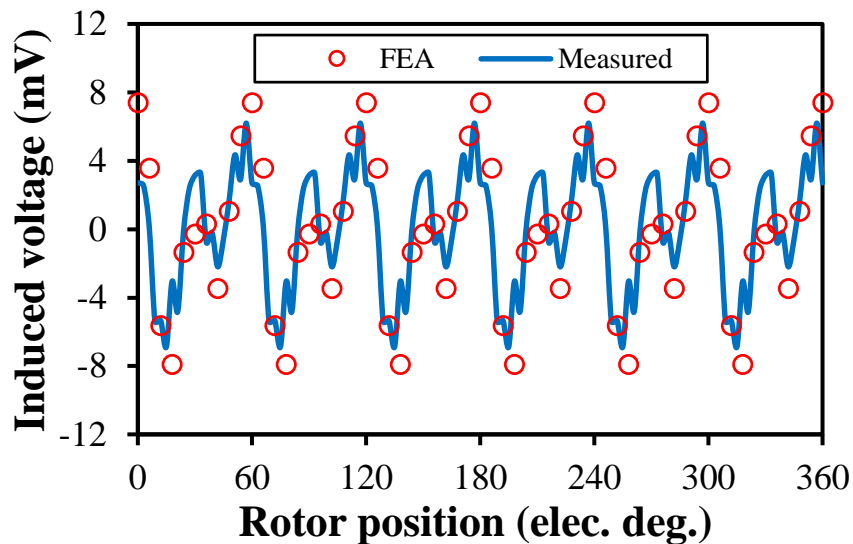


Fig. 5.42. Peak phase fundamental back-EMF against DC winding current at 400r/min.

The measured and FEA predicted DC winding induced voltages under both open-circuit and on-load conditions are compared in Fig. 5.43. It shows that the 12-slot/11-pole PS-HESF machine exhibits negligible DC winding induced voltage at both open-circuit and on-load conditions, which further verifies the analyses in section 5.3.4. The relatively large errors observed between the FEA and measured results are mainly attributed to the end-effect, manufacturing and measuring tolerances.



(a) Open-circuit



(b) On-load

Fig. 5.43. DC winding induced voltages under both open-circuit and on-load conditions at 400r/min.

5.7 Conclusion

This chapter analyses and suppresses the DC winding induced voltage in PS-HESFPM machines under both open-circuit and on-load conditions. The on-load DC winding induced voltage consists of two components, i.e., the open-circuit induced and the armature current induced voltages, respectively. It has been proved that the open-circuit DC winding induced voltage is caused by the variation of the equivalent air-gap magnetic reluctance when the rotor rotates. The variation of the equivalent air-gap reluctance is essentially caused by the doubly salient structure and flux modulation effect of the salient rotor. The armature current induced voltage results from the interaction between three-phase AC armature currents and the mutual inductances between DC field winding and AC armature windings. Rotor pole arc pairing and unevenly distributed rotor teeth are comparatively analyzed by the FEA method for the reduction of the open-circuit and on-load DC winding induced voltages. At open-circuit, by employing these two methods, both the DC winding induced voltage and cogging torque can be effectively reduced, as verified by FEA results. At on-load, the peak-to-peak value of the DC winding induced voltage can be suppressed by 92.81% by employing rotor pole arc pairing, whilst the average on-load torque can be maintained at 92.68%. For unevenly distributed rotor teeth, the peak-to-peak value of the on-load induced voltage can be reduced by 90.57%, whilst the average on-load torque can be maintained at 93.42%. In addition, the torque ripples are also reduced by 29.31% or 49.61% by rotor pole arc pairing or unevenly distributed rotor teeth, respectively.

The analyses presented in this chapter should be applicable to other partitioned stator hybrid excited switched flux PM machines [ZHU18].

CHAPTER 6

Voltage Pulsation Induced in DC Field Winding of Different Hybrid Excitation Switched Flux Machines

Voltage pulsation induced in DC field winding of hybrid excitation machines can cause current ripple in DC field winding and may even lead to unstable field excitation. Moreover, it may also impair the torque performance and complicate the drive, especially at high speed. In this chapter, the voltage pulsation induced in the DC field winding of different hybrid excitation switched flux machines (HESFMs) under both open-circuit and on-load conditions are comparatively studied. It shows that the HESFM topologies significantly affect the DC field winding induced voltage pulsations. To further suppress the induced voltage in field winding, three suppression methods, i.e., rotor step skewing, rotor pole notching, and rotor pole shaping are proposed and compared. It reveals that rotor step skewing has the best suppression performance. Finally, a prototype HESFM with both non-skewed and 2-step skewed rotors are fabricated and tested to confirm the finite element analyses (FEA).

This chapter is based the paper [SUN21b] published in IEEE Transactions on Industry Applications.

6.1 Introduction

Permanent magnet (PM) machines, which employ PMs for field excitation, have distinct advantages of high torque density and high efficiency due to the elimination of DC field excitation. They have been widely developed and employed for various applications [ZHU07] [ZHA18] [KOS10]. However, PM machines still face some problems and challenges. Firstly, the air-gap field produced by the PMs is constant no matter whether the PMs are located in stator side, rotor side, or both sides. Due to current and voltage limits of power inverters, complicated armature winding (AW) current control strategies need to be applied to PM machines for flux-weakening at high-speed operation [JAH86]. Nevertheless, the flux

weakening current may impair the torque/power density and efficiency in flux-weakening region. Besides, the potential irreversible demagnetization of PMs can be another big challenge, owing to the flux-weakening current. Moreover, PM machines may also suffer from serious uncontrolled overvoltage if a fault of control signals of power inverter switches occurs at high speed [LIA05]. Wound field synchronous machines (WFSMs) can be an alternative way to avoid the foregoing issues since they are free from PMs. However, compared with PM machines, WFSMs exhibit reduced torque/power density and efficiency due to DC field windings [ZHU15] [BAS11] [FUK12]. As a consequence, hybrid excitation machines (HEMs) are developed to inherit the merits of PM machines and WFSMs, e.g. high torque/power density, high efficiency, and excellent flux controllability. HEMs feature double field excitations, i.e. PM excitation and DC excitation, respectively. Thus, the air-gap field and the output torque/power can be regulated by controlling the DC field current [ZHU19].

Numerous HEM topologies have been developed and investigated since two excitation sources can be flexibly allocated on stator side, rotor side, or both sides. Based on the location of PMs and DC field windings, they can be broadly categorized as rotor-HEMs, mixed-HEMs, and stator-HEMs, respectively. In rotor-HEMs, PMs and DC field windings are both on the rotor [HEN94] [FOD07] [HWA18]. Most rotor-HEMs are derived from the conventional rotor-PM machines by introducing DC coils into rotor side to improve their flux controllability. As such, rotor-HEMs suffer from reduced system efficiency and reliability due to the utilization of slip rings and brushes for conducting field current. In mixed-HEMs, one excitation source is on the stator while the other is on the rotor [TAP03] [NED11] [CAI20]. For most mixed-HEMs, PMs are placed on rotor side to maintain high torque/power density while DC coils are allocated on stator side to realize brushless operation. Although they are free from sliding contacts, the rotor-PM structure has thermal management and mechanical strength issues, especially at high speed. In stator-HEMs, PMs and DC field windings are both on the stator, due to which they possess the obvious advantages of brushless operation, simple rotor structure, and high operation reliability etc. [ZHA12] [CHE14] [CAI19]. Consequently, stator-HEMs have gained a lot of attention in both academia and industry.

Based on the location of PMs, stator-HEMs mainly fall into four categories, i.e., doubly salient HEMs (stator yoke), flux-reversal HEMs (stator tooth tip), flux-switching HEMs (sandwiched between stator teeth), and stator slot HEMs, respectively [CHA02] [GAO18] [GAU14] [AFI15]. Recently, hybrid excitation switched flux machines (HESFMs), as a type of stator-HEMs, have been comprehensively developed and analyzed, owing to flux-concentrating effect and hence high torque/power density. The very first HESFM is obtained via the replacement of half the number of PMs with DC field coils and therefore the air-gap field is alternately established by PM flux and DC flux [AKE01]. Based on the conventional U-core SFPM machine, a novel HESFM is developed by attaching an extra iron ring to provide the flux path for DC field winding [HOA07]. In [HUA09], hybrid excitation is accomplished by means of reducing the volume of PMs to release some space for DC field winding. Besides, the influence of relative positions of PMs and DC coils on machine characteristics has also been investigated [HUA15]. Furthermore, in order to improve the flux control capability, different magnetic iron bridges are introduced and evaluated [OWE10]. To improve the flux controllability of the conventional U-core SFPM machine, a parallel HESFM is proposed by alternately arranging PM excited pole-pairs and DC excited pole-pairs along the stator teeth [OWE09]. Based on the conventional E-core SFPM, a novel HESFM is proposed in [CHE11] by allocating DC field coils on the middle teeth of the E-core stator. To ease the crowded stator in conventional HESFMs, i.e., with AC winding, DC winding, and PMs all in one stator, a novel partitioned-stator (PS) HESFM is proposed, which features enhanced torque capability and improved flux controllability compared to its conventional single stator counterpart due to improved inner space utilization ratio [HUA17].

By far, most literature focuses on developing and investigating novel HEM topologies and very few papers address the parasitic effects of HEMs. Voltage pulsation induced in DC field winding is an important parasitic effect in HEMs and cannot be ignored, especially at high speed. It can cause current ripple in DC field winding and may even lead to unstable field excitation, due to which additional torque/speed oscillations and losses may be produced as well. Besides, it may also impair the torque performance and complicate the drive system,

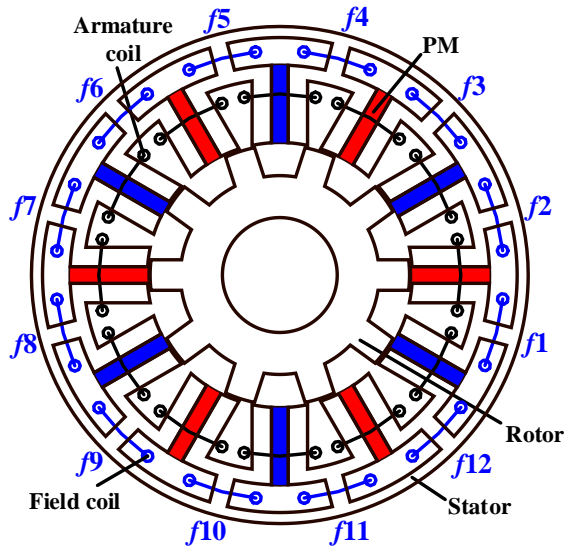
especially at high speed. The DC winding induced voltage issue is firstly investigated in [WU19a] [WU20] [WU18] by considering the influence of the open-circuit, the armature reaction field, and the DC winding configuration, respectively, based on three-phase WFSFMs having partitioned stators. Besides, the DC winding induced voltage in five-phase WFSFMs are analyzed in [WU19b] and [ZHA21]. Furthermore, the investigations of the induced voltage issue are extended to hybrid excited machines (HEMs) in [SUN20a] and [SUN21a]. In [SUN20a], the induced voltage in a 12-slot/10-pole HESF machine proposed in [OWE10] is investigated and suppressed. Moreover, in [SUN21a], the influence of slot-pole number combinations is studied since the investigation in [SUN20a] is restricted to a specific slot-pole number combination, i.e., 12-slot/10-pole. The HESFM topologies are diverse but there are no references for the selection of appropriate HESFMs to minimize the induced voltage pulsation in DC field winding. Therefore, the comparison of the DC winding induced voltage pulsations in typical HESFM topologies is important and necessary, which will be the subject of this paper. Firstly, both no-load and on-load induced voltage pulsations in DC field windings are compared between different HESFM topologies, aiming to provide initial guidance to select appropriate HESFM topologies with a low pulsating voltage. As an extension to [SUN20b], three rotor-based methods are subsequently proposed and compared to further reduce the pulsating voltage.

The chapter is organised as follows. In section 6.2, the machine topologies and operation principles of different HESFMs are illustrated and explained. Then, in section 6.3, the voltage pulsations induced in the DC field windings of different HESFMs are studied and compared under no-load, AC currents only, and on-load, respectively. Three rotor-based methods are proposed in section 6.4 to further reduce the pulsating voltage. Finally, experimental validation on a prototype HESFM is given in section 6.5, followed by conclusions in section 6.6.

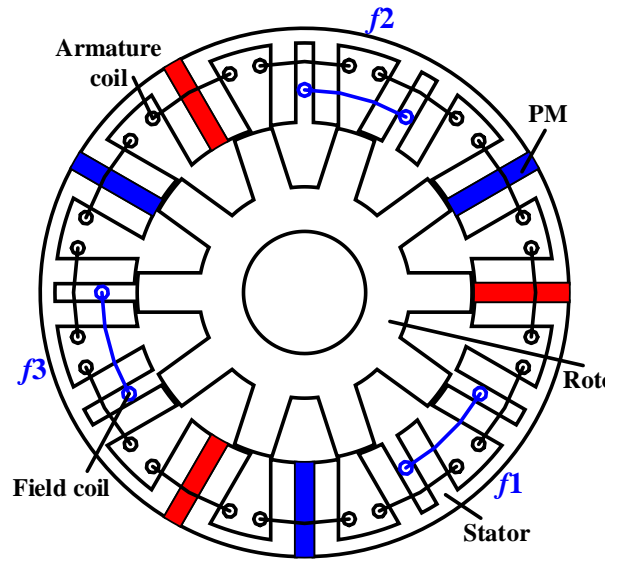
6.2 Hybrid Excitation Switched Flux Machine Topologies

6.2.1 Machine Topologies

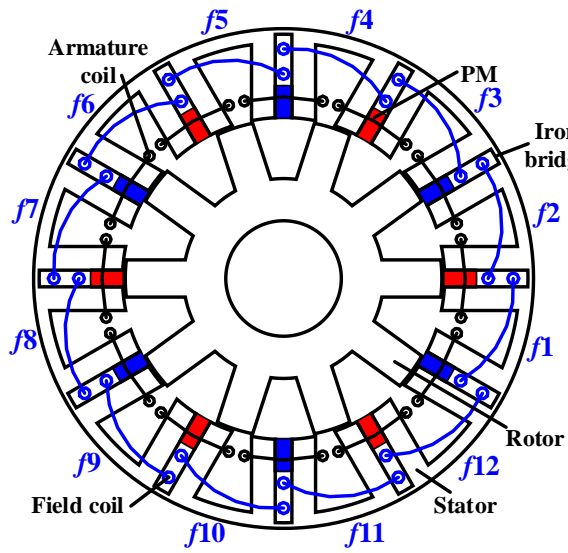
Figs. 6.1(a)-(e) show the investigated HEM topologies, which are referred as HE1, HE2, HE3, HE4, and HE5, respectively. In fact, these machines belong to the same family, i.e., HESFMs, and they are derivatives of the conventional U-core and E-core SFPM machines. Therefore, concentrated non-overlapping armature coils and tangentially magnetized PMs are inherited from the SFPM machines. The PMs are sandwiched between the stator teeth in the machines from HE1 to HE4, while the PMs are inserted into the inner stator yoke in HE5. HE1 employs an outermost iron bridge to place DC field coils, while HE3 reduces its magnet volume to vacate the space for DC field coils. In HE2, PM excited pole-pairs and DC excited pole-pairs are alternately allocated along the stator teeth. HE4 accommodates DC field coils on the middle teeth of its E-core stator, while HE5 adopts an additional inner stator for PMs and DC field coils to improve inner space utilization. Moreover, concentrated non-overlapping DC field coils are adopted in these machines for short end-winding, good fault-tolerant capability, and compact volume. For each phase of armature windings, different armature coils are series-connected. Similarly, the DC field coils of each machine's field winding are series-connected as well. The field windings of HE1, HE3 and HE5 contain 12 DC field coils (f_1, f_2, \dots, f_{12}), while the field windings of HE2 and HE4 contain 3 (f_1, f_2, f_3) and 6 DC field coils (f_1, f_2, \dots, f_6), respectively, as shown in Fig. 6.1. Basic geometric parameters of each HESFM can be found in Table 6.1. It is worth mentioning that HE3 machine has been investigated in chapters 3 and 4 while HE5 machine has been investigated in chapter 5. HE1, HE2, and HE4 machines have not been investigated in previous chapters.



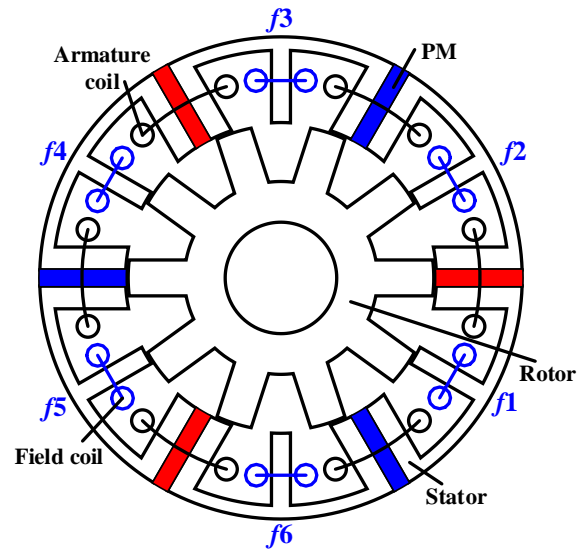
(a) HE1 [HOA07]



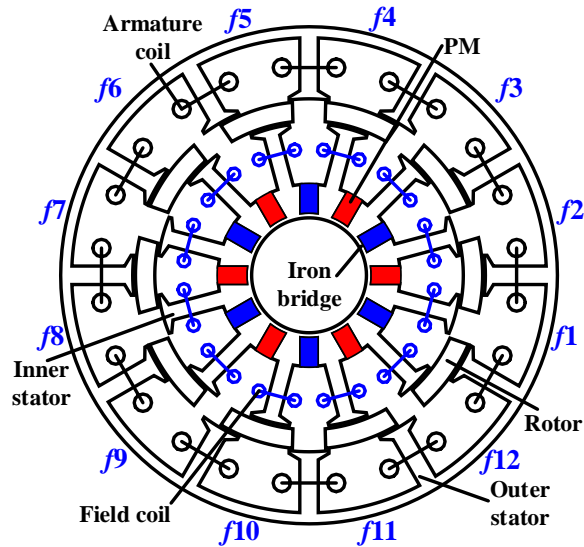
(b) HE2 [OWE09]



(c) HE3 [OWE10]



(d) HE4 [CHE11a]



(e) HE5 [HUA17]

Fig. 6.1. Different HESFM topologies.

6.2.2 Operation Principles

As a matter of fact, the operation principles of these HESFMs are very similar. Under open-circuit condition, bipolar flux-linkage and back-EMF are generated in each phase of armature windings as the rotor rotates. The air-gap field is excited by the PMs and DC field coils simultaneously. The PM excited air-gap field is fixed while the DC excited one is variable. The direction and strength of the DC excited field can be easily adjusted by controlling the polarity and magnitude of the current in DC field coils, and consequently, the resultant air-gap field and the output torque are regulatable. These machines are known as parallel HESFMs, in which the PM flux and DC excitation flux have different trajectories, i.e. the DC flux does not go through the PMs. To generate the same DC excited flux, the required DC winding ampere-turns are much lower for parallel HESFMs compared with series HESFMs (DC flux passes through PMs), since the reluctance of the DC flux path is low. Therefore, they exhibit good flux-controllability. In addition, the PMs do not suffer from the risk of irreversible demagnetization, as the DC flux does not pass them.

Table 6.1 Basic Geometric Parameters of Each HESFM

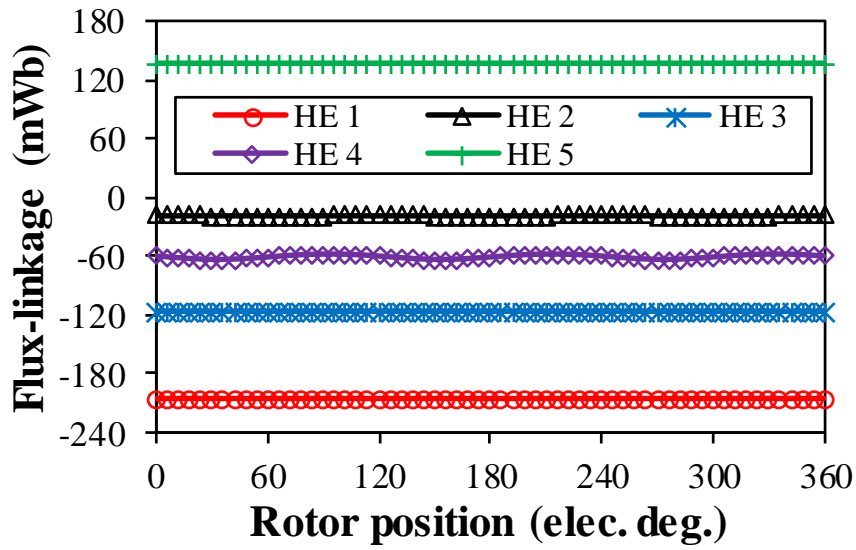
Parameters	Unit	HE1	HE2	HE3	HE4	HE5
Stator pole number, N_s	-	12	6	12	6	12
Rotor pole number, N_r	-			10		
Outer stator outer radius	mm			45		
Stack length	mm			25		
Outer stator yoke thickness	mm	2.5	2.5	2.5	3.8	2
Outer stator inner radius	mm	24	29	29	29	32
Outer stator tooth arc	°	8.5	8.5	8.5	7.5	13
Air-gap length	mm			0.5		
Rotor tooth height	mm	5.5	10.5	10.5	10.5	3.5
Rotor outer pole arc	°	13.5	13.5	13.5	12	25
Rotor inner pole arc	°	17.7	21.5	21.5	19.1	24
Iron bridge length	mm	2	N/A	0.5	N/A	0.5
PM remanence	T			1.2		
PM coercivity	kA/m			890		
Rotor shaft/inner stator radius	mm			10.4		
Rotor yoke thickness	mm	7.6	7.6	7.6	7.6	N/A
Inner stator yoke thickness	mm	N/A	N/A	N/A	N/A	6.1
Inner stator outer radius	mm	N/A	N/A	N/A	N/A	27.5
Inner stator tooth arc	°	N/A	N/A	N/A	N/A	15
PM width	mm	3	3	3	3.8	3
PM height	mm	14	16	5.6	16	5.6

6.3 Voltage Pulsation Induced in DC Field Winding

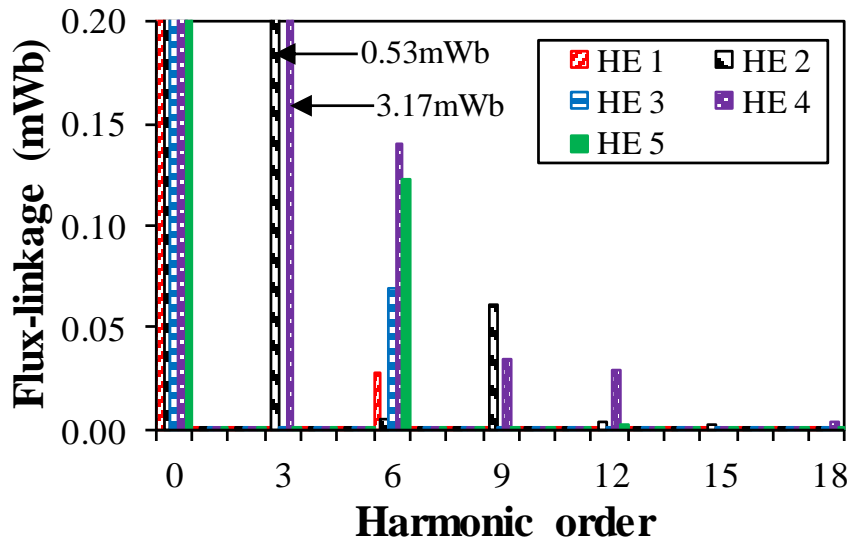
6.3.1 No-load Induced Voltage

It is worth mentioning that the FEA results illustrated in this paper are obtained from the commercial FEA package Ansys Maxwell using 2-dimensional transient solver. In HEMs, a constant DC excitation current is preferred in DC field winding under steady state from the perspective of both machine design and drive. It is expected that the flux-linkage of DC field winding is invariable if the injected DC excitation current is constant. Accordingly, voltage will not be induced in DC field winding since there is no variation of the field winding flux-linkage. But in reality, there are a lot of harmonics in the field winding flux-linkage of each HESFM apart from the DC component at no-load condition (with PMs and fixed DC current), as shown in Figs. 6.2(a) and 6.2(b). Therefore, pulsating voltages are produced in the field windings of different HESFMs due to the field winding flux-linkage pulsations, as illustrated in Figs. 6.3(a) and 6.3(b).

It reveals that the main difference between the no-load field winding induced voltage pulsation of each HESFM lies in two aspects. Firstly, the harmonic contents are different. It is shown in Fig. 6.3(b) that the resultant voltage harmonic orders are $6M$ for HE1, HE3 and HE5 while $3M$ for both HE2 and HE4, in which M should be a positive integer. Secondly, the peak to peak values of the voltage pulsations are different. HE2 and HE4 exhibit comparatively higher no-load pulsating voltages, i.e. 1.74V and 7.73V than HE1, HE3 and HE5, i.e. 0.15V, 0.33V and 0.63V, respectively. This is primarily attributed to the differences in harmonic content and the amplitude of low order harmonics.



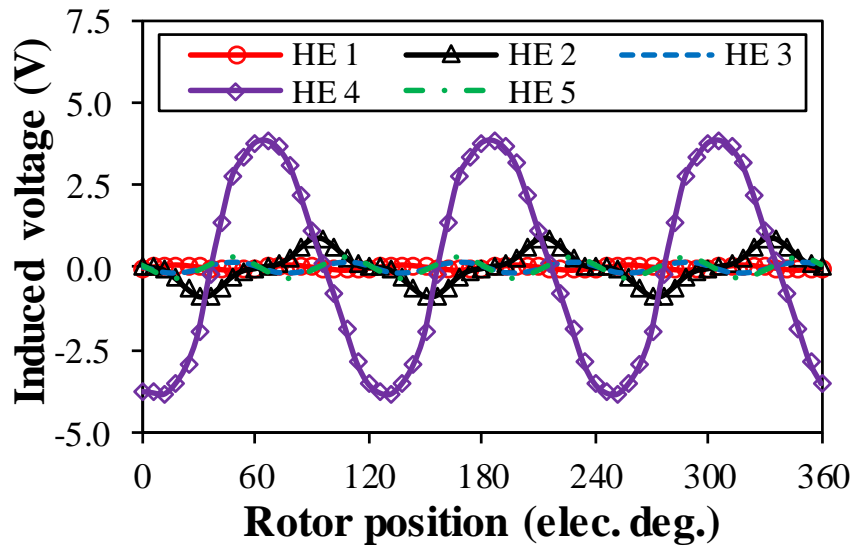
(a) Waveforms



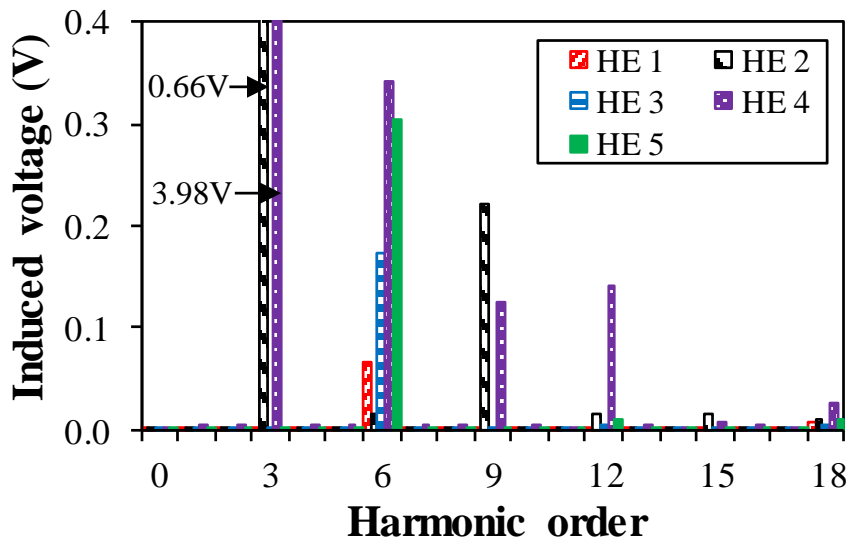
(b) Spectra

Fig. 6.2. No-load DC field winding flux-linkages of different HESFM.

A new parameter, i.e. voltage pulsation ratio (VPR), is introduced and expressed in (6.1) to reveal the influence of the induced voltage pulsation, where E_{IV} is the peak to peak value of the induced voltage pulsation in field winding, V_{DC} is the voltage drop of the field winding caused by electrical resistance. The no-load VPRs from HE1 to HE5 are 3.4%, 153%, 7.3%, 340.7%, and 13.9%, respectively. The HESFM with E-core stator (HE4) has the highest no-load E_{IV} and VPR among those machines since it contains abundant harmonics and the amplitudes of low order harmonics are quite high.



(a) Waveforms

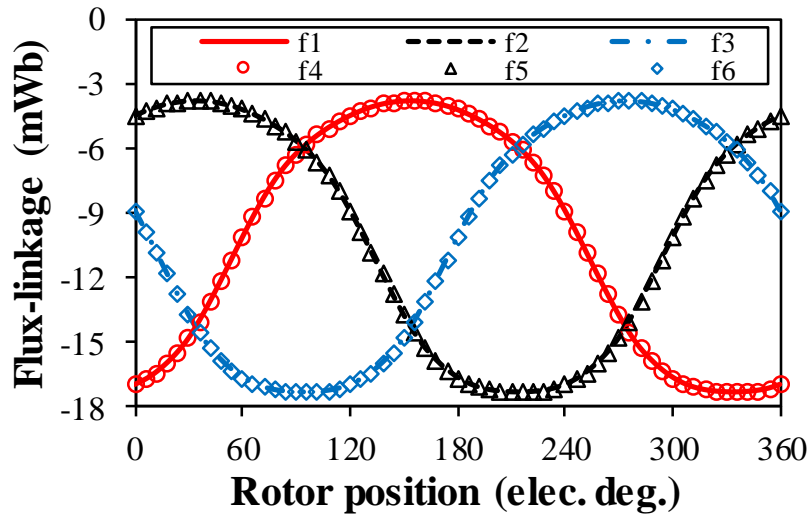


(b) Spectra

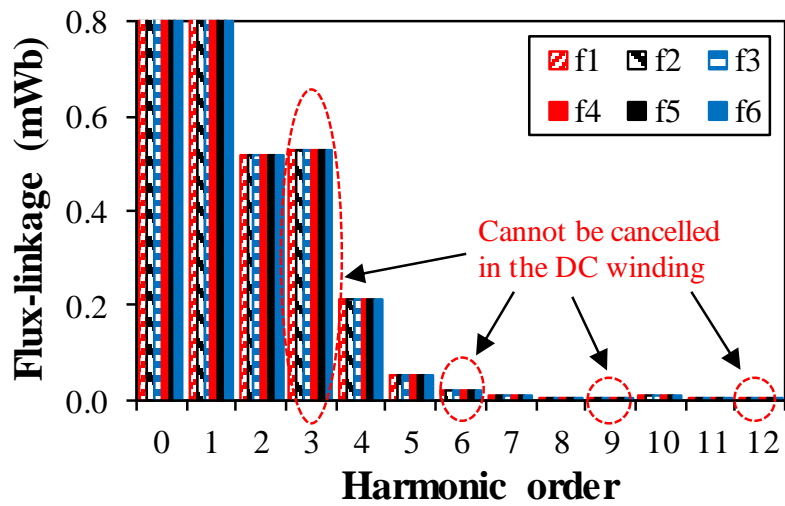
Fig. 6.3. No-load DC field winding induced voltage pulsations of different HESFM at 400rpm.

$$\text{VPR} = \frac{E_{IV}}{V_{DC}} \times 100\% \quad (6.1)$$

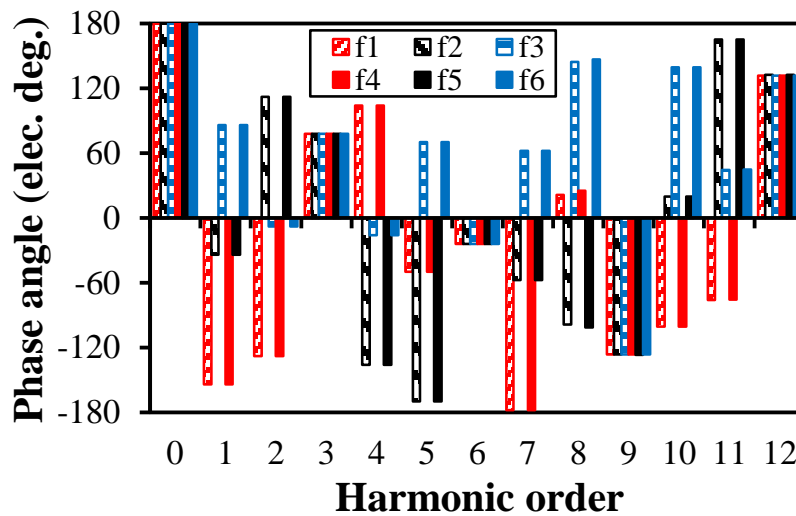
In order to explain the cause of the no-load induced voltage pulsation in field winding, the HESFM with E-core stator (HE4) is taken as an instance. HE4 has 6 field coils in the DC winding as illustrated in Fig. 6.1(d). As shown in Fig. 6.4, the flux-linkages of the field coils are variable versus the electric position (θ_e) of rotor and they contain both DC components and other harmonics. By way of example, the minimum value of the flux-linkage of DC field coil f_1 (Φ_1) occurs at $\theta_e=156^\circ$, while the maximum value of Φ_1 occurs at $\theta_e=336^\circ$. By referring to the flux distributions illustrated in Fig. 6.5(a), it can be observed that the maximum reluctance of Φ_1 occurs at $\theta_e=156^\circ$ since the middle tooth of the E-core stator that accommodates f_1 does not align with a rotor tooth but align with the middle of a rotor slot and hence very little flux pass through it. At $\theta_e=336^\circ$, the middle tooth of the E-core stator that with f_1 on it aligns with a rotor tooth and thus the majority of fluxes can flow through it, since Φ_1 's reluctance is minimum at this rotor position as depicted in Fig. 6.5(b). The variation of the flux-linkage exists in other field coils at the same time but with different phase angles for different coils as depicted in Fig. 6.4(a). As a matter of fact, 6 field coils possess the same flux-linkage spectrum as shown in Fig. 6.4(b). Besides, aside from the DC component and the harmonics of $3M$, the phase displacement is 120° between the corresponding harmonics of two adjoining field coils, as shown in Fig. 6.4(c). As a result, pulsating voltages are produced in the field coils as shown in Figs. 6.6(a) and 6.6(b), and likewise, they possess the same voltage spectrum and the phase displacement between the corresponding harmonics of two adjoining field coils is 120° as well, apart from the harmonics of $3M$, as shown in Fig. 6.6(c). At no-load condition, the above phase displacements from HE1 to HE5 are 60° , 120° , 60° , 120° , and 60° , respectively.



(a) Waveforms



(b) Spectra



(c) Initial phase

Fig. 6.4. No-load DC field coil flux-linkages of HE4 (E-core stator).

Different from other field coil flux-linkage/induced voltage harmonics, the corresponding harmonics of $3M$ have the same initial phase and hence they are in-phase. Therefore, the harmonic orders of $3M$ in different field coil flux-linkages shown in Fig. 6.4(b) cannot be counteracted in the DC field winding as shown in Fig. 6.2(b) and so do the field coil induced voltage harmonics illustrated in Fig. 6.6(b), which is confirmed in Fig. 6.3(b). For different machines, the harmonic orders (kM) of the flux-linkage/induced voltage pulsation in the field winding are different at no-load, i.e. $6M$, $3M$, $6M$, $3M$, and $6M$ for the HESFMs from HE1 to HE5, respectively. Furthermore, it can be described by (6.2), where LCM is the least common multiple. The number of stator/rotor pole (N_s/N_r) for the HESFMs from HE1 to HE5 is 12/10, 6/10, 12/10, 6/10, and 12/10, respectively.

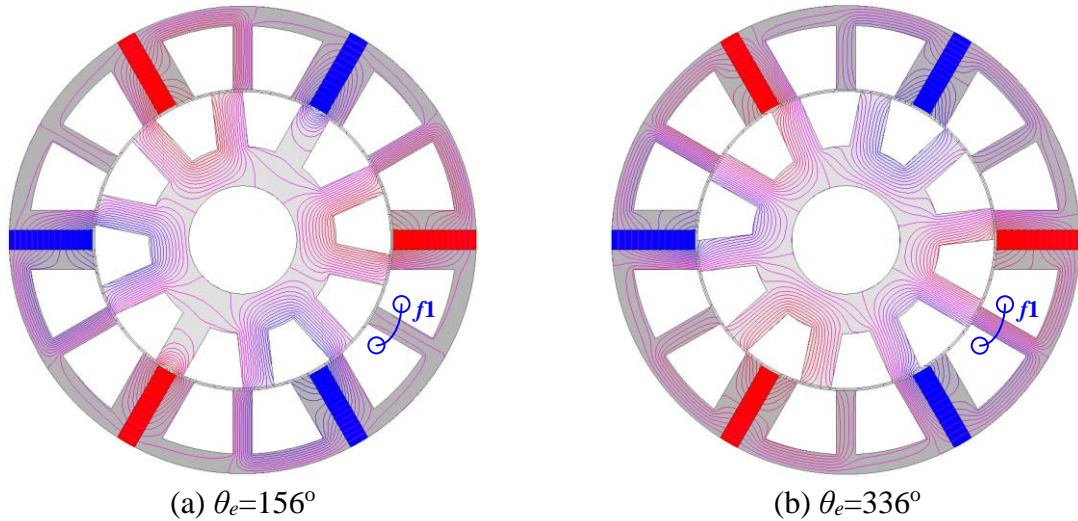
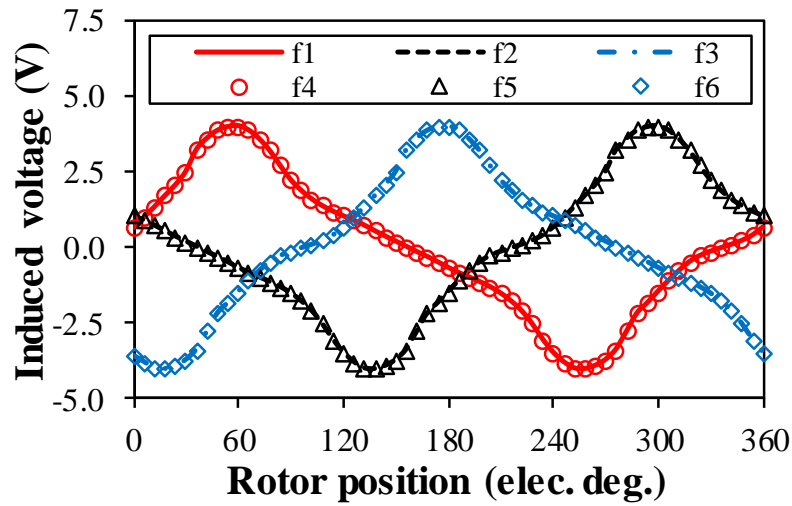
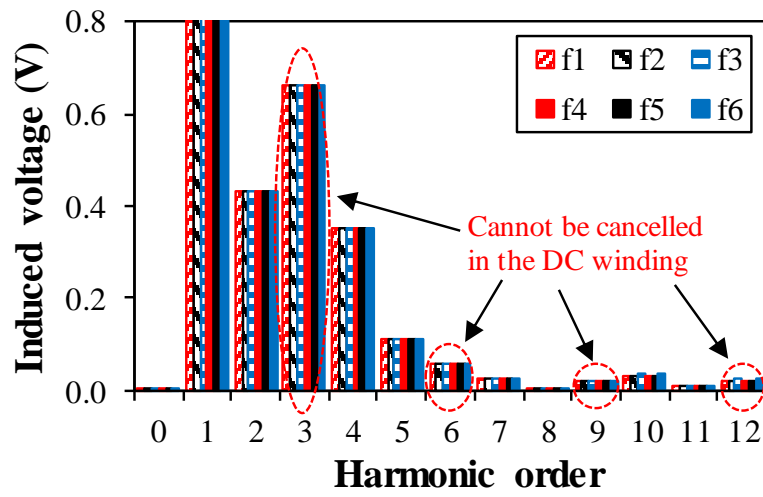


Fig. 6.5. No-load flux distributions of HE4 (E-core stator) at different rotor positions.

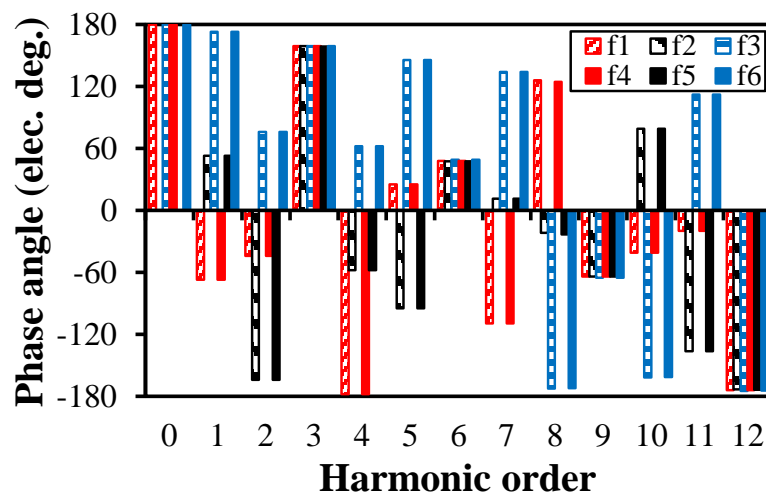
Based on the foregoing analyses, it can be concluded that the no-load induced voltage pulsation in field winding is resulted from the variation of the permeance in the air-gap with the change of the rotor position, owing to the utilization of doubly salient machine structures in all of these HESFMs. To be more specific, it is attributed to the self-inductance of the field winding and the equivalent mutual inductance between the PMs and the field winding. Owing to the doubly salient machine structure, the variation of the permeance in the air-gap cannot be avoided, as the HESFMs need to operate based on the doubly salient structure to generate variable flux-linkage/induced back electromotive force (back-EMF) in armature windings, and thus to produce a steady output torque.



(a) Waveforms

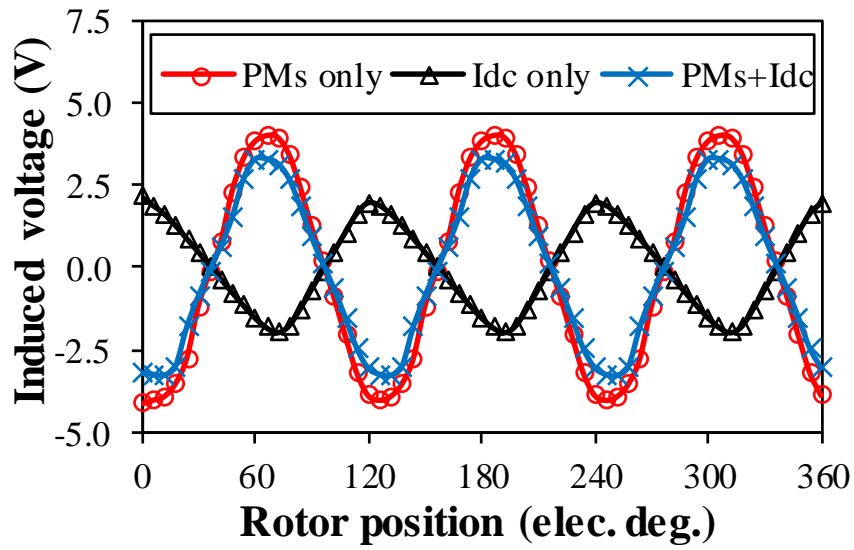


(b) Spectra

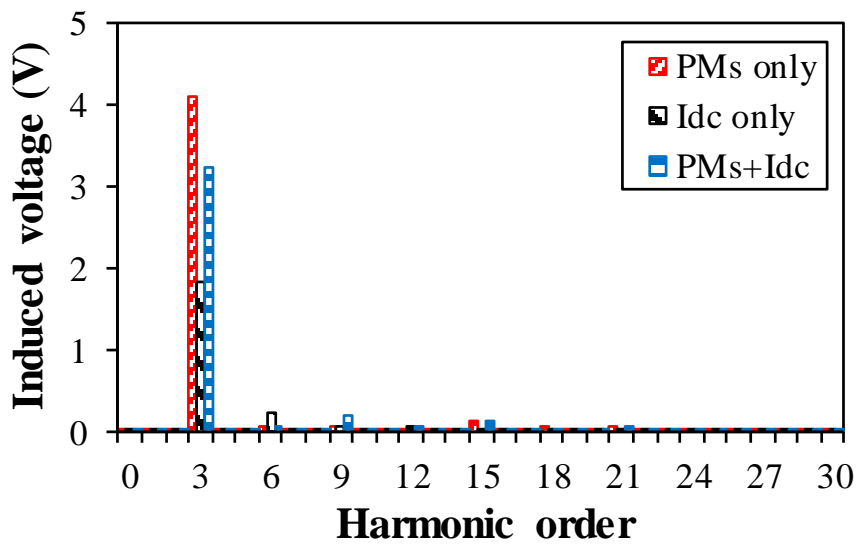


(c) Initial phase

Fig. 6.6. No-load DC field coil induced voltage pulsations of HE4 (E-core stator) at 400rpm.



(a) Waveforms



(b) Spectra

Fig. 6.7. No-load DC field winding induced voltage pulsations of HE4 (E-core stator) with different excitations at 400rpm.

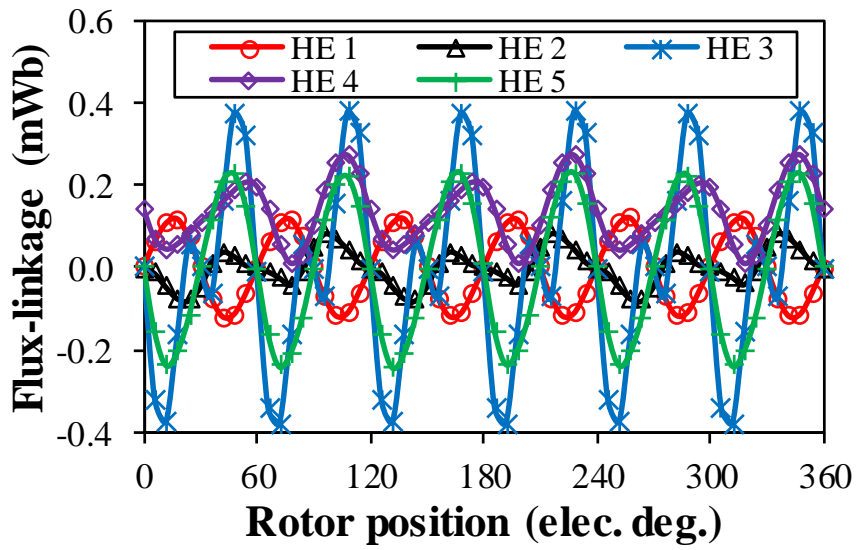
Fig. 6.7 shows the no-load field winding induced voltages of HE4 with different field excitations. In wound field synchronous machines, the no-load field is excited by the DC current of field winding only. Therefore, the no-load induced voltage is attributed to the interaction between the air-gap permeance and the magnetomotive force (MMF) of field winding, which corresponds to the black solid line with markers (with $I_{dc}=4A$ only) as shown in Fig. 6.7(a).

Different from WFSMs, the no-load pulsating voltage in field winding of HESFMs results from the interaction between the air-gap permeance and the MMF of both PMs and field winding, i.e. the blue solid line with markers (with PMs and $I_{dc}=4A$), as illustrated in Fig. 6.7(a). As shown in Fig. 6.7(a), there is still a high voltage pulsation in the field winding of HE4 even if the field current is zero, i.e. the red solid line with markers (with PMs only), which is due to the contribution of the MMF of PMs. Moreover, the peak to peak values of the induced voltage pulsations are different with different field excitations, owing to different no-load field distributions, but the harmonic orders remain unchanged, i.e. $3M$, as depicted in Fig. 6.7(b).

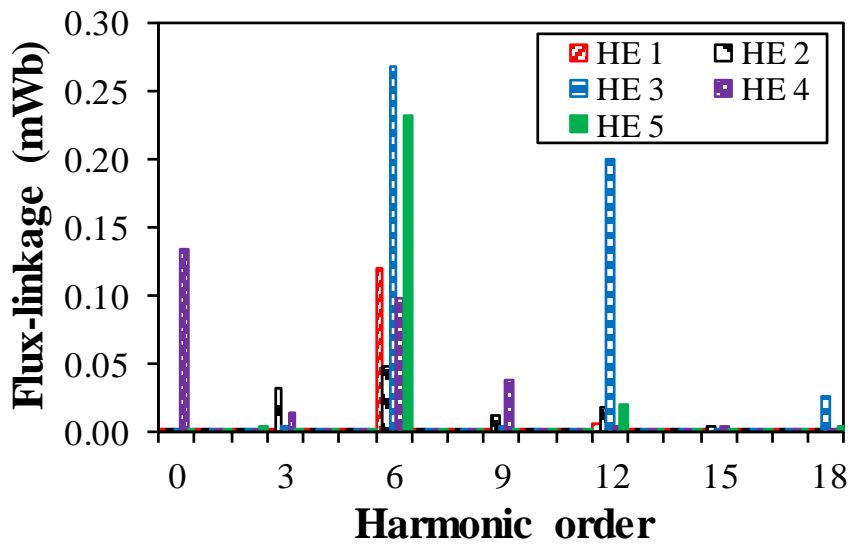
$$kM = \frac{\text{LCM}(N_s, N_r)}{N_r} M \quad (6.2)$$

6.3.2 AC Current Induced Voltage

When the armature windings of each HESFM are fed by three-phase AC currents and the PM and DC excitations are removed, the field winding flux-linkage of each machine still suffers from many harmonics as illustrated in Fig. 6.8. Voltages are therefore generated in the field winding of each HESFM as shown in Fig. 6.9. The resultant voltages shown in Fig. 6.9 are the AC current induced field winding voltage pulsations, which are attributed to the mutual inductances between armature and field windings. It should be noted that the injected three-phase AC currents in armature windings are pure sinusoidal currents and free from any other harmonics. Therefore, the AC current induced voltage pulsations are attributed to the harmonics of the mutual inductances between armature and field windings. As illustrated in Figs. 6.8(b) and 6.9(b), the harmonic orders of the field winding flux-linkages/induced voltage pulsations caused by AC currents are $3M$ for HE2 and HE4 but $6M$ for HE1, HE3 and HE5. It can also be observed that the harmonic orders of the AC current induced voltage pulsations are the same as that caused by no-load for each HESFM and can be described by (6.2) as well.



(a) Waveforms

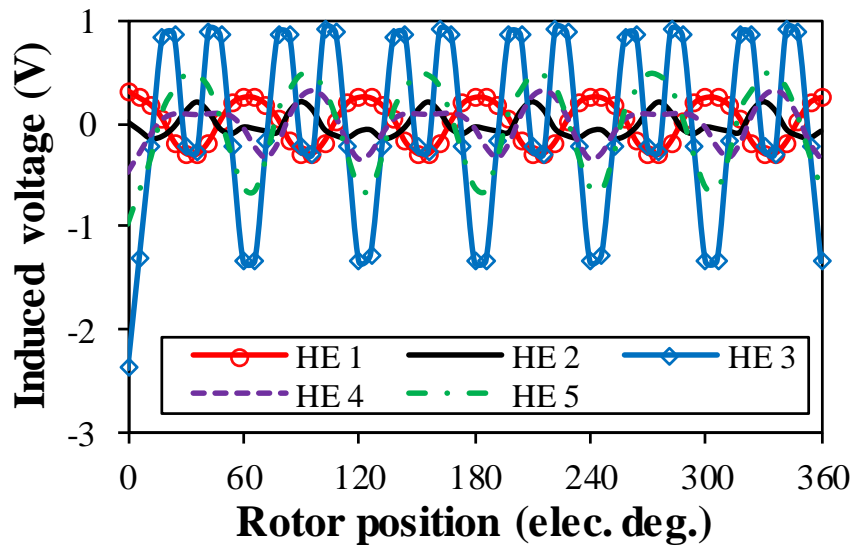


(b) Spectra

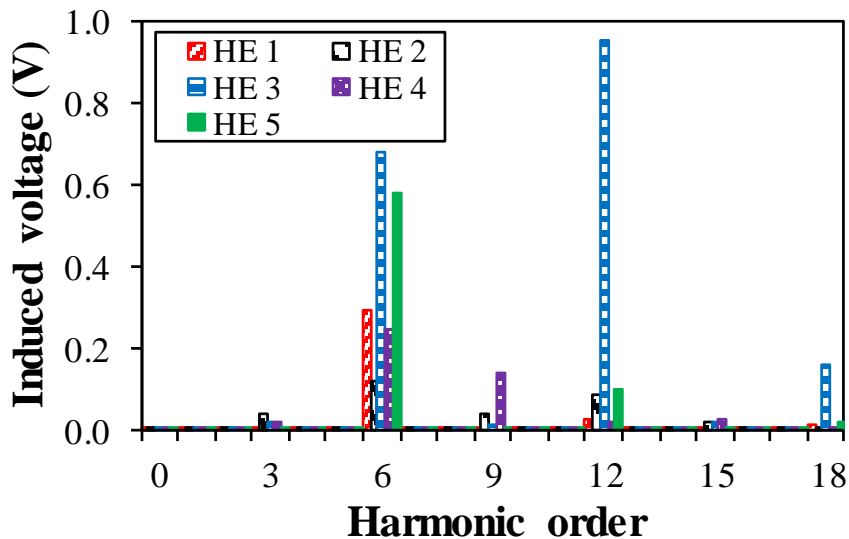
Fig. 6.8. DC field winding flux-linkages with AC currents excitation only.

Figs. 6.10 and 6.11 show the field coil flux-linkages and induced voltage pulsations of HE4 with AC currents excitation only. Similar to no-load condition, the flux-linkage/induced voltage pulsation of each field coil in HE4 possess the same spectrum as depicted in Figs. 6.10(b) and 6.11(b). Apart from the harmonic orders of $3M$, the phase displacement between the corresponding harmonics of two adjoining field coils is the same as that at no-load, i.e. 120° . As a result, only the corresponding harmonic orders with $3M$ may exhibit in the resultant field

winding flux-linkages and induced voltage pulsations since they are in-phase, as shown in Figs. 6.10(c) and 6.11(c). For the HESFMs from HE1 to HE5, the phase aforementioned displacement is 60° , 120° , 60° , 120° , and 60° , respectively, which is attributed to the difference of machine topologies. As a result, the HESFM topologies significantly affect the harmonic orders and peak to peak values of the field winding induced voltage pulsations caused by no-load and AC currents.

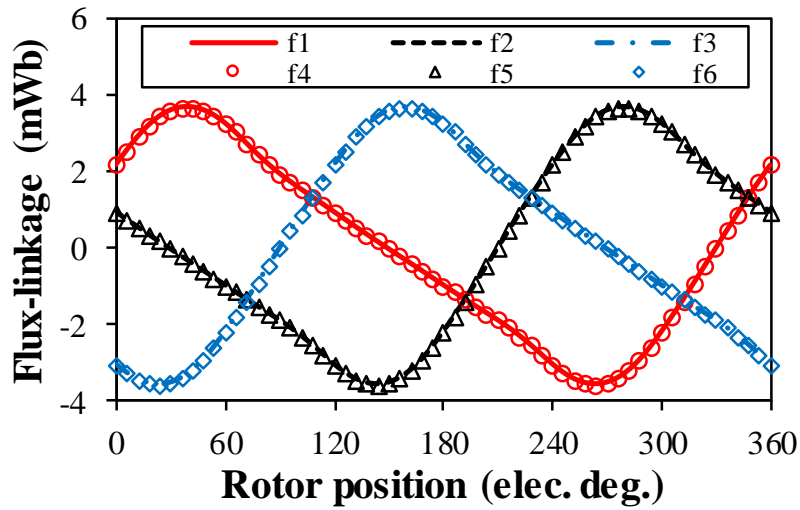


(a) Waveforms

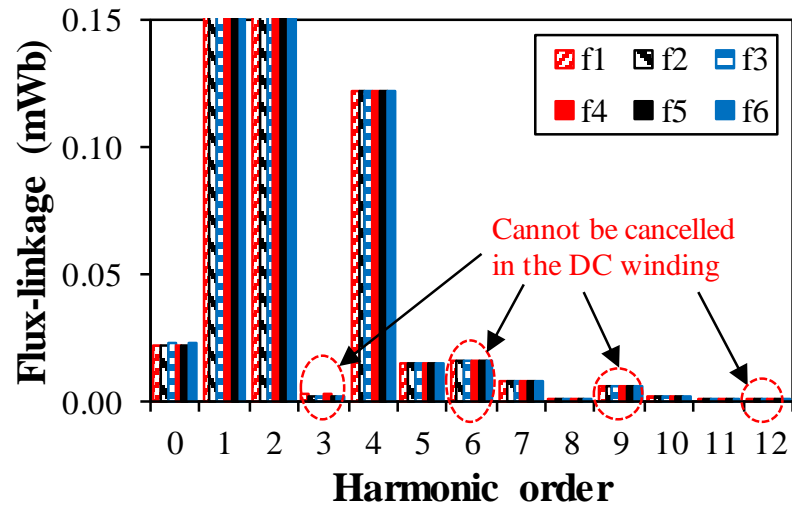


(b) Spectra

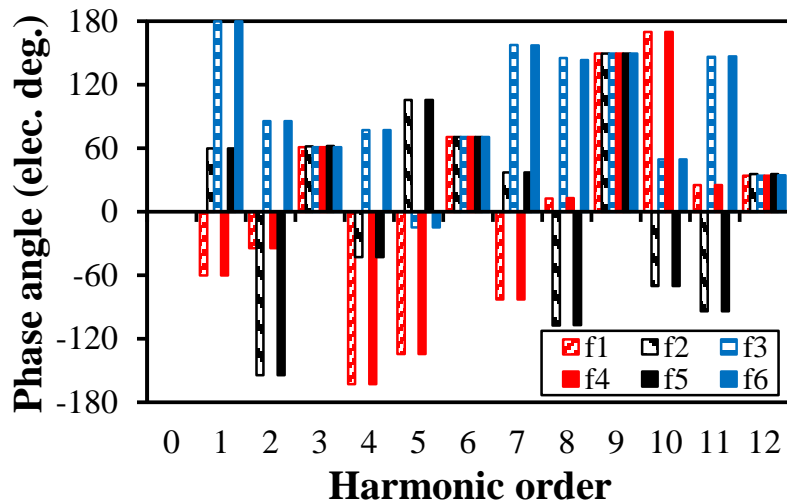
Fig. 6.9. DC field winding induced voltage pulsations with AC currents excitation only at 400rpm.



(a) Waveforms

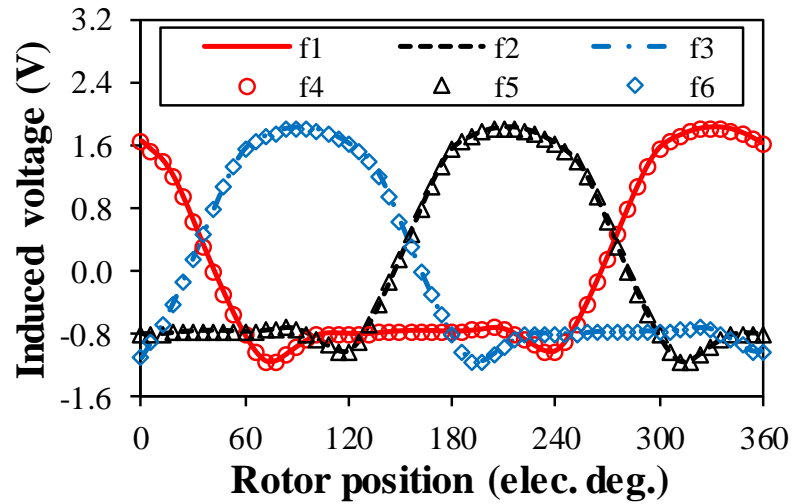


(b) Spectra

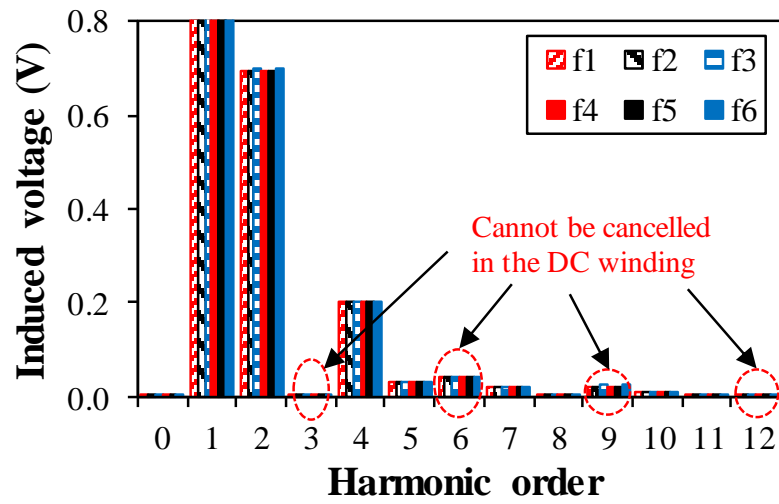


(c) Initial phase

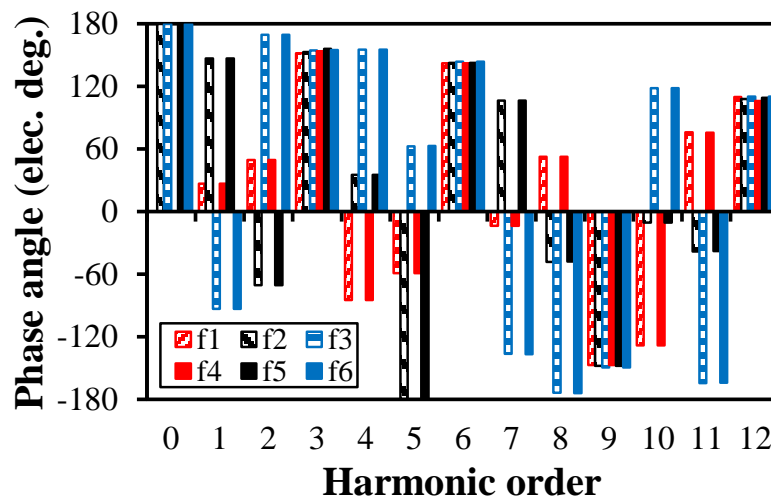
Fig. 6.10. DC field coil flux-linkages of HE4 (E-core stator) with AC currents excitation only.



(a) Waveforms



(b) Spectra

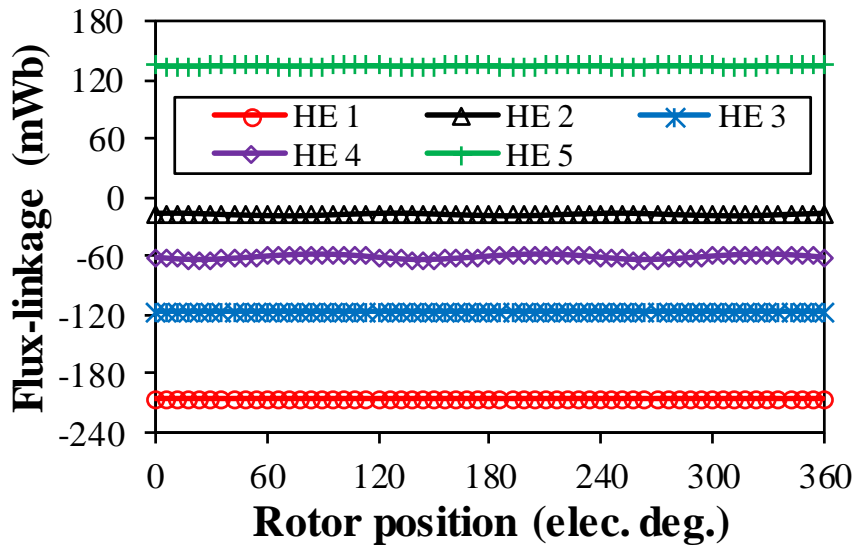


(c) Initial phase

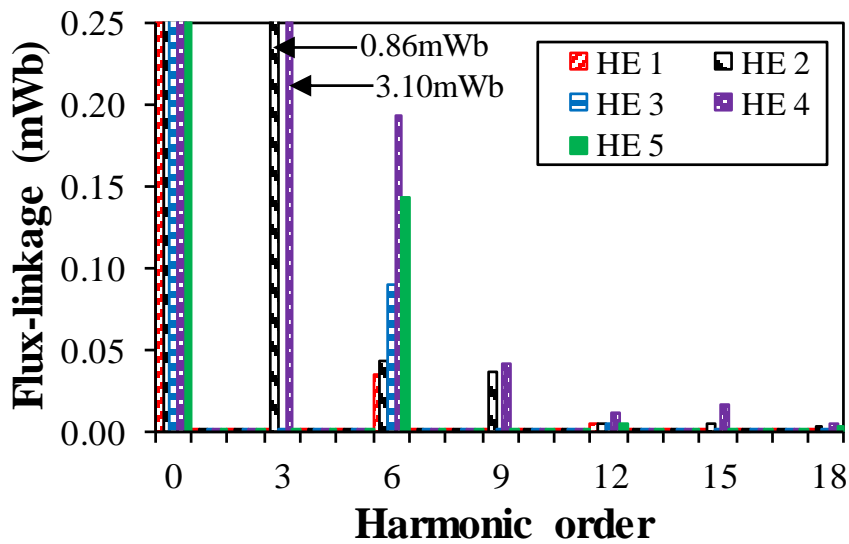
Fig. 6.11. DC field coil induced voltage pulsations of HE4 (E-core stator) with AC currents excitation only at 400rpm.

6.3.3 On-load Induced Voltage

Figs. 6.12 and 6.13 show the on-load (with PMs, DC, and AC currents) flux-linkage and induced voltage pulsation in the field winding of each HESFM. At on-load condition, the field winding of each machine suffers from the no-load and the AC current induced voltage pulsations simultaneously. As illustrated in Fig. 6.3(b), the harmonic orders of the no-load induced voltage pulsations are $3M$ for HE2 and HE4 while $6M$ for HE1, HE3 and HE5. In addition, the harmonic orders of the AC current induced voltage pulsations are the same as those of the corresponding no-load condition for each machine, i.e. $3M$ for HE2 and HE4 but $6M$ for HE1, HE3 and HE5, as indicated in Fig. 6.9(b). Therefore, the harmonics orders of the on-load induced field winding voltage pulsations are $6M$, $3M$, $6M$, $3M$, and $6M$ for the HESFMs from HE1 to HE5, respectively, as illustrated in Fig. 6.13(b) and therefore can still be described by (6.2). The HE4 machine (with E-core stator) has the largest on-load peak-to-peak induced voltage pulsation (E_{IV}), i.e. 7.89V, and the highest on-load voltage pulsation ratio (VPR), i.e. 348%. The on-load E_{IVs} of other machines are 0.22V, 2.26V, 0.51V, and 0.72V for HE1, HE2, HE3, and HE5, respectively, whilst the on-load VPRs of these machines are 4.8%, 199.3%, 11.2%, and 15.8%, respectively.



(a) Waveforms

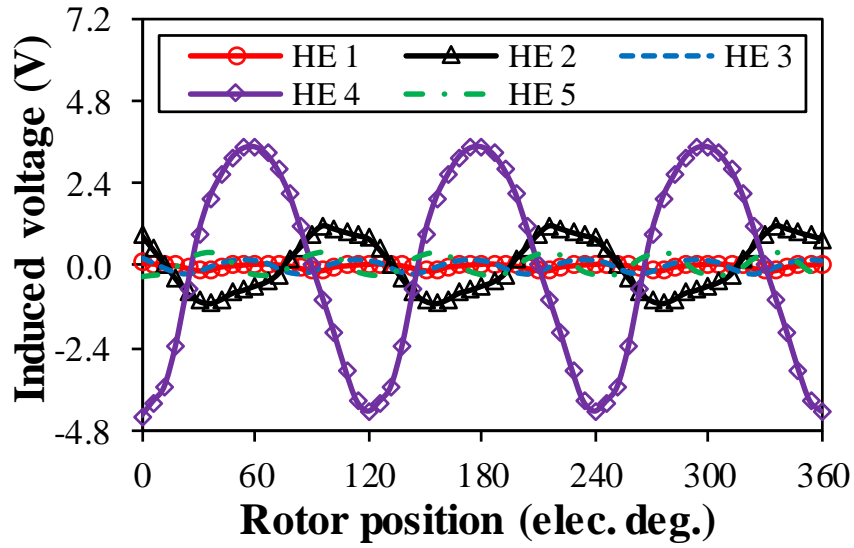


(b) Spectra

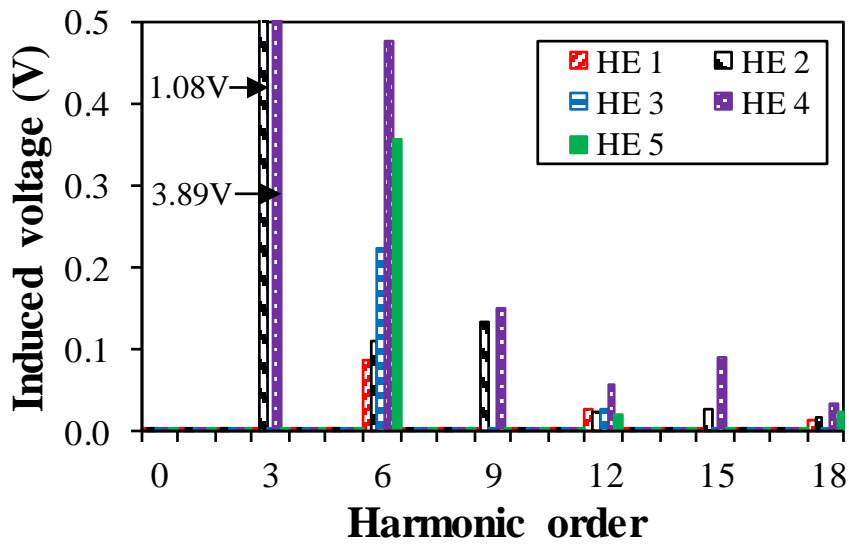
Fig. 6.12. On-load DC field winding flux-linkages of different HESFMs.

Amongst all HESFMs, the HE4 machine has the largest no-load and on-load E_{IV} and VPR as depicted in Fig. 6.14. This is mainly due to the fact that the field winding flux-linkages/induced voltage pulsations of HE4 contain abundant harmonics, i.e. the harmonic orders of $3M$. Besides, the amplitudes of low order harmonics, i.e. 3rd and 6th, are much higher than those of other HESFMs at both no-load and on-load conditions. As indicated in Fig. 6.14, the on-load E_{IV} and VPR of each HESFM are higher than those of the corresponding no-load

condition since the on-load induced voltage pulsation contains the no-load and the AC current induced voltage pulsations simultaneously. However, this is not always true, as the values of these two voltage pulsations vary with load levels.

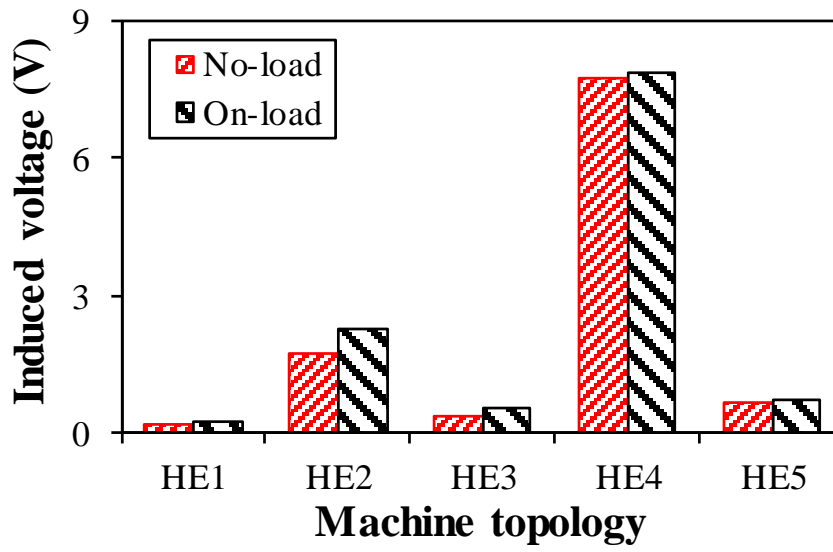


(a) Waveforms

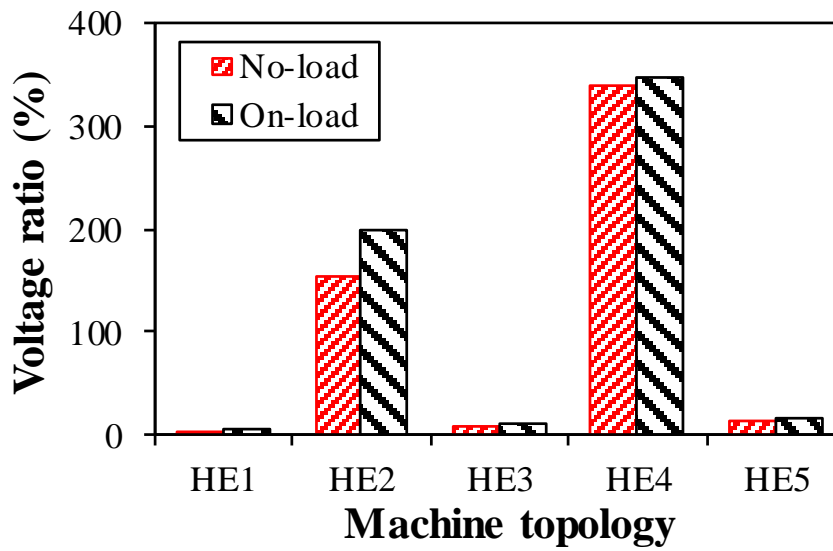


(b) Spectra

Fig. 6.13. On-load DC field winding induced voltage pulsations of different HESFMs at 400rpm.



(a) E_{IV}

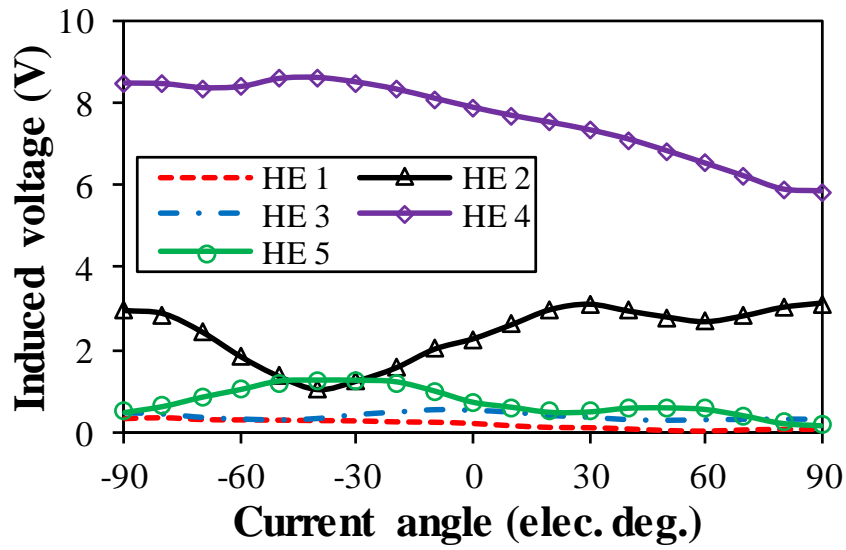


(b) VPR

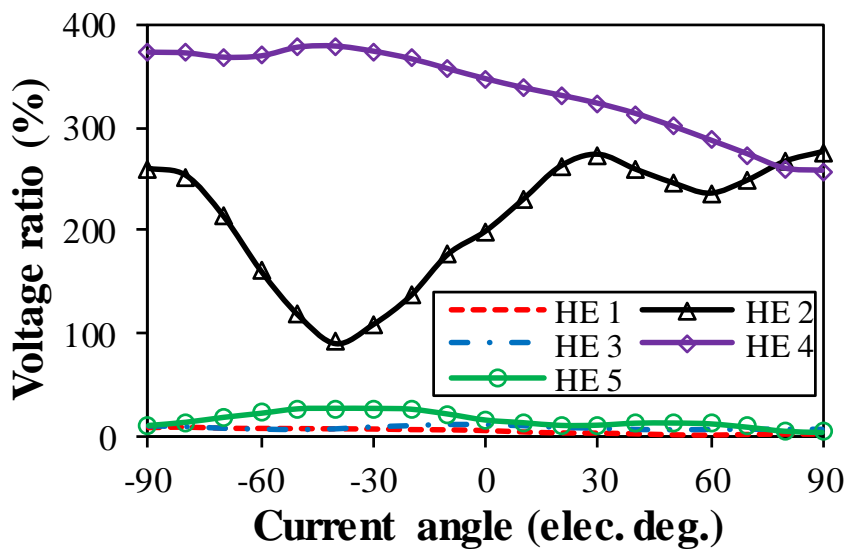
Fig. 6.14. E_{IV} and VPR of each HESFM at both no-load and on-load conditions at 400rpm.

6.3.4 Influence of Phase Current Advance Angle

As stated in the introduction, the main applications of HESFMs are those with variable speed requirements, i.e. HEVs/EVs. In these applications, flux-weakening is required at high speed considering the voltage limit of the inverter. Conventionally, d -axis current and current lead angle, i.e. the electric angle between stator current vector and d -axis, are controlled to realize flux-weakening operation. Consequently, the influences of the phase current advance angle (θ_a) on the on-load E_{IV} and VPR of different HESFMs are comparatively shown in Fig. 6.15. In constant torque region, these HESFMs normally operate at the point where $\theta_a=0^\circ$ (zero d -axis current) for maximum torque per ampere, owing to negligible reluctance torque. While in constant power region, these machines may operate under different θ_a for flux-weakening and thus high-speed operation. It shows that the on-load E_{IV} and VPR of each machine vary with the change of θ_a , as the permeability of the stator and rotor laminations varies when θ_a is changed. Therefore, both the no-load and the AC current induced voltage pulsations are related to θ_a and thus the on-load induced voltage pulsation. It can be found that the HE4 machine with E-core stator has the highest on-load E_{IV} and VPR among those machines over the whole range of θ_a due to abundant harmonics and higher amplitude of low order harmonics.



(a) E_{IV}



(b) VPR

Fig. 6.15. Influence of phase current advance angle on on-load E_{IV} and VPR of DC field winding of each HESFM at 400rpm.

Based on the foregoing analyses, it can be concluded that machine topology is a key factor that influences the induced voltage at most. As aforementioned, these five machines belong to the same family, i.e., hybrid excited switched flux machines. The main difference between these machines is the configuration of PMs and DC coils. HE1, HE3, and HE5 machines can be considered to possess the same configuration, since they have same number of PMs and DC coils. As such, the voltage harmonic orders of these three machines are the same under different conditions, i.e., $6M$. Different from HE1, HE3, and HE5 machines, HE2 and HE4 machines have different number of PMs and DC coils, due to which low order voltage harmonics, e.g., 3rd harmonic, cannot be compensated in the DC winding. Therefore, HE2 and HE4 machines exhibit relatively higher induced voltages among these machines. The induced voltage harmonic orders of each machine under different conditions are summarized in Table 6.2.

Table 6.2 Induced Voltage Harmonic Orders of All Machines

Conditions	HE1	HE2	HE3	HE4	HE5
No-load	$6M$	$3M$	$6M$	$3M$	$6M$
Armature Current	$6M$	$3M$	$6M$	$3M$	$6M$
On-load	$6M$	$3M$	$6M$	$3M$	$6M$

It can also be concluded that the air-gap permeance influences the voltage pulsation greatly. To illustrate the influence of the air-gap permeance on the voltage pulsation, HE3 machine is taken as an example. Fig. 6.16 shows the induced voltage under different conditions of HE3 machine having slotted and slotless rotors. It can be found that the induced voltage is negligible if the rotor is slotless. With a slotted rotor, the equivalent air-gap permeance is variable as the rotor rotates. While for the slotless rotor, the variation of the equivalent air-gap permeance and the DC winding flux-linkage is negligible. Therefore, the induced voltage is negligible when the slotless rotor is employed.

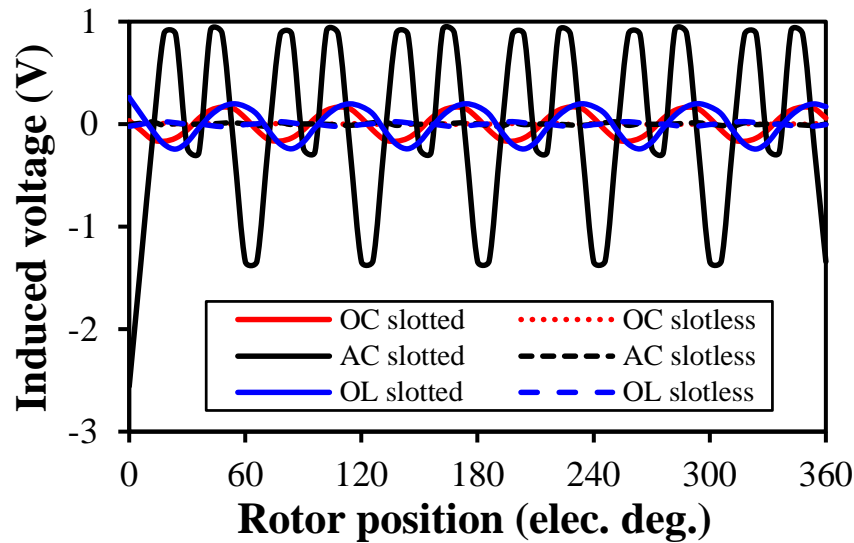


Fig. 6.16. Induced voltage under different conditions of HE3 machine having slotted and slotless rotors.

6.4 Suppression of On-load Induced Voltage Pulsation in Field Winding

As can be found from the foregoing analyses, the HESFM topologies significantly affect the DC field winding induced voltage pulsations of no-load and on-load. By selecting appropriate machine topologies, e.g., HE1, HE3, and HE5, the voltage pulsation issue can be mitigated to some extent. However, the voltage pulsation varies with field excitations and load levels. It is, therefore, necessary to provide some passive suppression methods for reference. Compared with the crowded stator in HESFMs, the rotor is very simple and robust. Therefore, the suppression methods based on the rotor are preferred to reduce the cost and complexity of manufacturing. To further suppress the pulsating voltage, three suppression methods, i.e., rotor step skewing, rotor pole notching, and rotor pole shaping are proposed and compared in this section. It should be emphasized that the following analyses are based on the HE3 machine at on-load condition.

6.4.1 Rotor Step Skewing

Conventionally, stator or rotor skewing is used for reducing torque ripple and skewing includes continuous skewing and step skewing [JAH96]. Compared with continuous skewing, step skewing can not only reduce the cost and complexity of manufacturing but also may achieve comparable performance as continuous skewing. Therefore, the step skewed rotor illustrated in Fig. 6.17 is adopted for minimizing the induced pulsating voltage in field winding.

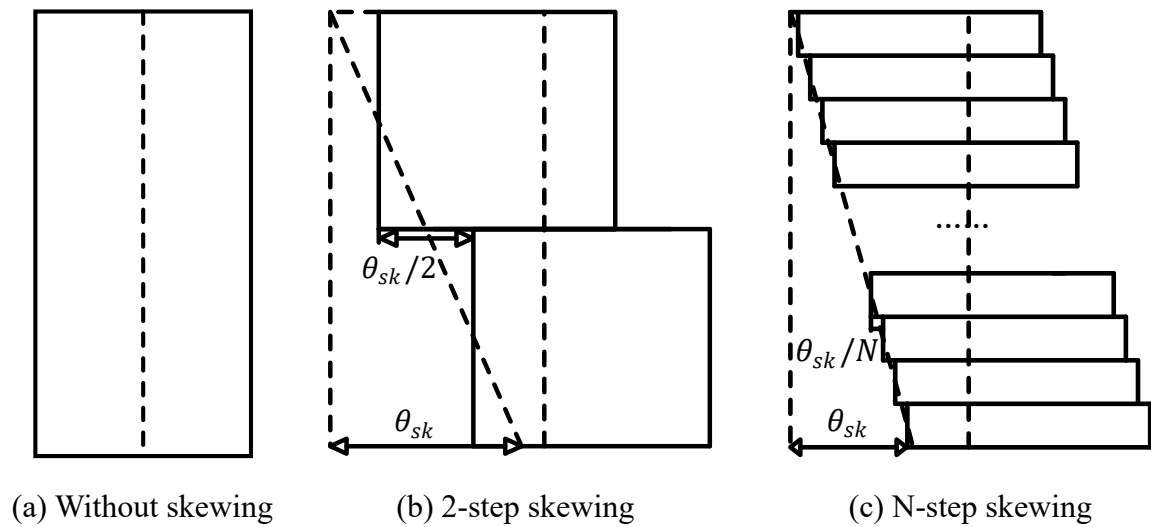


Fig. 6.17. Rotor step skewing along axial direction.

Fig. 6.18 shows the peak-to-peak on-load voltage ripple against skewing angle for different step skew numbers. It can be found that the higher the step skew number, the higher the potential for effectively reducing the voltage pulsation. However, it should be noted that the manufacturing difficulty and cost also increase with the increase of step skewing number. Therefore, the step skew number is selected to be 5 to balance the voltage ripple reduction performance and the manufacturing difficulty.

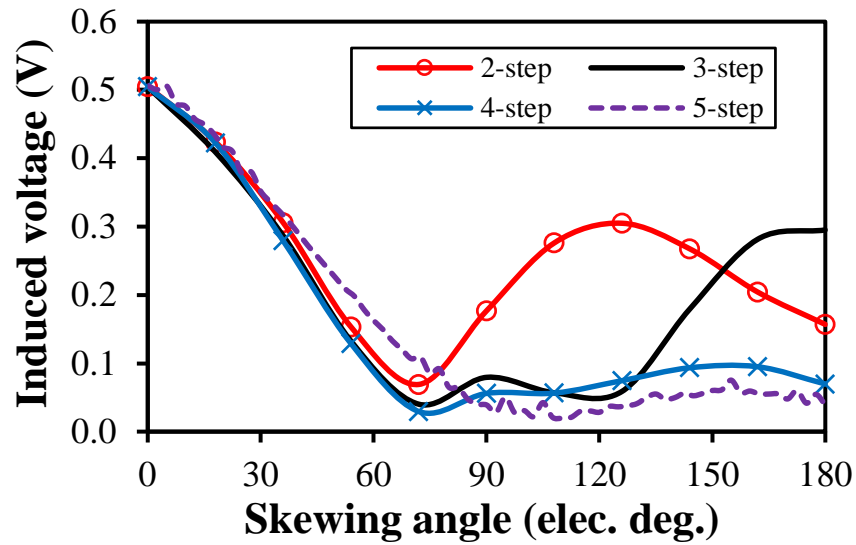


Fig. 6.18. Peak-to-peak on-load voltage ripple against skewing angle for different step skew numbers.

Besides, both the pulsating voltage and average torque decrease with the increase of the skewed rotor's step number. To balance the voltage reduction performance and the output torque, the step number is fixed at 5 ($N=5$) to obtain the optimal skew angle (θ_{sk}). As shown in Fig. 6.19, the peak-to-peak value of the pulsating voltage (E_{IV}) is minimum with $\theta_{sk}=110^\circ$ when $N=5$.

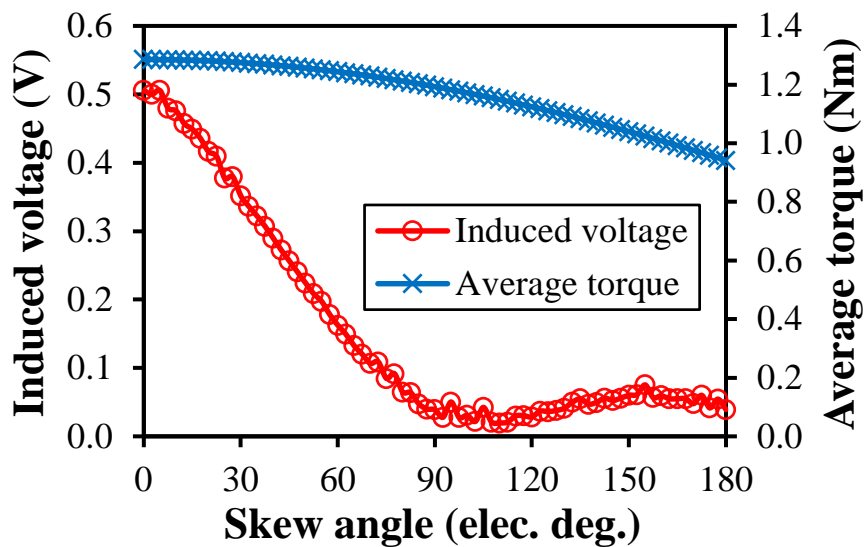


Fig. 6.19. Peak to peak on-load induced voltage and average torque versus skew angle ($N=5$).

With $\theta_{sk}=110^\circ$, E_{IV} is effectively suppressed from 0.51V to 0.02V and the suppression ratio is 96%, which is mainly attributed to the reduction of the 6th and 12th harmonics. Besides, the torque ripple suppression ratio is 90% and a smoother torque waveform is achieved by skewing. However, the average torque is slightly reduced by 10% since skewing also reduces the amplitude of the fundamental back-EMF harmonic.

6.4.2 Rotor Pole Notching

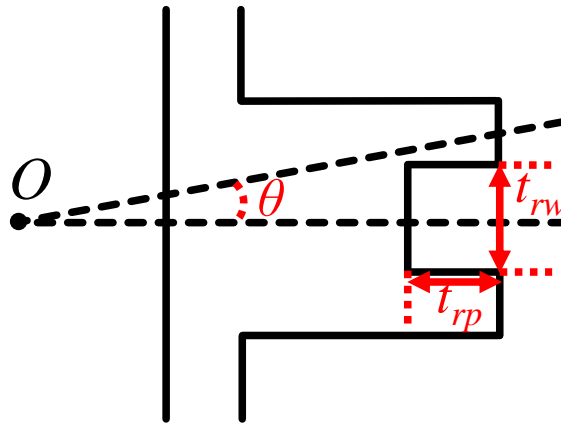
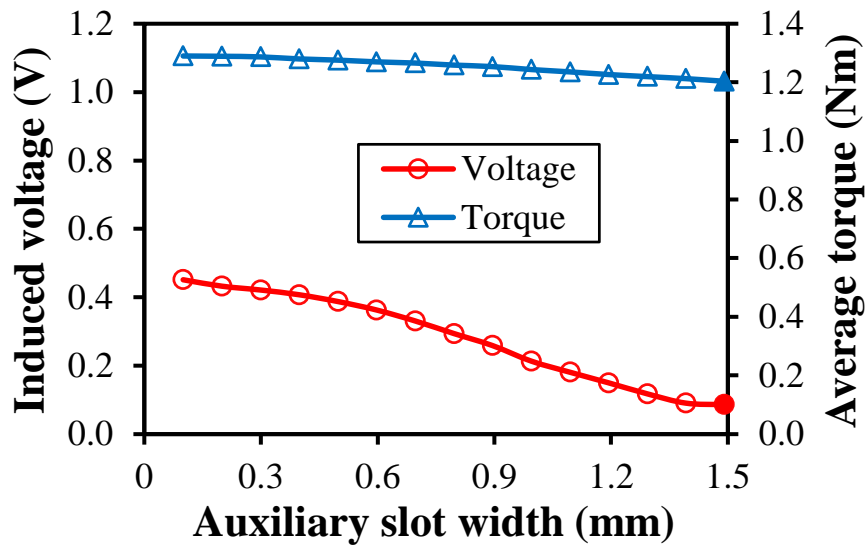


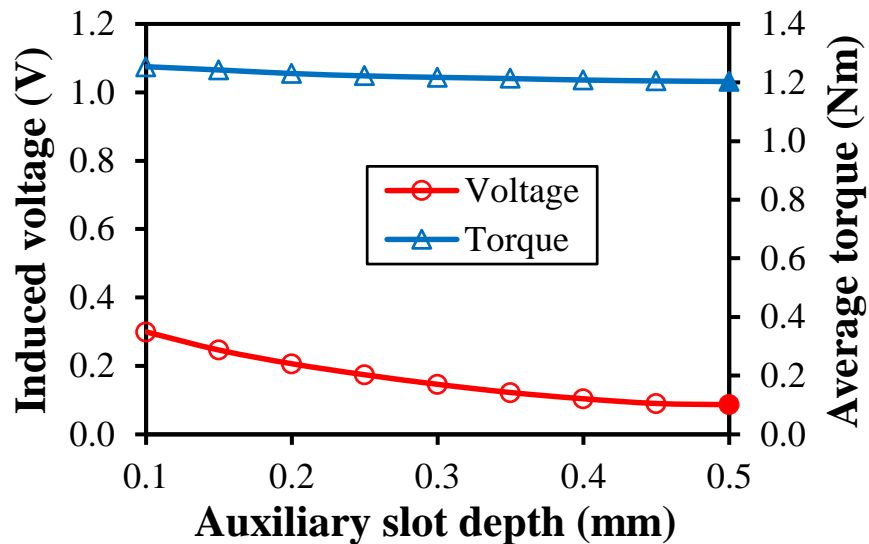
Fig. 6.20. Illustration of rotor pole notching.

Notching is capable of changing the equivalent length and permeance of the air-gap by introducing auxiliary slots in stator or rotor side [ZHA17]. As aforementioned, the rotor of HESFMs is composed of pure iron core without any active components. Consequently, rotor notching is easier than stator notching for HESFMs. A higher number of auxiliary slots is beneficial for the induced voltage reduction but will further compromise the output torque. Therefore, the rotor pole notching scheme shown in Fig. 6.20 is utilized, in which only one auxiliary slot exists to balance the suppression performance and the torque capability. The design dimensions of the auxiliary slot include the slot width t_{rw} , the slot depth t_{rp} , and the offset angle θ from the rotor pole centre. As shown in Fig. 6.21, θ has a higher influence on the induced voltage than that of t_{rw} and t_{rp} . Moreover, the average torque decreases with the increase of both t_{rw} and t_{rp} due to increased equivalent air-gap length.

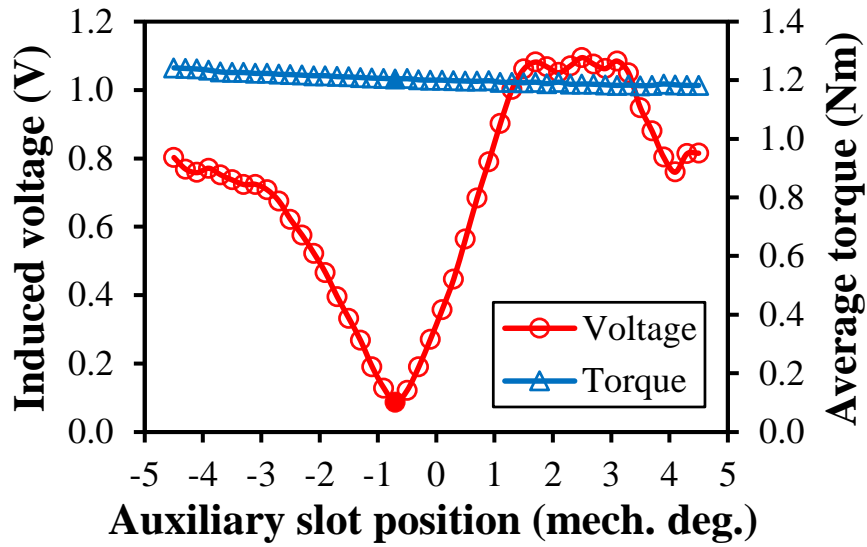
By scanning the possible values of the auxiliary slot dimensions, the combination of $t_{rp}=0.5\text{mm}$, $t_{rw}=1.5\text{mm}$, and $\theta=-0.7^\circ$ has the highest reduction ratio of the voltage pulsation, i.e. 83%. It should be noted that the negative symbol refers that the auxiliary slot moves in the clockwise direction. Despite the slight increase of the induced voltage harmonics of 18th and 24th, the 6th and 12th harmonics are greatly suppressed. Besides, the torque ripple is also suppressed by 24.7% with only 6.4% average torque reduction ratio.



(a) Slot width with $t_{rp}=0.5\text{mm}$ and $\theta=-0.7^\circ$



(b) Slot depth with $t_{rw}=1.5\text{mm}$ and $\theta=-0.7^\circ$



(c) Slot position with $t_{rw}=1.5\text{mm}$ and $t_{rp}=0.5\text{mm}$

Fig. 6.21. Influence of auxiliary slot dimensions on induced voltage and average torque.

6.4.3 Rotor Pole Shaping

Rotor pole shaping is another common technique for torque ripple reduction [ZHU16a]. The induced voltage pulsation in field winding can also be suppressed by rotor pole shaping since it can reduce the air-gap permeance's rate of change. As illustrated in Fig. 6.22, after shaping, the centre of the original rotor pole surface (red dash line) is moved from O_1 to O_2 along the radial direction and the radius of the shaped rotor pole surface is R . During the shaping process, the length of the lowest air-gap remains the same as the original one, i.e. 0.5mm.

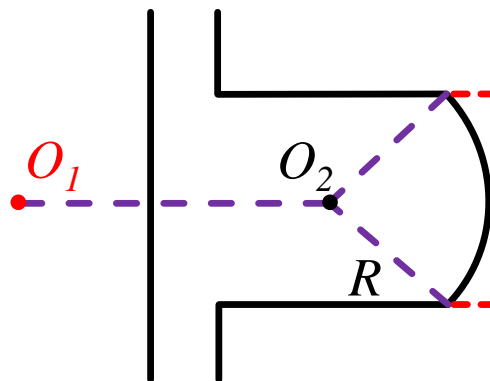


Fig. 6.22. Illustration of rotor pole shaping.

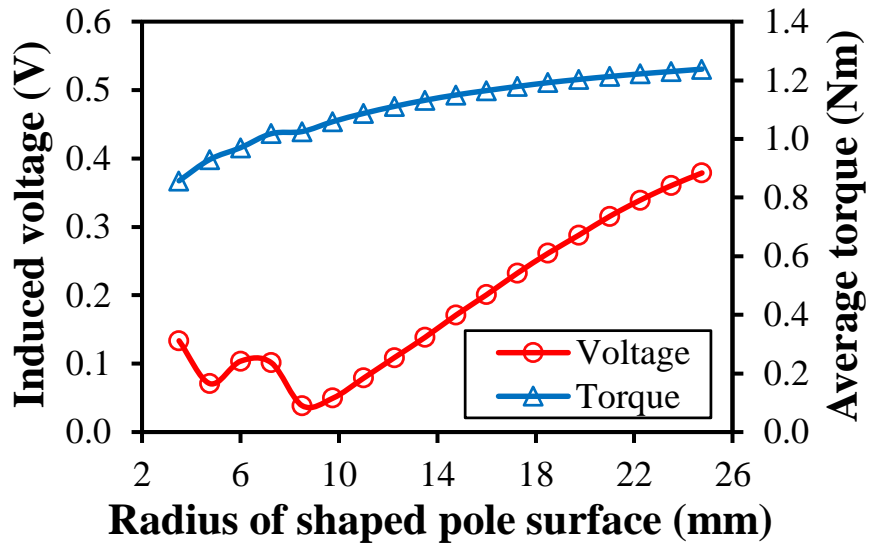


Fig. 6.23. Peak to peak on-load induced voltage and average torque versus radius of shaped rotor pole surface.

As shown in Fig. 6.23, the peak to peak induced voltage varies with the change of R and the average torque decreases with the decrease of R due to increased equivalent air-gap length. The peak to peak induced voltage reaches its minimum value, i.e. 0.04V when $R=8.5\text{mm}$. However, at this point, the average torque is 20% lower than the original one. To maintain at least 90% of the original torque and a higher voltage reduction ratio, $R=14.75\text{mm}$ is selected. With $R=14.75\text{mm}$, the voltage can be reduced by 66.2%. Moreover, the torque ripple is 58.7% lower than the original one.

Fig. 6.24 shows the peak-to-peak cogging torque and torque ripple against the radius of shaped rotor pole surface. From Figs. 6.23 and 6.24, it is revealed that there is a tradeoff between high average torque and low induced voltage ripple. It can also be found that a smaller radius tends to effectively reduce the voltage ripple, cogging torque, and torque ripple. However, a smaller radius would reduce the average torque due to increased equivalent air-gap length. As shown from Figs. 6.25-6.27, the induced voltage ripple, cogging torque, and torque ripple are effectively reduced with these methods. While the average torques are slightly reduced as well.

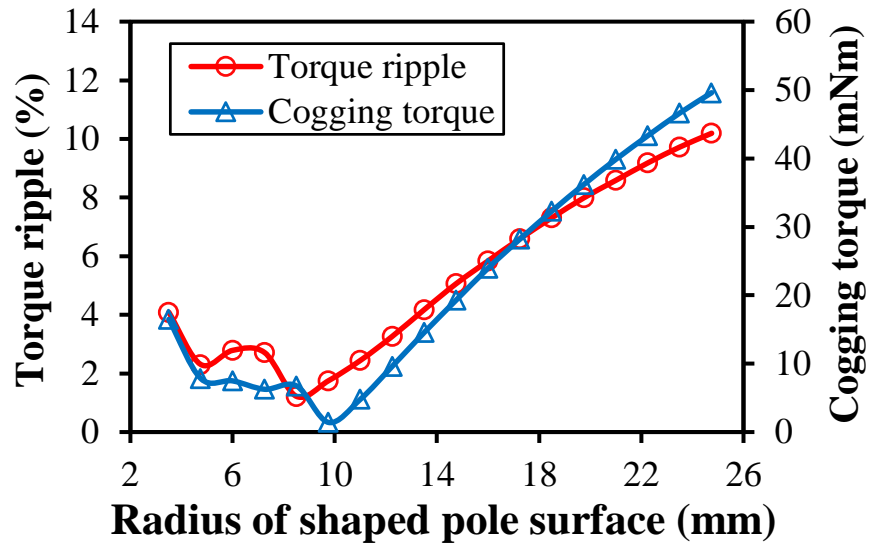


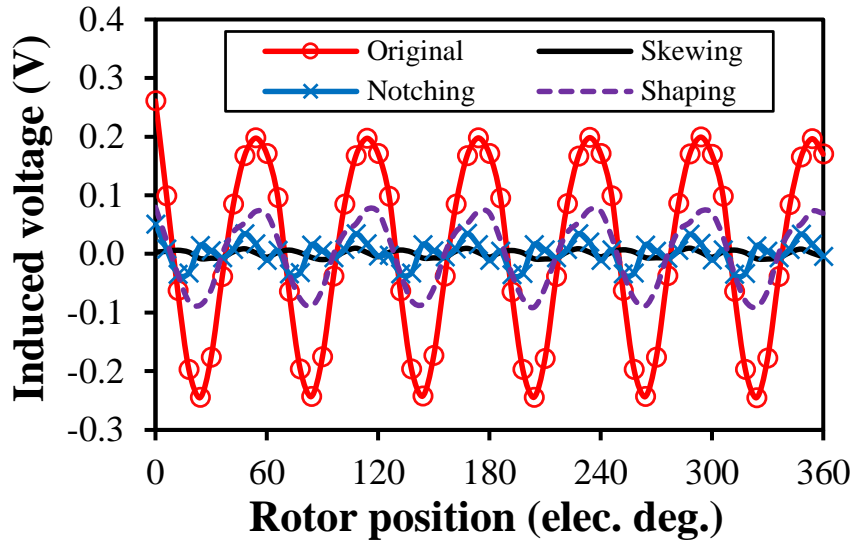
Fig. 6.24. Peak-to-peak cogging torque and torque ripple versus radius of shaped rotor pole surface.

6.4.4 Comparison of Suppression Methods

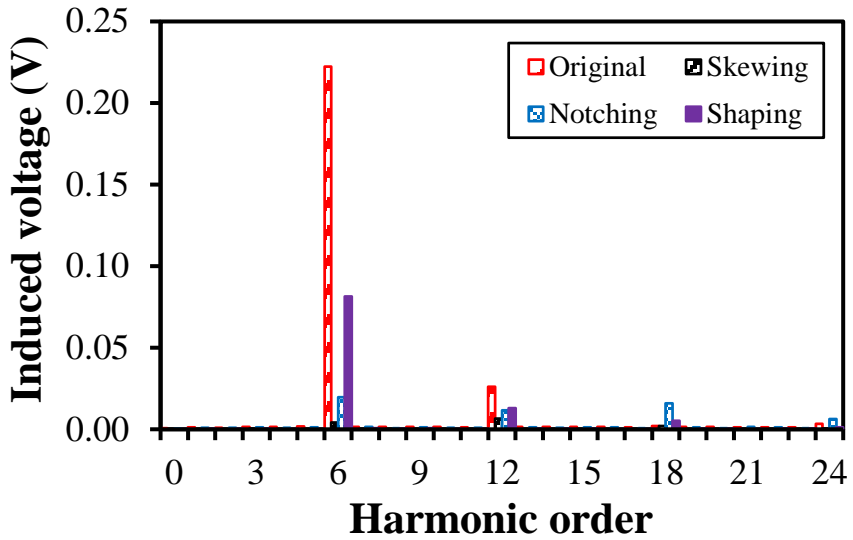
Figs. 6.25 and 6.26 compare the induced voltage and on-load torque of three suppression methods with the original machine. It reveals that skewing has the highest reduction ratios of induced voltage and torque ripple, i.e. 96% and 90%, respectively. However, the output torque after skewing is also reduced, which is 90% of the original torque. Notching offers a better trade-off between the voltage reduction and the torque capability, which reduces the voltage by 83% while maintaining the torque at 93.6% of the original one. Shaping has the lowest voltage reduction ratio, i.e. 66.2% but it exhibits better torque ripple reduction than notching.

The number of design parameters for shaping, skewing, and notching are 1, 2, and 3, respectively. For the rotor shaping method, only the radius of shaped rotor pole surface can be adjusted as shown in Fig. 6.22. Compared with rotor shaping method, rotor step skewing, Fig. 6.17, has two design parameters, i.e., step skew number and skewing angle., and both parameters have significant influences on the voltage pulsations as shown in Fig. 6.18. Although the rotor notching method, Fig. 6.20, has three design parameters, i.e., slot width, slot depth, and offset angle, only the offset angle has a significant influence on the voltage pulsation

as shown in Fig. 6.21. Therefore, 5-step rotor skewing has the highest voltage ripple reduction ratio among these three reduction schemes. For the rotor notching method, if the number of auxiliary slots is increased, it may exhibit comparable or even better voltage reduction performance than the rotor step skewing, albeit with increased manufacturing difficulty and cost.

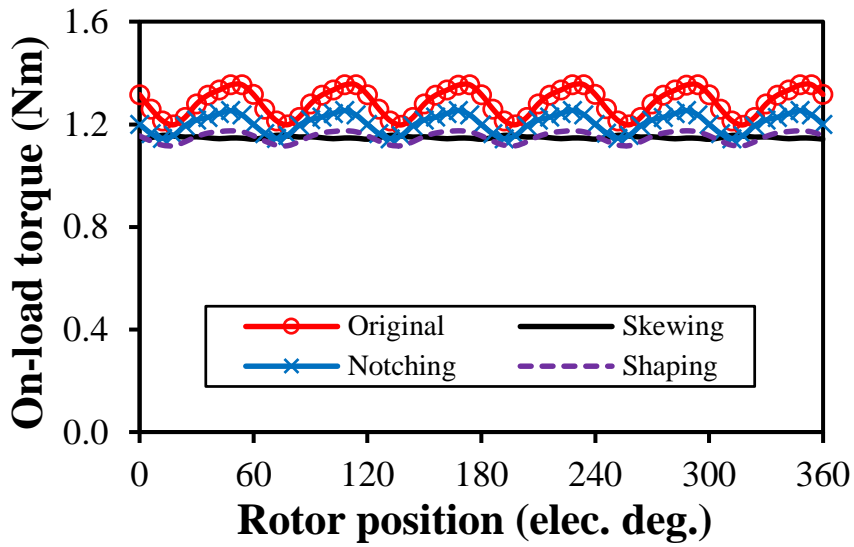


(a) Waveforms

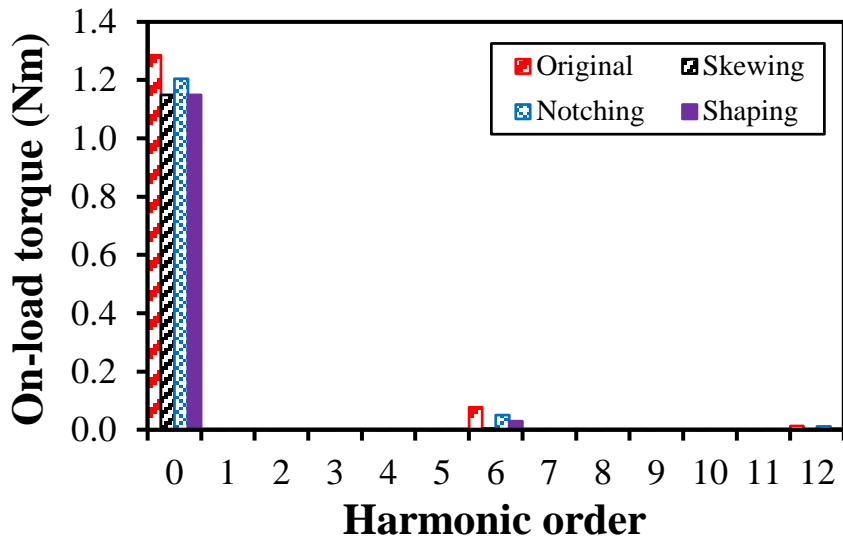


(b) Spectra

Fig. 6.25. On-load induced voltage pulsations in field winding with different suppression methods at 400rpm.



(a) Waveforms



(b) Spectra

Fig. 6.26. On-load torques with different suppression methods.

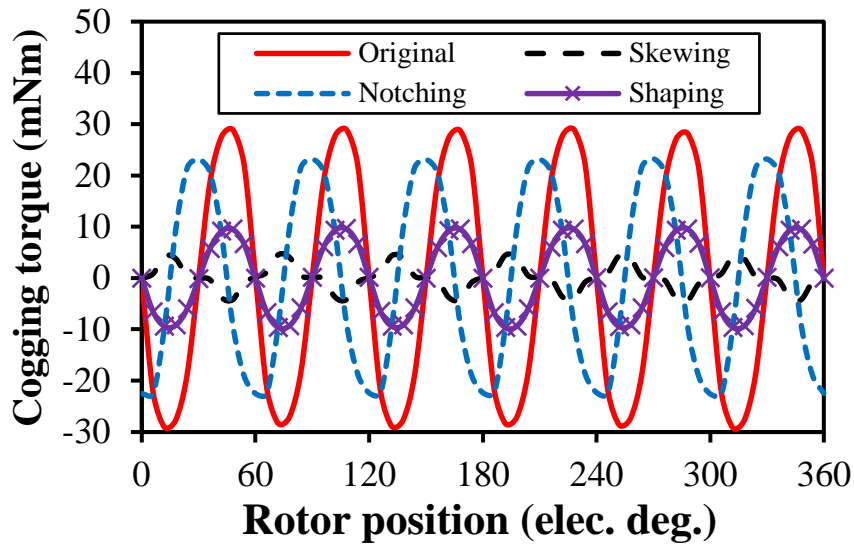


Fig. 6.27. Cogging torques with different suppression methods.

To calculate the iron loss, the following iron loss model has been adopted.

$$P_{core} = K_h f B_m^2 + K_c (f B_m)^2 + K_e (f B_m)^{1.5} \quad (6.3)$$

where P_{core} is the iron loss. k_h , k_c , and k_e are the hysteresis loss coefficient, classic eddy current loss coefficient and excess eddy current loss coefficient, respectively. f is the electrical frequency. B_m is the amplitude of the flux density.

Fig. 6.28 shows the iron losses with different suppression methods. The iron losses are not very high since the rated speed is only 400rpm. However, it can still be observed that the adopted methods are also able to reduce the iron losses by reducing the flux density pulsations.

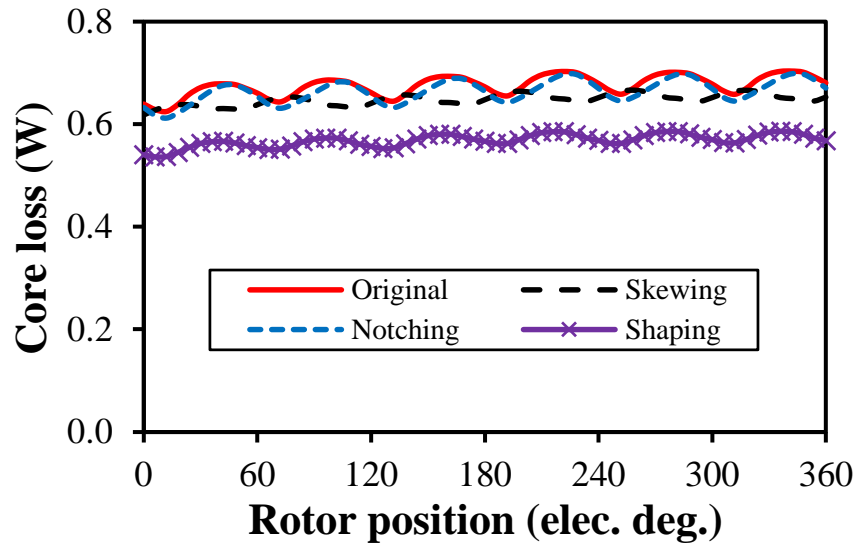
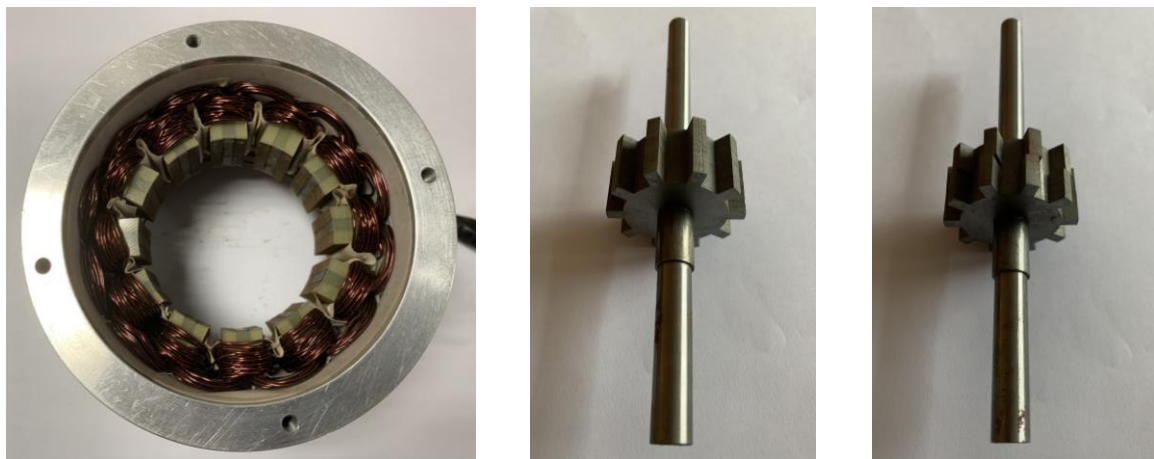


Fig. 6.28. Iron losses with different suppression methods at 400rpm.

6.5 Experimental Validation

As illustrated in Fig. 6.29, an existing HE3 prototype machine from the previous research with both non-skewed and skewed rotors is employed and tested for further verification of the previous finite element analyses. The parameters of the prototype machine are listed in table 6.3. It should be noted that switched flux permanent magnet machines, including both hybrid and non-hybrid variants, always suffer from magnet position tolerance during assembly [ZHU09c]. The prototype machine consists of a stator with 12-slots and two salient rotors with 10-poles. To reduce the manufacturing difficulty, the step number of the skewed rotor is designed as two and the skew angle is 60° elec. deg. The DC field winding of the prototype machine has twelve DC field coils, in which they are connected in series. In addition, each field coil contains 10 turns, which is lower than that of the previous FEA calculations to facilitate the winding process of the prototype machine.



(a) Stator and winding

(b) Non-skewed rotor

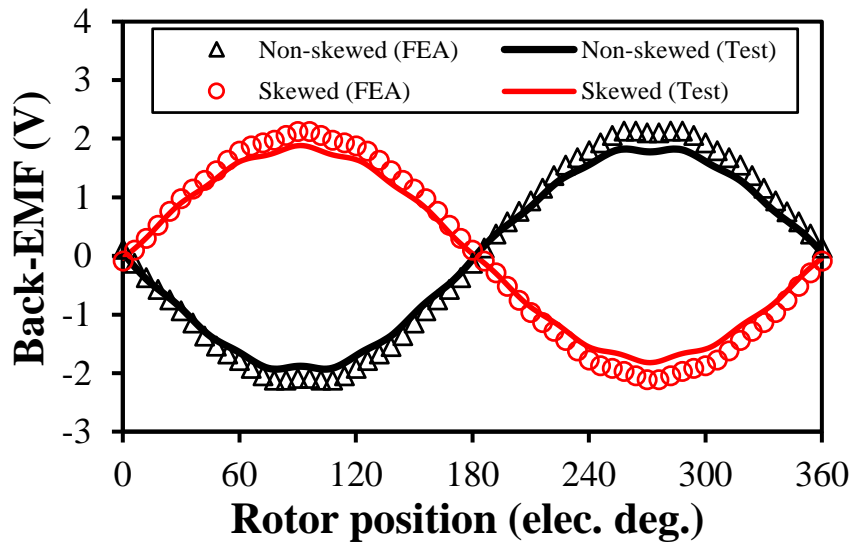
(c) 2-step skewed rotor

Fig. 6.29. Photos of the prototype HE3 machine.

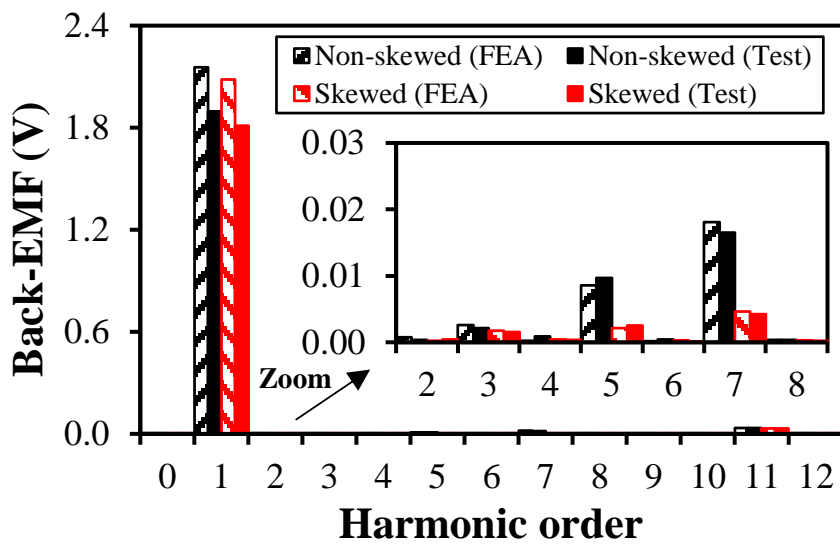
Table 6.3 Parameters of Prototype

Parameters	Values	Parameters	Values
Stator outer diameter	90mm	Stator inner diameter	54mm
Axial length	25mm	Stator tooth height	3.5mm
Stator slot number	12	Rotor shaft diameter	12mm
Rotor pole number	10	Rotor yoke thickness	14mm
Air-gap length	0.5mm	Rotor tooth height	5.1mm
Iron bridge thickness	1mm	Phase resistance	0.42 Ω
Back iron thickness	3.5mm	DC winding resistance	0.73 Ω
PM thickness	3.5mm	<i>d</i> -axis and <i>q</i> -axis inductances	0.38mH
PM length	7.5mm	DC winding self-inductance	0.21mH
PM remanence	1.2T	PM flux (non-skewed)	5.16mWb
PM relative permeability	1.05	PM flux (2-step skewed)	4.96mWb

As shown in Fig. 6.30, the measured phase back-EMFs are lower than the 2D FEA results of both non-skewed and skewed rotors, which is mainly attributed to the end-effect. It also shows that the back-EMF harmonics are effectively reduced by skewing, which is beneficial for low torque ripple.



(a) Waveforms

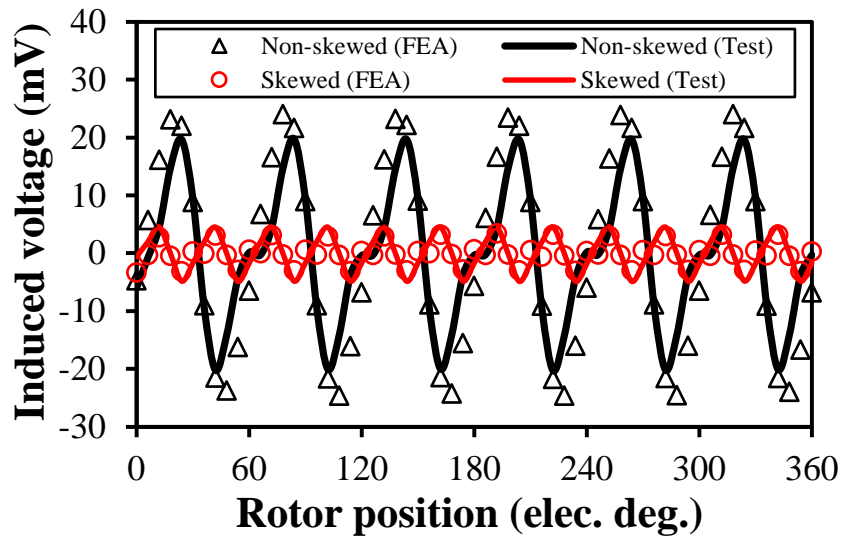


(b) Spectra

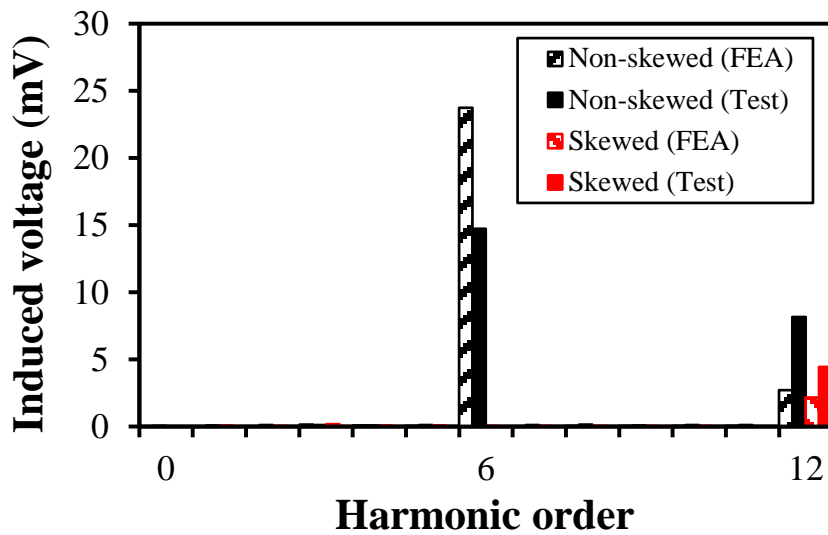
Fig. 6.30. Phase back-EMFs with non-skewed and skewed rotors under sole PM excitation at 400rpm ($I_{dc}=0A$).

As shown in Fig. 6.31, at no-load (with PMs and $I_{dc}=2A$), the measured and FEA calculated field winding induced voltage pulsations only exhibit the harmonic orders of $6M$ for both non-skewed and skewed rotors, owing to the harmonic counteraction effect between different field coils as analyzed in section 6.3.1. Similarly, as shown in Fig. 6.32, the harmonic orders of the measured and FEA predicted on-load (with PMs, $I_{dc}=2A$, and $I_{ac_rms}=2A$) induced voltage

pulsations are $6M$ as well as illustrated in section 6.3.3. The on-load torque waveforms of the two prototypes are provided in Fig. 6.33. It should be noted that the on-load computations and testes are carried out under zero d-axis current control since the reluctance torque component in this machine is negligible. It is revealed that by employing rotor step skewing, the induced voltage pulsations in field winding can be significantly suppressed at both no-load and on-load conditions. The errors between the measured and FEA predicted results are mainly attributed to the end-effect, manufacturing imperfection and test error.

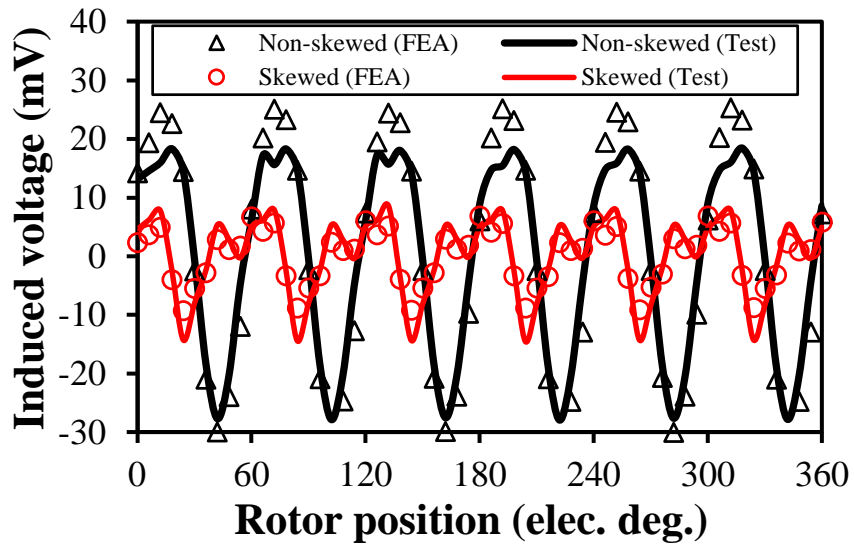


(a) Waveforms

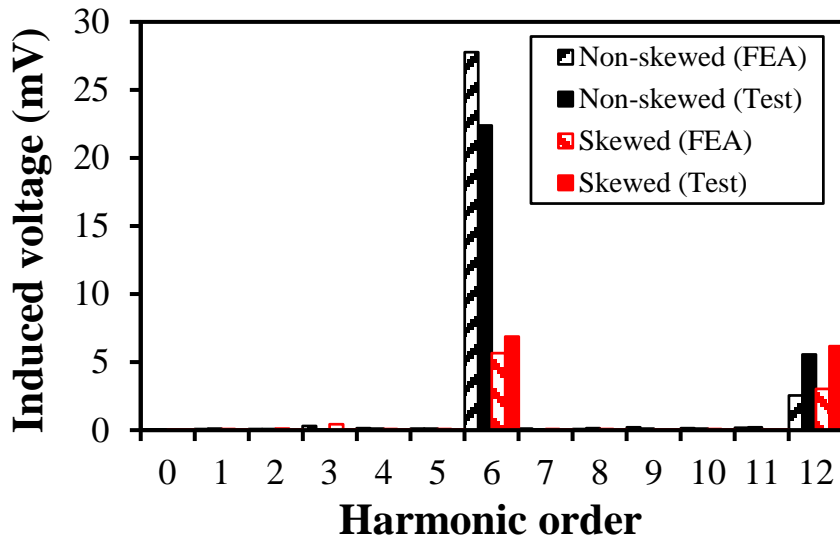


(b) Spectra

Fig. 6.31. Open-circuit induced voltage pulsations in field winding with non-skewed and skewed rotors at 400rpm ($I_{ac_rms}=0A$, $I_{dc}=2A$).



(a) Waveforms



(b) Spectra

Fig. 6.32. On-load induced voltage pulsations in field winding with non-skewed and skewed rotors at 400rpm ($I_{ac_rms}=2A$, $I_{dc}=2A$).

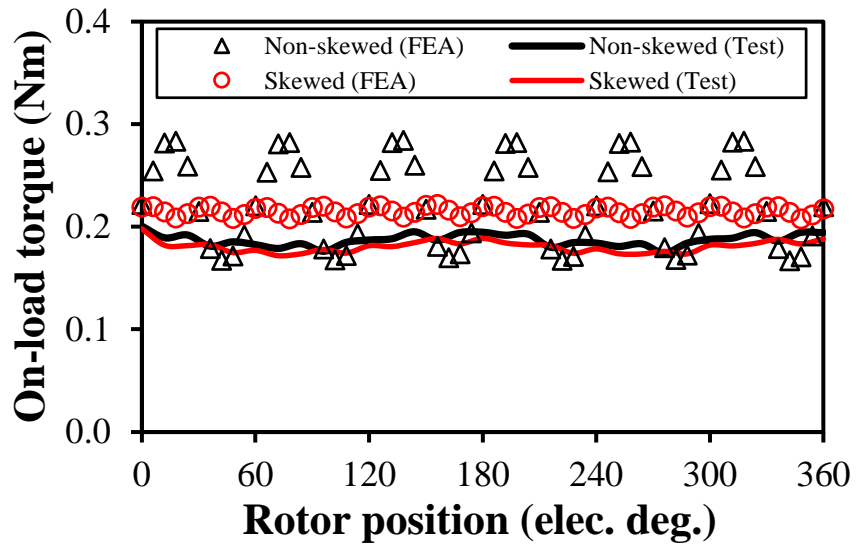


Fig. 6.33. On-load torques with non-skewed and skewed rotors ($I_{ac_rms}=2A$, $I_{dc}=2A$).

6.6 Conclusion

In this chapter, the voltage pulsations induced in the DC field winding of different HESFMs are comparatively studied under both no-load and on-load conditions. On-load induced voltage pulsation is attributed to the no-load and the AC current induced voltage components. The harmonic orders of the induced voltage pulsations caused by no-load, AC currents and on-load are identified for each HESFM. It is revealed that both no-load and AC current induced voltage pulsations are significantly influenced by the HESFM topologies and hence the on-load voltage. It also shows that the HESFM with E-core stator has the highest no-load and on-load E_{IV} and VPR, owing to abundant harmonics and higher amplitude of low order harmonics, compared to other machines. Three rotor-based suppression methods, i.e. rotor step skewing, rotor pole notching, and rotor pole shaping are proposed and compared. Rotor step skewing provides the best reduction performance for the pulsating voltage and torque ripple, albeit with the highest average torque reduction as well. Notching offers a better trade-off between the voltage reduction and the torque capability. Shaping has the lowest voltage reduction ratio, but exhibits better torque ripple reduction than notching. In theory, these suppression methods can be equally applied to other HESFMs with different topologies and dimensions. Finally, a 12-slot/10-pole HE3 prototype machine with non-skewed and 2-step skewed rotors is fabricated for the validation of the FEA predicted results. For future work, the combination of these suppression techniques could be applied to obtain better voltage reduction performance.

CHAPTER 7

General Conclusions and Future Work

7.1 General Conclusions

This thesis comprehensively investigates the DC winding induced voltage, a significant parasitic effect, in wound field and hybrid excited synchronous machines. The investigations of the DC winding induced voltage in this thesis can be divided into three aspects as illustrated in Fig. 7.1. Firstly, the phenomena and production mechanisms of the DC winding induced voltage under different conditions are investigated in stator WFSMs and HESFMs. Then, the major factors that influence the induced voltage are investigated, including slot and pole number combinations and machine topologies. Finally, various methods are proposed and employed to reduce the induced voltage, including rotor pole arc pairing, rotor step skewing, rotor pole notching, rotor pole shaping, unequal rotor teeth, and unevenly distributed rotor teeth. The potential of using open-winding technique to eliminate the DC winding and its induced voltage is demonstrated as well based on the F1A1 WFSM.

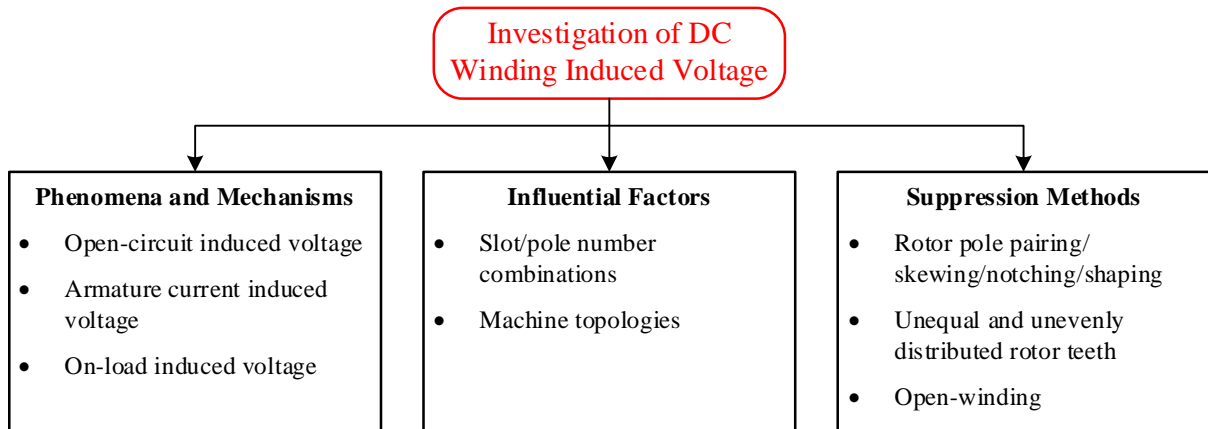


Fig. 7.1. Structure of thesis.

7.1.1 Phenomena and Production Mechanisms

Based on the investigations in all chapters, it can be concluded that the DC winding induced voltage of on-load condition contains two induced voltage components, which are the open-circuit induced voltage component and the armature current induced voltage component,

respectively. Table 7.1 summarizes the production mechanisms of the DC winding induced voltage under different conditions in stator WFSMs and HESMs. In stator WFSMs, the open-circuit induced voltage is caused by the field winding self-inductance harmonics. While in HESFMs, due to the presence of PMs, the open-circuit induced voltage is caused by the field winding self-inductance harmonics and the equivalent mutual-inductance harmonics between PMs and field winding. The armature current induced voltage is caused by the mutual inductance harmonics between armature and field windings in both stator WFSMs and HESMs. Similarly, the on-load induced voltage is caused by the open-circuit induced voltage component and the armature current induced voltage component in both stator WFSMs and HESMs as listed in Table 7.1. It is worth noting that the harmonics of these self- and mutual-inductances are introduced by the modulation effect of the salient-pole rotors. If the rotors are slotless, i.e., without the modulation effect of the rotors, the DC winding exhibits negligible induced voltage pulsations under different conditions as shown in Fig. 6.16.

Table 7.1 Comparison of Production Mechanisms of DC Winding Induced Voltage in Stator WFSMs and HESFMs

Conditions	Stator WFSMs	HESFMs
Open-circuit induced voltage	<ul style="list-style-type: none"> Caused by the field winding self-inductance harmonics 	<ul style="list-style-type: none"> Caused by the field winding self-inductance harmonics and the equivalent mutual-inductance harmonics between field winding and PMs
Armature current induced voltage	<ul style="list-style-type: none"> Caused by the mutual-inductance harmonics between field and armature windings 	
On-load induced voltage	<ul style="list-style-type: none"> Caused by the open-circuit induced voltage component and the armature current induced voltage component 	

7.1.2 Major Influential Factors

Based on the investigations in chapter 2, chapter 4, and chapter 5, it can be concluded that the slot and pole number combinations significantly influence the DC winding induced voltage under different conditions in both stator WFSMs and HESFMs. This is because that the harmonic orders of the DC winding voltage pulsations under different conditions are closely related to the slot and pole number combinations. It has also shown that the machines having low-order induced voltage harmonics tend to suffer from high peak-to-peak DC winding voltage pulsations. On the contrary, the machines having high-order induced voltage harmonics tend to exhibit low peak-to-peak DC winding voltage pulsations. Table 7.2, Table 7.3, and Table 7.4 summarize the harmonic orders (HO) and peak-to-peak (PTP) values of the DC winding voltage pulsations under different slot/pole number combinations and conditions in the F1A1 WFSMs (chapter 2), the HESFMs (chapter 4), and the PS-HESFMs (chapter 5), respectively. k is a positive integer in these tables.

Table 7.2 Harmonic Orders and Peak-to-Peak Values of DC Winding Induced Voltage Pulsations in F1A1 WFSMs

Slot/pole combination	Open-circuit induced voltage		Armature current induced voltage		On-load induced voltage	
	HO	PTP	HO	PTP	HO	PTP
6/4	$3k$	0.45V	$3k$	4.83V	$3k$	5.22V
6/5	$3k$	1.05V	$3k$	5.57V	$3k$	7.05V
6/7	$3k$	1.23V	$3k$	6.34V	$3k$	8.10V
6/8	$3k$	3.38V	$3k$	6.37V	$3k$	7.93V
12/10	$3k$	0.95V	$3k$	1.58V	$3k$	4.28V
12/11	$6k$	0.11V	$6k$	0.98V	$6k$	0.46V
12/13	$6k$	0.05V	$6k$	0.99V	$6k$	0.66V
12/14	$3k$	0.51V	$3k$	1.50V	$3k$	6.21V

Table 7.3 Harmonic Orders and Peak-to-Peak Values of DC Winding Induced Voltage Pulsations in HESFMs

Slot/pole combination	Open-circuit induced voltage		Armature current induced voltage		On-load induced voltage	
	HO	PTP	HO	PTP	HO	PTP
	6/4	3k	4.57V	3k	13.5V	3k
6/5	6k	0.88V	6k	5.2V	6k	0.82V
6/7	6k	0.73V	6k	10.9V	6k	0.67V
6/8	3k	1.43V	3k	26.3V	3k	1.46V
12/10	6k	0.33V	6k	3.30V	6k	0.51V
12/11	12k	0.11V	6k	10.3V	6k	0.09V
12/13	12k	0.08V	6k	11.2V	6k	0.16V
12/14	6k	0.13V	6k	2.7V	6k	0.22V

Table 7.4 Harmonic Orders and Peak-to-Peak Values of DC Winding Induced Voltage Pulsations in PS-HESFMs

Slot/pole combination	Open-circuit induced voltage		Armature current induced voltage		On-load induced voltage	
	HO	PTP	HO	PTP	HO	PTP
	12/10	6k	0.64V	6k	1.54V	6k
12/11	12k	0.05V	6k	0.44V	6k	0.14V
12/13	12k	0.01V	6k	0.27V	6k	0.13V
12/14	6k	0.37V	6k	0.98V	6k	0.51V

Apart from the slot and pole number combinations, another major factor for influencing the DC winding voltage pulsation is machine topologies. In chapter 6, the DC winding voltage pulsations of five HESFM topologies are comparatively investigated. The major difference between these five machines is the configuration of PMs and DC coils. It has shown that

HESFM topologies significantly influence the harmonic orders of DC winding voltage pulsations under different conditions and hence influencing its peak-to-peak values. Table 7.5 summarizes the harmonic orders and peak-to-peak values of the DC winding voltage pulsations under different conditions in these five HESFMs. It is worth mentioning that other factors such as armature winding phase number and AC/DC winding configurations may also have significant influence on DC winding voltage pulsation, as summarized in future work section.

Table 7.5 Harmonic Orders and Peak-to-Peak Values of DC Winding Induced Voltage Pulsations in Different HESFMs

Machine topology	Open-circuit induced voltage		Armature current induced voltage		On-load induced voltage	
	HO	PTP	HO	PTP	HO	PTP
HE1	6k	0.15V	6k	0.62V	6k	0.22V
HE2	3k	1.74V	3k	0.35V	3k	2.26V
HE3	6k	0.33V	6k	3.30V	6k	0.51V
HE4	3k	7.73V	3k	0.82V	3k	7.89V
HE5	6k	0.63V	6k	1.45V	6k	0.72V

7.1.3 Suppression Methods

Although the DC winding voltage pulsation can be actively suppressed by selecting appropriate slot/pole number combinations and machine topologies, it varies with geometric parameters, current advance angle, and load levels etc. Therefore, various passive suppression methods are proposed to further reduce the DC winding voltage pulsation, including unequal rotor teeth (chapter 3), rotor step skewing (chapter 3 and chapter 6), rotor pole arc pairing (chapter 5), unevenly distributed rotor teeth (chapter 5), rotor pole notching (chapter 6), and rotor pole shaping (chapter 6), as summarized in Table 7.6. It is worth mentioning that the proposed suppression methods are all rotor-based since the rotors of the investigated machines are very simple and do not contain any PMs or DC coils. Overall, all these methods can effectively reduce the DC winding voltage pulsation, cogging torque, back-EMF harmonics, and torque ripple. However, the average on-load torque will also be slightly reduced due to the reduction of the fundamental back-EMF harmonic. The performances of these methods are comparatively summarized in Table 7.7. Besides, for the machines having AC and DC conductors in the same slot, it is possible to eliminate the DC winding and its voltage pulsation and improve the torque density by using open-winding technique, as demonstrated in chapter 2. It has shown that, by using the open-winding technique, the rated average torque can be improved by 74% while the torque ripple is slightly reduced compared with the WFSM having separated AC and DC windings.

Table 7.6 Various Rotor-Based Suppression Methods

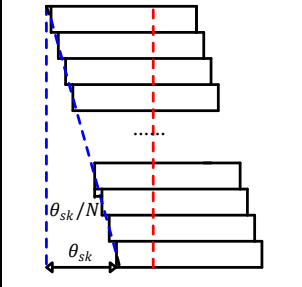
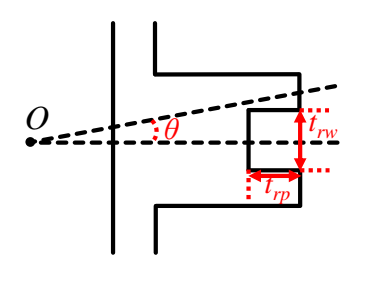
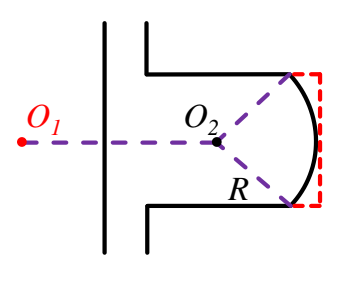
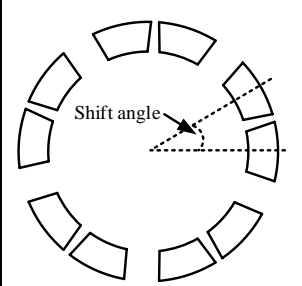
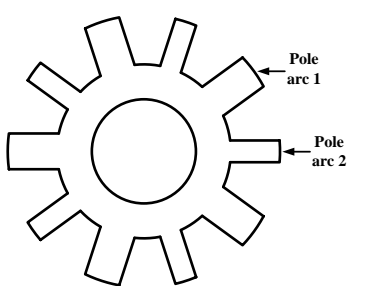
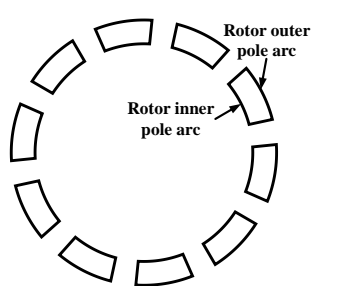
	Rotor step skewing	Rotor pole notching	Rotor pole shaping
Methods			
	Uneven rotor teeth	Unequal rotor teeth	Rotor pole arc pairing
			

Table 7.7 Performances of Various Suppression Methods

Suppression Methods	On-Load DC Winding Voltage Pulsation	Cogging Torque	Torque Ripple	Average Torque
Skewing	-96%	-85%	-90%	-10%
Notching	-83%	-21%	-25%	-6%
Shaping	-66%	-67%	-59%	-10%
Uneven teeth	-91%	-92%	-50%	-7%
Unequal teeth	-89%	-29%	-33%	-12%
Pairing	-93%	-39%	-29%	-7%

Note: “-” sign indicates the reduction ratio by using the corresponding method compared with the original machine.

7.2 Future Work

Based on the investigations in this thesis, some future work are suggested as follows.

- Quantitative analysis and separation of DC winding induced voltage of different conditions in hybrid excited switched flux machines using air-gap field modulation principle and frozen permeability method
- Influence of armature winding phase number (3-phase, 5-phase, dual-3-phase etc.) on DC winding induced voltage in hybrid excited switched flux machines
- Influence of AC and DC winding configurations (single/double layer, different coil pitches) on DC winding induced voltage in hybrid excited switched flux machines
- Comparison of DC winding induced voltage of other stator hybrid excited machines, including doubly salient hybrid excited machines, flux reversal hybrid excited machines and stator slot hybrid excited machines etc.
- Applying open-winding technique for those hybrid excited machines having AC and DC conductors in the same slot to eliminate the DC winding induced voltage and improve the torque performance
- Machine optimizations for wound field and hybrid excited synchronous machines considering both torque performance and DC winding induced voltage reduction
- Investigation of other DC winding induced voltage reduction methods. It is very likely that the methods for reducing cogging torque and torque ripple are also effective for reducing DC winding induced voltage
- Investigation of other parasitic effects in wound field and hybrid excited machines, such as losses, unbalanced magnetic force, PM demagnetization, and noise and vibration etc.

References

[AFI15]	I. A. A. Afinowi, Z. Q. Zhu, Y. Guan, J. C. Mipo, and P. Farah, "Hybrid-excited doubly salient synchronous machine with permanent magnets between adjacent salient stator poles," <i>IEEE Trans. Magn.</i> , vol. 51, no. 10, pp. 1-9, Oct. 2015.
[AFI16]	I. A. A. Afinowi, Z. Q. Zhu, Y. Guan, J. Mipo, and P. Farah, "A novel brushless AC doubly salient stator slot permanent magnet machine," <i>IEEE Trans. Energy Convers.</i> , vol. 31, no. 1, pp. 283-292, Mar. 2016.
[AKE00]	A. D. Akemakou and S. K. Phounsombat, "Electrical machine with double excitation, especially a motor vehicle alternator," U.S. Patent 6 147 429, Nov. 14, 2000.
[AKE01]	A. D. Akemakou, "Brushless polyphase machine in particular motor vehicle alternator," U.S. Patent 6 242 834, Jun. 5, 2001.
[ALI16]	Q. Ali, S. Atiq, T. A. Lipo, and B. I. Kwon, "PM assisted, brushless wound rotor synchronous machine," <i>J. Magn.</i> , vol. 21, no. 3, pp. 399-404, Nov. 2016.
[AMA09]	Y. Amara, L. Vido, M. Gabsi, E. Hoang, A. Ahmed, and M. Lecrivain, "Hybrid excitation synchronous machines: Energy-efficient solution for vehicles propulsion," <i>IEEE Trans. Veh. Technol.</i> , vol. 58, no. 5, pp. 2137-2149, Jun. 2009.
[AMA11]	Y. Amara, S. Hlioui, R. Belfkira, G. Barakat, and M. Gabsi, "Comparison of open circuit flux control capability of a series double excitation machine and a parallel double excitation machine," <i>IEEE Trans. Veh. Technol.</i> , vol. 60, no. 9, pp. 4194-4207, Nov. 2011.
[ATA00]	K. Atallah, D. Howe, P. H. Mellor, and D. A. Stone, "Rotor loss in permanent-magnet brushless AC machines," <i>IEEE Trans. Ind. Appl.</i> , vol. 36, no. 6, pp. 1612-1618, Nov.-Dec. 2000.
[ATA01]	K. Atallah and D. Howe, "A novel high-performance magnetic gear," <i>IEEE Trans. Magn.</i> , vol. 37, no. 4, pp. 2844-2846, July 2001.
[ATA03]	K. Atallah, J. Wang, and D. Howe, "Torque-ripple minimization in modular permanent-magnet brushless machines," <i>IEEE Trans. Ind. Appl.</i> , vol. 39, no. 6, pp. 1689-1695, Nov. 2003.
[ATA92]	K. Atallah, Z. Q. Zhu, and D. Howe, "An improved method for predicting iron losses in brushless permanent magnet DC drives," <i>IEEE Trans. Magn.</i> , vol. 28, no. 5, pp. 2997-2999, Sept. 1992.
[BAR15]	P. D. Barba, M. Bonislawski, R. Palka, P. Paplicki, and M. Wardach, "Design

	of hybrid excited synchronous machine for electrical vehicles,” <i>IEEE Trans. Magn.</i> , vol. 51, no. 8, pp. 1-6, Aug. 2015.
[BAS11]	M. L. Bash and S. D. Pekarek, “Modeling of salient-pole wound-rotor synchronous machines for population-based design,” <i>IEEE Trans. Energy Convers.</i> , vol. 26, no. 2, pp. 381-392, June 2011.
[BER85]	G. Bertotti, “Physical interpretation of eddy current losses in ferromagnetic materials, I. theoretical considerations”, <i>J. Appl. Phys.</i> , 1985, 57, (6), pp. 2110-2117.
[BIA06a]	N. Bianchi, S. Bolognani, and P. Frare, “Design criteria for high-efficiency SPM synchronous motors,” <i>IEEE Trans. Energy Convers.</i> , vol. 21, no. 2, pp. 396-404, June 2006.
[BIA06b]	N. Bianchi, S. Bolognani, M. D. Pré, and G. Grezzani, “Design considerations for fractional-slot winding configurations of synchronous machines,” <i>IEEE Trans. Ind. Appl.</i> , vol. 42, no. 4, pp. 997-1006, Aug. 2006.
[BIA16]	N. Bianchi, S. Bolognani, E. Carraro, M. Castiello, and E. Fornasiero, “Electric vehicle traction based on synchronous reluctance motors,” <i>IEEE Trans. Ind. Appl.</i> , vol. 52, no. 6, pp. 4762-4769, Nov.-Dec. 2016.
[BOG03]	A. Boglietti, A. Cavagnino, M. Lazzari, and M. Pastorelli, “Predicting iron losses in soft magnetic materials with arbitrary voltage supply: an engineering approach,” <i>IEEE Trans. Magn.</i> , vol. 39, no. 2, pp. 981-989, Mar. 2003.
[CAI19]	S. Cai, Z. Q. Zhu, J. Mipo, and S. Personna, “A novel parallel hybrid excited machine with enhanced flux regulation capability,” <i>IEEE Trans. Energy Convers.</i> , vol. 34, no. 4, pp. 1938-1949, Dec. 2019.
[CAI20]	S. Cai, Z. Q. Zhu, C. Wang, J. C. Mipo, and S. Personnaz, “A novel fractional slot non-overlapping winding hybrid excited machine with consequent-pole PM rotor,” <i>IEEE Trans. Energy Convers.</i> , vol. 35, no. 3, pp. 1628-1637, Sept. 2020.
[CAO12]	W. Cao, B. C. Mecrow, G. J. Atkinson, J. W. Bennett, and D. J. Atkinson, “Overview of electric motor technologies used for more electric aircraft (MEA),” <i>IEEE Trans. Ind. Electron.</i> , vol. 59, no. 9, pp. 3523-3531, Sept. 2012.
[CHA02]	K. T. Chau, Ming Cheng, and C. C. Chan, “Nonlinear magnetic circuit analysis for a novel stator doubly fed doubly salient machine,” <i>IEEE Trans. Magn.</i> , vol. 38, no. 5, pp. 2382-2384, Sept. 2002.
[CHA03]	K. T. Chau, J. Z. Jiang, and Y. Wang, “A novel stator doubly fed doubly salient permanent magnet brushless machine,” <i>IEEE Trans. Magn.</i> , vol. 39, no. 5, pp. 3001-3003, Sept. 2003.

[CHA07]	C. C. Chan, "The state of the art of electric, hybrid, and fuel cell vehicles," <i>Proc. IEEE</i> , vol. 95, no. 4, pp. 704-718, Apr. 2007.
[CHA08]	K. T. Chau, C. C. Chan, and C. Liu, "Overview of permanent-magnet brushless drives for electric and hybrid electric vehicles," <i>IEEE Trans. Ind. Electron.</i> , vol. 55, no. 6, pp. 2246-2257, Jun. 2008.
[CHA96a]	C. C. Chan, K. T. Chau, J. Z. Jiang, W. Xia, M. Zhu, and R. Zhang, "Novel permanent magnet motor drives for electric vehicles," <i>IEEE Trans. Ind. Electron.</i> , vol. 43, no. 2, pp. 331-339, Apr. 1996.
[CHA96b]	B. Chao, Z. J. Liu, and T. S. Low, "Analysis of Unbalanced-Magnetic-Pulls in hard disk drive spindle motors using a hybrid method," <i>IEEE Trans. Magn.</i> , vol. 32, no. 5, pp. 4308-4310, Sept. 1996.
[CHE00]	J. Y. Chen, C. V. Nayar, and L. Y. Xu, "Design and finite-element analysis of an outer-rotor permanent-magnet generator for directly coupled wind turbines," <i>IEEE Trans. Magn.</i> , vol. 36, no. 5, pp. 3802-3809, Sep. 2000.
[CHE05]	Y. Chen, P. Pillay, and A. Khan, "PM wind generator topologies," <i>IEEE Trans. Ind. Appl.</i> , vol. 41, no. 6, pp. 1619-1626, Nov.-Dec. 2005.
[CHE10a]	J. T. Chen and Z. Q. Zhu, "Comparison of all- and alternate-poles-wound flux-switching PM machines having different stator and rotor pole numbers," <i>IEEE Trans. Ind. Appl.</i> , vol. 46, no. 4, pp. 1406-1415, Jul./Aug. 2010.
[CHE10b]	J. T. Chen, Z. Q. Zhu, S. Iwasaki, and R. Deodhar, "Low cost flux-switching brushless AC machines," <i>2010 IEEE Vehicle Power and Propulsion Conference</i> , Lille, 2010, pp. 1-6.
[CHE10c]	J. T. Chen and Z. Q. Zhu, "Winding configurations and optimal stator and rotor pole combination of flux-switching PM brushless AC machines," <i>IEEE Trans. Energy Convers.</i> , vol. 25, no. 2, pp. 293-302, June 2010.
[CHE11a]	J. T. Chen, Z. Q. Zhu, S. Iwasaki, and R. P. Deodhar, "A novel hybrid-excited switched-flux brushless AC machine for EV/HEV applications," <i>IEEE Trans. Veh. Technol.</i> , vol. 60, no. 4, pp. 1365-1373, May 2011.
[CHE11b]	M. Cheng, W. Hua, J. Zhang, and W. Zhao, "Overview of stator-permanent magnet brushless machines," <i>IEEE Trans. Ind. Electron.</i> , vol. 58, no. 11, pp. 5087-5101, Nov. 2011.
[CHE11c]	J. T. Chen, Z. Q. Zhu, S. Iwasaki, and R. P. Deodhar, "Influence of slot opening on optimal stator and rotor pole combination and electromagnetic performance of switched-flux PM brushless AC machines," <i>IEEE Trans. Ind. Appl.</i> , vol. 47, no. 4, pp. 1681-1691, Jul./Aug. 2011.
[CHE11d]	J. T. Chen, Z. Q. Zhu, S. Iwasaki, and R. P. Deodhar, "A novel E-core switched-

	flux PM brushless AC machine,” <i>IEEE Trans. Ind. Appl.</i> , vol. 47, no. 3, pp. 1273-1282, May/Jun. 2011.
[CHE14]	Z. Chen, B. Wang, Z. Chen, and Y. Yan, “Comparison of flux regulation ability of the hybrid excitation doubly salient machines,” <i>IEEE Trans. Ind. Electron.</i> , vol. 61, no. 7, pp. 3155-3166, July 2014.
[CHE15]	J. Chen, D. Wang, S. Cheng, Y. Wang, Y. Zhu, and Q. Liu, “Modeling of temperature effects on magnetic property of nonoriented silicon steel lamination,” <i>IEEE Trans. Magn.</i> , vol. 51, no. 11, pp. 1-4, Nov. 2015.
[CHU14a]	W. Q. Chu, Z. Q. Zhu, and J. T. Chen, “Simplified analytical optimization and comparison of torque densities between electrically excited and permanent-magnet machines,” <i>IEEE Trans. Ind. Electron.</i> , vol. 61, no. 9, pp. 5000-5011, Sept. 2014.
[CHU14b]	W. Q. Chu, Z. Q. Zhu, J. Zhang, X. Ge, X. Liu, D. Stone, and M. Foster, “Comparison of electrically excited and interior permanent magnet machines for hybrid electric vehicle application,” <i>2014 17th International Conference on Electrical Machines and Systems (ICEMS)</i> , 2014, pp. 401-407.
[CHU15]	W. Q. Chu, Z. Q. Zhu, J. Zhang, X. Liu, D. A. Stone, and M. P. Foster, “Investigation on operational envelopes and efficiency maps of electrically excited machines for electrical vehicle applications,” <i>IEEE Trans. Magn.</i> , vol. 51, no. 4, pp. 1-10, Apr. 2015.
[DEN19]	W. Deng and S. Zuo, “Electromagnetic vibration and noise of the permanent-magnet synchronous motors for electric vehicles: An overview,” <i>IEEE Trans. Transp. Electrification</i> , vol. 5, no. 1, pp. 59-70, Mar. 2019.
[DEO97]	R. Deodhar, S. Andersson, I. Boldea, and T. J. E. Miller, “The flux reversal machine: A new brushless doubly-salient permanent magnet machine,” <i>IEEE Trans. Ind. Appl.</i> , vol. 33, no. 4, pp. 925-934, Jul. 1997.
[ELR05]	A. M. EL-Refaie and T. M. Jahns, “Optimal flux weakening in surface PM machines using fractional-slot concentrated windings,” <i>IEEE Trans. Ind. Appl.</i> , vol. 41, no. 3, pp. 790-800, May-June 2005.
[ELR10]	A. M. EL-Refaie, “Fractional-slot concentrated-windings synchronous permanent magnet machines: opportunities and challenges,” <i>IEEE Trans. Ind. Electron.</i> , vol. 57, no. 1, pp. 107-121, Jan. 2010.
[ELR13]	A. M. El-Refaie, “Motors/generators for traction/propulsion applications: A review,” <i>IEEE Veh. Technol. Mag.</i> , vol. 8, no. 1, pp. 90-99, Mar. 2013.
[FEI10]	W. Fei and P. C. K. Luk, “A new technique of cogging torque suppression in

	direct-drive permanent-magnet brushless machines,” <i>IEEE Trans. Ind. Appl.</i> , vol. 46, no. 4, pp. 1332-1340, Jul.-Aug. 2010.
[FOD07]	D. Fodorean, A. Djerdir, I. Viorel, and A. Miraoui, “A double excited synchronous machine for direct drive application-design and prototype tests,” <i>IEEE Trans. Energy Convers.</i> , vol. 22, no. 3, pp. 656-665, Sep. 2007.
[FUK10]	T. Fukami, Y. Matsuura, K. Shima, M. Momiyama, and M. Kawamura, “Development of a low-speed multi-pole synchronous machine with a field winding on the stator side,” in <i>Proc. Int. Conf. Elect. Mach. (ICEM)</i> , 2010, Rome, 2010, pp. 1-6.
[FUK12]	T. Fukami, Y. Matsuura, K. Shima, M. Momiyama, and M. Kawamura, “A multipole synchronous machine with nonoverlapping concentrated armature and field windings on the stator,” <i>IEEE Trans. Ind. Electron.</i> , vol. 59, no. 6, pp. 2583-2591, June 2012.
[GAL15]	M. Galea, L. Papini, H. Zhang, C. Gerada, and T. Hamiti, “Demagnetization analysis for Halbach array configurations in electrical machines,” <i>IEEE Trans. Magn.</i> , vol. 51, no. 9, pp. 1-9, Sept. 2015.
[GAO18]	Y. Gao, D. Li, R. Qu, X. Fan, J. Li, and H. Ding, “A novel hybrid excitation flux reversal machine for electric vehicle propulsion,” <i>IEEE Trans. Veh. Technol.</i> , vol. 67, no. 1, pp. 171-182, Jan. 2018.
[GAU12]	B. Gaussens, E. Hoang, O. de la Barriere, J. Saint-Michel, M. Lecrivain, and M. Gabsi, “Analytical approach for air-gap modeling of field-excited flux-switching machine: no-load operation,” <i>IEEE Trans. Magn.</i> , vol. 48, no. 9, pp. 2505-2517, Sept. 2012.
[GAU14]	B. Gaussens, E. Hoang, M. Lecrivain, P. Manfe, and M. Gabsi, “A hybrid-excited flux-switching machine for high-speed DC-alternator applications,” <i>IEEE Trans. Ind. Electron.</i> , vol. 61, no. 6, pp. 2976-2989, Jun. 2014.
[GEN15]	W. Geng, Z. Zhang, K. Jiang, and Y. Yan, “A new parallel hybrid excitation machine: Permanent-magnet/variable-reluctance machine with bidirectional field-regulation capability,” <i>IEEE Trans. Ind. Electron.</i> , vol. 62, no. 3, pp. 1372-1381, Mar. 2015.
[GIE06]	J. F. Gieras, C. Wang, and J. C. Lai, <i>Noise of polyphase electric motors</i> , Boca Raton, FL: Taylor & Francis/CRC Press, 2006.
[HEN94]	G. Henneberger, J. R. Hadji-Minaglou, and R. C. Ciorba, “Design and test of permanent magnet synchronous motor with auxiliary excitation winding for electric vehicle application,” in <i>Proc. Eur. Power Electron. Symp.</i> , Oct. 1994,

	pp. 645-649.
[HOA07]	E. Hoang, M. Lecrivain, and M. Gabsi, "A new structure of a switching flux synchronous polyphased machine with hybrid excitation," in <i>Proc. Eur. Conf. Power Electron. Appl.</i> , Sep. 2-5, 2007, pp. 1-8.
[HOA97]	E. Hoang, A. H. Ben-Ahmed, and J. Lucidarme, "Switching flux permanent magnet polyphased machines," in <i>Proc. Eur. Conf. Power Electron. Appl.</i> , 1997, pp. 3.903-3.908.
[HUA09]	W. Hua, M. Cheng, and G. Zhang, "A novel hybrid excitation flux-switching motor for hybrid vehicles," <i>IEEE Trans. Magn.</i> , vol. 45, no. 10, pp. 4728-4731, Oct. 2009.
[HUA15]	W. Hua, G. Zhang, and M. Cheng, "Flux-regulation theories and principles of hybrid-excited flux-switching machines," <i>IEEE Trans. Ind. Electron.</i> , vol. 62, no. 9, pp. 5359-5369, Sept. 2015.
[HUA16a]	H. Hua and Z. Q. Zhu, "Novel hybrid-excited switched-flux machine having separate field winding stator," <i>IEEE Trans. Magn.</i> , vol. 52, no. 7, pp. 1-4, July 2016.
[HUA16b]	H. Hua, Z. Q. Zhu, and H. L. Zhan, "Novel consequent-pole hybrid excited machine with separated excitation stator," <i>IEEE Trans. Ind. Electron.</i> , vol. 63, no. 8, pp. 4718-4728, Aug. 2016.
[HUA16c]	H. Hua and Z. Q. Zhu, "Novel parallel hybrid excited machines with separate stators," <i>IEEE Trans. Energy Convers.</i> , vol. 31, no. 3, pp. 1212-1220, Sept. 2016.
[HUA17]	H. Hua and Z. Q. Zhu, "Novel partitioned stator hybrid excited switched flux machines," <i>IEEE Trans. Energy Convers.</i> , vol. 32, no. 2, pp. 495-504, June 2017.
[HUA18]	H. Huang, L. Jing, R. Qu, and D. Li, "The demagnetizing protection of halbach consequent pole in a magnetic-gear machine," <i>21st Int. Conf. Elect. Mach. Syst. (ICEMS)</i> , Jeju, 2018, pp. 365-370.
[HUA19]	H. Hua and Z. Q. Zhu, "Novel partitioned stator hybrid excited machines with magnets on slot openings," <i>J. Eng.</i> , vol. 2019, no. 17, pp. 3568-3572, Jun. 2019.
[HUS18]	A. Hussain, S. Atiq, and B. Kwon, "Consequent-pole hybrid brushless wound rotor synchronous machine," <i>IEEE Trans. Magn.</i> , vol. 54, no. 11, pp. 1-5, Nov. 2018.
[HWA18]	S. Hwang, J. Sim, J. Hong, and J. Lee, "Torque improvement of wound field synchronous motor for electric vehicle by PM-assist," <i>IEEE Trans. Ind. Appl.</i> ,

	vol. 54, no. 4, pp. 3252-3259, July-Aug. 2018.
[ION07]	D. M. Ionel, M. Popescu, M. I. McGilp, T. J. E. Miller, S. J. Dellinger, and R. J. Heideman, "Computation of core losses in electrical machines using improved models for laminated steel," <i>IEEE Trans. Ind. Appl.</i> , vol. 43, no. 6, pp. 1554-1564, Nov.-dec. 2007.
[ISH06]	D. Ishak, Z. Q. Zhu, and D. Howe, "Comparison of PM brushless motors, having either all teeth or alternate teeth wound," <i>IEEE Trans. Energy Convers.</i> , vol. 21, no. 1, pp. 95-103, Mar. 2006.
[ISL05]	M. S. Islam, S. Mir., T. Sebastian, and S. Underwood, "Design consideration of sinusoidal excited permanent-magnet machines for low-torque-ripple applications," <i>IEEE Trans. Ind. Appl.</i> , vol. 41, no. 4, pp. 955-962, Jul./Aug. 2005.
[JAH86]	T. M. Jahns, G. B. Kliman, and T. W. Neumann, "Interior permanent-magnet synchronous motors for adjustable-speed drives," <i>IEEE Trans. Ind. Appl.</i> , vol. IA-22, no. 4, pp. 738-747, July 1986.
[JAH96]	T. M. Jahns and W. L. Soong, "Pulsating torque minimization techniques for permanent magnet AC motor drives-a review," <i>IEEE Trans. Ind. Electron.</i> , vol. 43, no. 2, pp. 321-330, Apr. 1996.
[JAH99]	T. M. Jahns and V. Caliskan, "Uncontrolled generator operation of interior PM synchronous machines following high-speed inverter shutdown," <i>IEEE Trans. Ind. Appl.</i> , vol. 35, no. 6, pp. 1347-1357, Nov.-Dec. 1999.
[JAN91]	G. Jang and D. Lieu, "The effect of magnet geometry on electric motor vibration," <i>IEEE Trans. Magn.</i> , vol. 27, pp. 5202-5204, Nov. 1991.
[JAN93]	G. Jang and D. Lieu, "Vibration reduction in electric machine by interlocking of the magnets," <i>IEEE Trans. Magn.</i> , vol. 29, pp. 1423-1426, Mar. 1993.
[JIA04]	G. Jiao and C. D. Rahn, "Field weakening for radial force reduction in brushless permanent-magnet DC motors," <i>IEEE Trans. Magn.</i> , vol. 40, no. 5, pp. 3286-3292, Sep. 2004.
[JIA16a]	S. Jia, R. Qu, J. Li, and D. Li, "Principles of stator DC winding excited vernier reluctance machines," <i>IEEE Trans. Energy Convers.</i> , vol. 31, no. 3, pp. 935-946, Sept. 2016.
[JIA16b]	S. Jia, R. Qu, J. Li, D. Li, and H. Fang, "Hybrid excited Vernier PM machines with novel DC-biased sinusoidal armature current," <i>2016 IEEE Energy Conversion Congress and Exposition (ECCE)</i> , Milwaukee, WI, 2016, pp. 1-8.
[JIA17]	S. Jia, R. Qu, D. Li, J. Li, and W. Kong, "Improved torque capacity for flux

	modulated machines by injecting DC currents into the armature windings,” <i>IEEE Trans. Magn.</i> , vol. 53, no. 6, pp. 1-5, June 2017.
[JUS07]	H. Jussila, P. Salminen, M. Niemelä, and J. Pyrhönen, “Guidelines for designing concentrated winding fractional slot permanent magnet machines,” in <i>Int. Conf. on Power Eng.-Energy and Electr. Drives Proc.</i> , pp. 191-194, Apr. 2007.
[KAN09]	G. Kang, J. Hur, W. Kim, and B. Lee, “The shape design of interior type permanent magnet BLDC motor for minimization of mechanical vibration,” <i>2009 IEEE Energy Conversion Congress and Exposition</i> , 2009, pp. 2409-2414.
[KAN17]	D. Kang, “Analysis of vibration and performance considering demagnetization phenomenon of the interior permanent magnet motor,” <i>IEEE Trans. Magn.</i> , vol. 53, no. 11, pp. 1-7, Nov. 2017.
[KAW09]	Y. Kawase, T. Yamaguchi, Z. Tu, M. Mizuno, N. Minoshima, and M. Watanabe, “Electrical loss and temperature analysis of interior permanent magnet motor with divided magnets,” <i>2009 International Conference on Electrical Machines and Systems</i> , 2009, pp. 1-4.
[KEF10]	L. Kefsi, Y. Touzani, and M. Gabsi, “Hybrid excitation synchronous motor control with a new flux weakening strategy,” <i>2010 IEEE Vehicle Power and Propulsion Conference</i> , 2010, pp. 1-5.
[KHA14]	F. Khan, E. Sulaiman, and M. Z. Ahmad, “Coil test analysis of wound-field three-phase flux switching machine with non-overlapping winding and salient rotor,” in <i>Proc. IEEE 8th Int. Power Eng. Optim. Conf. (PEOCO2014)</i> , Langkawi, 2014, pp. 243-247.
[KIM05]	T. H. Kim, S. H. Won, K. Bong, and J. Lee, “Reduction of cogging torque in flux-reversal machine by rotor teeth pairing,” <i>IEEE Trans. Magn.</i> , vol. 41, no. 10, pp. 3964-3966, Oct. 2005.
[KOS10]	T. Kosaka, M. Sridharbabu, M. Yamamoto, and N. Matsui, “Design studies on hybrid excitation motor for spindle drive in machine tools,” <i>IEEE Trans. Ind. Electron.</i> , vol. 57, no. 11, pp. 3807-3013, Nov. 2010.
[LEE18]	C. Lee, K. T. Chau, C. Liu, and C. C. Chan, “Overview of magnetless brushless machines,” <i>IET Elect. Power Appl.</i> , vol. 12, no. 8, pp. 1117–1125, Aug. 2018.
[LI10]	J. Li, K. T. Chau, J. Z. Jiang, C. Liu, and W. Li, “A new efficient permanent-magnet vernier machine for wind power generation,” <i>IEEE Trans. Magn.</i> , vol. 46, no. 6, pp. 1475-1478, June 2010.
[LI16]	Y. X. Li, Z. Q. Zhu, and G. Li, “Comparative study of voltage distortion in

	fractional-slot PM machines having different winding and stator configurations,” <i>2016 Eleventh International Conference on Ecological Vehicles and Renewable Energies (EVER)</i> , 2016, pp. 1-9.
[LI17]	Y. X. Li, Q. F. Lu, and Z. Q. Zhu, “Unbalanced magnetic force prediction in permanent magnet machines with rotor eccentricity by improved superposition method,” <i>IET Elec. Power Appl.</i> , vol. 11, no. 6, 2017.
[LI95]	Y. Li and T. A. Lipo, “A doubly salient permanent magnet motor capable of field weakening,” <i>Proceedings of PESC '95 - Power Electronics Specialist Conference</i> , 1995, pp. 565-571 vol. 1.
[LIA05]	C. Z. Liaw, W. L. Soong, B. A. Welchko, and N. Ertugrul, “Uncontrolled generation in interior permanent-magnet machines,” <i>IEEE Trans. Ind. Appl.</i> , vol. 41, no. 4, pp. 945-954, July-Aug. 2005.
[LIA95]	Y. F. Liao, F. Liang, and T. A. Lipo, “A novel permanent magnet motor with doubly salient structure,” <i>IEEE Trans. Ind. Appl.</i> , vol. 31, no. 5, pp. 1069-1078, Sept.-Oct. 1995.
[LIU10]	C. Liu, K. T. Chau, and J. Z. Jiang, “A permanent-magnet hybrid brushless integrated starter-generator for hybrid electric vehicles,” <i>IEEE Trans. Ind. Electron.</i> , vol. 57, no. 12, pp. 4055-4065, Dec. 2010.
[LIU12a]	H. Liu, L. Xu, M. Shangguan, and W. N. Fu, “Finite element analysis of 1 MW high speed wound-rotor synchronous machine,” <i>IEEE Trans. Magn.</i> , vol. 48, no. 11, pp. 4650-4653, Nov. 2012.
[LIU12b]	X. Liu, Z. Q. Zhu, M. Hasegawa, A. Pride, and R. Deodhar, “Vibration and noise in novel variable flux reluctance machine with DC-field coil in stator,” in <i>Proc. Int. Conf. Power Electron. Motion Control</i> , Harbin, 2012, pp. 1100-1107.
[LUO00]	X. Luo and T. A. Lipo, “A synchronous/permanent magnet hybrid AC machine,” <i>IEEE Trans. Energy Convers.</i> , vol. 15, no. 2, pp. 203-210, June 2000.
[MA17]	J. Ma, Z. Q. Zhu, and L. Wu, “Influence of slot/pole combination and magnet thickness on unbalanced magnetic force in PM machines with different rotor eccentricities and magnetizations,” <i>2017 20th International Conference on Electrical Machines and Systems (ICEMS)</i> , 2017, pp. 1-6.
[MA18]	J. Ma and Z. Q. Zhu, “Mitigation of unbalanced magnetic force in a PM machine with asymmetric winding by inserting auxiliary slots,” <i>IEEE Trans. Ind. Appl.</i> , vol. 54, no. 5, pp. 4133-4146, 2018.
[MCC87]	F. B. McCarty, “Hybrid excited generator with flux control of consequent-pole rotor,” U.S. Patent No. 4656379, Apr. 04, 1987.

[MEC06]	B. C. Mecrow, T. J. Bedfrod, J. W. Bennett, and T. Celik, "The use of segmental rotors for 2 phase flux-switching motots," in <i>Proc. Int. Conf. Electr. Mach.</i> , Chania, Greece, 2006.
[MEL11]	P. Mellor, R. Wrobel, A. Mlot, T. Horseman, and D. Staton, "Influence of winding design on losses in brushless AC IPM propulsion motors," <i>2011 IEEE Energy Conversion Congress and Exposition</i> , 2011, pp. 2782-2789.
[NAK07]	K. Nakamura, K. Murota, and O. Ichinokura, "Characteristics of a novel switched reluctance motor having permanent magnets between the stator pole-tips," <i>2007 European Conference on Power Electronics and Applications</i> , 2007, pp. 1-5.
[NED11]	B. Nedjar, S. Hlioui, Y. Amara, L. Vido, M. Gabsi, and M. Lecrivain, "A new parallel double excitation synchronous machine," <i>IEEE Trans. Magn.</i> , vol. 47, no. 9, pp. 2252-2260, Sept. 2011.
[OJO97]	O. Ojo and Z. Wu, "Synchronous operation of a dual-winding reluctance generator," <i>IEEE Trans. Energy Convers.</i> , vol. 12, no. 4, pp. 357-362, Dec. 1997.
[OWE09]	R. L. Owen, Z. Q. Zhu, and G. W. Jewell, "Hybrid excited flux-switching permanent magnet machines," in <i>Proc. 2009 13th European Conference on Power Electronics and Applications</i> , Barcelona, 2009, pp. 1-10.
[OWE10]	R. Owen, Z. Q. Zhu, and G. Jewell, "Hybrid-excited flux-switching permanent-magnet machines with iron flux bridges," <i>IEEE Trans. Magn.</i> , vol. 46, no. 6, pp. 1726-1729, Jun. 2010.
[PAN14]	Y. Pang and Z. Q. Zhu, "Reduction of unbalanced magnetic force in 2-pole 3-slot permanent magnet machine," <i>7th IET International Conference on Power Electronics, Machines and Drives (PEMD 2014)</i> , 2014, pp. 1-6.
[PAT08]	N. Patin, L. Vido, E. Monmasson, J. Louis, M. Gabsi, and M. Lecrivain, "Control of a hybrid excitation synchronous generator for aircraft applications," <i>IEEE Trans. Ind. Electron.</i> , vol. 55, no. 10, pp. 3772-3783, Oct. 2008.
[PET15]	I. Petrov, P. Ponomarev, Y. Alexandrova, and J. Pyrhönen, "Unequal teeth widths for torque ripple reduction in permanent magnet synchronous machines with fractional-slot non-overlapping windings," <i>IEEE Trans. Magn.</i> , vol. 51, no. 2, pp. 1-9, Feb. 2015, Art. ID 8100309.
[POL06]	H. Polinder, F. F. A. van der Pijl, G. J. de Vilder, and P. J. Tavner, "Comparison of direct-drive and geared generator concepts for wind turbines," <i>IEEE Trans. Energy Convers.</i> , vol. 21, no. 3, pp. 725-733, Sept. 2006.

[POL99]	C. Pollock and M. Wallace, "The flux-switching motor, a DC motor without magnets or brushes," in <i>Proc. Conf. Rec. IEEE IAS Annu. Meeting</i> , 1999, pp. 1980-1987.
[POP13]	M. Popescu and D. G. Dorrell, "Skin effect and proximity losses in high speed brushless permanent magnet motors," <i>2013 IEEE Energy Conversion Congress and Exposition</i> , 2013, pp. 3520-3527.
[POT19]	N. Pothi, Z. Q. Zhu, and Y. Ren, "Comparison of flux-weakening control strategies of novel hybrid-excited doubly salient synchronous machines," <i>IEEE Trans. Ind. Appl.</i> , vol. 55, no. 4, pp. 3589-3597, July-Aug. 2019.
[RAM11]	T. Raminosoa, C. Gerada, and M. Galea, "Design considerations for a fault-tolerant flux-switching permanent-magnet machine," <i>IEEE Trans. Ind. Electron.</i> , vol. 58, no. 7, pp. 2818-2825, July 2011.
[RAU55]	S. E. Rauch and L. J. Johnson, "Design principles of flux-switch alternators," <i>AIEE Trans.</i> , pt. III, vol. 74, no. 3, pp. 1261-1268, Jan. 1955.
[SON20]	P. Song, W. Li, S. Mukundan, and N. C. Kar, "An overview of noise-vibration-harshness analysis for induction machines and permanent magnet synchronous machines," <i>2020 10th International Electric Drives Production Conference (EDPC)</i> , 2020, pp. 1-8.
[SOO02]	W. L. Soong and N. Ertugrul, "Field-weakening performance of interior permanent-magnet motors," <i>IEEE Trans. Ind. Appl.</i> , vol. 38, no. 5, pp. 1251-1258, Sept.-Oct. 2002.
[SOO94]	W. L. Soong and T. J. E. Miller, "Field-weakening performance of brushless synchronous AC motor drives," <i>IEE Proc. Elec. Power Appl.</i> , vol. 141, no. 6, pp. 331-340, Nov. 1994.
[STE92]	C. P. Steinmetz, "On the law of hysteresis", <i>Trans. Am. Inst. Electr. Eng.</i> , 1892, 9, (1), pp. 3-64.
[SUL11]	E. Sulaiman, T. Kosaka, and N. Matsui, "A new structure of 12slot-10pole field-excitation flux switching synchronous machine for hybrid electric vehicles," in <i>Proc. 14th European Conf. on Power Electronics and Applications</i> , Birmingham, 2011, pp. 1-10.
[SUL12]	E. B. Sulaiman, T. Kosaka, and N. Matsui, "Design study and experimental analysis of wound field flux switching motor for HEV applications," in <i>Proc. Int. Conf. Electr. Mach. (ICEM)</i> , Marseille, 2012, pp. 1269-1275.
[SUN19a]	X. Y. Sun and Z. Q. Zhu, "Reduction of open-circuit DC winding induced voltage in hybrid-excited switched-flux permanent magnet machine," in <i>Proc.</i>

	<i>Inter. Conf. Ecological Vehicles and Renewable Energies (EVER)</i> , Monaco, May 8-10, 2019, pp. 1-8.
[SUN19b]	X. Y. Sun and Z. Q. Zhu, "Analysis of open-circuit DC winding induced voltage in partitioned-stator hybrid-excited switched-flux machine," in <i>Proc. Inter. Conf. Ecological Vehicles and Renewable Energies (EVER)</i> , Monaco, May 8-10, 2019, pp. 1-8.
[SUN20a]	X. Y. Sun and Z. Q. Zhu, "Investigation of DC winding induced voltage in hybrid-excited switched-flux permanent magnet machine," <i>IEEE Trans. Ind. Appl.</i> , vol. 56, no. 4, pp. 3594-3603, July-Aug. 2020.
[SUN20b]	X. Y. Sun, Z. Q. Zhu, and F. R. Wei, "Voltage pulsation induced in DC field winding of different hybrid excitation switched flux machines," <i>2020 IEEE Energy Conversion Congress and Exposition (ECCE)</i> , Detroit, MI, USA, 2020, pp. 4681-4688.
[SUN20c]	X. Y. Sun and Z. Q. Zhu, "Analysis and suppression of on-load DC winding induced voltage in partitioned-stator hybrid-excited switched-flux machine," <i>10th IET International Conference on Power Electronics, Machines and Drives (PEMD 2020)</i> , Nottingham, 2020.
[SUN21a]	X. Y. Sun, Z. Q. Zhu, S. Cai, L. Wang, F. R. Wei, and B. Shao, "Influence of stator slot and rotor pole number combination on field winding induced voltage ripple in hybrid excitation switched flux machine," <i>IEEE Trans. Energy Convers.</i> , early access, doi: 10.1109/TEC.2020.3035258.
[SUN21b]	X. Y. Sun, Z. Q. Zhu, and F. R. Wei, "Voltage pulsation induced in DC field winding of different hybrid excitation switched flux machines," <i>IEEE Trans. Ind. Appl.</i> , revised and awaiting decision.
[SUN21c]	X. Y. Sun and Z. Q. Zhu, "Analysis of excitation winding induced EMF in non-overlapped stator wound field synchronous machine," <i>IEEE Trans. Energy Convers.</i> , awaiting revision.
[TAP03]	J. Tapia, F. Leonardi, and T. A. Lipo, "Consequent-pole permanent-magnet machine with extended field-weakening capability," <i>IEEE Trans. Ind. Appl.</i> , vol. 39, no. 6, pp. 1704-1709, Nov./Dec. 2003.
[TOD04]	H. Toda, Z. Xia, J. Wang, K. Atallah, and D. Howe, "Rotor eddy-current loss in permanent magnet brushless machines," <i>IEEE Trans. Magn.</i> , vol. 40, no. 4, pp. 2104-2106, July 2004.
[WAN19]	Y. Wang, M. Filippini, N. Bianchi, and P. Alotto, "A review on magnetic gears: topologies, computational models, and design aspects," <i>IEEE Trans. Ind. Appl.</i> ,

	vol. 55, no. 5, pp. 4557-4566, Sept.-Oct. 2019.
[WAN99]	C. Wang, S. A. Nasar, and I. Boldea, "Three-phase flux reversal machine (FRM)," <i>Proc. IEE. Elec. Power Appl.</i> , vol. 146, no. 2, pp. 139-146, Mar. 1999.
[WU14]	D. Wu, J. T. Shi, Z. Q. Zhu, and X. Liu, "Electromagnetic performance of novel synchronous machines with permanent magnets in stator yoke," <i>IEEE Trans. Magn.</i> , vol. 50, no. 9, Sep. 2014.
[WU15a]	D. Wu and Z. Q. Zhu, "On-load voltage distortion in fractional slot surface-mounted permanent magnet machines considering local magnetic saturation," <i>IEEE Trans. Magn.</i> , vol. 51, no. 8, pp. 1-10, Aug. 2015.
[WU15b]	D. Wu and Z. Q. Zhu, "Influence of slot and pole number combinations on voltage distortion in surface-mounted permanent magnet machines with local magnetic saturation," <i>IEEE Trans. Energy Convers.</i> , vol. 30, no. 4, pp. 1460-1471, Dec. 2015.
[WU16a]	D. Wu, Z. Q. Zhu, and X. Ge, "Effectiveness of terminal voltage distortion minimization methods in fractional slot surface-mounted permanent magnet machines considering local magnetic saturation," <i>IEEE Trans. Energy Convers.</i> , vol. 31, no. 3, pp. 1090-1099, Sept. 2016.
[WU16b]	D. Wu, Z. Q. Zhu, and W. Chu, "Reduction of on-load terminal voltage distortion in fractional slot interior permanent magnet machines," <i>IEEE Trans. Energy Convers.</i> , vol. 31, no. 3, pp. 1161-1169, Sept. 2016.
[WU17]	Z. Z. Wu and Z. Q. Zhu, "Design and analysis of a novel partitioned stator hybrid excitation machine," <i>Proc. Chin. Soc. Electr. Eng.</i> , 2017, 37, (22), pp. 6543-6556.
[WU18]	Z. Z. Wu, Z. Q. Zhu, C. Wang, J. C. Mipo, S. Personnaz, and P. Farah, "Influence of DC winding configuration on its induced voltage in wound field machines," <i>IEEE Trans. Energy Convers.</i> , vol. 33, no. 4, pp. 1825-1836, Dec. 2018.
[WU19a]	Z. Z. Wu, Z. Q. Zhu, C. Wang, J. C. Mipo, S. Personnaz, and P. Farah, "Reduction of open-circuit DC winding induced voltage in wound field switched flux machines by skewing," <i>IEEE Trans. Ind. Electron.</i> , vol. 66, no. 3, pp. 1715-1726, Mar. 2019.
[WU19b]	Z. Z. Wu, Z. Q. Zhu, W. Hua, S. Akehurst, X. F. Zhu, W. T. Zhang, J. Hu, H. Y. Li, and J. M. Zhu, "Analysis and suppression of induced voltage pulsation in DC winding of five-phase wound-field switched flux machines," <i>IEEE Trans. Energy Convers.</i> , vol. 34, no. 4, pp. 1890-1905, Dec. 2019.

[WU20]	Z. Z. Wu, Z. Q. Zhu, C. Wang, J. C. Mipo, S. Personnaz, and P. Farah, "Analysis and reduction of on-load DC winding induced voltage in wound field switched flux machines," <i>IEEE Trans. Ind. Electron.</i> , vol. 67, no. 4, pp. 2655-2666, Apr. 2020.
[XU16]	D. Xu, M. Lin, X. Fu, L. Hao, W. Zhang, and N. Li, "Cogging torque reduction of a hybrid axial field flux-switching permanent-magnet machine with three methods," <i>IEEE Trans. Appl. Supercond.</i> , vol. 26, no. 4, pp. 1-5, June 2016.
[XUE16]	S. Xue, W. Q. Chu, Z. Q. Zhu, J. Peng, S. Guo, and J. Feng, "Iron loss calculation considering temperature influence in non-oriented steel laminations", <i>IET Sci. Meas. Technol.</i> , vol. 10, 2016, pp. 846-854.
[YAH14]	K. Yahia, D. Matos, J. O. Estima, and A. J. M. Cardoso, "Modeling synchronous reluctance motors including saturation, iron losses and mechanical losses," <i>2014 International Symposium on Power Electronics, Electrical Drives, Automation and Motion</i> , 2014, pp. 601-606.
[YAN14]	H. Yang and Y. Chen, "Influence of radial force harmonics with low mode number on electromagnetic vibration of PMSM," <i>IEEE Trans. Energy Convers.</i> , vol. 29, no. 1, pp. 38-45, Mar. 2014.
[YU15]	C. Yu and S. Niu, "Development of a magnetless flux switching machine for rooftop wind power generation," <i>IEEE Trans. Energy Convers.</i> , vol. 30, no. 4, pp. 1703-1711, Dec. 2015.
[ZHA12]	Z. Zhang, Y. Tao, and Y. Yan, "Investigation of a new topology of hybrid excitation doubly salient brushless dc generator," <i>IEEE Trans. Ind. Electron.</i> , vol. 59, no. 6, pp. 2550-2556, Jun. 2012.
[ZHA15a]	G. Zhang, W. Hua, M. Cheng, J. Liao, K. Wang, and J. Zhang, "Investigation of an improved hybrid-excitation flux-switching brushless machine for HEV/EV applications," <i>IEEE Trans. Ind. Appl.</i> , vol. 51, no. 5, pp. 3791-3799, Sept.-Oct. 2015.
[ZHA15b]	J. Zhao, M. Lin, D. Xu, L. Hao, and W. Zhang, "Vector control of a hybrid axial field flux-switching permanent magnet machine based on particle swarm optimization," <i>IEEE Trans. Magn.</i> , vol. 51, no. 11, pp. 1-4, Nov. 2015.
[ZHA16]	G. Zhang, W. Hua, M. Cheng, and J. Liao, "Design and comparison of two six-phase hybrid-excited flux-switching machines for EV/HEV applications," <i>IEEE Trans. Ind. Electron.</i> , vol. 63, no. 1, pp. 481-493, Jan. 2016.
[ZHA17]	G. Zhao, W. Hua, X. Zhu, and G. Zhang, "The influence of dummy slots on stator surface-mounted permanent magnet machines," <i>IEEE Trans. Magn.</i> , vol.

	53, no. 6, pp. 1-5, June 2017.
[ZHA18]	Z. Zhang, Y. Liu, and J. Li, "A HESM-based variable frequency AC starter-generator system for aircraft applications," <i>IEEE Trans. Energy Convers.</i> , vol. 33, no. 4, pp. 1998-2006, Dec. 2018.
[ZHA20]	W. Zhang, Z. Wu, W. Hua, and Z. Q. Zhu, "Reduction of open-circuit DC winding induced voltage and torque pulsation in the wound field switched flux machine by stator axial pairing of tooth-tips," <i>2020 International Conference on Electrical Machines (ICEM)</i> , 2020, pp. 522-528.
[ZHA21]	W. Zhang, W. Hua, Z. Wu, G. Zhao, Y. Wang, and W. Xia, "Analysis of DC winding induced voltage in wound-field flux-switching machine with air-gap field modulation principle," <i>IEEE Trans. Ind. Electron.</i> , early access.
[ZHO12]	P. Zhou, D. Lin, Y. Xiao, N. Lambert, and M. A. Rahman, "Temperature-dependent demagnetization model of permanent magnets for finite element analysis," <i>IEEE Trans. Magn.</i> , vol. 48, no. 2, pp. 1031-1034, Feb. 2012.
[ZHO14a]	Y. J. Zhou and Z. Q. Zhu, "Comparison of low-cost single-phase wound-field switched-flux machines," <i>IEEE Trans. Ind. Appl.</i> , vol. 50, no. 5, pp. 3335-3345, Sept.-Oct. 2014.
[ZHO14b]	Y. J. Zhou and Z. Q. Zhu, "Comparison of wound-field switched-flux machines," <i>IEEE Trans. Ind. Appl.</i> , vol. 50, no. 5, pp. 3314-3324, Sept.-Oct. 2014.
[ZHU00]	Z. Q. Zhu and D. Howe, "Influence of design parameters on cogging torque in permanent magnet machines," <i>IEEE Trans. Energy Convers.</i> , vol. 15, no. 4, pp. 407-412, Dec. 2000.
[ZHU05]	X. Y. Zhu and M. Cheng, "A novel stator hybrid excited doubly salient permanent magnet brushless machine for electric vehicles," <i>2005 International Conference on Electrical Machines and Systems</i> , Nanjing, 2005, pp. 412-415, vol. 1.
[ZHU06]	X. Zhu, M. Cheng, W. Hua, J. Zhang, and W. Zhao, "Design and analysis of a new hybrid excited doubly salient machine capable of field control," <i>Conference Record of the 2006 IEEE Industry Applications Conference Forty-First IAS Annual Meeting</i> , Tampa, FL, 2006, pp. 2382-2389.
[ZHU07a]	Z. Q. Zhu and D. Howe, "Electrical machines and drives for electric, hybrid, and fuel cell vehicles," in <i>Proceedings of the IEEE</i> , vol. 95, no. 4, pp. 746-765, April 2007.
[ZHU07b]	Z. Q. Zhu, D. Ishak, D. Howe, and J. T. Chen, "Unbalanced magnetic forces in

	permanent-magnet brushless machines with diametrically asymmetric phase windings,” <i>IEEE Trans. Ind. Appl.</i> , vol. 43, no. 6, pp. 1544-1553, 2007.
[ZHU08]	Z. Q. Zhu, J. T. Chen, Y. Pang, D. Howe, S. Iwasaki, and R. Deodhar, “Analysis of a novel multi-tooth flux-switching PM brushless AC machine for high torque direct-drive applications,” <i>IEEE Trans. Magn.</i> , vol. 44, no. 11, pp. 4313-4316, Nov. 2008.
[ZHU09a]	L. Zhu, S. Z. Jiang, Z. Q. Zhu, and C. C. Chan, “Analytical methods for minimizing cogging torque in permanent-magnet machines,” <i>IEEE Trans. Magn.</i> , vol. 45, no. 4, pp. 2023-2031, Apr. 2009.
[ZHU09b]	Z. Q. Zhu, “A simple method for measuring cogging torque in permanent magnet machines,” <i>2009 IEEE Power & Energy Society General Meeting</i> , Calgary, AB, 2009, pp. 1-4.
[ZHU09c]	Z. Q. Zhu, A. S. Thomas, J. T. Chen, and G. W. Jewell, “Cogging torque in flux-switching permanent magnet machines,” <i>IEEE Trans. Magn.</i> , vol. 45, no. 10, pp. 4708-4711, Oct. 2009.
[ZHU15a]	Z. Q. Zhu, Y. J. Zhou, J. T. Chen, and J. E. Green, “Investigation of nonoverlapping stator wound-field synchronous machines,” <i>IEEE Trans. Energy Convers.</i> , vol. 30, no. 4, pp. 1420-1427, Dec. 2015.
[ZHU15b]	Z. Q. Zhu and D. Wu, “On-load voltage distortion in fractional-slot interior permanent magnet machines,” <i>IEEE Trans. Magn.</i> , vol. 51, no. 10, pp. 1-9, Oct. 2015.
[ZHU15c]	Z. Q. Zhu, D. Wu, M. C. Wu, and I. W. Lan, “Influence of on-load voltage distortion on torque-speed characteristic of interior permanent magnet machines,” <i>2015 IEEE Energy Conversion Congress and Exposition (ECCE)</i> , 2015, pp. 760-767.
[ZHU16a]	X. Zhu, W. Hua, and M. Cheng, “Cogging torque minimization in flux-switching permanent magnet machines by tooth chamfering,” <i>2016 IEEE Energy Conversion Congress and Exposition (ECCE)</i> , Milwaukee, WI, 2016, pp. 1-7.
[ZHU16b]	Z. Q. Zhu, B. Lee, and X. Liu, “Integrated field and armature current control strategy for variable flux reluctance machine using open winding,” <i>IEEE Trans. Ind. Appl.</i> , vol. 52, no. 2, pp. 1519-1529, Mar.-Apr. 2016.
[ZHU16c]	Z. Q. Zhu, D. Wu, and X. Ge, “Investigation of voltage distortion in fractional slot interior permanent magnet machines having different slot and pole number combinations,” <i>IEEE Trans. Energy Convers.</i> , vol. 31, no. 3, pp. 1192-1201,

	Sept. 2016.
[ZHU18a]	Z. Q. Zhu, H. Y. Li, R. Deodhar, A. Pride, and T. Sasaki, "Recent developments and comparative study of magnetically geared machines," <i>CES Trans. Electr. Mach. Syst.</i> , vol. 2, no. 1, pp. 13-22, Mar. 2018.
[ZHU18b]	M. Zhu, W. Hu, and N. C. Kar, "Acoustic noise-based uniform permanent-magnet demagnetization detection in SPMSM for high-performance PMSM drive," <i>IEEE Trans. Transp. Electrification</i> , vol. 4, no. 1, pp. 303-313, Mar. 2018.
[ZHU19a]	Z. Q. Zhu and S. Cai, "Hybrid excited permanent magnet machines for electric and hybrid electric vehicles," <i>CES Transactions on Electrical Machines and Systems</i> , vol. 3, no. 3, pp. 233-247, Sept. 2019.
[ZHU19b]	Z. Q. Zhu, N. Pothi, P. L. Xu, and Y. Ren, "Uncontrolled generator fault protection of novel hybrid-excited doubly salient synchronous machines with field excitation current control," <i>IEEE Trans. Ind. Appl.</i> , vol. 55, no. 4, pp. 3598-3606, July-Aug. 2019.
[ZUL10]	A. Zulu, B. C. Mecrow, and M. Armstrong, "A wound-field three-phase flux-switching synchronous motor with all excitation sources on the stator," <i>IEEE Trans. Ind. Appl.</i> , vol. 46, no. 6, pp. 2363-2371, Nov.-Dec. 2010.
[ZWY09]	C. Zwysig, J. W. Kolar, and S. D. Round, "Megasp speed drive systems: pushing beyond 1 million r/min," <i>IEEE/ASME Trans. Mechatron.</i> , vol. 14, no. 5, pp. 564-574, Oct. 2009.

Appendix A: Potential to Eliminate Excitation Winding Induced EMF Using Open-Winding

The main purpose of this section is to illustrate the feasibility of an advanced winding topology for eliminating the excitation winding induced EMF, i.e., open-winding. In the previous analyses in chapter 2, the non-overlapped SWFSMs are equipped with two separated sets of windings, i.e., AC armature winding and DC excitation winding. In this section, the potential to eliminate the DC excitation winding and hence the corresponding induced EMF by open-winding topology is investigated. The open-winding topology is firstly employed in [ZHU16b] from the perspective of machine control to integrate the armature and excitation windings for a three-phase variable flux reluctance machine. In conventional three-phase machines, there is a neutral point in the star-connected three-phase armature windings, as shown in Fig. A.1. To inject the zero-sequence current component (DC excitation current) and the sinusoidal current component into a single coil, the neutral point is opened and each phase is connected to two inverters simultaneously, as shown in Fig. A.2.

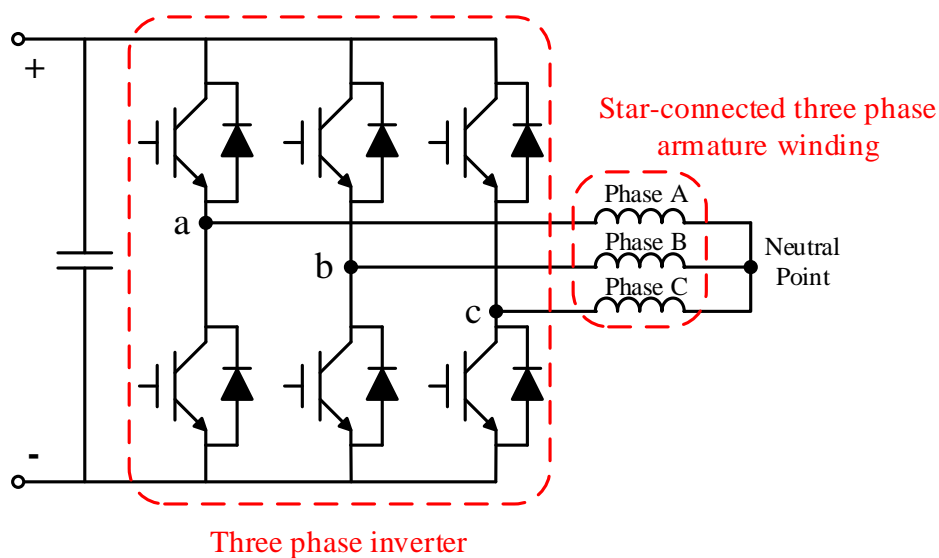


Fig. A.1. Conventional three phase voltage source inverter.

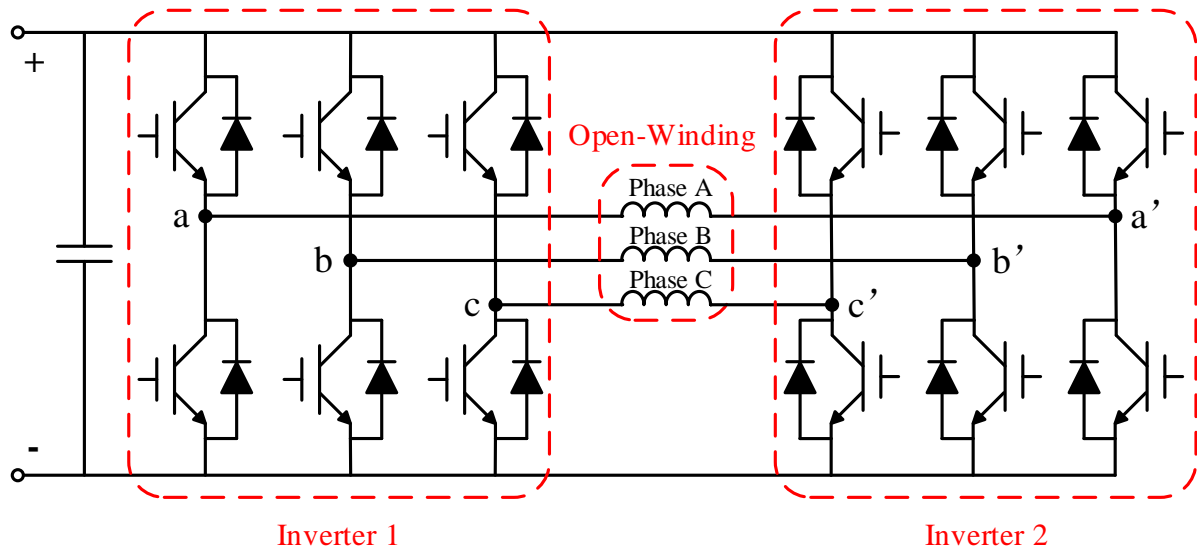
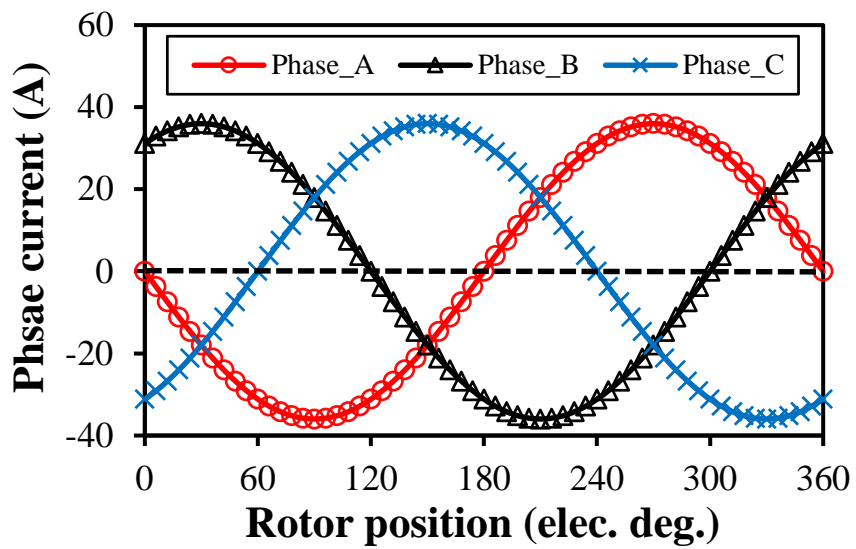
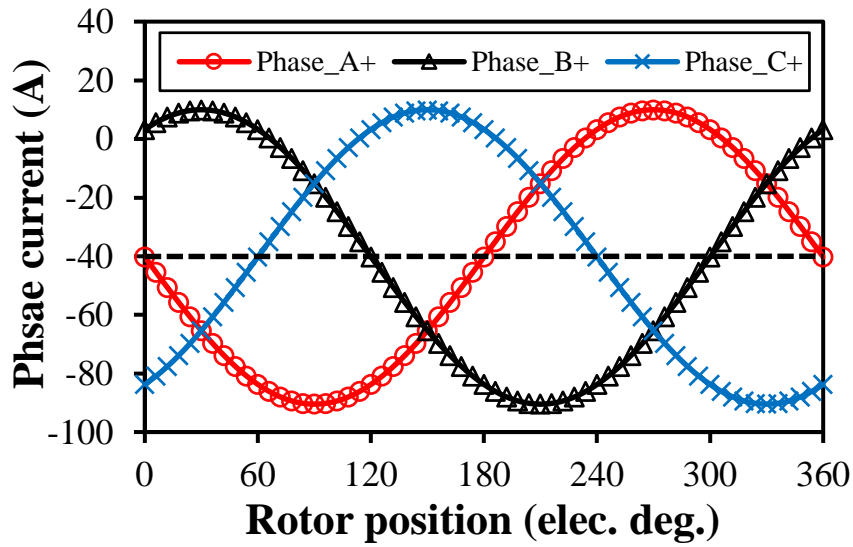


Fig. A.2. Open-winding inverter with a single voltage source.

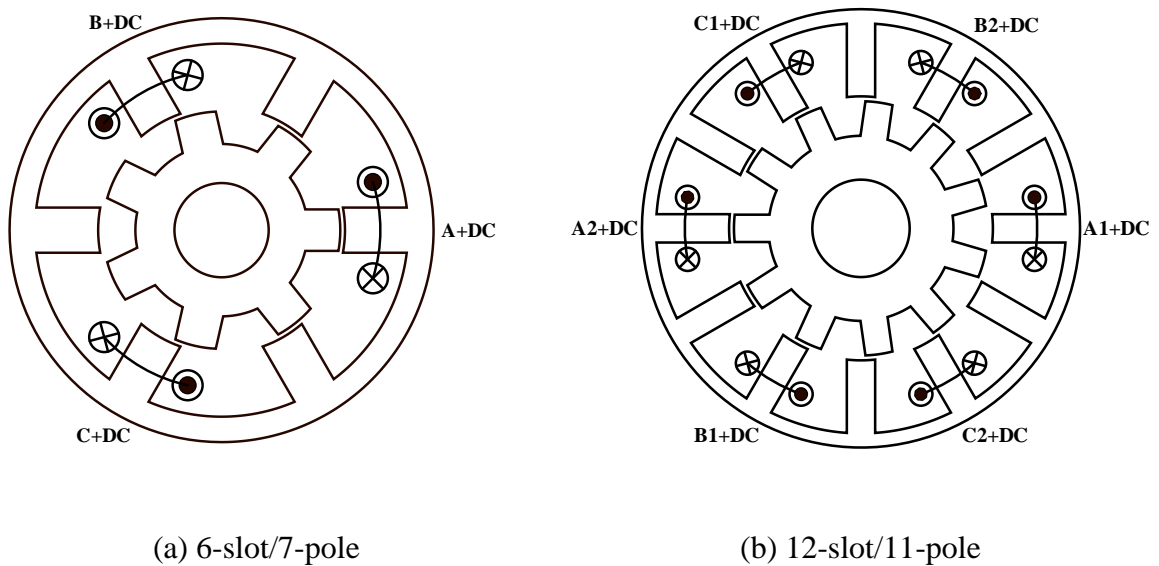


(a) Without DC bias



(b) With DC bias

Fig. A.3. Three-phase armature currents without and with DC bias.



(a) 6-slot/7-pole

(b) 12-slot/11-pole

Fig. A.4. Topology of three-phase non-overlapped SWFSMs with integrated armature and excitation windings.

For the SWFSMs with separated armature and excitation windings, symmetrical three-phase sinusoidal currents without DC bias are injected into the armature windings as shown in Fig. A.3(a). Besides, the excitation winding is separately excited by current source or H-bridge converter. By using the open-winding inverter in Fig. A.2, DC-biased sinusoidal current can be produced in a single coil, as shown in Fig. A.3(b), and it can be described by (A.1). As such,

the separated armature and excitation windings in Fig. 2.1 can be integrated as one set of winding through open-winding inverter, as illustrated in Fig. A.4. Consequently, the SWFSMs with open-winding topology are free from the excitation winding induced EMF since the excitation coils are removed. Meanwhile, the torque performance can be significantly improved using open-winding, which will be discussed later.

$$\begin{aligned}
I_a &= \sqrt{2}I_{ac} \cos(\omega_e t + \alpha) + I_{dc} \\
I_a &= \sqrt{2}I_{ac} \cos(\omega_e t + \alpha) + I_{dc} \\
I_b &= \sqrt{2}I_{ac} \cos(\omega_e t + \alpha - \frac{2\pi}{3}) + I_{dc} \\
I_c &= \sqrt{2}I_{ac} \cos(\omega_e t + \alpha + \frac{2\pi}{3}) + I_{dc}
\end{aligned} \tag{A.1}$$

where I_a , I_b and I_c are the three-phase armature currents. I_{ac} and I_{dc} are the root-mean-square (RMS) values of the AC and DC components, respectively. ω_e is the electrical angular velocity of the AC current component.

For the conventional three-phase sinusoidal currents without DC bias, the RMS value of the phase current is I_{ac} . While for the DC-biased three-phase sinusoidal currents in (A.1), the RMS value of the phase current I_{rms} can be expressed as

$$\begin{aligned}
I_{rms} &= \sqrt{\frac{1}{T} \int_0^T (\sqrt{2}I_{ac} \cos(\omega_e t) + I_{dc})^2 dt} \\
&= \sqrt{I_{ac}^2 + I_{dc}^2}
\end{aligned} \tag{A.2}$$

The current ratio k is defined as

$$k = \frac{I_{dc}}{I_{rms}} \tag{A.3}$$

Based on (A.2) and (A.3), the RMS value of the AC component can be expressed by

$$I_{ac} = \sqrt{(1 - k^2)} I_{rms} \quad (\text{A.4})$$

As illustrated in Fig. 2.2, the reluctance torque is negligible and therefore $i_d=0$ control is more suitable to achieve MTPA operation. In dq reference frame, the average torque T_{ave} of the SWFSMs under $i_d=0$ control can be described by,

$$\begin{aligned} T_{ave} &= \frac{3}{2} N_r (\Psi_d i_q - \Psi_q i_d) \\ T_{ave} &= \frac{3}{2} N_r (\Psi_d i_q - \Psi_q i_d) \\ &= \frac{3}{2} N_r M_{df} I_{dc} i_q \end{aligned} \quad (\text{A.5})$$

where N_r is the rotor pole number. Ψ_d and Ψ_q are the d -axis and q -axis flux-linkages. i_d and i_q are the d -axis and q -axis currents. M_{df} is the mutual inductance between the d -axis and the excitation winding.

Based on (A.1) to (A.4), the average torque in (A.5) can be rewritten as

$$T_{ave} = \frac{3}{2} \sqrt{2} N_r M_{df} k \sqrt{1 - k^2} I_{rms}^2 \quad (\text{A.6})$$

The optimal k for achieving the maximum average torque can be obtained by solving (A.7).

$$\frac{dT_{ave}}{dk} = 0 \quad (\text{A.7})$$

$$\frac{dT_{ave}}{dk} = \frac{3}{2} \sqrt{2} N_r M_{df} I_{rms}^2 \left(\sqrt{1 - k^2} - \frac{k^2}{\sqrt{1 - k^2}} \right) \quad (\text{A.8})$$

Based on (A.7) and (A.8), it can be found that the average torque reaches its maximum value when $k = \sqrt{2}/2 \approx 0.71$.

It should be noted that the numerical examples in the following analyses are based on the 12-slot/11-pole SWFSM operating at 400rpm. However, the open-winding technique can be equally applied to the SWFSMs having other stator slot and rotor pole number combinations to eliminate the excitation winding induced EMF and improve the torque performance.

The total copper loss (P_{cut}) of the SWFSMs with separated armature and excitation windings is fixed at 60W as aforementioned. To simplify the analysis and illustrate the benefits of open-winding topology, the geometric parameters of the 12-slot/11-pole SWFSM with open-winding topology remain the same as those listed in Table 2.1 and the total copper loss is fixed as 60W as well. As shown in Fig. A.5, the average torque varies against the current ratio under $P_{cut}=60W$ and the optimal current ratio for achieving the maximum average torque is 0.75, which is very close to the foregoing theoretical value.

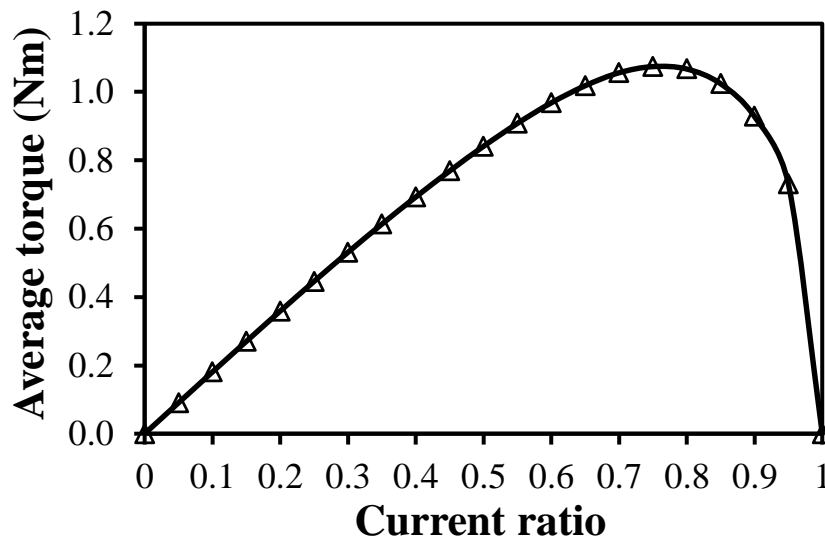
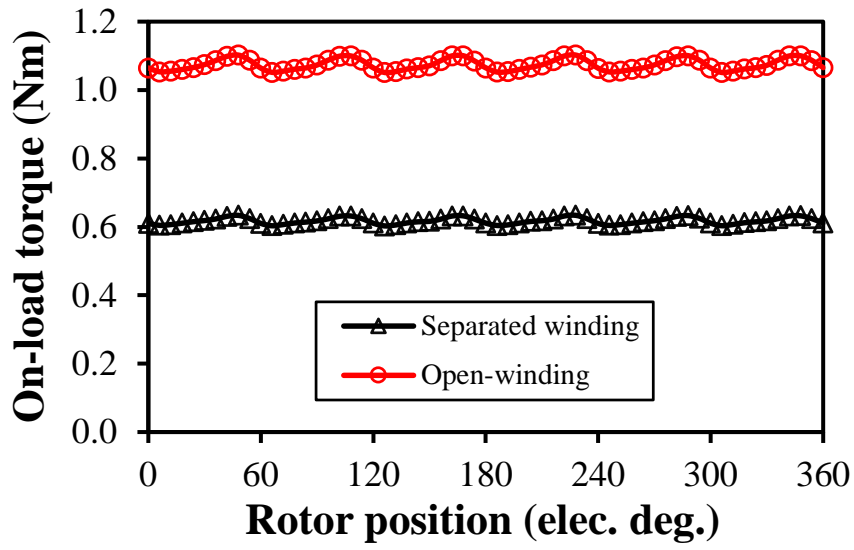
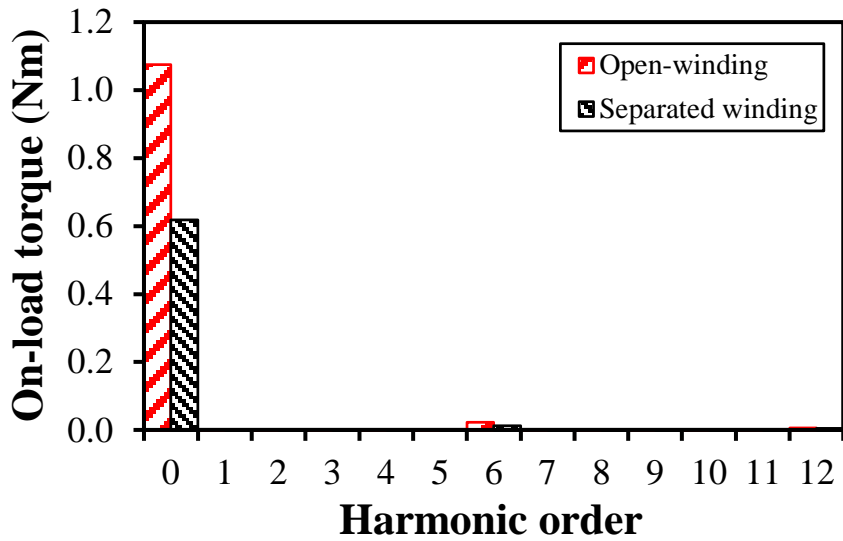


Fig. A.5. Average torque variation against current ratio of the SWFSM with open-winding under $P_{cut}=60W$.



(a) Waveforms



(b) Spectra

Fig. A.6. Optimal on-load torque waveforms of the SWFSM with separated and integrated windings under $P_{cut}=60W$.

Fig. A.6 compares the optimal on-load torque waveforms of the SWFSM with separated and integrated windings under $P_{cut}=60W$. It can be found that the maximum average torque is significantly increased from 0.62Nm to 1.07Nm by open-winding topology and the increase ratio is 73.88%. This is mainly because the conducting area for both AC and DC components is doubled due to the elimination of the excitation winding. Therefore, both AC and DC excitations are significantly increased under the same total copper loss. Besides, the torque ripple is also slightly reduced from 5.02% to 4.74% with open-winding topology due to significantly increased average torque, albeit with increased 6th torque ripple harmonic.

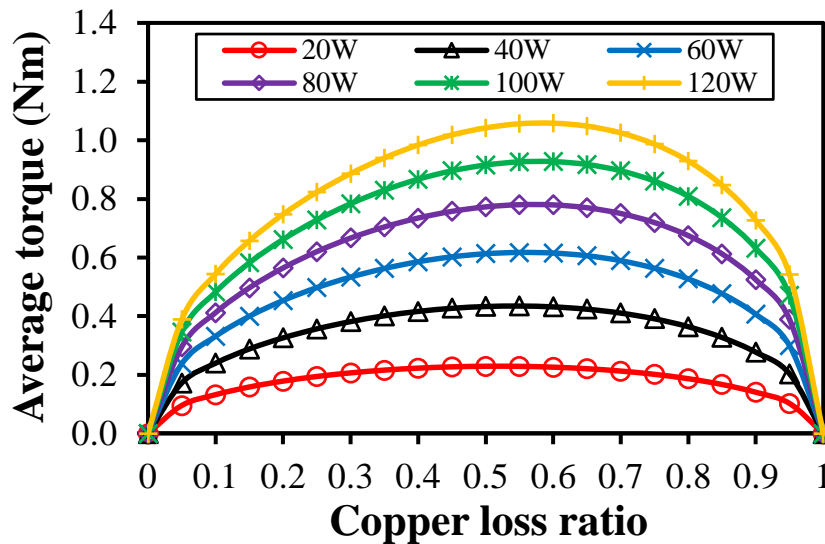


Fig. A.7. Average torque variations against copper loss ratio (P_{cu}/P_{cut}) of the SWFSM with separated excitation and armature windings under different P_{cut} .

For the SWFSMs with separated armature and excitation windings, the optimal excitation winding copper loss to total copper loss ratio (P_{cuf}/P_{cut}) is 0.5 under a fixed total copper loss, which can be derived by using similar derivations illustrated in [CHE10b]. Fig. A.7 shows the average torque variations against the copper loss ratio (P_{cuf}/P_{cut}) of the SWFSM with separated armature and excitation windings under different P_{cut} . It can be found that the optimal copper loss ratio for achieving the maximum average torque is very close to the theoretical value, i.e., 0.5 under low P_{cut} . However, it will be shifted away from 0.5 and become higher than 0.5 under high P_{cut} due to magnetic saturation. Fig. A.8 shows the average torque variations against the current ratio of the SWFSM with open-winding topology under different P_{cut} . It shows that the optimal current ratio for obtaining the maximum average torque is 0.75 for different P_{cut} , which further confirms the foregoing analytical result. However, it should be noted that the optimal current ratio may be changed under higher saturation levels, i.e., higher P_{cut} .

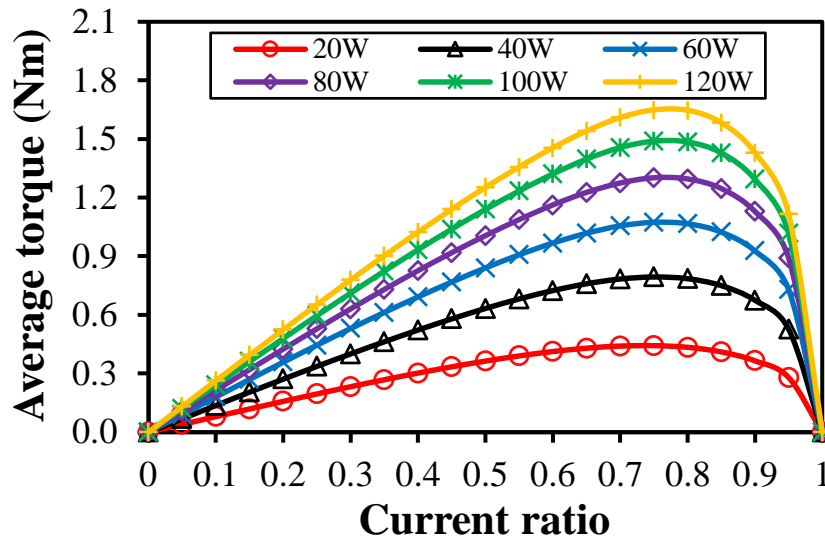


Fig. A.8. Average torque variations against current ratio k of the SWFSM with open-winding under different P_{cut} .

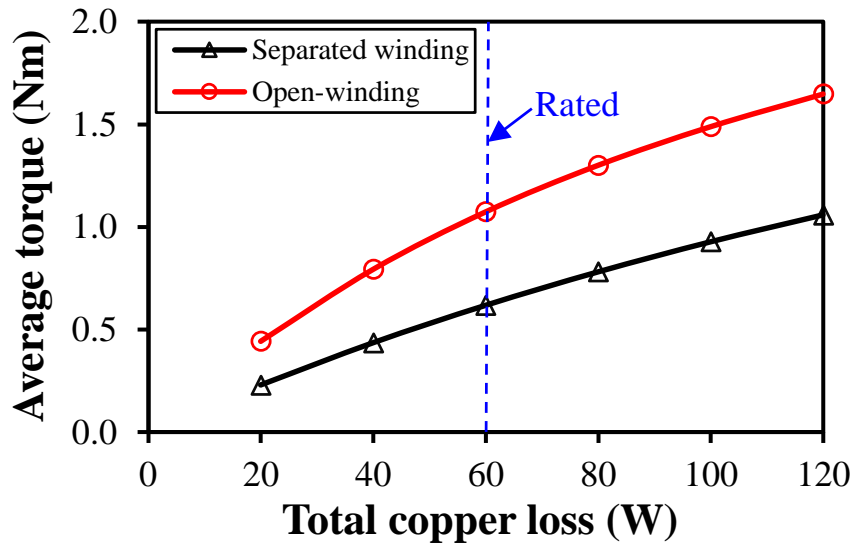


Fig. A.9. Maximum average torque of the SWFSM with separated and integrated windings against total copper loss.

Fig. A.9 compares the maximum average torque of the SWFSM with separated and integrated windings under different total copper losses. It reveals that by employing open-winding topology, the maximum average torque can be greatly enhanced under different P_{cut} , which confirms the benefits of open-winding.

Appendix B: Analytical Derivations of DC Winding Induced Voltage Harmonic Orders for HESFMs and PS-HESFMs

For the HESFMs in chapters 3 and 4 and the PS-HESFMs in chapter 5, the no-load field coil induced voltage ripple contains many harmonics with various orders. Therefore, the no-load induced voltage $v_{fm_no_load}$ of field coil f_m can be described by [WU19] [WU19a] [WU20],

$$v_{fm_no_load}(\theta_e) = \sum_{i=1,2,3,\dots}^{\infty} V_i \sin(i(\theta_e + \alpha_m) + \beta_i) \quad (\text{B. 1})$$

where V_i is the amplitude of the i^{th} induced voltage harmonic in the field coil. β_i is the corresponding initial phase. α_m is the electric angle in space between field coil f_i and f_m , which can be expressed as,

$$\alpha_m = \frac{2\pi N_r}{N_s} (m - 1) \quad (\text{B. 2})$$

The field winding is formed by connecting all field coils in series. Therefore, the no-load field winding induced voltage ripple v_{no_load} can be expressed as,

$$v_{no_load}(\theta_e) = \sum_{m=1,2,3,\dots}^{N_s} v_{fm_no_load} \quad (\text{B. 3})$$

Based on (B.1), (B.2), and (B.3), v_{no_load} can be simplified as,

$$v_{no_load}(\theta_e) = \sum_{i=1,2,3,\dots}^{\infty} V_i \frac{\sin(i\pi N_r)}{\sin(\frac{i\pi N_r}{N_s})} \sin(i\theta_e + \beta_i - i\frac{N_r\pi}{N_s} + iN_r\pi) \quad (\text{B. 4})$$

It can be found from (B.4) that the i^{th} induced voltage harmonic in field winding exists only when iN_r/N_s is an integer. Therefore, i can be described by,

$$i = \frac{\text{LCM}(N_s, N_r)}{N_s} k \quad (\text{B. 5})$$

where k is a positive integer.

If the magnetic saturation in stator and rotor laminations is neglected, the flux-linkage

captured by the filed winding due to the three-phase armature currents Ψ_{FAW} can be expressed by,

$$\begin{aligned}\Psi_{FAW}(\theta_e) &= \Psi_{FA}(\theta_e) + \Psi_{FB}(\theta_e) + \Psi_{FC}(\theta_e) \\ &= M_{AF}(\theta_e)I_a(\theta_e) + M_{BF}(\theta_e)I_b(\theta_e) + M_{CF}(\theta_e)I_c(\theta_e)\end{aligned}\quad (\text{B.6})$$

where Ψ_{FA} , Ψ_{FB} , and Ψ_{FC} are the flux-linkages captured by the filed winding due to the phase A-, B-, and C-currents, respectively. M_{AF} , M_{BF} , and M_{CF} are the mutual inductances between three-phase armature and field windings, respectively. I_a , I_b , and I_c are the three-phase armature winding currents, respectively, which can be given by,

$$\begin{aligned}I_a &= I_p \cos(\theta_e + \theta_a) \\ I_b &= I_p \cos(\theta_e - \frac{2\pi}{3} + \theta_a) \\ I_c &= I_p \cos(\theta_e - \frac{4\pi}{3} + \theta_a)\end{aligned}\quad (\text{B.7})$$

where I_p is the peak phase current. θ_a is the phase current angle.

In (B.6), the mutual inductances between three-phase armature and field windings can be further expressed by,

$$\begin{aligned}M_{AF}(\theta_e) &= \sum_{j=1,2,3,\dots}^{\infty} M_j k_{wj} \cos(j\theta_e + \beta_j) \\ M_{BF}(\theta_e) &= \sum_{j=1,2,3,\dots}^{\infty} M_j k_{wj} \cos(j(\theta_e - \frac{2\pi}{3}) + \beta_j) \\ M_{CF}(\theta_e) &= \sum_{j=1,2,3,\dots}^{\infty} M_j k_{wj} \cos(j(\theta_e - \frac{4\pi}{3}) + \beta_j)\end{aligned}\quad (\text{B.8})$$

where $M_j k_{wj}$ is the amplitude of the j^{th} harmonic of mutual inductance. k_{wj} is the winding factor of the j^{th} harmonic. β_j is the corresponding initial phase.

Based on (B.6), (B.7), and (B.8), the field winding induced voltage caused by the three-phase armature currents $v_{armature}$ can be simplified as,

$$v_{armature}(\theta_e) = \sum_{j=1,2,3,\dots}^{\infty} \frac{3}{2} I_p N_r \Omega M_j k_{wj} \times \begin{cases} -(j-1) \sin((j-1)\theta_e + \beta_j - \theta_a), & \text{when } j = 3m - 2 \\ -(j+1) \sin((j+1)\theta_e + \beta_j + \theta_a), & \text{when } j = 3m - 1 \\ 0, & \text{when } j = 3m \end{cases} \quad (\text{B. 9})$$

where Ω is the mechanical speed of the rotor. m is a positive integer.

When the field winding is excited by a voltage source, the field current ripple I_{rip} caused by the field winding induced voltage can be expressed by,

$$I_{rip}(\theta_e) = \frac{v_{no_load} + v_{armature}}{R_f + j2\pi fL} \quad (\text{B. 10})$$

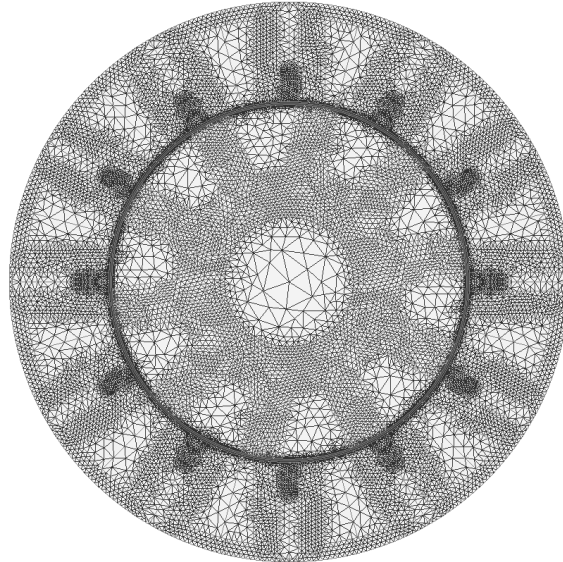
where f is the electrical frequency of the field winding induced voltage. L is the equivalent inductance of the field winding. R_f is the resistance of the field winding, which can be further expressed by,

$$R_f = \frac{2N_s \rho_{cu} l_a N_{dc}^2}{S_b k_f} \quad (\text{B. 11})$$

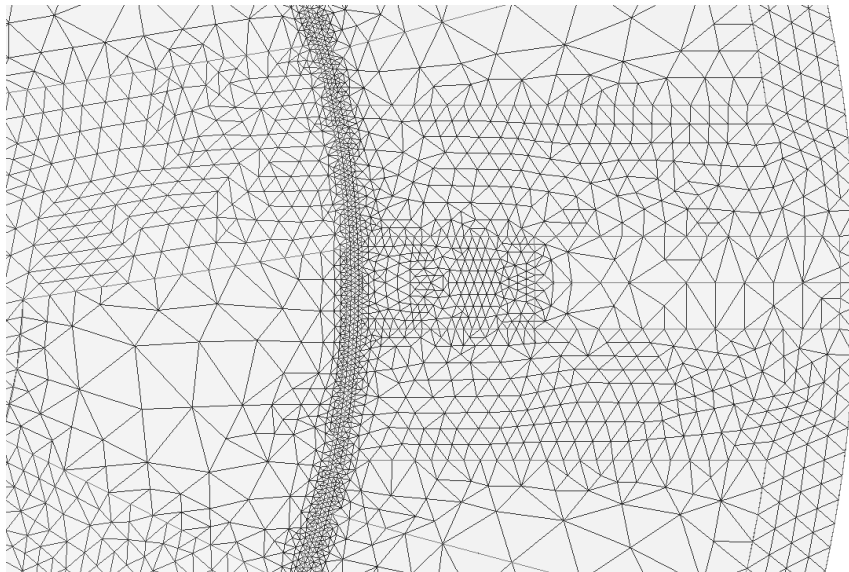
where ρ_{cu} is the resistivity of copper. l_a is the stack length. N_{dc} is the number of turns for each field coil. S_b is the slot area for field coil side. k_f is the field slot filling factor.

Appendix C: Mesh of the Investigated HE3 Machine

Fig. C.1 shows the mesh of the investigated HE3 machine in chapter 6.



(a) Whole machine



(b) Local zoom

Fig. C.1. Mesh of the investigated HE3 machine.

Publications

Journal papers:

- [J1] **X. Y. Sun**, Z. Q. Zhu, S. Cai, L. Wang, F. R. Wei, and B. Shao, “Influence of stator slot and rotor pole number combination on field winding induced voltage ripple in hybrid excitation switched flux machine,” *IEEE Trans. Energy Convers.*, vol. 36, no. 2, pp. 1245-1261, June 2021.
- [J2] **X. Y. Sun** and Z. Q. Zhu, “Investigation of DC winding induced voltage in hybrid-excited switched-flux permanent magnet machine,” *IEEE Trans. Ind. Appl.*, vol. 56, no. 4, pp. 3594-3603, July-Aug. 2020.
- [J3] **X. Y. Sun**, Z. Q. Zhu, and L. Xu, “Analysis of excitation winding induced EMF in non-overlapped stator wound field synchronous machine,” *IEEE Trans. Energy Convers.*, early access, doi: 10.1109/TEC.2021.3107593.
- [J4] **X. Y. Sun**, Z. Q. Zhu, and F. R. Wei, “Voltage pulsation induced in DC field winding of different hybrid excitation switched flux machines,” *IEEE Trans. Ind. Appl.*, vol. 57, no. 5, pp. 4815-4830, Sept.-Oct. 2021.

Conference papers:

- [C1] **X. Y. Sun**, Z. Q. Zhu, and F. R. Wei, “Voltage pulsation induced in DC field winding of different hybrid excitation switched flux machines,” *2020 IEEE Energy Conversion Congress and Exposition (ECCE)*, Detroit, MI, USA, 2020, pp. 4681-4688.
- [C2] **X. Y. Sun** and Z. Q. Zhu, “Analysis and suppression of on-load excitation winding voltage pulsating in partitioned-stator hybrid-excited switched-flux machine,” *10th IET International Conference on Power Electronics, Machines and Drives (PEMD 2020)*, Nottingham, 2020.
- [C3] **X. Y. Sun** and Z. Q. Zhu, “Reduction of open-circuit DC winding induced voltage in hybrid-excited switched-flux permanent magnet machine,” *2019 Fourteenth International Conference on Ecological Vehicles and Renewable Energies (EVER)*, Monte-Carlo, Monaco, 2019, pp. 1-8.
- [C4] **X. Y. Sun** and Z. Q. Zhu, “Analysis of open-circuit DC winding induced voltage in partitioned-stator hybrid-excited switched-flux machine,” *2019 Fourteenth International Conference on Ecological Vehicles and Renewable Energies (EVER)*, Monte-Carlo, Monaco, 2019, pp. 1-8.
- [C5] F. R. Wei, Z. Q. Zhu, and **X. Y. Sun**, “Investigation of asymmetric consequent-pole hybrid excited flux reversal machines,” *2020 IEEE Energy Conversion Congress and Exposition (ECCE)*, Detroit, MI, USA, 2020.